N°d'ordre NNT : 2024ISAL0017

THESE de DOCTORAT DE L'INSA LYON, membre de l'UNIVERSITE DE LYON

délivré en partenariat international avec
Tohoku University

Ecole Doctorale N° ED160
Électronique, Électrotechnique et Automatique
Spécialité / discipline de doctorat :
Génie Électrique

Soutenue publiquement le 01/02/2024, par :

Gaspard Taxil

Modeling, characterization and implementation of ferroelectric materials and their phase transitions for energy harvesting under extreme conditions

Devant le jury composé de :

Gautier Brice	Professeur/INSA Lyon	Président
Defay Emmanuel	Professeur/University of Luxembourg	Rapporteur
Kanno Isaku	Professeur/Kobe University	Rapporteur
Laffez Isabelle	Professeur/Université de Tours	Examinatrice
Lallart Mickaël	Professeur/INSA Lyon	Directeur de thèse
Ono Takahito	Professeur/Tohoku University	Directeur de thèse
Sebald Gaël	Professeur/INSA Lyon	Invité
Ducharne Benjamin	Maître de conférences/INSA Lyon	Invité

Thèse accessible à l'adresse : https://theses.insa-lyon.fr/publication/2024ISAL0017/these.pdf © [G. Taxil], [2024], INSA Lyon, tous droits réservés

Thèse accessible à l'adresse : https://theses.insa-lyon.fr/publication/2024ISAL0017/these.pdf © [G. Taxil], [2024], INSA Lyon, tous droits réservés

Département FEDORA – INSA Lyon - Ecoles Doctorales

SIGLE	ECOLE DOCTORALE	NOM ET COORDONNEES DU RESPONSABLE
ED 206 CHIMIE	**CHIMIE DE LYON** https://www.edchimie-lyon.fr Sec. : Renée EL MELHEM Bât. Blaise PASCAL, 3e étage secretariat@edchimie-lyon.fr	**M. Stéphane DANIELE** C2P2-CPE LYON-UMR 5265 Bâtiment F308, BP 2077 43 Boulevard du 11 novembre 1918 69616 Villeurbanne directeur@edchimie-lyon.fr
ED 341 E2M2	**ÉVOLUTION, ÉCOSYSTÈME, MICROBIOLOGIE, MODÉLISATION** http://e2m2.universite-lyon.fr Sec. : Bénédicte LANZA Bât. Atrium, UCB Lyon 1 Tél : 04.72.44.83.62 secretariat.e2m2@univ-lyon1.fr	**Mme Sandrine CHARLES** Université Claude Bernard Lyon 1 UFR Biosciences Bâtiment Mendel 43, boulevard du 11 Novembre 1918 69622 Villeurbanne CEDEX e2m2.codir@listes.univ-lyon1.fr
ED 205 EDISS	**INTERDISCIPLINAIRE SCIENCES-SANTÉ** http://ediss.universite-lyon.fr Sec. : Bénédicte LANZA Bât. Atrium, UCB Lyon 1 Tél : 04.72.44.83.62 secretariat.ediss@univ-lyon1.fr	**Mme Sylvie RICARD-BLUM** Laboratoire ICBMS - UMR 5246 CNRS - Université Lyon 1 Bâtiment Raulin - 2ème étage Nord 43 Boulevard du 11 novembre 1918 69622 Villeurbanne Cedex Tél : +33(0)4 72 44 82 32 sylvie.ricard-blum@univ-lyon1.fr
ED 34 EDML	**MATÉRIAUX DE LYON** http://ed34.universite-lyon.fr Sec. : Yann DE ORDENANA Tél : 04.72.18.62.44 yann.de-ordenana@ec-lyon.fr	**M. Stéphane BENAYOUN** Ecole Centrale de Lyon Laboratoire LTDS 36 avenue Guy de Collongue 69134 Ecully CEDEX Tél : 04.72.18.64.37 stephane.benayoun@ec-lyon.fr
ED 160 EEA	**ÉLECTRONIQUE, ÉLECTROTECHNIQUE, AUTOMATIQUE** https://edeea.universite-lyon.fr Sec. : Philomène TRECOURT Bâtiment Direction INSA Lyon Tél : 04.72.43.71.70 secretariat.edeea@insa-lyon.fr	**M. Philippe DELACHARTRE** INSA LYON Laboratoire CREATIS Bâtiment Blaise Pascal, 7 avenue Jean Capelle 69621 Villeurbanne CEDEX Tél : 04.72.43.88.63 philippe.delachartre@insa-lyon.fr
ED 512 INFOMATHS	**INFORMATIQUE ET MATHÉMATIQUES** http://edinfomaths.universite-lyon.fr Sec. : Renée EL MELHEM Bât. Blaise PASCAL, 3e étage Tél : 04.72.43.80.46 infomaths@univ-lyon1.fr	**M. Hamamache KHEDDOUCI** Université Claude Bernard Lyon 1 Bât. Nautibus 43, Boulevard du 11 novembre 1918 69 622 Villeurbanne Cedex France Tél : 04.72.44.83.69 direction.infomaths@listes.univ-lyon1.fr
ED 162 MEGA	**MÉCANIQUE, ÉNERGÉTIQUE, GÉNIE CIVIL, ACOUSTIQUE** http://edmega.universite-lyon.fr Sec. : Philomène TRECOURT Tél : 04.72.43.71.70 Bâtiment Direction INSA Lyon mega@insa-lyon.fr	**M. Etienne PARIZET** INSA Lyon Laboratoire LVA Bâtiment St. Exupéry 25 bis av. Jean Capelle 69621 Villeurbanne CEDEX etienne.parizet@insa-lyon.fr
ED 483 ScSo	**ScSo**[1] https://edsciencessociales.universite-lyon.fr Sec. : Mélina FAVETON Tél : 04.78.69.77.79 melina.faveton@univ-lyon2.fr	**M. Bruno MILLY** (INSA : J.Y. TOUSSAINT) Univ. Lyon 2 Campus Berges du Rhône 18, quai Claude Bernard 69365 LYON CEDEX 07 Bureau BEL 319 bruno.milly@univ-lyon2.fr

Thèse ~~accessible à l'adresse : https://theses.in~~sa-lyon.fr/publication/2024ISAL0017/these.pdf © [G. Taxil], [2024], INSA Lyon, tous droits réservés

[1] ScSo : Histoire, Géographie, Aménagement, Urbanisme, Archéologie, Science politique, Sociologie, Anthropologie

Thèse accessible à l'adresse : https://theses.insa-lyon.fr/publication/2024ISAL0017/these.pdf © [G. Taxil], [2024], INSA Lyon, tous droits réservés

Abstract

Mechanical energy harvesting presents a viable approach for powering devices and sensors, particularly given the rising prevalence of interconnected devices. Despite the abundance of sudden pulsed mechanical energy sources in the environment, such as footsteps, tires on road or door openings, non-resonant systems have not garnered substantial attention in the scientific community when compared to their resonant counterparts. One of the main challenges with such an approach is the requirement to maximize energy scavenging per cycle to make it viable. Thus, employing thermodynamic cycles allow to optimize the harvested energy. Moreover, leveraging nonlinearities, generally avoided in resonant systems, can lead to further improvement of the harvested energy. Then, comprehending the intrinsic mechanisms of the materials, assessing their electromechanical capabilities through such cycles, and incorporating them into prototypes are crucial steps for potential future applications.

Significant research efforts have been dedicated to the use of thermodynamic cycles to enhance output power. The Ericsson cycle, commonly known as the Olsen cycle in the realm of pyroelectric energy harvesting, has attracted attention due to its notable energy conversion capabilities. While this cycle has primarily been investigated for pyroelectric applications, its application in mechanical energy harvesting has been limited. The cycle involves two isostress processes and two isoelectric processes. These thermodynamic cycles present a viable solution for capturing energy from low-frequency sources (<10Hz) and non-resonant mechanical energy harvesting. The implementation of these cycles, coupled with the associated electrical interface, remains feasible even in degraded modes.

Within this framework, ferroelectric materials (a particular class of piezoelectric materials) show significant potential for use in mechanical energy harvesting as a transducer due to their outstanding properties. A noteworthy feature of these materials is their unique ability to maintain polarization even in the absence of an electric field. Another captivating aspect is their capacity to display phase transitions induced by variations of temperature, electric field, and stress, which yield significant change in the material properties that can be used in favor of energy harvesting enhancement. Exploiting these phase transitions emerges as a viable approach to enhance energy harvesting, given that the material's properties display non-linear characteristics in the vicinity of these transitions.

Understanding the intricate mechanism of phase transitions is challenging, and only a handful of theories successfully elucidate them. The Landau-Devonshire theory based on the mean-field approximation has been a good solution for describing ferroelectric materials. This formulation, recognized as the Landau-Devonshire theory, involves developing the free energy term through a power expansion of an order parameter, which is the polarization in the case of ferroelectric materials.

Based on this approach, Chapter 2 introduces a novel approach for simulating thermodynamic cycles in the context of pyroelectric and mechanical energy harvesting. The simulation results for pyroelectric energy harvesting are compared with

Thèse accessible à l'adresse : https://theses.insa-lyon.fr/publication/2024ISAL0017/these.pdf © [G. Taxil], [2024], INSA Lyon, tous droits réservés

existing literature, whereas the mechanical outcomes contribute to the analysis of the characterization results presented in Chapter 3.

Therefore, the subsequent chapter explores the characterization results obtained from diverse ferroelectric materials. Ericsson cycles were conducted under elevated stress levels and high electric fields. A comparative analysis among different materials revealed a convergence in the energy density of materials with increasing stress and electric field. Subsequently, attention was directed toward PMN-25PT and PZN-8PT single crystals due to their notably high energy density. Experimental testing and modeling of various operating temperatures were conducted using the simulation framework developed in Chapter 2. Optimal working temperatures, crucial for achieving high-level energy conversion, were successfully identified and predicted through simulation. The polarization mechanisms induced under these extreme conditions for energy harvesting are elucidated based on experimental and modeling results. Notably, results obtained at elevated stress levels suggest that operating along the polarization direction yields the most favorable outcomes, contrary to conclusions drawn in the case of domain-engineered crystals.

The final chapter centers on the practical implementation of ferroelectric materials in real devices, incorporating the high levels of stress and electric field identified through modeling and characterization. In the first device, operating in 33-mode, a substantial volume of materials was integrated into a smart tile. Ericsson cycles were conducted, and the output energy reached values as high as 800mJ per cycle. From a pragmatic standpoint, a passive electrical interface based on Bennet's doubler was implemented and compared to the Ericsson cycles in terms of output energy. This electrical energy management strategy proved to be effective, extracting nearly 40% of the energy from the Ericsson cycle while allowing a fully standalone operation. Comparative analysis with the state of the art revealed that the output energy surpassed existing results by nearly two decades. Subsequently, a cantilever beam-based device operating in 31-mode was presented, sharing similar objectives with the smart tile but with dimensions scaled down. Unfortunately, the results were not promising for energy harvesting applications under ultra-high levels and non-resonant conditions. The experiment indicated that the range of tensile stress applied was insufficient to induce depolarization, while higher stress will easily break the samples. Nevertheless, these results did not exclude the feasibility of 31-mode operating devices in non-resonant energy harvesting, especially with materials not bonded to a beam. By delving into the modeling, characterization, and implementation of ferroelectric materials, this study sheds light on their exceptional potential for achieving ultra-high energy conversion when exposed to significant levels of stress and electric field. The traditionally perceived counter-productive nonlinearities of polarization induced by these conditions have been shown to be an effective solution for devices operating in non-resonant conditions.

Thèse accessible à l'adresse : https://theses.insa-lyon.fr/publication/2024ISAL0017/these.pdf © [G. Taxil], [2024], INSA Lyon, tous droits réservés

Résumé

La récupération d'énergie mécanique présente une approche viable pour alimenter des appareils et des capteurs, en particulier compte tenu de l'augmentation croissante des dispositifs interconnectés. Malgré l'abondance de sources soudaines et intermittentes d'énergie mécanique dans l'environnement, telles que les pas, les pneus sur la route ou les ouvertures de porte, les systèmes non résonants n'ont pas suscité autant d'attention au sein de la communauté scientifique que leurs homologues résonants. L'un des principaux défis de cette approche réside dans la nécessité de maximiser la récupération d'énergie par cycle pour la rendre viable. Ainsi, l'utilisation de cycles thermodynamiques permet d'optimiser l'énergie récupérée. De plus, tirer parti des non-linéarités, généralement évitées dans les systèmes résonants, peut conduire à une amélioration supplémentaire de l'énergie récoltée. Comprendre les mécanismes intrinsèques des matériaux, évaluer leurs capacités électromécaniques à travers de tels cycles et les intégrer dans des prototypes sont donc des étapes cruciales pour des applications futures.

Des efforts de recherche significatifs ont été consacrés à l'exploitation des cycles thermodynamiques pour améliorer la puissance de sortie. Le cycle d'Ericsson, communément appelé cycle d'Olsen dans le domaine de la récupération d'énergie pyroélectrique, a attiré l'attention en raison de ses remarquables capacités de conversion d'énergie. Bien que ce cycle ait principalement été étudié pour des applications pyroélectriques, son application dans la récupération d'énergie mécanique reste limitée. Le cycle implique deux processus isostatiques et deux processus isoélectriques. Ces cycles thermodynamiques présentent une solution viable pour la récupération d'énergie avec des sources basse fréquence (<10 Hz) ou non résonante. L' implémentation de ces cycles, couplée à l'interface électrique associée, reste réalisable même en mode dégradé.

Dans ce cadre, les matériaux ferroélectriques (une classe particulière de matériaux piézoélectriques) montrent un potentiel significatif pour être utilisés dans la récupération d'énergie mécanique en tant que transducteurs en raison de leurs propriétés exceptionnelles. Une caractéristique notable de ces matériaux est leur capacité unique à maintenir une polarisation même en l'absence d'un champ électrique. Un aspect attractif est également leur capacité à afficher des transitions de phase induites par des variations de température, de champ électrique et de contrainte. Exploiter ces transitions de phase émerge comme une approche viable pour améliorer la récupération d'énergie, étant donné que les propriétés du matériau présentent des caractéristiques non linéaires à proximité de ces transitions.

La compréhension du mécanisme complexe des transitions de phase est difficile, et seules quelques théories les décrivent avec succès. La théorie de Landau-Devonshire basée sur l'approximation du champ moyen offre une bonne solution pour décrire les matériaux ferroélectriques. Cette formulation, connue sous le nom de théorie de Landau-Devonshire, implique le développement du terme d'énergie libre par un développement en puissance d'un paramètre d'ordre, qui est la polarisation dans le cas des matériaux ferroélectriques.

Thèse accessible à l'adresse : https://theses.insa-lyon.fr/publication/2024ISAL0017/these.pdf © [G. Taxil], [2024], INSA Lyon, tous droits réservés

Sur la base de cette approche, le chapitre 2 introduit une nouvelle approche pour simuler des cycles thermodynamiques dans le contexte de la récupération d'énergie pyroélectrique et mécanique. Les résultats de simulation pour la récupération d' énergie pyroélectrique sont comparés à la littérature existante, tandis que les résultats mécaniques contribuent à l'analyse des résultats de caractérisation présentés au chapitre 3.

Par conséquent, le chapitre suivant explore les résultats de caractérisation sur différents matériaux ferroélectriques. Des cycles d'Ericsson ont été réalisés sous des niveaux de contrainte et des champs électriques élevés. Une analyse comparative entre différents matériaux a révélé une convergence de la densité d'énergie des matériaux avec l'augmentation de la contrainte et du champ électrique. Ensuite, l'attention a été portée sur les cristaux de PMN-25PT et PZN-8PT en raison de leurs densités d'énergies particulièrement élevées. Des tests expérimentaux ainsi que la modélisation à différentes températures de fonctionnement ont été réalisés en utilisant le cadre de simulation développé au chapitre 2. Les températures de fonctionnement optimales, où la conversion d'énergie est la plus importante, ont été identifiées avec succès et prédites par simulation. Les mécanismes de polarisation induits dans ces conditions extrêmes pour la récupération d'énergie sont élucidés sur la base des résultats expérimentaux et de la modélisation. Notamment, les résultats obtenus à des niveaux de contrainte élevés suggèrent que fonctionner le long de la direction de polarisation produit les résultats les plus favorables, contrairement aux conclusions tirées dans le cas de l'ingénierie de domaine des cristaux ferroélectriques.

Le dernier chapitre se concentre sur la mise en œuvre pratique des matériaux ferroélectriques dans des dispositifs réels, intégrant les niveaux élevés de contrainte et de champ électrique identifiés par la modélisation et la caractérisation. Dans le premier dispositif, fonctionnant en mode 33, un large volume de matériaux a été intégrée dans une dalle intelligente. Les cycles d'Ericsson ont été réalisés, et l'énergie de sortie a atteint 800 mJ par cycle. D'un point de vue applicatif, une interface électrique passive basée sur le doubleur de Bennet a été mise en œuvre et comparée aux cycles Ericsson en termes d'énergie de sortie. Cette stratégie s'est avérée efficace, extrayant près de 40% de l'énergie du cycle d'Ericsson. Une analyse comparative avec l'état de l'art a révélé que l'énergie de sortie surpassait les résultats existants de près de deux ordres de grandeurs. Ensuite, un dispositif basé sur une poutre en porte-à-faux fonctionnant en mode 31 a été présenté, partageant des objectifs similaires avec la dalle intelligente. Malheureusement, les résultats n'ont pas été prometteurs pour des applications de récupération d'énergie dans des conditions extrêmes et non résonantes. L'expérience a indiqué que la plage de contrainte appliquée était insuffisante pour induire une dépolarisation suffisante, tandis qu'une contrainte plus élevée engendrait une rupture mécanique des échantillons. Néanmoins, ces résultats n'excluent pas la faisabilité de dispositifs fonctionnant en mode 31 dans la récupération d'énergie non résonante, en particulier avec des matériaux non liés à une poutre. En explorant la modélisation, la caractérisation et la mise en œuvre des matériaux ferroélectriques, cette étude met en lumière leur potentiel exceptionnel pour atteindre une conversion d'énergie ultra-élevée lorsqu'ils sont soumis à des niveaux significatifs de contrainte et de champ électrique. Les non-linéarités traditionnellement perçues comme contre-productives se sont révélées être une solution efficace pour les dispositifs fonctionnant dans des conditions non résonantes.

Thèse accessible à l'adresse : https://theses.insa-lyon.fr/publication/2024ISAL0017/these.pdf © [G. Taxil], [2024], INSA Lyon, tous droits réservés

Contents

French part **1**

1 Introduction **17**
1.1 Generalities on ferroelectricity . . . 18
1.1.1 Piezoelectricity . . . 18
1.1.2 Pyroelectricity . . . 19
1.1.3 Ferroelectricity . . . 20
1.1.4 Perovskite structure and ferroelectricity . . . 22
1.2 Modeling and theoretical aspects on ferroelectricity . . . 24
1.2.1 Spontaneous symmetry breaking and soft mode . . . 24
1.2.2 Landau-Devonshire theory . . . 25
1.2.3 Highly piezoelectric perovskites . . . 28
1.2.4 Polar nanoregions . . . 30
1.3 Energy harvesting . . . 32
1.3.1 Generalities on energy harvesting . . . 32
1.3.2 Pyroelectric energy harvesting . . . 33
1.3.3 Mechanical energy harvesting . . . 34
Electrostatic . . . 35
Electromagnetic . . . 36
Piezoelectric . . . 37
1.3.4 Structures for energy harvesting . . . 38
Stack structure . . . 38
Cantilever beam . . . 39
Plucked method . . . 39
Cymbal structure . . . 39
1.3.5 Non-resonant mechanical energy harvesting . . . 40
1.3.6 Thermodynamic cycles . . . 41
Pyroelectric cycles . . . 41
Mechanical cycles . . . 43
1.4 Context and objectives of the Ph.D . . . 45
1.4.1 FIESTA Project . . . 45
1.4.2 Objectives of the thesis . . . 46
1.4.3 Outline of the thesis . . . 47

2 Modeling for Pyroelectric and mechanical energy harvesting **49**
2.1 Pyroelectric energy harvesting . . . 50
2.1.1 Modeling of Olsen cycle . . . 50
2.1.2 Model . . . 51
2.1.3 Electrocaloric effect . . . 55
2.1.4 Energy harvesting . . . 59
2.2 Mechanical energy harvesting . . . 63
2.2.1 Modeling of Ericsson cycle . . . 64
2.2.2 Model for <001> orientation . . . 65

Thèse accessible à l'adresse : https://theses.insa-lyon.fr/publication/2024ISAL0017/these.pdf © [G. Taxil], [2024], INSA Lyon, tous droits réservés

2.3 Orientation in mechanical energy harvesting . . . 69
2.3.1 Model . . . 69
2.3.2 Piezoelectric coefficicient . . . 71
2.3.3 Low level vs High level energy harvesting . . . 73
2.4 Summary . . . 75

3 Experimental characterization **77**
3.1 Experimental methods . . . 78
3.1.1 Samples . . . 78
3.1.2 Test-bench . . . 79
3.1.3 Ericsson cycles and bipolar hysteresis loops . . . 81
3.2 Material comparisons . . . 83
3.2.1 Results . . . 84
3.2.2 Discussion . . . 87
3.3 <001> oriented crystals investigation . . . 88
3.3.1 Polarization under stress . . . 89
3.3.2 Polarization vs temperature . . . 90
3.3.3 Polarization under different thermodynamic conditions . . . 91
3.3.4 Operating temperature for energy harvesting . . . 95
3.4 <111> PMN-30PT . . . 99
3.5 Summary . . . 102

4 Device implementation **105**
4.1 Smart tile . . . 106
4.1.1 Design and fabrication . . . 106
4.1.2 Experimental methods . . . 109
4.1.3 Characterization results . . . 110
4.1.4 Electrical interface . . . 114
4.1.5 Comparison with the state of the art . . . 117
4.2 Device based on a cantilever . . . 120
4.2.1 Device fabrication and methods . . . 121
4.2.2 Modeling for stress evaluation . . . 125
Analytical stress evaluation . . . 125
Finite elements modeling . . . 128
4.2.3 Experimental results and discussion . . . 129
4.3 Summary . . . 135

5 Conclusion and perspectives **137**
5.1 Thesis summary . . . 137
5.2 Perspectives . . . 140

Publications **142**

Acknowledgements **145**

Bibliography **147**

Thèse accessible à l'adresse : https://theses.insa-lyon.fr/publication/2024ISAL0017/these.pdf © [G. Taxil], [2024], INSA Lyon, tous droits réservés

List of Figures

1 Comparaison entre les différentes sources d'énergies et leurs densités d'énergies [Ann+17] . . . 1
2 Exemple d'une courbe d'hystérésis d'un matériau ferroélectrique . . . 2
3 Illustration d'un cycle d'Ericsson (a) P-E (Polarisation-Champ électrique) cycle; (b) $\epsilon - \sigma$ (Déformation-Contrainte) cycle . . . 3
4 Les différentes orientations possibles de la polarisation pour les phases tétragonaux, orthorhombiques et rhomboédriques (de gauche à droite). (a) Configurations possibles sans champ électrique et contrainte appliqués ; (b) Configurations possibles lorsqu'un champ électrique est appliqué ; (c) Configurations possibles lorsqu'une contrainte uniaxiale est appliquée. Les flèches rouges représentent le champ électrique et les flèches noires représente la contrainte. . . . 6
5 (a) illustration schématique du banc expérimental [Tax+23]; (b) Photo du banc expérimental [Tax+23] . . . 7
6 Photo de tous les échantillons testés [Tun+22] . . . 8
7 Graphique de la composante de polarisation P_3 en fonction de la contrainte uniaxiale σ_3 et du champ électrique E_3 pour le PMN-25PT [Tax+23]. (a) Expérience à 20°C ; (b) Modélisation à 20°C ; (c) Expérience à 50°C ; (d) Modélisation à 50°C ; (e) Expérience à 80°C ; (f) Modélisation à 80°C. . . . 9
8 Graphique de la composante de polarisation P_3 en fonction de la contrainte uniaxiale σ_3 et du champ électrique E_3 pour le PZN-8PT [Tax+23]. (a) Expérience à 20°C ; (b) Modélisation à 20°C ; (c) Expérience à 50°C ; (d) Modélisation à 50°C ; (e) Expérience à 80°C ; (f) Modélisation à 80°C. . . . 10
9 Graphique de la densité d'énergie en fonction de la température de travail du cycle [Tax+23]. (a) Expérience pour le PMN-25PT ; (b) Modélisation pour le PMN-25PT ; (c) Expérience pour le PZN-8PT ; (d) Modélisation pour le PZN-8PT. . . . 11
10 (a) Schéma illustrant la dalle; (b) Photo du dispositif. . . . 12
11 Cycles d'Ericsson avec des vrais pas; (a) 500N; (b) 700N. . . . 13
12 (a) Circuit électrique du doubleur de Bennet; (b) Charge vs Tension avec le cycle d'Ericsson (ligne rouge) et doubleur de Bennet (ligne bleu) à 700N [Seb+23]. . . . 13
13 Tendance générale de l'énergie de sortie des dispositifs de récupération d'énergie piézoélectrique en fonction du volume des éléments piézoélectriques [Seb+23]. . . . 15

1.1 Illustration of the piezoelectric effect. (a) Direct piezoelectric effect; (b) converse piezoelectric effect. . . . 18
1.2 Pyroelectric effect representation . . . 19
1.3 Diagram presenting the relation between the materials . . . 20

Thèse accessible à l'adresse : https://theses.insa-lyon.fr/publication/2024ISAL0017/these.pdf © [G. Taxil], [2024], INSA Lyon, tous droits réservés

1.4 Example of an hysteresis curve of a ferroelectric material with associated quantities . . . 21
1.5 Illustration of the evolution of the domains of polarization during an hysteresis cycle . . . 22
1.6 (a) Illustration of a perovskite lattice cells; (b) Polarized tetragonal state 23
1.7 The different possible orientations of the polarization for a ferroelectric crystal. (a) Referential of the cubic basis of the crystal; (b) Tetragonal phase; (c) Orthorhombic state; (d) Rhombohedral phase. 23
1.8 Illustration of a spontaneous symmetry breaking. (a) Paraelectric metastable state; (b) Ferroelectric stable state . . . 25
1.9 Free energy of a ferroelectric material for different electric fields 27
1.10 Concentration−Temperature phase diagrams (a) $(1-x)PMN-xPT$; (b) $(1-x)PZN-xPT$ . . . 28
1.11 Illustration of the ferroelectric state depending on the crystal orientation 29
1.12 Illustration of the enhanced piezoelectric properties of ferrolectric relaxors. (a) Polarization rotation mechanisms; (b) Flat Gibbs free energy 30
1.13 Dielectric permittivity as a function of the electric field for different temperature for $KNa_{0.5}Nb_{0.5}0_3 - SrTiO_3$ ceramics [Liu+16]; (a) T=20°C; (b) T=140°C . . . 32
1.14 Comparison between the different energy sources and their energy densities [Ann+17] . . . 32
1.15 Illustration of the processes in energy harvesting . . . 33
1.16 Evolution of the number of scientific papers on pyroelectric energy harvesting. The data have been taken from "Web of Science" database (https://www.webofknowledge.com) . . . 34
1.17 (a) Electrostatic transduction method for energy harvesting [Zha+18]; (b) 3D schematic of the electrostatic energy harvester [Zha+18] . . . 36
1.18 (a) Electromagnetic transduction method [AC98]; (b) Flashlight powered by an electromagnetic generator (https://www.arborsci.com) . . 37
1.19 (a) A direct conversion microgenerator [Hug18]; (b) An inertial conversion microgenerator [Hug18] . . . 37
1.20 (a) A schematic illustration of a piezoelectric stack [Xu+18b]; (b) A photo of a piezoelectric stack . . . 38
1.21 (a) A schematic illustration of a cantilever beam [Xu+18b]; (b) A photo of a cantilever beam (cf. Chapter 4) . . . 39
1.22 (a) The plucked method [LS14]; (b) An inertial conversion microgenerator using cymbal structure [SK21] . . . 40
1.23 Illustration of the Tokyo subway implementation [VK15] . . . 41
1.24 Illustration of an Olsen cycle (a) P-E cycle; (b) S-T cycle . . . 42
1.25 Evolution of the polarization during an Olsen cycle . . . 43
1.26 Illustration of an Ericsson cycle (a) P-E cycle; (b) $\epsilon - \sigma$ cycle . . . 44
1.27 (a) Evolution of the number of connected devices with time [Dev]; (b) Energy harvesting comparison with FIESTA ambitions [Ann+17] . . . 46

2.1 (a) Modeling of an Olsen cycle [Tax+22]; (b) Temporal evolution of the temperature and of the electric field [Tax+22] . . . 50
2.2 Illustration of the crystal in the different orientations with the associates projection vector and basis [Tax+22]. (a) <001> Orientation; (b) <011> orientation; (c) <111> orientation . . . 54

Thèse accessible à l'adresse : https://theses.insa-lyon.fr/publication/2024ISAL0017/these.pdf © [G. Taxil], [2024], INSA Lyon, tous droits réservés

2.3 Electrocaloric effect for $BaTiO_3$ in function of the temperature for different applied electric fields [Tax+22]. (a) <001> orientation; (b) <011> orientation; (c) <111> orientation; (d) comparison between the three orientations. . . . 57
2.4 Electrocaloric effect for PMN-30PT in function of the temperature for different applied electric fields [Tax+22] (a) <001> orientation; (b) <011> orientation; (c) <111> orientation; (d) comparison between the three orientations. . . . 58
2.5 Harvested energy as a function of the working temperature T_l for PMN-30PT [Tax+22]. (a) <001> orientation; (d) <011> orientation; (g) <111> orientation. Temperature-Electric field phase diagram versus polarization for PMN-30PT. (b) <001> orientation; (e) <011> orientation; (h) <111> orientation. A plot of the associated P(E) cycles for PMN-30PT. (c) <001> orientation; (f) <011> orientation; (i) <111> orientation. . . . 60
2.6 Harvested energy as a function of the working temperature T_l for $BaTiO_3$ [Tax+22]. (a) <001> orientation; (d) <011> orientation; (g) <111> orientation. Temperature-Electric field phase diagram versus polarization for $BaTiO_3$. (b) <001> orientation; (e) <011> orientation; (h) <111> orientation. A plot of the associated P(E) cycles for $BaTiO_3$. (c) <001> orientation; (f) <011> orientation; (i) <111> orientation. . . . 61
2.7 Illustration of the different phase transitions possible for different crystal orientations [Tax+22]. . . . 62
2.8 A plot of the harvested energy in function of the temperature variation $T_h - T_l$ for an Olsen cycle with $E_i = 0kV/mm$ and $E_f = 2kV/mm$ for a <011> oriented single crystal of PZN-4.5PT and an electric field applied in the [110] direction [Tax+22; Kho+09a]. . . . 63
2.9 (a) Illustration of an Ericsson cycle [Tax+23]; (b) Temporal evolution of the stress and of the electric field . . . 64
2.10 The different possible orientations of polarization for tetragonal, orthorhombic and rhombohedral (left to right) single crystals. (a) Possible configurations without applied electric field and stress; (b) Possible configurations when an electric field is applied; (c) Possible configurations when an uniaxial stress is applied. Red arrows represent the electric field and black ones the stress . . . 67
2.11 Simulated phase diagram of $(1-x)PZN - xPT$ . . . 68
2.12 Illustration of the two basis and of the direction of the electric field and stress in these basis . . . 69
2.13 3D plot of the polarization P_3' in different orientations of $BaTiO_3$ (a) At 150K; (b) At 220K; (c) At 320K; (d) P_3' in particular crystal orientaions in function of the temperature . . . 71
2.14 3D plot of the d_{33} in different orientations of $BaTiO_3$ (a) At 150K; (b) At 220K; (c) At 320K; (d) Different piezoelectric coefficients in function of the temperature . . . 73
2.15 Illustration of the crystal symmetries of PMN-30PT (a) At 20°C; (b) At 100°C; 3D plot of the d_{33} in different orientations of PMN-30PT (c) At 20°C; (b) At 100°C; 3D plot of the harvested energy via Ericsson cycle in 33-mode in different orientations of PMN-30PT (e) At 20°C; (f) At 100°C . . . 74

3.1 Image of all the tested samples [Tun+22] . . . 79

Thèse accessible à l'adresse : https://theses.insa-lyon.fr/publication/2024ISAL0017/these.pdf © [G. Taxil], [2024], INSA Lyon, tous droits réservés

3.2 Dielectric permittivity as a function of the temperature of PMN-25PT . 80
3.3 (a) Schematic illustration of the test-bench [Tax+23]; (b) Photo of the test-bench [Tax+23] 80
3.4 Schematic diagram of the measurement system [Tun+22] 81
3.5 (a) Estimation of the Ericsson cycle from the bipolar hysteresis loops; (b) Real Ericsson cycle 82
3.6 (a) Voltage function for bipolar hysteresis loop; (b) Associated current; (c) Voltage and stress function for real Ericsson cycle; (d) Associated current 83
3.7 Real Ericsson cycles under intermediate levels of stress for different materials [Tun+22]. (a) PZT C203; (b) PZT C6; (c) PZT C9; (d) PMN-25PT; (e) PZN-8PT; (f) PMN 15 84
3.8 Real Ericsson cycles under high levels of stress for different materials [Tun+22]. (a) PZT C203; (b) PZT C6; (c) PZT C9; (d) PMN-25PT; (e) PZN-8PT; (f) PMN 15 85
3.9 Different materials with their associated energy densities under different levels (a) high levels; (b) Intermediate levels; (c) Low levels. . . . 86
3.10 Polarization mechanisms during an Ericsson cycle under high levels for PZN-8PT 87
3.11 Bipolar hysteresis loops under different uniaxial stress [Tax+23]; (a) PMN-25PT (b) PZN-8PT. Remnant and saturation polarization under different uniaxial stress [Tax+23]; (c) PMN-25PT; (d) PZN-8PT. 89
3.12 Bipolar hysteresis loops under different temperatures; (a) PMN-25PT (b) PZN-8PT. Remnant and saturation polarization under different temperatures; (c) PMN-25PT; (d) PZN-8PT. 90
3.13 Plot of the component of polarization P_3 depending of uniaxial stress σ_3 and electric field E_3 for PMN-25PT [Tax+23]. (a) Experiment at 20°C; (b) Modeling at 20°C; (c) Experiment at 50°C; (d) Modeling at 50°C; (e) Experiment at 80°C; (f) Modeling at 80°C. 92
3.14 Plot of the component of polarization P_3 depending of uniaxial stress σ_3 and electric field E_3 for PZN-8PT [Tax+23]. (a) Experiment at 20°C; (b) Modeling at 20°C; (c) Experiment at 50°C; (d) Modeling at 50°C; (e) Experiment at 80°C; (f) Modeling at 80°C. 93
3.15 Bipolar loops of PMN-25PT and PZN-8PT with their associated Ericcson cycle at different temperature [Tax+23]. (a) PMN-25PT at 20°C; (b) PZN-8PT at 20°C; (c) PMN-25PT at 60°C; (d) PZN-8PT at 60°C; (e) PMN-25PT at 100°C; (f) PZN-8PT at 100°C ; (g) PMN-25PT at 140°C; (h) PZN-8PT at 140°C. 96
3.16 Plot of the energy density depending of the temperature of work of the cycle [Tax+23]. (a) Experiment for PMN-25PT; (b) Modeling for PMN-25PT; (c) Experiment for PZN-8PT; (d) Modeling for PZN-8PT. . 97
3.17 Schematic illustration of the polarization mechanisms during an Ericsson cycle for PMN-25PT; (a) At 20°C; (b) At 60°C. 98
3.18 Schematic illustration of the polarization mechanisms during an Ericsson cycle for PZN-8PT; (a) At 20°C; (b) At 60°C. 99
3.19 (a) Illustration of a 1R domain engineered crystal; (b) Photo of a sample of PMN-30PT <111>-oriented crystals. 100
3.20 (a) Bipolar hysteresis loops under different uniaxial stress for PMN-30PT <111>-oriented crystal; (b) Remnant and saturation polarization under different uniaxial stress for PMN-30PT <111>-oriented crystal. . 100

Thèse accessible à l'adresse : https://theses.insa-lyon.fr/publication/2024ISAL0017/these.pdf © [G. Taxil], [2024], INSA Lyon, tous droits réservés

3.21 (a) Bipolar hysteresis loops of PMN-30PT <111>-oriented crystal with an associated Ericcson cycle at 100MPa; (b) Energy density as a function of applied stress for <001> PMN-25PT and <111> PMN-30PT. . . . 101
3.22 (a) histogram of the modeling and the experimental results of the energy harvested for an Ericsson cycle at 100MPa for <001> PMN-25PT and <111> PMN-30PT; (b) histogram of the modeling and experimental results of the d_{33} piezoelectric coeffificient for <001> PMN-25PT and <111> PMN-30PT 102

4.1 Schematic of the mechanical amplification system [Seb+23]. 106
4.2 Fabrication steps of the device 107
4.3 Fabrication steps of the device 108
4.4 (a) Photograph of device, with piezoelectric stacks mechanically assembled in series. The force is applied vertically on the top white plate, which is converted into a larger horizontal force squeezing the piezoelectric stacks [Seb+23]; Photograph of the device when stepping on it [Seb+23]. 108
4.5 (a) Piezoelectric stack illustration taken from "Digikey" (https://www.digikey.com); (b) Photo of the piezoelectric stack. 109
4.6 (a) Voltage and current as a function of time when performing an Ericsson cycle by stepping on the device; (b) Displacement as a function of time when performing an Ericsson cycle by stepping on the device. 110
4.7 (a) Bipolar cycles at 1 MPa and 100 MPa on a piezoelectric stack, with the estimated Ericsson cycle area in blue dotted line [Seb+23]; (b) Ericsson unipolar cycles on a piezoelectric stack [Seb+23]. 111
4.8 Ericsson cycles performed on the tile; (a) 100N; (b) 200N; (c) 300N; (d) 400N; (e) 500N; (f) 600N; (g) 700N 112
4.9 Stored mechanical energy (red curve) and converted energy (blue curve) as a function of the input force 113
4.10 Ericsson cycles with a true step; (a) 500N; (b) 700N. 114
4.11 (a) Bennet doubler electrical circuit; (b) Bennet doubler associated Q-V cycle. 115
4.12 (a) Equivalent electrical circuit during the charging process; (b) Equivalent electrical circuit during the discharging process 115
4.13 (a) Piezoelectric voltage as a function time [Seb+23]; (b) Associated stored energy as a function of time [Seb+23] 116
4.14 Charge vs voltage using Ericsson cycle (red line) and Bennet doubler (blue line) at 700N. 117
4.15 General trend of the output energy of piezoelectric energy harvesting devices, as a function of the volume of the piezoelectric elements [Seb+23]. 119
4.16 General trend of the output energy of piezoelectric energy harvesting systems, as a function of the volume of the devices. 120
4.17 Schematic illustration of an idealized Ericsson cycle with a cantilever beam. 121
4.18 Schematic illustration of the desired device. 122
4.19 Photographs of the beam steel. 122
4.20 Photographs of the epoxy glue and the associated mixture. 123
4.21 Different steps for the bonding of the materials on the beam. 123
4.22 Photographs of the full electromechanical cantilever beams mounted on the test-bench 124

Thèse accessible à l'adresse : https://theses.insa-lyon.fr/publication/2024ISAL0017/these.pdf © [G. Taxil], [2024], INSA Lyon, tous droits réservés

4.23 Photo of the test-bench . . . 125
4.24 (a) Force and voltage as a function of time for an Ericsson cycle with a beam deflection of 4mm; (b) Associated measured displacement. . . . 126
4.25 Schematic illustration of the beam and the piezoelectric material with different associated dimensions. . . . 127
4.26 (a) Calculated stresses as a function of x (longitudinal direction) and y (thickness direction) for a beam deflection of 4mm; (b) Calculated stress in the beam and in the material as a function of y for a beam deflection of 4mm at x=15mm. . . . 128
4.27 (a) Finite elements simulation of the Von Mises stress distribution in the global device for a beam deflection of 4mm; (b) Finite elements simulation of the Von Mises stress distribution in a slice in the xy plane of the piezoelectric material for a deflection of 4mm. . . . 129
4.28 (a) Bipolar hysteresis curves of PZT C9 under tensile stress; (b) Bipolar hysteresis curves of PZT C9 under compressive stress . . . 130
4.29 Bipolar hysteresis curves of PZN-8PT ([100] and [010] lateral crystal directions) under tensile stress . . . 131
4.30 Bipolar Real Ericsson cycles on PZN-8PT ([100] and [010] lateral crystal directions) under different beam deflections. (a) 2mm; (b) 4mm. . . . 132
4.31 (a) Oscillating forces as a function of time for different beam deflections; (b) Associated variation of polarizations as a function of time for different beam deflections . . . 133
4.32 (a) Polarization variations as a function of the beam deflections (b) Polarization variations as a function of the associated calculated tensile stresses. . . . 133
4.33 Finite elements simulation of the Von Mises stress distribution for a beam deflection of 4mm with different thicknesses of epoxy glue. (a) 5 μm; (b) 20 μm; (c) 50 μm; (d) 100 μm. . . . 134

Thèse accessible à l'adresse : https://theses.insa-lyon.fr/publication/2024ISAL0017/these.pdf © [G. Taxil], [2024], INSA Lyon, tous droits réservés

List of Tables

1 Propriétés des différentes phases ferroélectriques 5

1.1 Domain configuration names depending on crystal orientations 29
1.2 Piezoelectric coefficients for different materials and crystal orientations at room temperature 30
1.3 comparison of different vibration sources with their associated accelerations and frequencies [RWR03] 35

2.1 Properties of the different ferroelectric phases 53
2.2 List of Landau coefficients and physical properties [Tax+22] 53
2.3 Properties of the different ferroelectric phases [Tax+23] 66
2.4 List of Landau coefficients and physical properties [Tax+23] 68

3.1 Properties of the different ferroelectric materials at room temperature [Tun+22] 78

4.1 Different tests and their corresponding energies 111
4.2 Examples of energy harvesting prototypes, with their piezoelectric elements volume, and the output energy per cycle [Seb+23]. 118
4.3 Properties and dimensions of the piezoelectric materials and the steel beam. 127

Thèse accessible à l'adresse : https://theses.insa-lyon.fr/publication/2024ISAL0017/these.pdf © [G. Taxil], [2024], INSA Lyon, tous droits réservés

Thèse accessible à l'adresse : https://theses.insa-lyon.fr/publication/2024ISAL0017/these.pdf © [G. Taxil], [2024], INSA Lyon, tous droits réservés

French part

Introduction

La récupération d'énergie à partir de sources d'énergies ambiantes représente une approche prometteuse pour alimenter des capteurs sans fil et d'autres dispositifs à faible consommation, en particulier dans des environnements difficiles ou isolés. Cette méthode présente des avantages notables, notamment en termes de rentabilité et d'élimination des tâches de maintenance telles que le remplacement des batteries, souvent nécessaire en raison de leur auto-décharge. Par conséquent, on a constaté une augmentation des efforts de recherche à la fois au niveau académique et industriel et développement axés sur la récupération d'énergie au cours des dernières décennies. Cette poussée est largement stimulée par la prolifération de l'Internet des Objets (IoT), qui nécessite l'interconnexion de nombreux dispositifs à faible consommation capables d'échanger des données de manière autonome. Diverses formes d'énergies présentes dans l'environnement tel que les vibrations, le rayonnement solaire, le vent et la chaleur résiduelle, peuvent être récupérées et converties en énergie électrique. Dans le contexte actuel du réchauffement climatique et de la nécessité pour l'humanité d'utiliser des énergies plus propres, la récupération d'énergie est une bonne solution alternative. Cependant, elle souffre d'une faible puissance de sortie et les efforts de recherche se sont donc concentrés sur l'augmentation de l'énergie produite [KKK18; RYK19; Dha+13]. Une comparaison illustrant la densité de puissance entre diverses sources d'énergie et types de récupération d'énergie est présentée dans la Figure 1. En récupération d'énergie, les sources d'énergie mé-

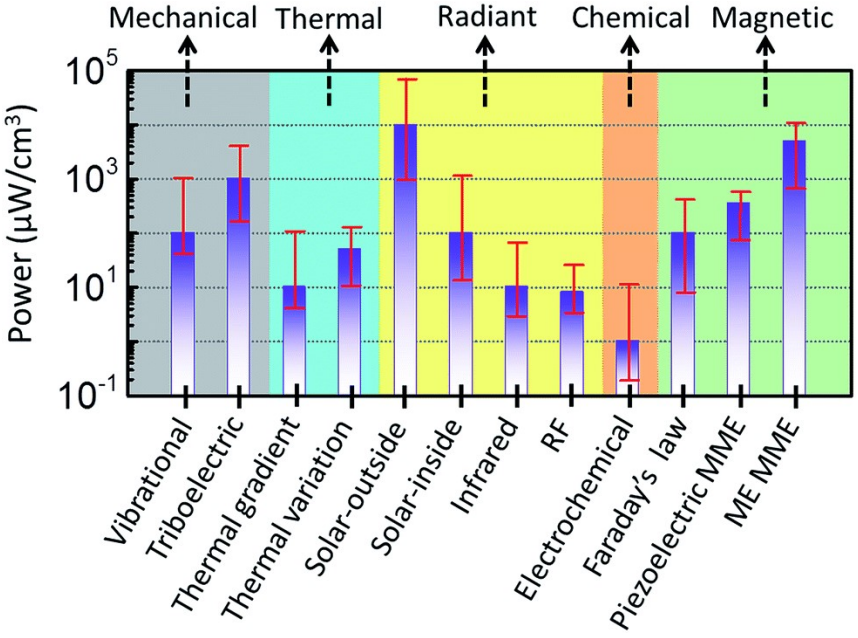

FIGURE 1: Comparaison entre les différentes sources d'énergies et leurs densités d'énergies [Ann+17]

Thèse accessible à l'adresse : https://theses.insa-lyon.fr/publication/2024ISAL0017/these.pdf © [G. Taxil], [2024], INSA Lyon, tous droits réservés

canique ont été parmi les plus étudiées en raison de l'abondance de cette forme d'énergie dans la nature. Dans le domaine de la récupération d'énergie mécanique, la plupart des travaux de recherche portent sur des dispositifs résonnants fonctionnant avec des sources vibratoires [BTW06; Mun+16; Cle+21]. Cependant, il existe de nombreuses sources d'énergies mécaniques impulsionnelles et aléatoires qui peuvent être récupérées dans la vie quotidienne (interrupteurs, pas, pneu sur la route, ouverture de porte, etc.) [AAMF19; SVP16; Xu+18a].

Dans ce contexte, les matériaux ferroélectriques, qui font partie d'une classe de matériaux piézoélectriques, sont très prometteurs pour de telles applications en raison de leurs propriétés remarquables comme leur intégrabilité et leur bonne densité de puissance. Une particularité de ces matériaux est de conserver une polarisation résiduelle à un champ électrique nul. De plus, il est possible d'inverser leur polarisation par l'application appropriée d'un champ électrique. La courbe caractéristique des matériaux ferroélectriques (et également des matériaux ferromagnétiques) est le cycle d'hystérésis bipolaire. Cette courbe illustre comment la polarisation du matériau change lorsqu'un champ électrique est appliqué, puis retiré, présentant une hystérésis sous la forme d'un motif en boucle comme illustré sur la Figure 2.

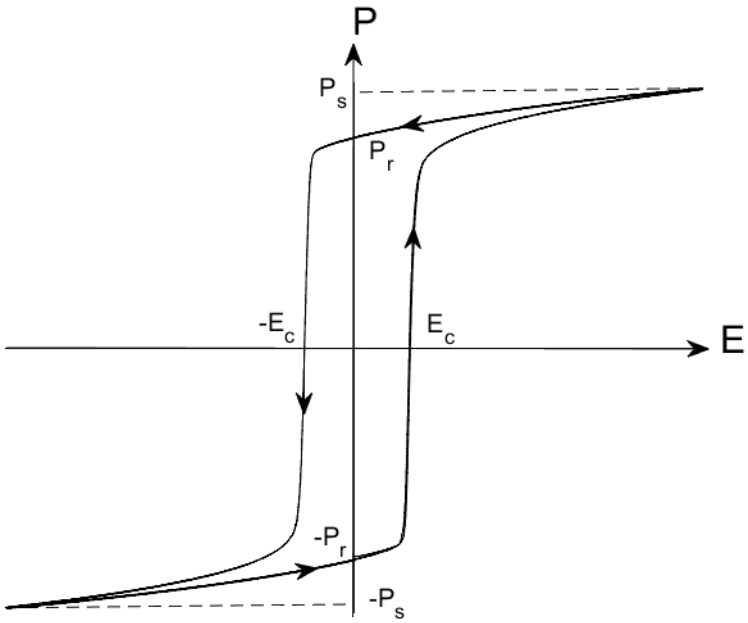

FIGURE 2: Exemple d'une courbe d'hystérésis d'un matériau ferroélectrique

Les matériaux ferroélectriques suscitent un intérêt significatif pour une gamme diversifiée d'applications, notamment les capteurs sans fil, les mémoires RAM et les transducteurs [Yao+22; KKD20; Wei+22]. Leur capacité remarquable à convertir diverses formes d'énergie, telles que les vibrations mécaniques et les fluctuations de température, en signaux électriques, et vice versa, représente l'une de leurs caractéristiques les plus convaincantes. Une autre caractéristique intéressante est la possibilité pour ces matériaux de présenter des transitions de phase avec la variation de la température, du champ électrique et de la contrainte. La plupart des systèmes en récupération d'énergie considèrent classiquement ces transitions de phases comme

Thèse accessible à l'adresse : https://theses.insa-lyon.fr/publication/2024ISAL0017/these.pdf © [G. Taxil], [2024], INSA Lyon, tous droits réservés

une limitation. Cependant, Il est possible d'améliorer la récupération d'énergie en utilisant ces transitions de phase judicieusement, car les propriétés du matériau sont non linéaires à proximité de ces transitions [Kho+09a; GPS08a].

En ce qui concerne la récupération d'énergie mécanique à travers l'application d'une force unique, l'objectif est de maximiser la conversion de l'énergie mécanique en énergie électrique. En travaillant à une fréquence plus basse, il est alors possible d'utiliser des cycles thermodynamiques et d'exploiter les non-linéarités des matériaux induites par la contrainte et le champ électrique élevés par rapport aux systèmes à haute fréquence. Un effort de recherche important a été déployé en utilisant des cycles thermodynamiques pour augmenter la puissance de sortie. Le cycle d'Ericsson, généralement appelé cycle d'Olsen pour la récupération d'énergie pyroélectrique, a beaucoup été étudié en raison de ses capacités élevées de conversion d'énergie [OBB85; Lhe+22; MKP12]. Il a cependant peu été utilisé pour la récupération d'énergie mécanique. Ce cycle se décompose en plusieurs étapes. Tout d'abord, le champ électrique est appliqué (étape 1-2), les domaines de polarisation s'alignent dans la direction du champ électrique. Cela a pour conséquence d'augmenter la déformation du matériau et la polarisation. À l'inverse, lorsque la contrainte est appliquée (étape 2-3), la déformation et la polarisation diminuent. Le relâchement du champ électrique (étape 3-4) diminue davantage la déformation et la polarisation. Enfin, lorsque la contrainte est libérée, la polarisation augmente, complétant le cycle et ramenant la déformation à son état initial. Une illustration de ce cycle est donnée sur la Figure 3.

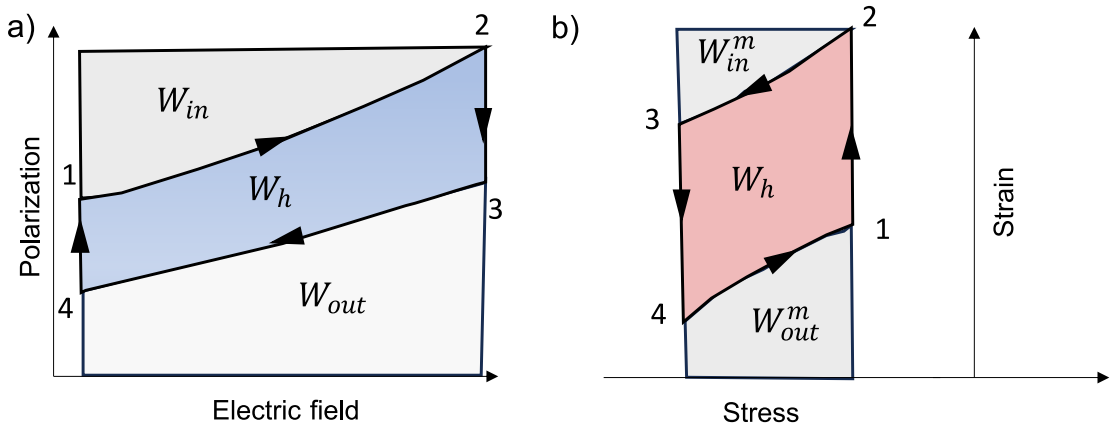

FIGURE 3: Illustration d'un cycle d'Ericsson (a) P-E (Polarisation-Champ électrique) cycle; (b) $\epsilon - \sigma$ (Déformation-Contrainte) cycle

Il est possible de déduire de l'équation de conservation de l'énergie et de la Figure 1.26(a) et (b) l'énergie récupérée W_h en fonction du travail mécanique entrant W_{in}^m et sortant W_{out}^m ainsi que du travail électrique entrant W_{in} et sortant W_{out}:

$$W_h = W_{out}^m - W_{in}^m \tag{1}$$

$$W_h = W_{out} - W_{in} \tag{2}$$

On voit facilement aisi facilement grâce à cette équation et à la Figure 3 que l'énergie récupérée est donnée par l'aire du cycle fermé P-E.

Thèse accessible à l'adresse : https://theses.insa-lyon.fr/publication/2024ISAL0017/these.pdf © [G. Taxil], [2024], INSA Lyon, tous droits réservés

Dans ce contexte, l'objectif principal de cette thèse est d'améliorer la récupération d'énergie en exploitant les non-linéarités de la polarisation induites par ces transitions de phase. Pour atteindre cet objectif, ce travail a été divisé en trois parties avec leurs propres objectifs interdépendants, en suivant une approche du matériau au système:

- Identifier les conditions thermodynamiques idéales via une approche de modélisation. Pour atteindre cet objectif, la théorie de Landau-Devonshire est employée pour modéliser les transitions de phase des matériaux ferroélectriques en fonction de la température, du champ électrique et de la contrainte. Cela permet de prédire les conditions optimales pour la récupération d'énergie en utilisant un cycle thermodynamique à la fois pour la récupération d'énergie pyroélectrique et mécanique.
- Identifier expérimentalement les conditions thermodynamiques optimales et les transitions de phase associées, confirmées par les résultats de la modélisation. Pour la récupération d'énergie pyroélectrique, une comparaison des résultats de l'effet électrocalorique dans la littérature est réalisée. Pour la récupération d'énergie mécanique, un banc d'essai dédié a été développé pour appliquer une forte contrainte uniaxiale et un fort champ électrique aux matériaux tout en contrôlant leur température.
- Développer une structure électromécanique avec l'interface électrique associée capable d'atteindre la contrainte et le champ électrique ciblés. Cet objectif est réalisé par le développement d'une dalle intelligente et d'une poutre en porte-à-faux. Dans les deux dispositifs, la contrainte appliquée a été amplifiée pour atteindre environ 100 MPa et un champ électrique de 1,5 kV/mm a été appliqué. Une interface électrique (Bennet Doubler) est proposée comme solution réaliste par rapport à la récupération d'énergie en utilisant le cycle d'Ericsson.

Modélisation de cycles de récupération d'énergie

Afin de décrire les transitions de phases, La théorie de Landau a largement été utilisée par la communauté scientifique [Wan+10b; Bai+19; LWL16]. Pour les matériaux ferroélectriques, dans les années 1950, Devonshire a utilisé cette approche pour décrire les transitions de phase du titanate de baryum [Dev49]. Cette théorie consiste à développer l'énergie libre en une expansion de puissance d'un paramètre d'ordre qui est la polarisation dans le cas des matériaux ferroélectriques. La théorie de Landau repose sur l'approximation de champ moyen. Cependant, près des transitions, généralement cette approximation échoue à décrire correctement les observations expérimentales. Heureusement, dans les matériaux ferroélectriques, l'approximation de champ moyen est plus que satisfaisante pour les décrire en raison des interactions à longue portée [Rab+07]. En adoptant la convention de sommation d'Einstein, l'énergie libre classique introduite par Devonshire est exprimée comme suit :

$$\begin{aligned} F_{lgd} \quad = \quad & \alpha_{ij}P_iP_j + \alpha_{ijkl}P_iP_jP_kP_l + \alpha_{ijklmn}P_iP_jP_kP_lP_mP_n \\ & + \alpha_{ijklmnop}P_iP_jP_kP_lP_mP_nP_oP_p + ... \end{aligned} \tag{3}$$

où P_i sont les composantes de la polarisation; α_{ij}, α_{ijkl}, α_{ijklmn} et $\alpha_{ijklmnop}$ sont des tenseurs représentant les différents ordres de la rigidité diélectrique. Un avantage significatif de cette approche est la possibilité de prendre en compte la température, le champ électrique et la contrainte appliqués au matériau. L'enthalpie libre correspond au potentiel thermodynamique approprié pour décrire ce type de systèmes et

Thèse accessible à l'adresse : https://theses.insa-lyon.fr/publication/2024ISAL0017/these.pdf © [G. Taxil], [2024], INSA Lyon, tous droits réservés

est donnée en notation tensorielle par :

$$\Delta G = F_{lgd} - E_i P_i - \frac{1}{2} s_{ijkl}\sigma_{ij}\sigma_{kl} - Q_{ijkl}\sigma_{ij}P_k P_l \tag{4}$$

où E_i sont les composantes du champ électrique, σ_{ij} est le tenseur des contraintes, et s_{ijkl} et Q_{ijkl} sont respectivement les tenseurs de compliance et électrostrictif. Cette énergie libre doit être invariante par symétrie d'une phase mère [Cao08a; Li+12] (ici la phase cubique). Ainsi en adoptant la symétrie cubique m$\bar{3}$m et la notation de Voigt, son expression est donnée par :

$$\begin{aligned}
\Delta G \;=\; & \alpha_1({P_1}^2 + {P_2}^2 + {P_3}^2) + \alpha_{11}({P_1}^4 + {P_2}^4 + {P_3}^4) + \alpha_{12}({P_1}^2{P_2}^2 + {P_1}{P_3}^2 + {P_2}^2{P_3}^2) \\
& + \alpha_{123}{P_1}^2{P_2}^2{P_3}^2 + \alpha_{111}({P_1}^6 + {P_2}^6 + {P_3}^6) + \alpha_{112}\Big[{P_1}^2({P_2}^4 + {P_3}^4) + {P_2}^2({P_1}^4 + {P_3}^4) \\
& + {P_3}^2({P_1}^4 + {P_2}^4)\Big] + \alpha_{1111}({P_1}^8 + {P_2}^8 + {P_3}^8) + \alpha_{1122}({P_1}^4{P_2}^4 + {P_1}^4{P_3}^4 + {P_2}^4{P_3}^4) \\
& + \alpha_{1112}\Big[{P_1}^6({P_2}^2 + {P_3}^2) + {P_2}^6({P_1}^2 + {P_3}^2) + {P_3}^6({P_1}^2 + {P_2}^2)\Big] + \alpha_{1123}({P_1}^4{P_2}^2{P_3}^2 \\
& + {P_1}^2{P_2}^4{P_3}^2 + {P_1}^2{P_2}^2{P_3}^4) - \tfrac{1}{2}s_{11}(\sigma_1^2 + \sigma_2^2 + \sigma_3^2) - s_{12}(\sigma_1\sigma_2 + \sigma_1\sigma_3 + \sigma_2\sigma_3) \\
& - \tfrac{1}{2}s_{44}(\sigma_4^2 + \sigma_5^2 + \sigma_6^2) - Q_{11}(\sigma_1 P_1^2 + \sigma_2 P_2^2 + \sigma_3 P_3^2) - Q_{12}\Big[\sigma_1(P_2^2 + P_3^2) \\
& + \sigma_2(P_1^2 + P_3^2) + \sigma_3(P_1^2 + P_2^2)\Big] - Q_{44}(\sigma_4 P_2 P_3 + \sigma_5 P_1 P_3 + \sigma_6 P_1 P_2) \\
& - E_1 P_1 - E_2 P_2 - E_3 P_3
\end{aligned} \tag{5}$$

En minimisant l'enthalpie libre, il est alors possible d'obtenir la polarisation correspondante pour chaque état thermodynamique. Le champ électrique et la contrainte, ainsi que leurs directions d'application, peuvent conduire à diverses configurations de phase et même permettre la création de structures cristallines distinctes. La nouveauté dans cette approche de modélisation est de simuler des cycles thermodynamiques en calculant la structure crystalline stable (c'est-à-dire qui minimise l'énergie) avec sa polarisation associée pour chaque pas de contrainte, de température et de champ électrique du cycle.

State	Polarization components	Number of configurations	Symmetry
Cubic	$(0,0,0)$	1	m$\bar{3}$m
Tetragonal	$(0,0,P)$	6	4mm
Orthorhombic	$(\frac{P}{\sqrt{2}},\frac{P}{\sqrt{2}},0)$	12	mm2
Rhombohedral	$(\frac{P}{\sqrt{3}},\frac{P}{\sqrt{3}},\frac{P}{\sqrt{3}})$	8	3m1

TABLE 1: Propriétés des différentes phases ferroélectriques

Lors d'une expérience, la polarisation est déterminée en mesurant les variations du courant passant à travers les échantillons. Ces cristaux sont orientés le long de la

Thèse accessible à l'adresse : https://theses.insa-lyon.fr/publication/2024ISAL0017/these.pdf © [G. Taxil], [2024], INSA Lyon, tous droits réservés

direction <001>, ce qui signifie que la polarisation mesurée correspond à une projection le long de l'axe z (P_3). Dans le processus de modélisation, les états ferroélectriques considérés sont les états tétragonal (T), orthorhombique (O) et rhomboédrique (R). Les différentes phases et leurs propriétés de polarisations sont données dans le Tableau 1. Lorsque le champ électrique et la contrainte sont appliqués simultanément, il devient difficile de prédire quel état cristallin le matériau adoptera. En effet, le champ électrique a tendance à favoriser l'alignement le long de sa direction d'application, comme illustré dans la Figure 4 (b), tandis que la contrainte uniaxiale a tendance à favoriser des états perpendiculaires à sa direction d'application, comme représenté dans la Figure 4 (c).

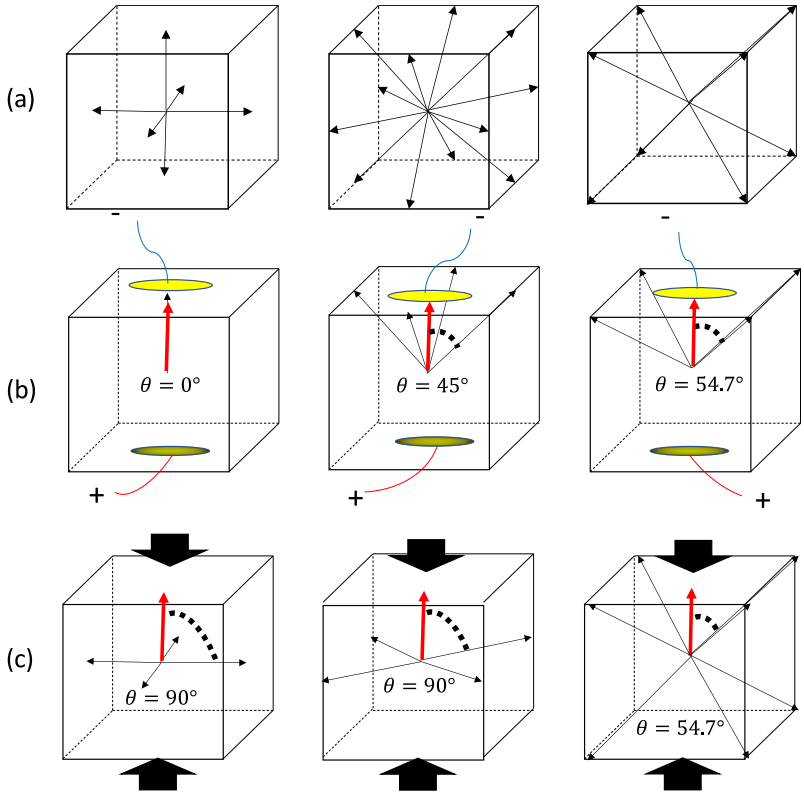

FIGURE 4: Les différentes orientations possibles de la polarisation pour les phases tétragonaux, orthorhombiques et rhomboédriques (de gauche à droite). (a) Configurations possibles sans champ électrique et contrainte appliqués ; (b) Configurations possibles lorsqu'un champ électrique est appliqué ; (c) Configurations possibles lorsqu'une contrainte uniaxiale est appliquée. Les flèches rouges représentent le champ électrique et les flèches noires représente la contrainte.

Il convient de noter que certaines approximations sont faites dans les simulations. En effet, on suppose ici que le cristal est monodomaine, ce qui peut ne pas être vrai dans une expérience réelle. Néanmoins, comme détaillé précédemment, cette approximation est raisonnablement précise sous un champ électrique suffisamment élevé [CL07]. De plus, l'hystérésis du matériau et les pertes diélectriques ne sont pas prises en compte. Il est important de noter que cette approche de modélisation est bien adaptée pour prédire qualitativement la phase ferroélectrique optimale dans des conditions de travail spécifiques et est principalement axée sur l'évaluation de la réponse non linéaire des matériaux à des champs électriques et des contraintes

Thèse accessible à l'adresse : https://theses.insa-lyon.fr/publication/2024ISAL0017/these.pdf © [G. Taxil], [2024], INSA Lyon, tous droits réservés

élevés.

Par soucis de concision, les résultats de modélisations seront présentés dans la partie suivante où ils seront comparés aux résultats expérimentaux réalisés sur des cristaux de PMN-25 et PZN-8PT. De plus, l'intégralité du travail de modélisation n'a pas été présenté ici. En effet, des cycles d'Olsen pour la récupération d'énergie pyroélectrique ont également été simulés. Plus de détails seront donnés dans la version anglaise de ce manuscrit.

Caractérisation expérimentale

Un des objectifs principaux de ce travail est de caractériser expérimentalement différents matériaux ferroélectriques et leurs capacités de conversion d'énergie, et de confronter les résultats avec les prédictions de la simulation. Un banc d'essai capable d'atteindre des niveaux élevés de contrainte, un fort champ électrique et différentes températures a ainsi été conçu.

Une machine de compression Shimadzu® AGS-X a été utilisée pour appliquer la force souhaitée sur les échantillons. Un générateur de fonctions arbitraires Tektronix® AFG1022 et un amplificateur haute tension Trek® 10/10B-HS ont été utilisés pour appliquer le champ électrique. Le courant a été mesuré en utilisant un amplificateur de courant à faible bruit (Stanford research®, Sunnyvale, CA, États-Unis). Les échantillons pour les mesures ont été placés dans un bain d'huile de silicone pour appliquer le champ électrique et réguler la température. La température a été contrôlée avec une chambre thermostatique Shimadzu® TCE-N300A. Des illustrations du banc d'essai expérimental et des différents échantillons testés sont présentées respectivement sur la Figure 5 et 6.

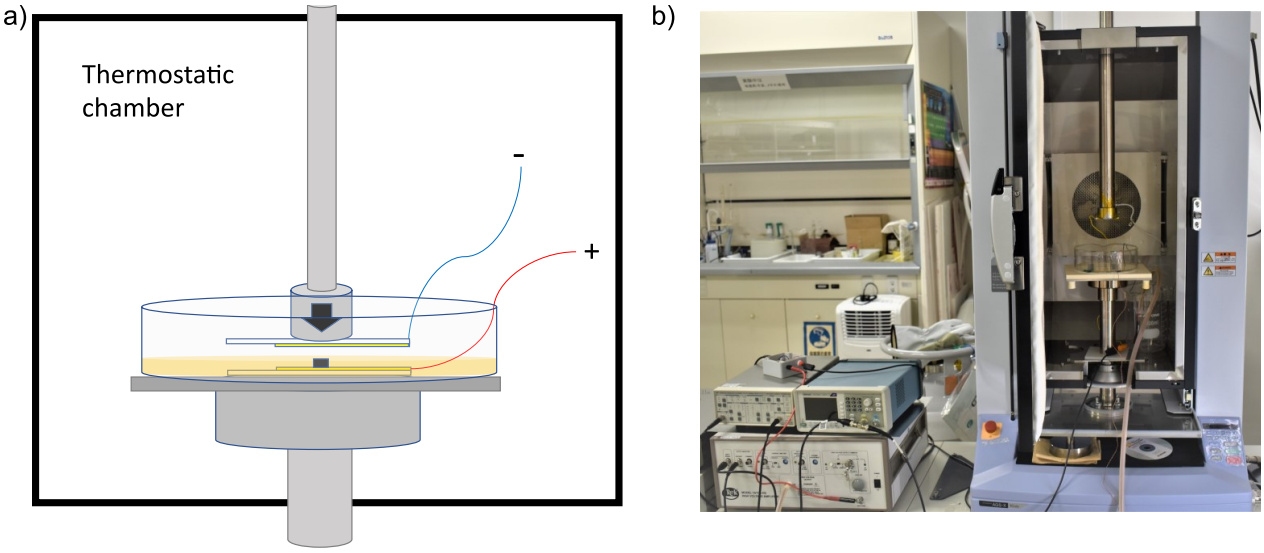

FIGURE 5: (a) illustration schématique du banc expérimental [Tax+23]; (b) Photo du banc expérimental [Tax+23]

Les résultats expérimentaux sur les cristaux de PMN-25PT et de PZN-8PT, tous deux orientés selon la direction cristallographique $[001]_c$, sont présentés ici car ils

Thèse accessible à l'adresse : https://theses.insa-lyon.fr/publication/2024ISAL0017/these.pdf © [G. Taxil], [2024], INSA Lyon, tous droits réservés

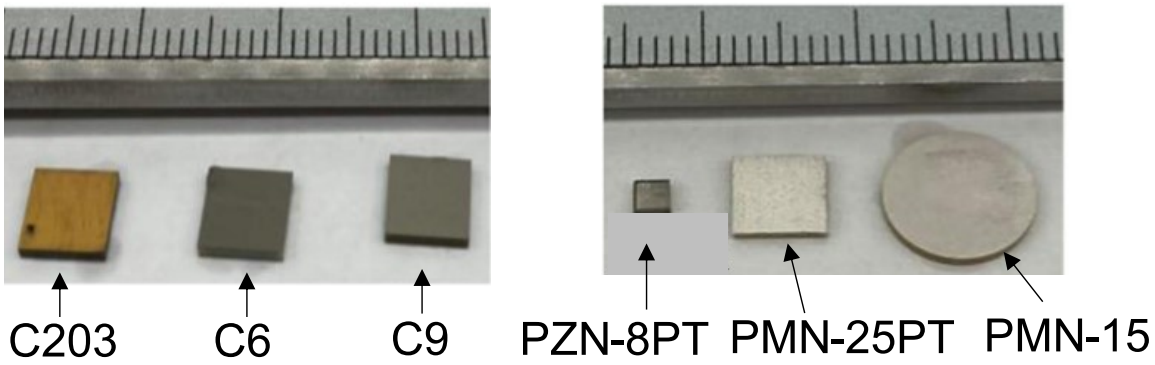

FIGURE 6: Photo de tous les échantillons testés [Tun+22]

présentent les plus grandes densités d'énergies et sont adaptés à l'approche de modélisation. Cependant de nombreux autres matériaux et tests expérimentaux ont été réalisés et seront présentés plus en détail dans la partie anglaise de ce travail.

Pour mieux comprendre la réponse des matériaux et identifier les mécanismes de polarisation les plus efficaces pour la récupération d'énergie, les résultats expérimentaux ainsi que les résultats simulés pour la composante de polarisation P_3 sont présentés par rapport au champ électrique appliqué E_3 et à la contrainte uniaxiale σ_3 pour les monocristaux de PMN-25PT et PZN-8PT orientés selon <001> à différentes températures. Ces résultats sont illustrés sur les Figures 7 et 8.

À température ambiante, les résultats expérimentaux (Figure 7 (a)) révèlent une surface de polarisation plate, indiquant une réponse entièrement linéaire du matériau à la contrainte et au champ électrique appliqués. Le PMN-25PT à cette température présente une phase rhomboédrique (R), en accord avec les prédictions du modèle théorique. Le PZN-8PT quant à lui présente une réponse différente en termes de projection de la polarisation P_3 par rapport au PMN-25PT. À 20 °C, une forte non-linéarité de la polarisation est observée experimentalement et théoriquement sous faible contrainte, allant de 0 à 50 MPa, et même sous des champs électriques appliqués élevés, comme le montre la Figure 8(a). Ces larges variations de polarisation sont atttribuées à des basculements dans le plan de la polarisation induite par la contrainte. Il est intéressant de noter qu'à plus haute température le PMN-25PT présente lui aussi des nonlinéarités particulièrement pour les contraintes élevées et les faibles champs électriques. De son côté le PZN-8PT semble moins sensible avec la température et ces non-linéarités ne semblent pas évoluer avec la température. On peut tout de même remarquer que les prédictions du modèle sont assez bonnes pour les deux matériaux ainsi que sur l'ensemble des contraintes, champs électriques et températures testée, confirmant sa capacité à prédire l'état du matériau.

Par la suite, la conversion d'énergie des cristaux de PMN-25PT et de PZN-8PT a été évaluée à l'aide des cycles d'Ericsson. L'évaluation des capacités de récupération d'énergie a été réalisée en analysant les courbes descendantes des boucles bipolaires à 0 et 100 MPa. Cette évaluation a été réalisée à différentes températures tout en maintenant des conditions similaires pour le cycle d'Ericsson, avec des contraintes variant de 0 à 100 MPa et un champ électrique s'étendant de 0 à 1500 kV/m. La densité d'énergie correspondante en fonction de la température de travail du cycle, sur la base des résultats expérimentaux et modélisés à l'aide de l'approche de Landau-Devonshire est donnée sur la Figure 9.

Thèse accessible à l'adresse : https://theses.insa-lyon.fr/publication/2024ISAL0017/these.pdf © [G. Taxil], [2024], INSA Lyon, tous droits réservés

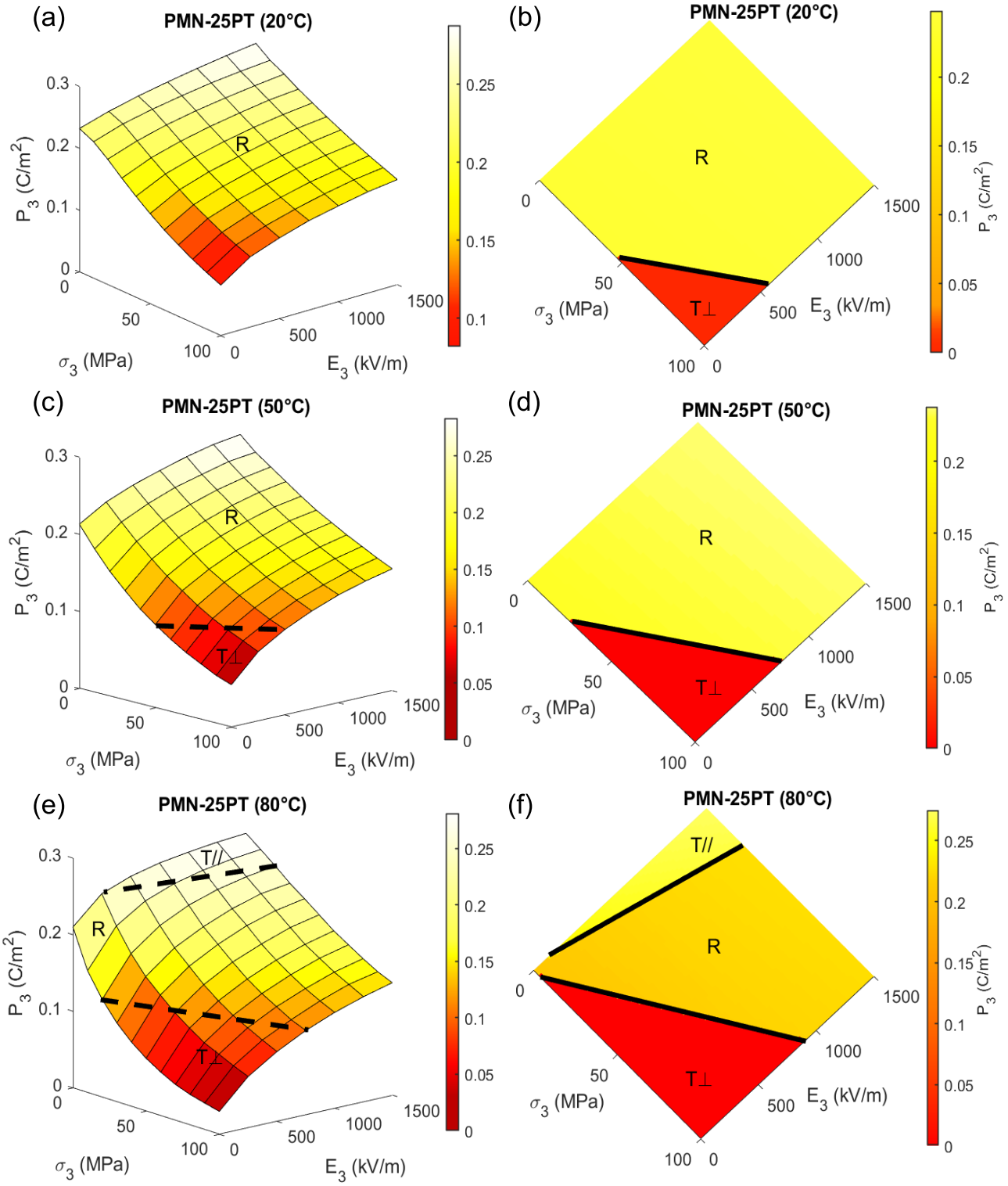

FIGURE 7: Graphique de la composante de polarisation P_3 en fonction de la contrainte uniaxiale σ_3 et du champ électrique E_3 pour le PMN-25PT [Tax+23]. (a) Expérience à 20°C ; (b) Modélisation à 20°C ; (c) Expérience à 50°C ; (d) Modélisation à 50°C ; (e) Expérience à 80°C ; (f) Modélisation à 80°C.

Thèse accessible à l'adresse : https://theses.insa-lyon.fr/publication/2024ISAL0017/these.pdf © [G. Taxil], [2024], INSA Lyon, tous droits réservés

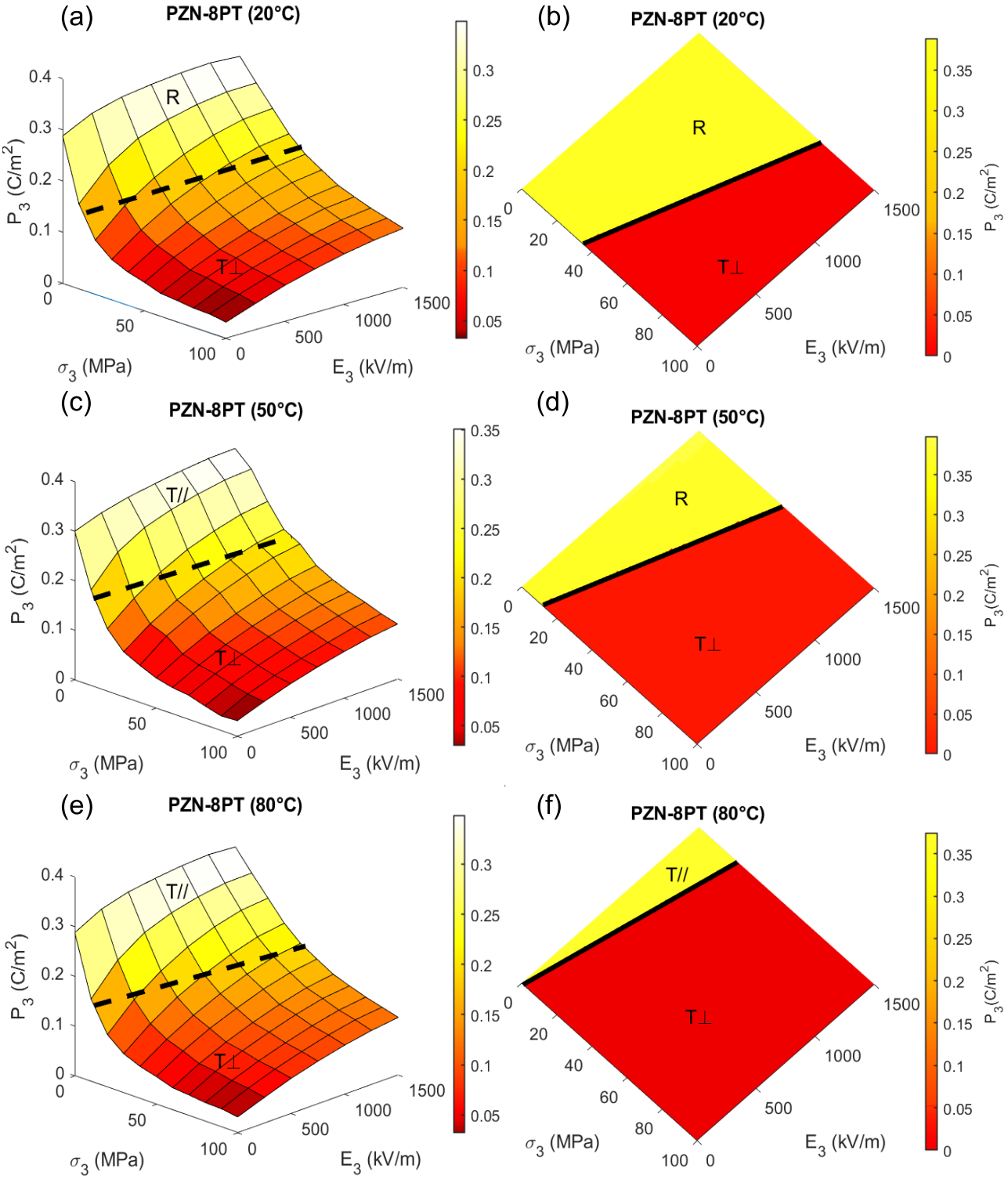

FIGURE 8: Graphique de la composante de polarisation P_3 en fonction de la contrainte uniaxiale σ_3 et du champ électrique E_3 pour le PZN-8PT [Tax+23]. (a) Expérience à 20°C ; (b) Modélisation à 20°C ; (c) Expérience à 50°C ; (d) Modélisation à 50°C ; (e) Expérience à 80°C ; (f) Modélisation à 80°C.

Thèse accessible à l'adresse : https://theses.insa-lyon.fr/publication/2024ISAL0017/these.pdf © [G. Taxil], [2024], INSA Lyon, tous droits réservés

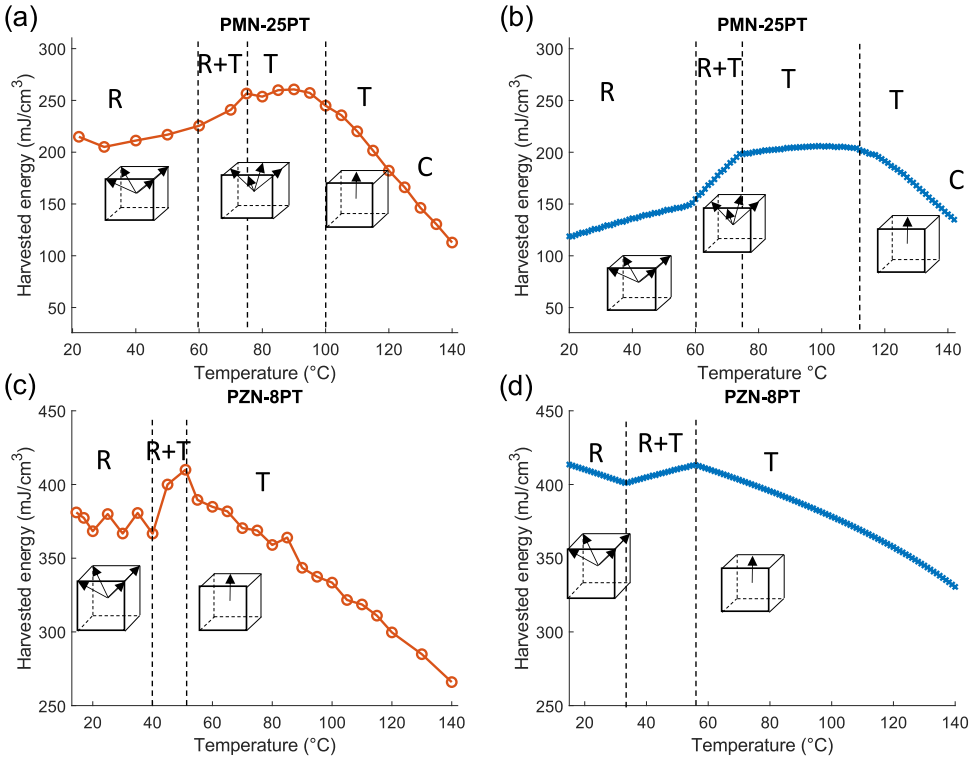

FIGURE 9: Graphique de la densité d'énergie en fonction de la température de travail du cycle [Tax+23]. (a) Expérience pour le PMN-25PT ; (b) Modélisation pour le PMN-25PT ; (c) Expérience pour le PZN-8PT ; (d) Modélisation pour le PZN-8PT.

La température de travail idéale pour le cycle d'Ericsson a été déterminée pour les deux cristaux. Les résultats soulignent que les performances optimales sont atteintes à la température à laquelle le cristal devient entièrement tétragonal. Cette observation a le potentiel d'être extrapolée à tous les cristaux ferroélectriques orientés <001> dans des conditions de contrainte significative, permettant un basculement dans le plan de la polarisation. En effet, une variation plus importante de la polarisation est possible avec une augmentation de la contrainte uniaxiale suivant la direction de la polarisation spontanée. Ainsi, les résultats sous des conditions de contrainte élevée suggèrent que le fonctionnement en alignement avec la direction de polarisation produit les densités d'énergie les plus élevées, ce qui contredit les conclusions tirées de l'ingénierie de domaine dans les cristaux et apporte un nouvel éclairage quant à l'utilisation de ces matériaux pour la récupération d'énergie sous conditions extrêmes.

Structures électromécaniques

Il a été mis en lumière qu'exploiter les comportements non linéaires induits par la contrainte et le champ électrique dans les matériaux ferroélectriques est d'un grand interêt dans le contexte de la récupération d'énergie mécanique non résonante. Dans ce contexte, la conception mécanique d'un dispositif de récupération d'énergie dans son ensemble doit être adaptée à la source mécanique, garantissant que la contrainte mécanique est suffisamment élevée pour maximiser la conversion d'énergie au travers de transitions de phase. L'objectif ici est de développer des systèmes

Thèse accessible à l'adresse : https://theses.insa-lyon.fr/publication/2024ISAL0017/these.pdf © [G. Taxil], [2024], INSA Lyon, tous droits réservés

applicatifs réels avec les conditions de contrainte et de champ électrique précédemment considérées dans la modélisation et la caractérisation des matériaux ferroélectriques. Le but principal est de tirer profit des non-linéarités largement discutées dans ce manuscrit pour démontrer leur potentiel pour la récupération d'énergie.

Divers défis doivent être relevés pour parvenir à un dispositif entièrement fonctionnel, notamment garantir un volume suffisant en matériaux actifs et mettre en œuvre une interface électrique appropriée pour extraire l'énergie. Ici, une dalle intelligente opérant en mode 33 basée sur un mécanisme d'amplification de force est utilisée dans le but de fonctionner dans le régime non linéaire. L'objectif est alors de libérer le potentiel pour une densité de conversion d'énergie ultra-élevée. Un dispositif a aussi été développé basée sur une poutre en porte à faux opérant cette fois en mode 31 et sera présenté plus en détails dans la version anglaise de ce manuscrit.

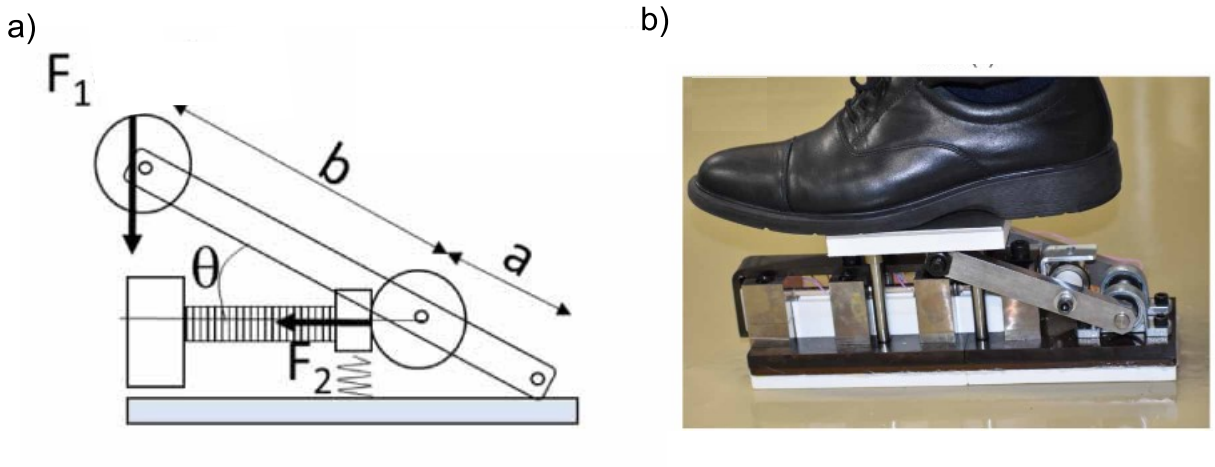

FIGURE 10: (a) Schéma illustrant la dalle; (b) Photo du dispositif.

Des "stacks" de PZT ont été sélectionnés pour maximiser la quantité totale de matériau actif tout en restant compatibles avec des forces de l'ordre de plusieurs centaines de Newtons afin d'atteindre des niveaux de contrainte d'environ $\approx 100, \mathrm{MPa}$ (qui sont nécessaires pour induire une dépolarisation significative sous contrainte). La force mécanique d'entrée a été amplifiée grâce à un bras de levier, représenté schématiquement sur la Figure 10(a). Ce dispositif est composé de 3 empilements piézoélectriques connectés électriquement en parallèle et mécaniquement en série. Une photo illustrant le dispositif est donnée sur la Figure 10(b).

Dans une des expériences réalisées sur la dalle, l'application de la force a été réalisé en marchant sur le plateau supérieur du dispositif comme illustré sur la Figure 10(b). Avec une force de 700 N, l'énergie convertie mesurée expérimentalement en appliquant des cycles d'Ericsson a atteint une valeur de 776 mJ par pas, tandis qu'une force de 500 N a donné une énergie de 578 mJ. Ces deux cycles d'Ericsson réalisés en marchant sur le dispositif sont présentés sur la Figure 11.

Tous les résultats précédents se sont concentrés sur les cycles d'Ericsson, qui, dans une mise en œuvre pratique, pourraient être difficiles à réaliser en raison de leur dépendance à une source de tension entièrement contrôlable. Une telle approche consomme en effet une énergie excessive lorsqu'elle fonctionne de manière

Thèse accessible à l'adresse : https://theses.insa-lyon.fr/publication/2024ISAL0017/these.pdf © [G. Taxil], [2024], INSA Lyon, tous droits réservés

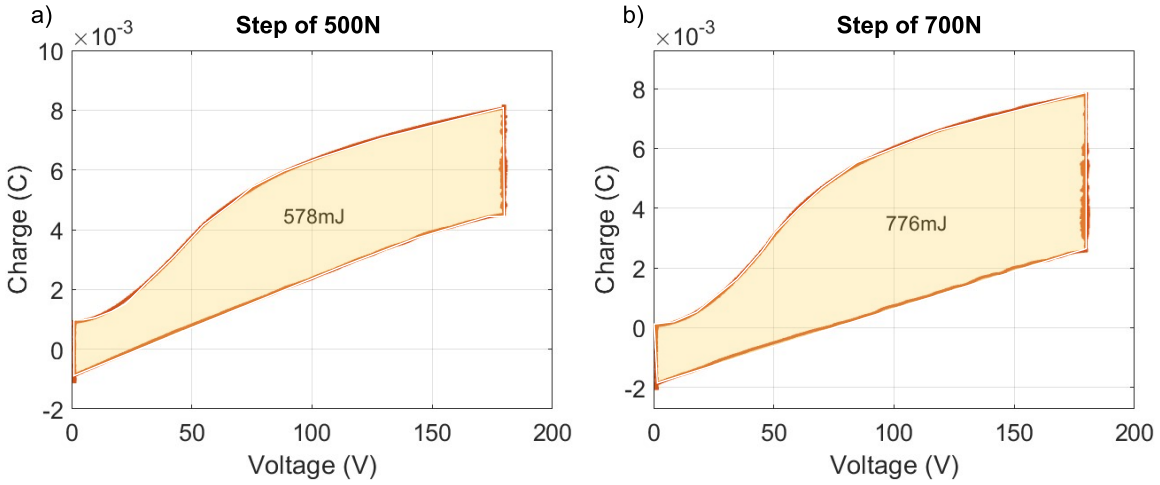

FIGURE 11: Cycles d'Ericsson avec des vrais pas; (a) 500N; (b) 700N.

entièrement autonome, compromettant ainsi l'équilibre énergétique global du dispositif. Dans ce travail, l'objectif était de créer un prototype entièrement opérationnel et réaliste capable de fonctionner de manière indépendante. Tenant compte de ces aspects, l'interface choisie est une adaptation électrique du doubleur de Bennet [QD11] (représentés sur la figure 12(a)). Avec ce circuit et la disposition particulière des diodes, le processus de charge implique une configuration en parallèle de la source de tension et des capacité tampon et de stockage, tandis que le processus de décharge consiste en une connexion en série de la capacité tampon et de la capacité de stockage. Cette disposition a pour résultat que le matériau ferroélectrique est exposé à une tension successivement égale à une et deux fois la valeur de la tension de la capacité de stockage.

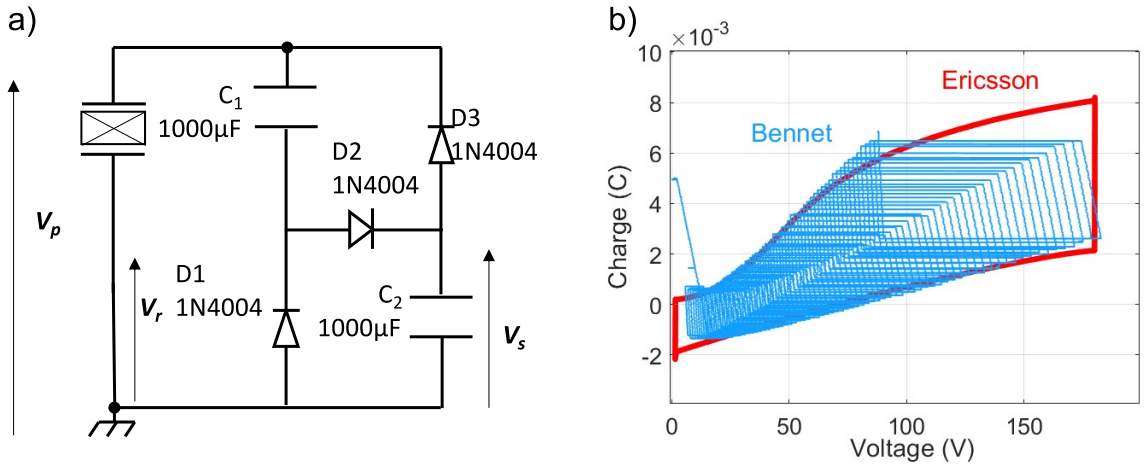

FIGURE 12: (a) Circuit électrique du doubleur de Bennet; (b) Charge vs Tension avec le cycle d'Ericsson (ligne rouge) et doubleur de Bennet (ligne bleu) à 700N [Seb+23].

Le fabricant recommandait de ne pas appliquer une tension supérieure à 180V pour éviter le claquage. Ainsi, les cycles ont été interrompus lorsque la tension atteignait cette limite. Par conséquent, dans le dernier cycle, les condensateurs de stockage ont été chargés jusqu'à 90 V et la tension des stacks de PZT varie alors

Thèse accessible à l'adresse : https://theses.insa-lyon.fr/publication/2024ISAL0017/these.pdf © [G. Taxil], [2024], INSA Lyon, tous droits réservés

entre 90 V et 180 V. Dans un tel scénario, l'énergie par cycle a atteint 320 mJ par cycle. Curieusement, les cycles du convertisseur de Bennet surpassent ceux des cycles d'Ericsson comme on peut l'observer sur la Figure 12(b) Ce comportement est interprété en termes de dépolarisation irréversible induite par la contrainte appliquée. Lors de la réalisation d'un cycle d'Ericsson, la courbe de charge commence à champ électrique nul, et la partie initiale de la courbe correspond au processus de repolarisation, à partir d'un état partiellement dépolarisé. Cependant, le convertisseur de Bennet ne retourne pas à une valeur de tension nulle, entraînant une dépolatisation plus faible. Par conséquent, la branche de charge équivalente correspond à une valeur de polarisation plus élevée. En conséquence, les cycles du convertisseur Bennet étaient plus élevés que prévu, atteignant environ 40% du cycle d'Ericsson réel.

Afin de fournir une vision plus complète, une analyse comparative de divers travaux en récupération d'énergie piézoélectrique, englobant à la fois les régimes dynamiques et statiques, a été faite. Il est essentiel de noter que les prototypes varient significativement en termes de géométries, de conditions de fonctionnement, de fréquences de travail et d'entrées d'énergie mécanique. Néanmoins, cette approche comparative aide à évaluer le potentiel global de la récupération d'énergie, en tenant compte à la fois de l'énergie mécanique d'entrée et de la partie convertie et récupérée sous forme d'énergie électrique. Bien que chaque point de données puisse nécessiter une investigation spécifique pour une analyse détaillée, l'objectif principal est de discerner une tendance générale. Ainsi, sur la Figure 13, un graphique de l'énergie de sortie par cycle en fonction du volume des éléments piézoélectriques ainsi que la tendance globale sont donnés (les réfèrences associées peuvent être trouvées dans le tableau 4.2 de la partie anglaise). On peut noter qu'une tendance générale émerge, fournissant une indication de l'énergie de sortie réalisable en fonction du volume du matériau piézoélectrique. Dans ce travail, le doubleur de Bennet a permis d'exploiter le comportement électrique non linéaire combiné à une amplification de force. Cette intégration a produit une énergie de sortie significativement plus élevée, atteignant des niveaux jusqu'à deux ordres de grandeur supérieurs aux tendances établies. De plus, compte tenu du fait que les cycles d'Ericsson ont atteint une énergie de sortie deux à trois fois plus élevée que celle de l'interface électrique de Bennet, il existe ainsi un potentiel d'améliorations supplémentaires avec des circuits électriques innovants.

Conclusion

Ce travail se concentrait sur la récupération d'énergie mécanique non résonnante tirant partie des comportements non-linéaires, notamment les transistions de phase, sous conditions extrêmes (mais réalisables en pratiques). Comme détaillé, cette approche est une bonne solution pour des sources d'énergie mécanique soudaines et aléatoires telles que des pas et des pneus sur les routes. Cette méthode est d'un intérêt particulier compte tenu des exigences actuelles en matière de production électrique propre et dans le contexte des dispositifs interconnectés. Le principal problème de cette approche est la faible énergie de sortie. Par conséquent, récupérer le plus d'énergie possible par cycle est essentiel pour des applications réalistes. Ce travail, en considérant différents aspects tels que les propriétés des matériaux, la structure électromécanique et l'interface électrique, visait à améliorer les capacités de conversion d'énergie des matériaux ferroélectriques. En particulier, profiter des non-linéarités de la polarisation induites par l'application d'un champ électrique élevé et d'une contrainte importante sur les matériaux ferroélectriques était l'objectif

Thèse accessible à l'adresse : https://theses.insa-lyon.fr/publication/2024ISAL0017/these.pdf © [G. Taxil], [2024], INSA Lyon, tous droits réservés

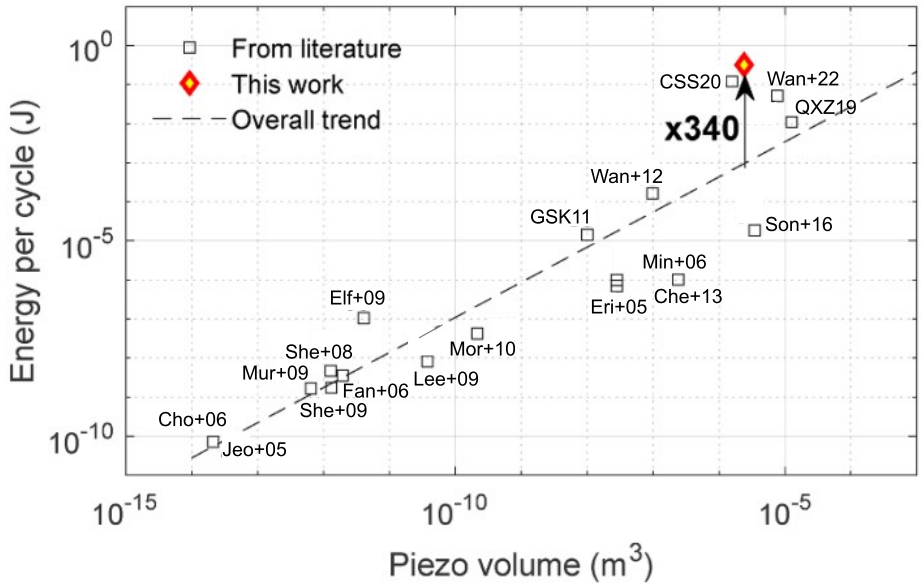

FIGURE 13: Tendance générale de l'énergie de sortie des dispositifs de récupération d'énergie piézoélectrique en fonction du volume des éléments piézoélectriques [Seb+23].

principal de ce travail.

Ainsi, en considérant la modélisation, la caractérisation et la mise en œuvre des matériaux ferroélectriques au sein de dispositifs, ce travail a mis en lumière leur potentiel unique de conversion d'énergie ultra-élevée lorsqu'ils sont soumis à des niveaux suffisants de contrainte et de champ électrique. Les non-linéarités de la polarisation induites par ces conditions ont été démontrées comme une solution efficace pour les dispositifs fonctionnant dans des conditions non résonnantes. Certains aspects examinés dans ce travail pourraient faire l'objet de recherches approfondies, tandis que des pistes potentielles non abordées dans cette recherche pourraient servir de base à des investigations futures. Parmi ces possibilités, développer une nouvelle interface électrique qui correspond davantage au cycle d'Ericsson dans l'espace Q-V et augmenter la contrainte et le champ électrique appliqués en mode 33 semblent être les plus simples à mettre en oeuvre.

Thèse accessible à l'adresse : https://theses.insa-lyon.fr/publication/2024ISAL0017/these.pdf © [G. Taxil], [2024], INSA Lyon, tous droits réservés

Thèse accessible à l'adresse : https://theses.insa-lyon.fr/publication/2024ISAL0017/these.pdf © [G. Taxil], [2024], INSA Lyon, tous droits réservés

Chapter 1

Introduction

This chapter provides a comprehensive overview of the various central themes addressed in this research project. It also introduces the framework of the study and outlines the various objectives of the thesis.

In the first part, a broad introduction to piezoelectric, pyroelectric, and ferroelectric materials is presented. It introduces the distinctive characteristics of these materials and explores the origins of ferroelectricity.

Then, a theoretical background on ferroelectricity and their phase transitions is proposed along with some unique features of ferroelectric relaxors. Particularly, it introduces the Landau-Devonshire theory which will be an important part on this research work.

After that, a broad introduction to energy harvesting, with particular emphasis on non-resonant mechanical energy harvesting, which is the primary focus of this research work.

Finally, an overview is proposed on the FIESTA project, which has a strong connection to this work as it was carried out within the framework of this project. Then, the various objectives of the thesis are presented along with its structure.

Thèse accessible à l'adresse : https://theses.insa-lyon.fr/publication/2024ISAL0017/these.pdf © [G. Taxil], [2024], INSA Lyon, tous droits réservés

1.1 Generalities on ferroelectricity

Ferroelectric materials is a particular class of materials and have attracted the attention of the scientific community in the last decades due to their unique properties. A specific characteristic of these materials is their capability to undergo phase transitions in response to changes in temperature, electric field, and stress. Made profit of these phase transitions can enhance energy harvesting, as the material's properties exhibit non-linear behavior in the proximity of these transitions. Within the scope of this research, the primary objective is to exploit the non-linear behaviors exhibited by ferroelectrics for the purpose of energy harvesting. In this part, an introduction to this materials is proposed by presenting first, their remarkable features such as piezoelectricity and pyroelectricity. After that, this part will be dedicated to the inherent mechanisms of ferroelectricity and to the perovskite structure which is strongly linked to ferroelectricity.

1.1.1 Piezoelectricity

Piezoelectricity was first discovered in 1880 by Pierre and Jacques Curie in Rochelle salt. The particularity of these materials is the ability to generate an electrical voltage in response to a mechanical excitation (direct piezoelectric effect). On the other hand, converse (or reverse) piezoelectric effect consists of applying a voltage which induces strain. Piezoelectricity occurs only in non-centrosymmetric crystalline classes. Twenty one crystalline classes are non-centrosymmetric among the thirty two existing ones. In piezoelectricity, the barycenter of the positive and negative charges is non-centrosymmetric and applying an electric field or a force will move this barycenter. An illustration of the direct and of the converse piezoelectric effect is presented in Figure 1.1.

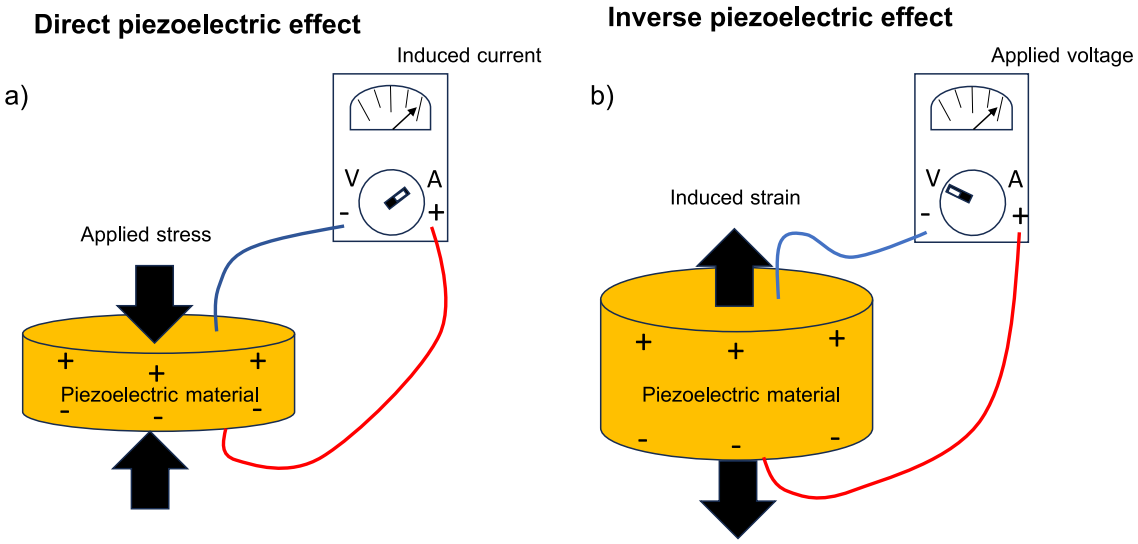

FIGURE 1.1: Illustration of the piezoelectric effect. (a) Direct piezoelectric effect; (b) converse piezoelectric effect.

By adopting the Einstein notation, the governing equations for direct and converse piezoelectric effect are given respectively by:

$$D_i = d_{ijk}\sigma_{jk} + \kappa_{ij}E_j \tag{1.1}$$

$$\epsilon_{ij} = s_{ijkl}\sigma_{kl} + d_{ijk}E_k \tag{1.2}$$

Thèse accessible à l'adresse : https://theses.insa-lyon.fr/publication/2024ISAL0017/these.pdf © [G. Taxil], [2024], INSA Lyon, tous droits réservés

where E_j and D_i are the components of the electric field and of the electric displacement. σ_{ij}, ϵ_{ij} and κ_{ij} are respectively the stress, strain and dielectric permittivity tensors, d_{ijk} is the piezoelectric tensor of rank 3 and s_{ijkl} the 4th rank tensor of compliance.

Piezoelectric materials have diverse applications, from sensors measuring pressure and acceleration to energy harvesting systems through ultrasound imaging devices and actuators [SCZ07; GG02; KKK11]. They play vital roles in converting mechanical energy into electrical signals and precise mechanical motion in various technologies across industries.

1.1.2 Pyroelectricity

Among piezoelectric materials, 10 of the 20 piezoelectric crystal classes are pyroelectric. Their particularity is their ability to induce a polarization change by a temperature variation. The origin of this effect lies from the entropy change induced by the temperature variation that modifies dipole alignment order which will cause a polarization variation. An illustration of this mechanism is given in Figure 1.2. To describe these materials, generally, the pyroelectric coefficient is defined as:

$$p_i = \left(\frac{\partial P_i}{\partial T}\right)_S \tag{1.3}$$

where S is the entropy and p_i and P_i are respectively the components of the pyroelectric coefficient and of the polarization. On the other hand, the electrocaloric effect is the reciprocal effect of pyroelectricity and consists in a change of temperature caused by an electric field variation. It is possible to obtain the temperature variation from the Maxwell relation:

$$\left(\frac{\partial S}{\partial E}\right)_T = \left(\frac{\partial P}{\partial T}\right)_E \tag{1.4}$$

and ΔT is obtain as follows:

$$\Delta T = -\frac{T}{\rho C}\int_{E_i}^{E_f}\left(\frac{\partial P}{\partial T}\right)_E dE \tag{1.5}$$

Even if this approximation is not always verified, it is largely common and generally sufficient. Pyroelectric materials are of interest for different applications such as infrared detectors, which are largely used nowadays [Wha91]. One of their other field of application is for generating voltage from temperature variation [Rav+11; Bow+14], for instance in the framework of enrgy harvesting which will be the main interest for this work.

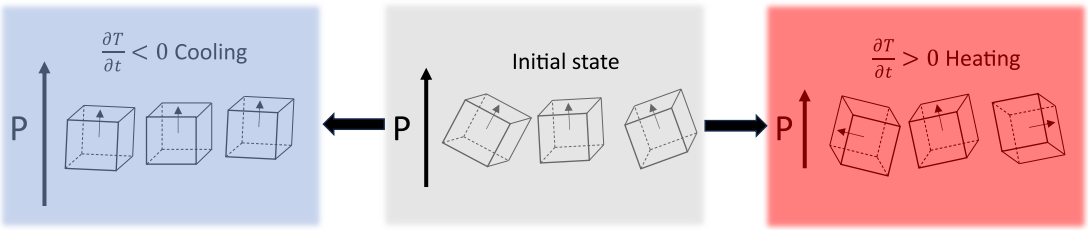

FIGURE 1.2: Pyroelectric effect representation

Thèse accessible à l'adresse : https://theses.insa-lyon.fr/publication/2024ISAL0017/these.pdf © [G. Taxil], [2024], INSA Lyon, tous droits réservés

1.1.3 Ferroelectricity

Ferroelectricity concerns a smaller set of materials within the 10 pyroelectric crystalline classes (9 over 10). All ferroelectric materials are also piezoelectric and pyroelectric (Figure 1.3). Their distinctive feature is the presence of a remnant polarization without an applied electric field. Moreover, it is possible to reverse the polarization by the proper application of an electric field. Ferroelectric materials hold significant appeal for a diverse range of applications, including wireless sensors, random access memories and transducers [Yao+22; KKD20; Wei+22]. Their remarkable ability to convert various forms of energy, such as mechanical vibrations and temperature fluctuations, into electrical signals, and conversely, represents one of their most compelling features. Ferroelectric materials typically exhibit ferroelectric behavior only within a certain temperature range. Above a critical temperature called the Curie temperature (T_c), they lose their ferroelectric properties and become paraelectric, without a remnant polarization. Ferroelectric materials are often compared to ferromagnetic materials because the couple magnetization-magnetic field is similar to the polarization-electric field one. However, the physics behind these effects are very different. Ferromagnetism originates from the exchange interaction due to the anti-symmetric wave function of electrons, which is a purely quantum aspect. In contrast, ferroelectricity comes from the lattice distortion for bulk materials, resulting in a net polarization. It can be noted, that ferroelectricity can also manifest in polymers when the polymer chain adopts a specific conformation. However, it's important to clarify that this study will exclusively concentrate on ferroelectric ceramics and crystals, omitting the discussion of ferroelectricity in polymers.

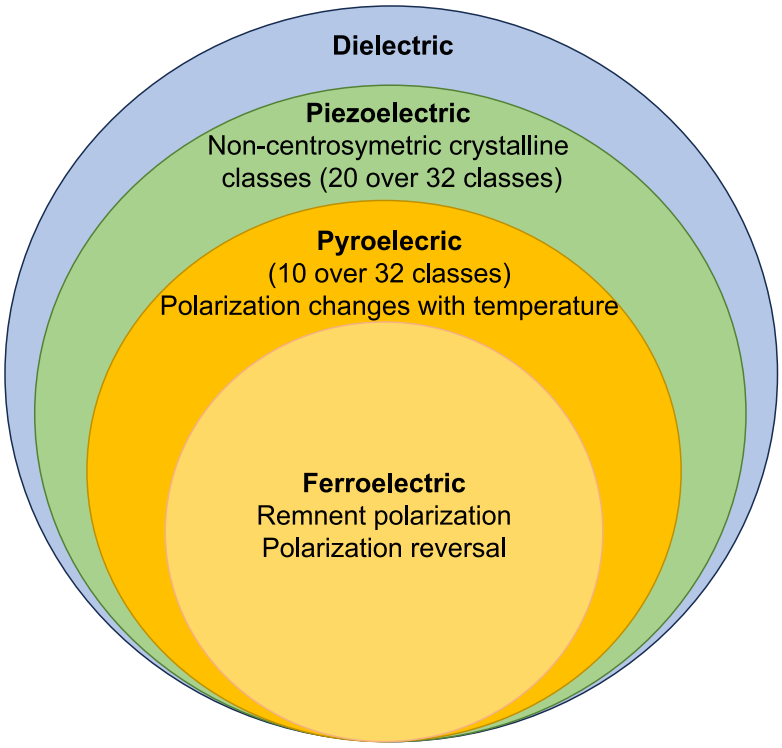

FIGURE 1.3: Diagram presenting the relation between the materials

The characteristic curve of ferroelectric materials (and of ferromagnetic materials as well) is the bipolar hysteresis loop. This curve illustrates how the polarization of the material changes as an electric field is applied and then removed, displaying

Thèse accessible à l'adresse : https://theses.insa-lyon.fr/publication/2024ISAL0017/these.pdf © [G. Taxil], [2024], INSA Lyon, tous droits réservés

hysteresis in the form of a loop-shaped pattern. Different quantities are typically identified on this curve: the remnant polarization (P_r) which is the value of polarization that remains in the material when the electric field returns to zero after a complete cycle through the hysteresis loop. The coercive field (E_c), which is the minimum electric field required to reverse the direction of polarization in the material and the saturation polarization (P_s), which is the maximum achievable polarization, when an electric field is applied. An hysteresis curve for ferroelectric materials with its associated key values is displayed in Figure 1.4.

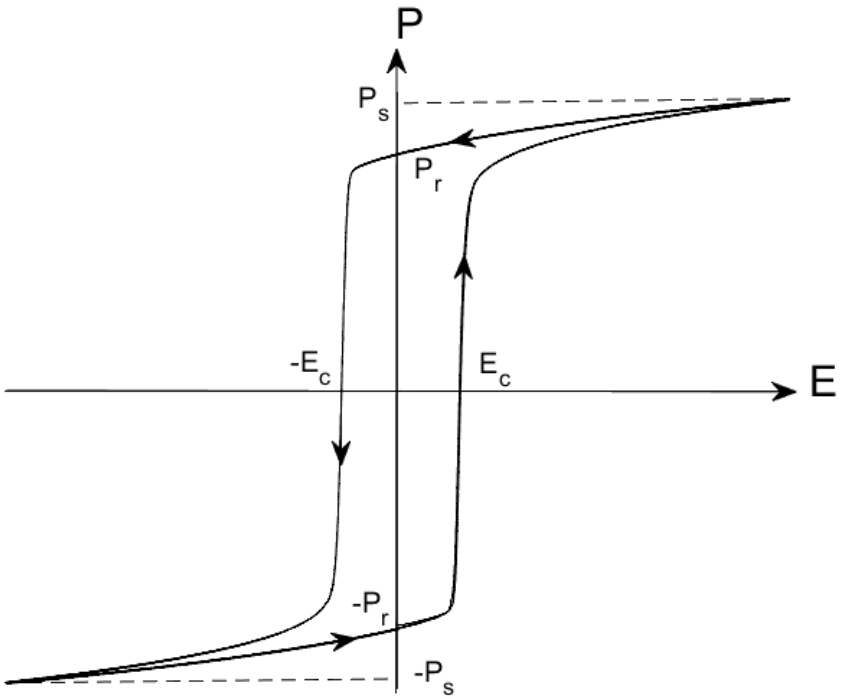

FIGURE 1.4: Example of an hysteresis curve of a ferroelectric material with associated quantities

In ferroelectric materials, the polarization is distributed in domains as it minimizes energy in the material. This distribution is responsible of different aspects of the properties of ferroelectrics. For instance, the hysteresis of ferroelectic materials originates from these domains configurations. Indeed, when an bipolar hysteresis curve is performed, the material starts from a random state which depends of the history of the material. When the electric field increases, the domains start to align with it until the maximum alignment is reached, which corresponds to the saturation polarization. After that, the electric field decreases and with it the alignment order of the domains. At zero electric field, the non zero value of the polarization is explained by the supplementary electrical energy originating from domain interactions required to return in a homogeneous orientation distribution which is the case when the electric field become negative and reach the coercive field. Finally, the cycle continues and is closed in a symmetric way as it reachs respectively the negative saturation polarization, the negative remnant polarization and the positive coercive field. An illustration of the domain evolution in the process is provided in Figure 1.5.

The boundary region separating two domains is called domain wall. This border

Thèse accessible à l'adresse : https://theses.insa-lyon.fr/publication/2024ISAL0017/these.pdf © [G. Taxil], [2024], INSA Lyon, tous droits réservés

position can evolves with time and is responsible of different properties of ferroelectric materials (domain wall motion) [Mer54; Pra+12]. There is a lot of study in the literature that investigates the role of domain wall motion [Nat+20; MS22] and it is important to notice the influence of such phenomena. However, it is an aspect of ferroelectric materials which will not be the main focus of this work.

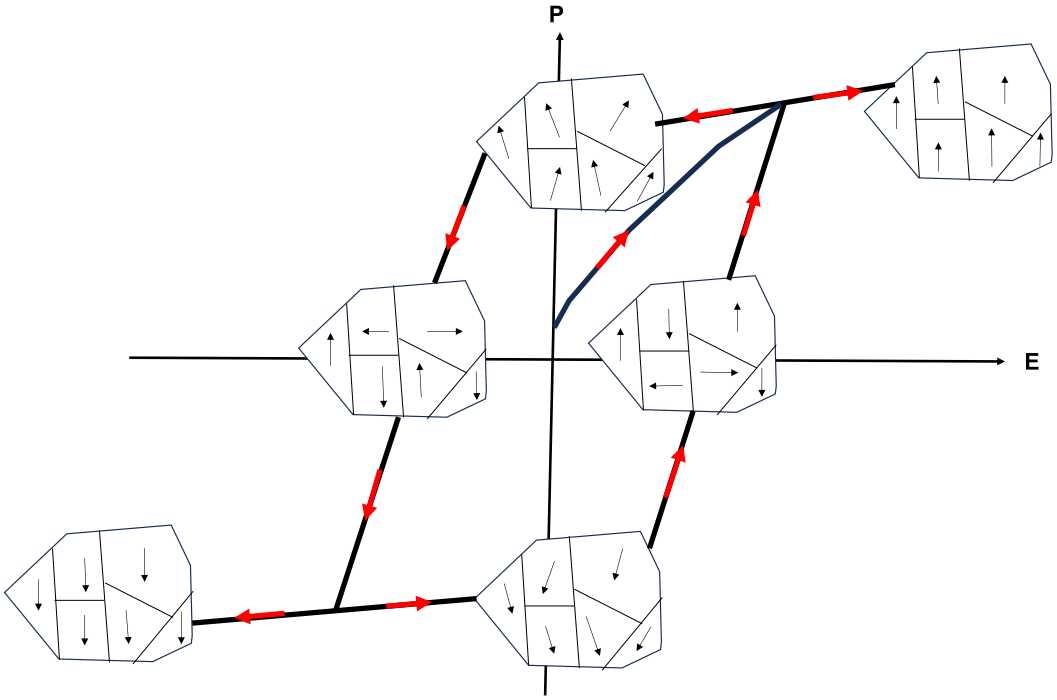

FIGURE 1.5: Illustration of the evolution of the domains of polarization during an hysteresis cycle

1.1.4 Perovskite structure and ferroelectricity

A significant part of ferroelectric materials utilized in practical applications and studied both theoretically and experimentally, exhibits an ABO_3 perovskite structure which has a face-centered cubic lattice. In this configuration, the A chemical element is a large atom with a positive charge (cation) situated at the edges of the cube. The B element is a cation positioned at the lattice's central location. Finally, the 3 oxygen atoms are anions (negatively charged) located on the faces of the cube. An illustration of the perovskite structure is given in Figure 1.6. Within the perovskite structure, ferroelectric distortion leads to a relative displacement of the cations in relation to the anions, thereby inducing a net polarization [Coh92]. This crystalline structure is important for the rest of this work. Indeed, all the materials studied in this work are ceramics or single crystals with a perovskite structure

Among ferroelectric perovskites, barium titanate ($B_aT_iO_3$) has been largely studied and is generally considered due to its classical ferroelectric behavior [Smi+08; Gig+22]. Moreover, it presents a high Curie temperature (around 120°C) and it undergoes successive FE-FE (Ferroelectric-Ferroelectric) phase transitions and FE-PA (Ferroelectric-Paraelectric) transitions with temperature. It goes from Rhombohedral (R) to Orthorhombic (O), from Orthorhombic to Tetragonal (T) and finally from Tetragonal to Cubic (C) phases. These different ferroelectric phases have different physical properties such as different polarization orientations depending of

Thèse accessible à l'adresse : https://theses.insa-lyon.fr/publication/2024ISAL0017/these.pdf © [G. Taxil], [2024], INSA Lyon, tous droits réservés

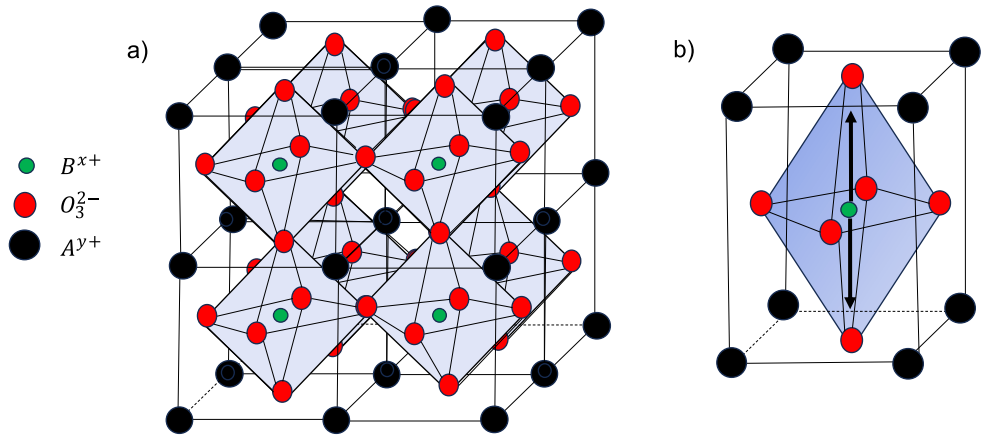

FIGURE 1.6: (a) Illustration of a perovskite lattice cells; (b) Polarized tetragonal state

the crystal symmetry. These different ferroelectric phases with their polarization orientations are depicted in Figure 1.7 and are typical of ferroelectric perovkskites. With increasing temperature, the symmetry of the different ferroelectric phases become higher and reachs its maximum symmetry level in the cubic paraelectric state.

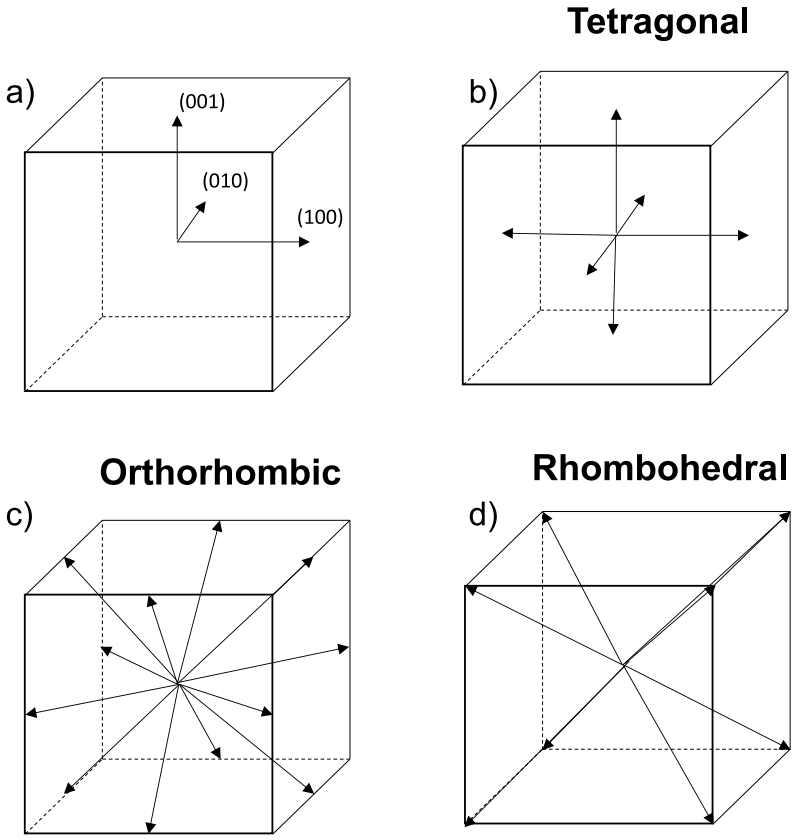

FIGURE 1.7: The different possible orientations of the polarization for a ferroelectric crystal. (a) Referential of the cubic basis of the crystal; (b) Tetragonal phase; (c) Orthorhombic state; (d) Rhombohedral phase.

The study of perovskite ferroelectric materials has led to significant advances

Thèse accessible à l'adresse : https://theses.insa-lyon.fr/publication/2024ISAL0017/these.pdf © [G. Taxil], [2024], INSA Lyon, tous droits réservés

in understanding ferroelectricity, paving the way to the development of new materials with improved properties. There is a strong research effort to continue for exploring novel perovskite compositions and structures, including lead-free alternatives, to address environmental concerns associated with some lead-based perovskites [Kum+15; SL12]. In summary, the perovskite crystal structure is essential in ferroelectricity because it provides the necessary non-centrosymmetric lattice structure for the emergence of spontaneous polarization. Moreover, it presents a high versatility and tunability which further contribute to its significance in the field of ferroelectric materials.

1.2 Modeling and theoretical aspects on ferroelectricity

In the preceeding section, various facets of ferroelectricity were introduced. Continuing with this introduction, the upcoming section delves into fundamental aspects of ferroelectricity and the modeling approaches employed for these materials. Particularly, the Landau-devonshire theory is introduced along with unique features of particular ferroelectric relaxors. These concepts are essential as it is highly related to the modeling and the experimental work conducted in this research project.

1.2.1 Spontaneous symmetry breaking and soft mode

Ferroelectricity has been largely theoretically investigated and different models have been used to describe it. One major problem to model ferroelectric materials is to consider their phase transitions. Landau phenomenological theory based on mean field approximation (no long range correlations) has been largely employed and the approximation works well for describing ferroelectric materials far from the transitions. However, the theory inevitably becomes less accurate when approaching the transition. Indeed, phase transitions are critical phenomena and it is complex to describe them due to the large fluctuations of physical quantities when getting closer to the transition. However, with the development of renormalization group, it allowed to give a theoretical framework to better describe phase transitions in condensed matter [Vas04]. In this approach, when a spontaneous symmetry breaking occurs, a "Goldstone" boson is emitted (Higgs boson in particle physic) [Pol75]. In the case of ferroelectricity, this boson is a phonon and it is known as "Goldstone mode" which correspond to a lattice vibrational mode [Val20]. A classical illustration of this spontaneous symmetry breaking is to consider a sombrero hat energy profile with a ball in a central minimum energy point. Approaching the transition, the energy barrier is very low and the material is in a metastable state as illustrated in Figure 1.8 (a)). Finally, the ball fall in a more stable lower energy state which corresponds to a ferroelectric state with lower symmetry (Figure 1.8 (b)). There was few report in the literature of measurements of this mode [Pro+20; Mar+18] but it remains very challenging to observe.

Another phonon mode which has been largely investigated in the literature is called "the soft mode". Contrary to the Goldstone mode, the soft mode is easily measured via optical spectroscopy (Raman, Brillouin) or inelastic neutron scattering [Han+07; Shi+70]. Indeed, significant advancements in understanding the physics of ferroelectricity were greatly facilitated by the examination of how polar phonons change with temperature [Bov+04; GPS00]. This mode amplitude varies with temperature, particularly when approaching the Curie temperature (T_c), this phonon

Thèse accessible à l'adresse : https://theses.insa-lyon.fr/publication/2024ISAL0017/these.pdf © [G. Taxil], [2024], INSA Lyon, tous droits réservés

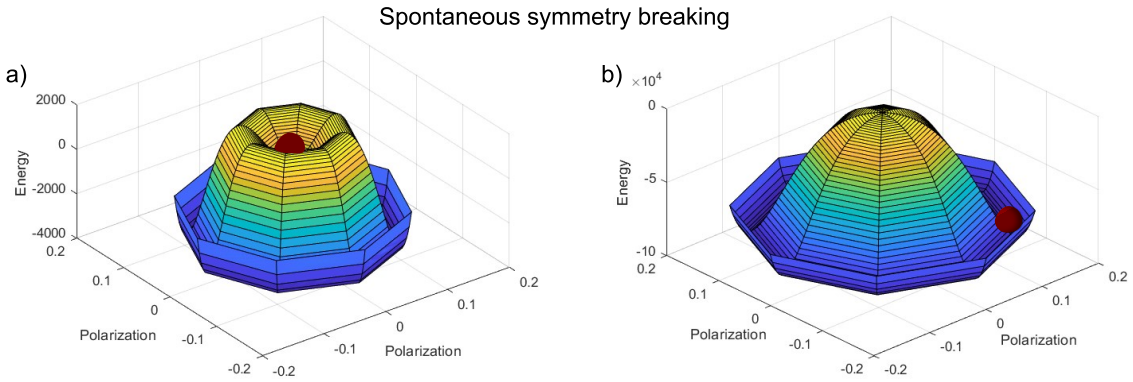

FIGURE 1.8: Illustration of a spontaneous symmetry breaking. (a) Paraelectric metastable state; (b) Ferroelectric stable state

mode becomes "soft". This means that the energy required to excite this mode decreases significantly, and it becomes the dominant vibrational mode. The spontaneous symmetry breaking that occurs at the FE-PA transition is inherent of a second order transition. This has the consequence of diverging the dielectric permittivity at the FE-PA transition [Rab+07]. Thus, Lyddane–Sachs–Teller relation has been largely employed [Tan69] because it links the ratio of the frequency of longitudinal and transverse optical phonons to the ratio of the static dielectric permittivity and high frequencies dielectric permittivity. This relation is derived from the Newton equation of the lossless Lorentzian oscillator model and is expressed as:

$$\frac{\omega_{LO}^2}{\omega_{TO}^2} = \frac{\kappa_{st}}{\kappa_\infty} \tag{1.6}$$

where ω_{LO} and ω_{TO} are respectively the frequencies of the longitudinal and transverse optical phonons and κ_{st} and κ_∞ are respectively the static dielectric permittivity and the dielectric permittivity at high frequencies. It can be noted that the dielectric permittivity divergence appears clear with this relation as the polar phonon (transverse optical) frequency tend to zero at the FE-PA transition. Despite having been discovered and used for a long time in ferroelectrics, soft mode concept remains largely investigated as it give fundamental informations on ferroelectric materials and their transitions.

1.2.2 Landau-Devonshire theory

The Landau theory is a mean field theory introduced by Lev Landau to describe firstly second order (continuous) phase transitions [Lan37]. Landau relied on two assumptions to develop his theory. First, the free energy should respect the hamiltonian symmetry and finally, the free energy and its gradient should be an analytical function of the order parameter (polarization in the case of ferroelectrics). Thus, he expressed the free energy in series expansion of the order parameter in the form of:

$$F = A(T)\eta^2 + B(T)\eta^4 + C(T)\eta^6 + ... \tag{1.7}$$

where A(T), B(T) and C(T) are temperature dependants variable and η is the order parameter. The Landau theory is strongly linked to the concept of soft mode as the order parameter is directly connected to the phonon mode that vanishes at the transition. Particularly, at the phase transition temperature, a specific lattice mode

Thèse accessible à l'adresse : https://theses.insa-lyon.fr/publication/2024ISAL0017/these.pdf © [G. Taxil], [2024], INSA Lyon, tous droits réservés

undergoes a "softening" of its restoring force, resulting in a significantly greater amplitude than all other modes in the vicinity of the phase transition temperature. Consequently, the total energy, originally thought to be the sum of all lattice modes, can now be approximated through a series expansion solely based on the amplitude of this particular mode [Cao08b].

The Landau theory was first employed for ferroelectrics by Devonshire in 1949 [Dev49] to describe phase transitions of barium titanate. $B_aT_iO_3$ presents first order transition which implied that the mode is not totally softened at the transition, thus, the approximation of the development in a serie expansion of an unique mode is not as rigorous as for second order transition [Cao08b]. However, in ferroelectrics the Landau approach works surprisingly well even for first order transition and has been strongly experimentally confirmed along the year. The success of the Landau-Devonshire theory for describing ferroelectrics lies on the long range interactions so the mean field approximation is pretty accurate in these materials [CL07]. The free energy proposed by Devonshire is expressed in tensorial notation as:

$$\begin{aligned} F_{lgd} &= F_0 + \alpha_{ij}P_iP_j + \alpha_{ijkl}P_iP_jP_kP_l + \alpha_{ijklmn}P_iP_jP_kP_lP_mP_n \\ &\quad + \alpha_{ijklmnop}P_iP_jP_kP_lP_mP_nP_oP_p + ... \end{aligned} \tag{1.8}$$

where P_i are components of the spontaneous polarization; α_{ij}, α_{ijkl}, α_{ijklmn} and $\alpha_{ijklmnop}$ are tensors representing the different orders of the dielectric stiffness and F_0 is the energy of the cubic phase (generally set to zero). This free energy must be invariant to a parent phase which is chosen to be the $m\bar{3}m$ cubic symmetry [Cao08a; Li+12]. It is possible to add other contributions to the free energy and here lies the success of phenomenological approach. As long as these new terms respect the symmetry of the free energy, new couplings can be added even if they are not directly linked to the soft mode [Cao08b]. Indeed, as explained before, the soft mode and associated polarization corresponds to a transverse optical mode. Yet, strain of the material can be added to the free energy even if it corresponds to an acoustic mode because it respects the free energy symmetry. In ferroelectrics the possible contributions to the free energy are expressed as:

$$F = F_{lgd} + F_{elas} + F_{elec} + F_{grad} \tag{1.9}$$

F_{lgd} is the classical Landau free energy introduced above. F_{elec} is associated with the energy of an applied electric field and is given by:

$$F_{elec} = -E_iP_i \tag{1.10}$$

where E_i and P_i are the different components of the electric field and the polarization. F_{elas} corresponds to the strain contributions to the free energy and is expressed as:

$$F_{elas} = \tfrac{1}{2}C_{ijkl}(\epsilon_{ij} - \epsilon^0_{ij})(\epsilon_{kl} - \epsilon^0_{kl}) \tag{1.11}$$

where C_{ijkl} is the elastic stiffness tensor and ϵ_{ij} and ϵ^0_{ij} are the total strain and the spontaneous strain tensors. F_{grad} denotes the free energy contributions from the domain walls and was first introduce by Ginzburg for superconductivity [GGL09]

Thèse accessible à l'adresse : https://theses.insa-lyon.fr/publication/2024ISAL0017/these.pdf © [G. Taxil], [2024], INSA Lyon, tous droits réservés

and is given by:

$$\begin{aligned} F_{grad} &= \tfrac{1}{2}G_{11}\Big[(\tfrac{\partial P_1}{\partial x})^2+(\tfrac{\partial P_1}{\partial y})^2+(\tfrac{\partial P_1}{\partial z})^2+(\tfrac{\partial P_2}{\partial x})^2+(\tfrac{\partial P_2}{\partial y})^2 \\ &\quad +(\tfrac{\partial P_3}{\partial z})^2+(\tfrac{\partial P_3}{\partial x})^2+(\tfrac{\partial P_3}{\partial y})^2+(\tfrac{\partial P_3}{\partial z})^2\Big] \end{aligned} \tag{1.12}$$

where G_{11} is the gradient energy coefficient. In the rest of this work we will not consider the gradient energy term (Domain walls) as ferroelectric materials are investigated here under large electric fields. In such conditions the crystal can be considered in a single domain state and this term can be neglected [CL07]. Also, instead of considering free energy variations, free enthalpy variations will be considered in the rest of this manuscript because we will have stress variations as an input rather than strain ones. The total free enthalpy variations by performing a Legendre transformation and by neglecting the gradient energy term is given in tensorial notation by:

$$\begin{aligned} \Delta G &= \alpha_{ij}P_iP_j+\alpha_{ijkl}P_iP_jP_kP_l+\alpha_{ijklmn}P_iP_jP_kP_lP_mP_n+\alpha_{ijklmnop}P_iP_jP_kP_lP_mP_nP_oP_p \\ &\quad -\tfrac{1}{2}s_{ijkl}\sigma_{ij}\sigma_{kl}-Q_{ijkl}\sigma_{ij}P_kP_l-E_iP_i \end{aligned} \tag{1.13}$$

where σ_{ij} is the stress tensor and s_{ijkl} and Q_{ijkl} are respectively the compliance and electrostrictive tensors. The stable crystal state of the material is found by minimizing the free enthalpy with respects to the polarization ($\frac{\partial \Delta G}{\partial P}=0$). The interest of such a theoretical approach is to take into account the temperature, the electric field and the stress applied to the material while predicting the different phase transitions of ferroelectric materials. An illustration of the free energy of ferroelectric materials under different electric field with the associated stable state are presented in Figure 1.9.

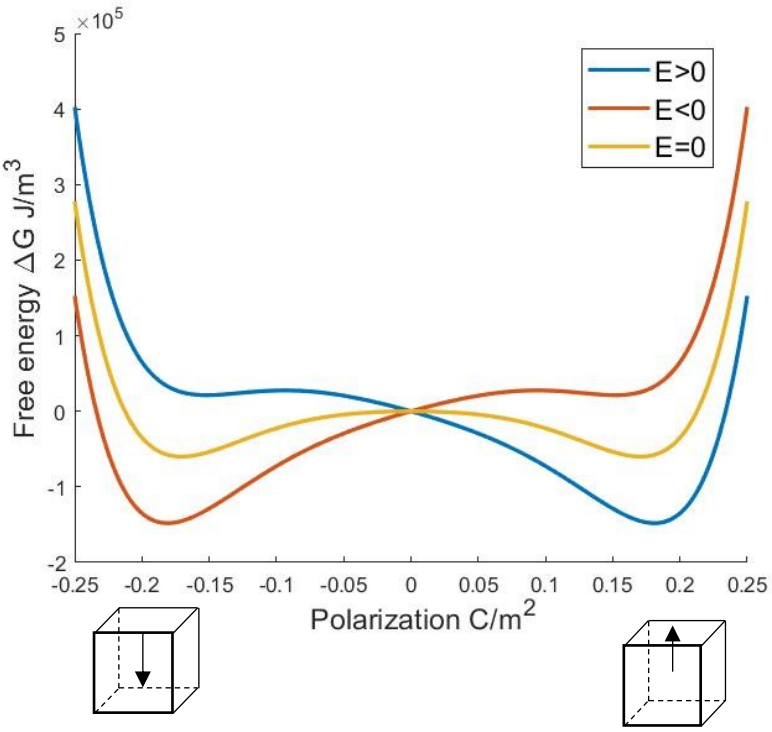

FIGURE 1.9: Free energy of a ferroelectric material for different electric fields

Thèse accessible à l'adresse : https://theses.insa-lyon.fr/publication/2024ISAL0017/these.pdf © [G. Taxil], [2024], INSA Lyon, tous droits réservés

More details will be given in the next chapter on Landau-Devonshire theory applied to multiphysic coupling and energy conversion especially in the framework of energy harvesting.

1.2.3 Highly piezoelectric perovskites

In the 2000's, $(1-x)PMN-xPT$ and $(1-x)PZN-xPT$ single crystals gained a lot of interest from the scientific community due to their remarkable features [PS97a; Kia+02]. One of their remarkable properties is to present particularly high piezoelectric coefficients (d_{ij}) around an order of magnitude over classical ferroelectric materials. However, they exhibit these exceptional properties only for particular compositions [Raj+07]. This range of composition is called morphotropic phase boundaries (MPB) and it is a region where the material can easily transit from a ferroelectric phase to another one by external applied stress or electric field [Dav07; WC17]. $(1-x)PMN-xPT$ and $(1-x)PZN-xPT$ phase diagrams have similar shape. They both are in a rhombohedral state for low x concentration of $PbTiO_3$ and both present a tetragonal one for higher x concentration of $PbTiO_3$. In the concentration range of $0.3 < x < 0.35$ for PMN-PT and in the range of $0.08 < x0.12$ for PZN-PT, both are in the MPB and the associated ferroelectric phases are monoclinic which is a phase in which the polarization is typically not along any of the principal crystallographic axes. The phase diagrams of PMN-PT and PZN-PT are illustrated in Figure 1.10

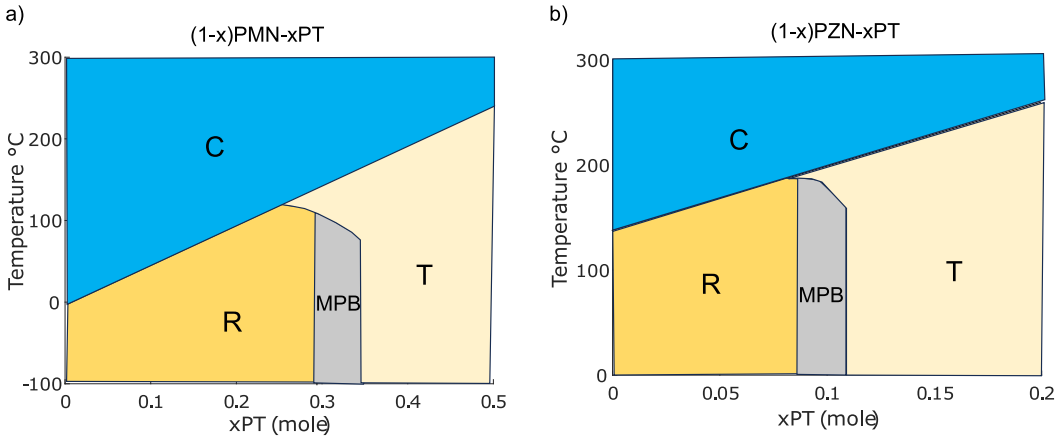

FIGURE 1.10: Concentration−Temperature phase diagrams (a) $(1-x)PMN-xPT$; (b) $(1-x)PZN-xPT$

Another particularity of these materials is that they are relaxors. Unlike traditional ferroelectric materials, which have well-defined phase transitions and sharp polarization vs. temperature curves, ferroelectric relaxors display a more gradual and diffuse transition, over a wide range of temperatures [Ye98].

A surprising result in the scientific community for such perovskites ferroelectric relaxors was to find out that they exhibit their outstanding properties when crystal orientation is not in the same direction than the spontaneous polarization. This leads to the development in ferroelectric materials of the concept of domain engineering which consists in tayloring concentration, crystal orientation or doping to enhance the properties of the material [SC14; Sch+17]. The inherent structure of ferroelectrics in various domains leads to the outcome that when the crystal is poled along a specific direction (macroscopic symmetry), the orientation of spontaneous

Thèse accessible à l'adresse : https://theses.insa-lyon.fr/publication/2024ISAL0017/these.pdf © [G. Taxil], [2024], INSA Lyon, tous droits réservés

Ferroelectric state	$[001]_c$ poled	$[011]_c$ poled	$[111]_c$ poled
Rhombohedral	4R	2R	1R
Orthorhombic	4O	1O	3O
Tetragonal	1T	2T	3T

TABLE 1.1: Domain configuration names depending on crystal orientations

polarization within the domains, at a microscopic level, may not exhibit the same symmetry (microscopic symmetry) as that of the crystal lattice. A list of the different domain configurations depending on the crystal orientation is provided in Table 1.1 and an associated illustration is given in Figure 1.11.

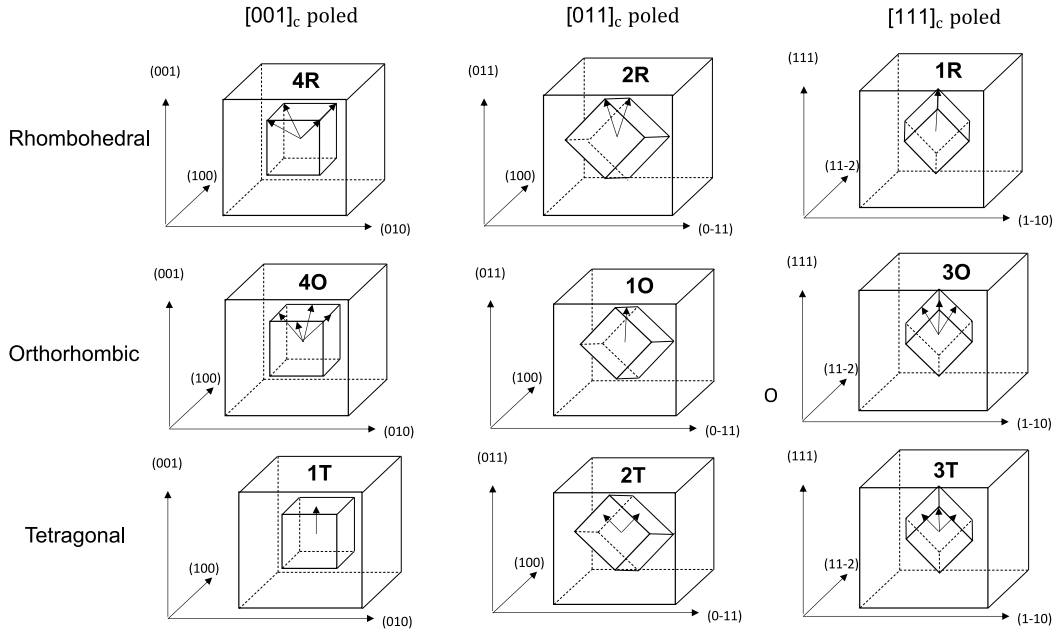

FIGURE 1.11: Illustration of the ferroelectric state depending on the crystal orientation

Depending on the crystal orientation, piezoelectric coefficients of the PMN-PT and PZN-PT vary largely. As mentioned before the highest d_{33} is found to be in <001> oriented crystals. More surprisingly, in <111> oriented crystals the d_{33} value is much smaller even if the crystal cut correspond to the polarization direction. In the litterature, different works focused on characterization of the different piezoelectric coefficients in such ferroelectric relaxors. For comparison, Table. 1.2 proposed the different piezoelectric coefficients found in the literature depending on the orientation for relaxors PMN-PT and PZN-PT and for the more "classical" ferroelectric $BaTiO_3$

In the case of PMN-xPT and PZN-xPT with composition close to the MPB, the highest values of the d_{33} (stress and electric field applied along the 3 direction) were found in $[001]_c$ poled single crystal even if the crystal was in a rhombohedral state. This behavior has been explained by rotation of the polarization vector induced by the electric field [FC00; Liu+23]. It is possible to explain this phenomena in the frame

Thèse accessible à l'adresse : https://theses.insa-lyon.fr/publication/2024ISAL0017/these.pdf © [G. Taxil], [2024], INSA Lyon, tous droits réservés

Piezoelectric coefficients	PMN-30PT (Rhombohedral)	PZN-8PT (Rhombohedral)	$BaTiO_3$ (Tetragonal)
<001> d_{31}	-1250 pC/N [Sha+07]	-1600 pC/N [Sha+07]	-33.4 pC/N [Wad+05]
<001> d_{33}	2350 pC/N [Sha+07]	2700 pC/N[Sha+07]	90 pC/N [Zgo+94]
<011> d_{31}	-2300 pC/N [Sha+07]	-1200 pC/N [M03]	-23.85 pC/N [LL03]
<011> d_{33}	800 pC/N [LB21]	N/A	219 pC/N [LL03]
<111> d_{31}	-90 pC/N [Dav06]	-42 pC/N [Bar+00]	-62 pC/N [LB21]
<111> d_{33}	125 pC/N [LB21]	70 pC/N [Dav06]	203pC/N [Wad+99]

TABLE 1.2: Piezoelectric coefficients for different materials and crystal orientations at room temperature

of the Landau approach. Indeed, close to the MPB, the Gibbs free energy profile is more flat and the correlation between this flattening and high piezoelectricity has been reported in the literature [Wan+23; Dam05]. An illustration of the polarization rotation mechanisms with associated Gibbs free energy for 4R engineered domains is presented in Figure 1.12. The theoretical comprehension of the origin of such a high piezolectricity in PMN-PT and PZN-PT in the MPB remains a hot research topic. A lot of studies still focuses on understanding the physics and polarization mechanisms in such relaxors due to the attractive properties of these materials and the different complex physical coupling inherent to these materials [Sun+22; Rol+22].

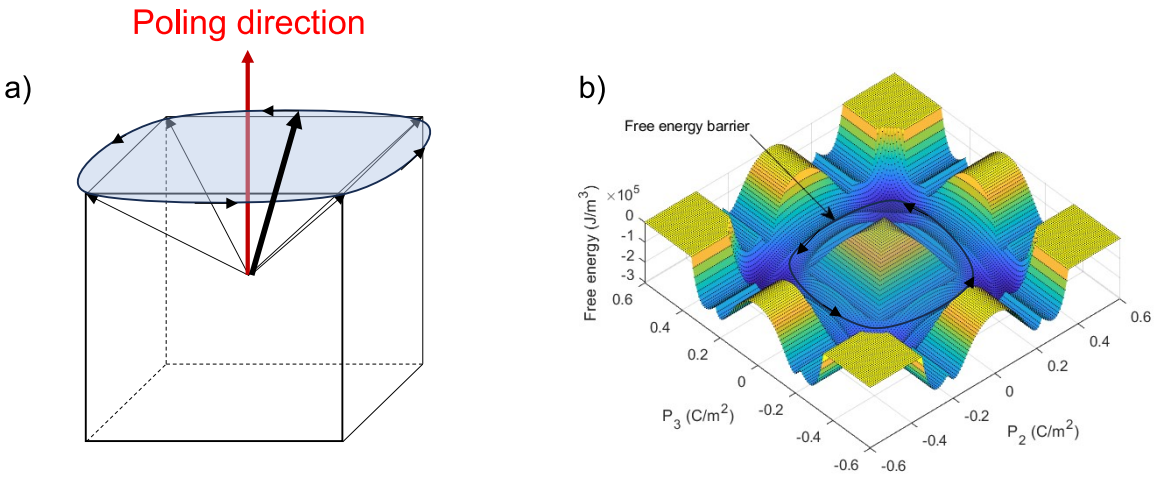

FIGURE 1.12: Illustration of the enhanced piezoelectric properties of ferrolectric relaxors. (a) Polarization rotation mechanisms; (b) Flat Gibbs free energy

1.2.4 Polar nanoregions

One characteristic of ferroelectric relaxors like PMN-PT and PZN-PT is to present Polar nanoregions. Polar nanoregions (PNRs) are small, nanoscale regions within

Thèse accessible à l'adresse : https://theses.insa-lyon.fr/publication/2024ISAL0017/these.pdf © [G. Taxil], [2024], INSA Lyon, tous droits réservés

certain materials that exhibit local polarization. These regions are characterized by a spontaneous electric polarization that arises from the arrangement of electric dipoles in the material. PNRs are a phenomenon commonly observed in relaxor ferroelectric materials. These PNRs appear only in a certain range of temperature. The Burns temperature (T_B) is generally introduced and indicates the limit temperature above which, the PNRs appear and their contributions to the properties of the material being very important [Li+17a; SC10; BD83].

Ferroelectric relaxors are renowned for their tunable dielectric properties, and this tunability is intimately linked to the presence of polar nanoregions within these materials [Ren+14; Xu+13]. The contribution to the polarization in ferroelectric relaxors is generally divided in two distinct contributions. The contribution inherent to the non-centro symmetric lattice and the resulting polarization is generally called "intrisinc contribution". Finally, the contribution to the polarization induced by domain walls or PNRs is qualified as "extrinsic contribution" [Tan+16]. Different approaches have been proposed to describe these PNRs in the frame of ferroelectric relaxors. Some works proposed to employ phenomenological approach and defined two distinct free energies [Li+17b]. Another possibility lied in considering the intrinsic contribution in the frame of the Landau-Devonshire theory and to consider the extrinsic contributions with a Langevin term derived from statistical physics [Wu+09; MMG21]. This approach has been used in the literature to estimate the dielectric permittivity depending on the applied electric field. Here, the dielectric permittivity is expressed in the form of:

$$\kappa(E) = \kappa_{intr}(E) + \kappa_{extr}(E) \tag{1.14}$$

The intrinsic permittivity $\kappa_{intr}(E)$ is called the Johnson term and is derived from Landau-Devonshire theory yielding:

$$\kappa_{intr}(E) = \frac{\kappa(0)}{(1+(\lambda(\kappa_0\kappa(0))^3)E^2)^{\frac{1}{3}}} \tag{1.15}$$

where κ_0 represents the vacuum dielectric permittivity, λ serves as a coefficient that characterizes the extent of non-harmonic contributions of polarization to the free energy, and E denotes the applied electric field. On the other hand, the extrinsic contribution term to the dielectric permittivity is expressed as follow:

$$\kappa_{extr}(E) = \frac{P_r x}{\kappa_0}(cosh(Ex))^{-2} \tag{1.16}$$

where $x = \frac{P_r V}{2k_b T}$, P_r is the polarization of a polar nanocluster, V is the volume of a PNR, k_b is the Boltzmann constant, and T is the temperature. The total dielectric permittivity depending on applied electric field is expressed as:

$$\kappa(E) = \frac{\kappa(0)}{(1+(\lambda(\kappa_0\kappa(0))^3)E^2)^{\frac{1}{3}}} + \frac{P_r x}{\kappa_0}(cosh(Ex))^{-2} \tag{1.17}$$

Different typical values were taken from the literature for ferroelectric relaxors [Liu+16] in order to plot permittivity in function of the electric field and the temperature as illustrated in Figure 1.13. This plot illustrates that the contribution of PNRs when a sufficient electric field is applied can be neglected as the crystal tend to be in a single domain state [CL07]. Moreover, when working in a temperature range sufficiently far from the Burns temperature, their effects can be neglected. In the rest of this work, the contributions of such PNRs will not be considered. Indeed, the

Thèse accessible à l'adresse : https://theses.insa-lyon.fr/publication/2024ISAL0017/these.pdf © [G. Taxil], [2024], INSA Lyon, tous droits réservés

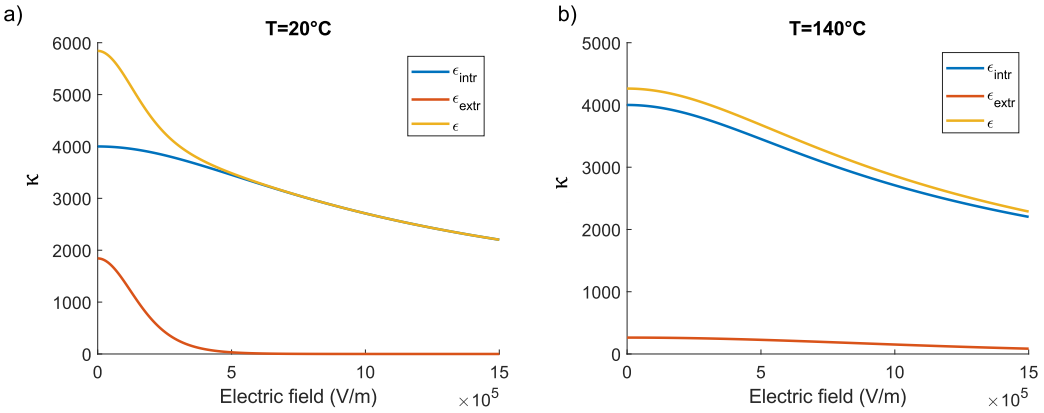

FIGURE 1.13: Dielectric permittivity as a function of the electric field for different temperature for $KNa_{0.5}Nb_{0.5}0_3 - SrTiO_3$ ceramics [Liu+16]; (a) T=20°C; (b) T=140°C

electric field applied to the materials were in the order of $1kV/mm$ and the sample were studied sufficiently far from the Burn temperature. However, it has be proven that PNRs have an importance in ferroelectric relaxors properties. Thus, considering their impact could be the topic of future investigation in the frame of the work reported in this study.

1.3 Energy harvesting

1.3.1 Generalities on energy harvesting

Harvesting energy from ambient sources presents a promising approach to powering wireless sensors and other low-power devices, particularly in challenging or remote environments. This method offers notable advantages, including cost effec-

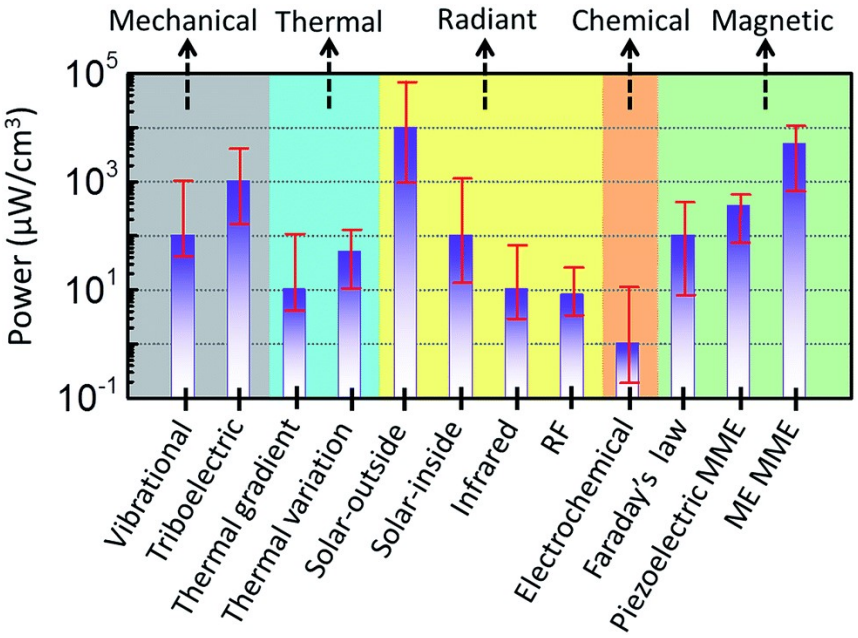

FIGURE 1.14: Comparison between the different energy sources and their energy densities [Ann+17]

Thèse accessible à l'adresse : https://theses.insa-lyon.fr/publication/2024ISAL0017/these.pdf © [G. Taxil], [2024], INSA Lyon, tous droits réservés

tiveness and the elimination of maintenance tasks like battery replacements, which are often necessitated because of their self-discharge. Consequently, there has been a substantial increase in research and development efforts focused on energy harvesting in recent decades. This surge is largely driven by the proliferation of the 'Internet of Things' (IoT), which required interconnection of numerous low-power devices capable of autonomously exchanging data. Various forms of environmental energy, such as vibration, solar radiation, wind, and waste heat, can be scavenged and converted into electrical energy. In the actual context of global warming and the requirement for humanity to use cleaner energies, energy harvesting is a good alternative solution. However, it suffers from low output power and research efforts have been then focused on increasing the output energy [KKK18; RYK19; Dha+13]. A comparison illustrating the power density between various energy sources and types of energy harvesting is presented in Figure 1.14. In energy harvesting, the energy source passes through a transducer that will convert this energy in electrical one. An schematic illustration of this process is proposed in Figure 1.15.

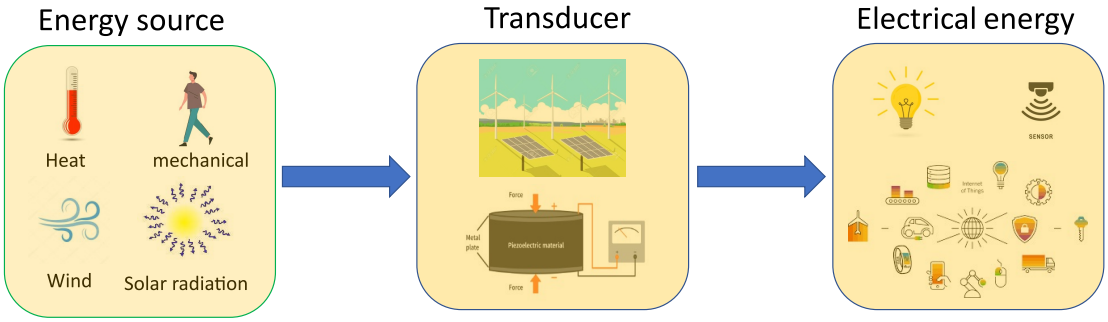

FIGURE 1.15: Illustration of the processes in energy harvesting

In this work, the only transducers we will consider are based on ferrolectric materials. As explained in the previous sections, these materials are unique due to their piezoelectric and pyroelectric properties as well as their polarization reversal capabilities. Thus, this work will focus specifically on energy harvesting through the use of piezoelectricity or pyroelectricity and unique properties of ferroelectricity. Energy harvesting via the piezoelectric effect is, as we will explore, one of the most extensively researched areas in terms of ambient energy harvesting. However, energy recovery through the pyroelectric effect is nonetheless a promising candidate for energy harvesting.

1.3.2 Pyroelectric energy harvesting

Waste heat is a valuable energy source that is frequently underestimated and not fully exploited. In the United States, for instance, approximately two-thirds of the energy generated ends up being dissipated as unused heat [Liv13]. This wasted energy is prevalent in various sectors, from industrial settings like power plants and oil refineries, to everyday sources like hot water systems and vehicle exhaust pipes. Furthermore, emerging areas such as the heat emanating from data centers and solar panels offer good opportunities for thermal energy recovery [McK13]. Another noteworthy example includes the heat released by the human body or the temperature gradient created by solar radiation, both of which have been used for pyroelectric energy harvesting [Sul+18; Sod+07; Pan+19]. One disadvantage of pyroelectric energy harvesting is to present a low efficiency to convert the input energy. However,

Thèse accessible à l'adresse : https://theses.insa-lyon.fr/publication/2024ISAL0017/these.pdf © [G. Taxil], [2024], INSA Lyon, tous droits réservés

the energy source involved are higher compared to other methods such as vibrations. Ultimately, this leads to a comparable energy density per cycle. During the last decade, the interest of the scientists for energy harvesting with pyroelectric materials has grown, even if this increase has slightly slowed down during last years. This tendency is illustrated in Figure 1.16 and shows that the part of research publications in pyroelectricity dedicated to energy harvesting represents a significant amount.

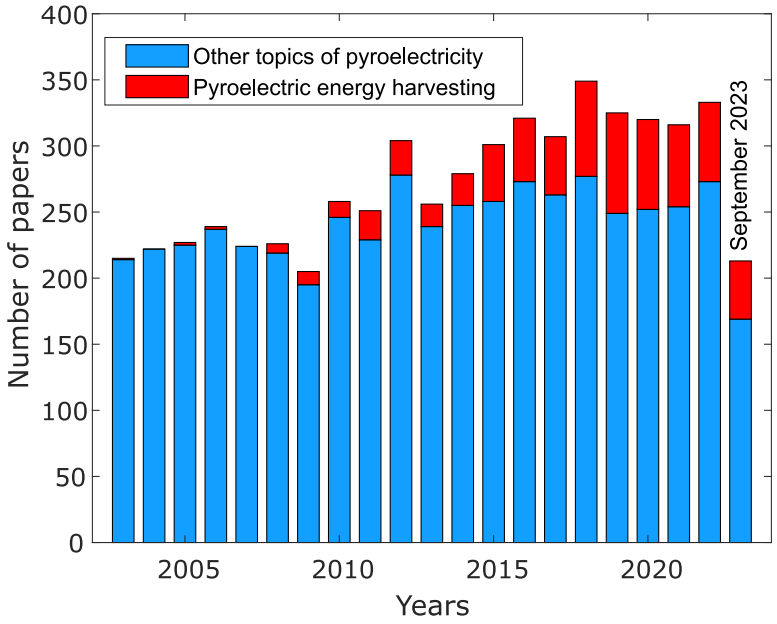

FIGURE 1.16: Evolution of the number of scientific papers on pyroelectric energy harvesting. The data have been taken from "Web of Science" database (https://www.webofknowledge.com)

As mentioned before and as for any energy sources, the major issue remains the low output power. Nonetheless, there are numerous approaches available to improve the effectiveness of pyroelectric energy harvesting and other energy harvesting systems in general, including the development of inventive electrical circuits [Guy+05; LG08]. Employing innovative electromechanical structure with diverse geometries is another avenue to explore [AYH14]. Additionally, using the proper material with optimal pyrolectric properties [SLG08] can enhance the converted energy. Finally, employing phase transitions of ferroelectric materials presents a viable option for energy harvesting, although this approach remains relatively underexplored [Kho+09b; Hof+15], with limited dedicated studies in the field. For instance, Lheritier, *et al* [Lhe+22] reported recently more than 10J harvested per cycle showing the possible interest of pyroelectric materials and the possible implementation in real devices.

1.3.3 Mechanical energy harvesting

In energy harvesting, among all the energy sources, mechanical energy sources have been the most studied due to the abundance of this energy form in the nature. Another interesting feature of mechanical energy harvesting is to work with vibrating energy sources featuring resonant condition with optimized devices [BTW06; Mun+16]. Vibrating energy sources are numerous in the environment, for instance:

Thèse accessible à l'adresse : https://theses.insa-lyon.fr/publication/2024ISAL0017/these.pdf © [G. Taxil], [2024], INSA Lyon, tous droits réservés

- **Machinery and Industrial Equipment:** Vibrations generated by rotating machinery, engines, conveyor belts, and other industrial equipments;
- **Transportation:** Vibrations from cars, trucks and trains;
- **Human Motion:** Kinetic energy from human motion, such as walking, running, or body movements;
- **Structural Vibrations:** Buildings and infrastructure can experience vibrations due to wind, traffic, or seismic activity.

Vibration source	Acceleration ($m.s^{-2}$)	Frequency (Hz)
Car engine	12	200
Base of 3-axis machine tool	20	70
Blender casing	6.4	121
Clothes dryer	3.5	121
Person nervously tapping their heel	3	1
Car instrument panel	3	13
Door frame just after door closes	3	125
Small microwave oven	2.5	121
HVAC vents in office building	0.2 - 15	60
Windows next to a busy road	0.7	100
CD on notebook computer	0.6	75
Second story floor of busy office	0.2	100

TABLE 1.3: comparison of different vibration sources with their associated accelerations and frequencies [RWR03]

Table 1.3 proposed a list of potential vibration sources with their associated accelerations and vibrations. Extensive research has been undertaken to exploit this energy source due to its abundance and high potential energy density, as highlighted in previous studies [Cle+21; Yan+22a]. Typically, three primary technologies (transduction methods) are employed to transform mechanical vibrational energy into electrical energy: piezoelectricity, electromagnetism, and electrostatic energy.

Electrostatic

Electrostatic energy harvesting consists of employing a capacitive structure with two parallel plates separated by a small gap. When subjected to mechanical vibrations, such as bending or movement, the gap between these plates fluctuates, leading to

Thèse accessible à l'adresse : https://theses.insa-lyon.fr/publication/2024ISAL0017/these.pdf © [G. Taxil], [2024], INSA Lyon, tous droits réservés

variations in the capacitance. Consequently, when biased by an electrical source, charge separation occurs, with electrons accumulating on one plate and leaving a deficit on the other. This charge imbalance creates an electric potential difference, which, when connected to an external circuit, generates an electrical current [Har11]. The mechanism and an illustration of an electrostatic energy harvester is proposed in Figure 1.17. Electrostatic energy harvesters are particularly advantageous in applications with low-frequency, high-displacement mechanical vibrations, offering durability, low maintenance requirements, and suitability for micro-scale and wearable technologies. Nonetheless, they may exhibit lower efficiency compared to other energy harvesting methods for high-frequency vibrations. Indeed, these types of transducers generally have the capacity to provide power on the order of hundreds of milliwatts (mW). Moreover, electrostatic transducers required a polarization source to initially charge the capacitor. Nevertheless, electrostatic energy remains an active field of research and researchers make strong efforts to use the broad bandwidth and to combine it with high output power like the recent work of Zhang, *et al* [Zha+18].

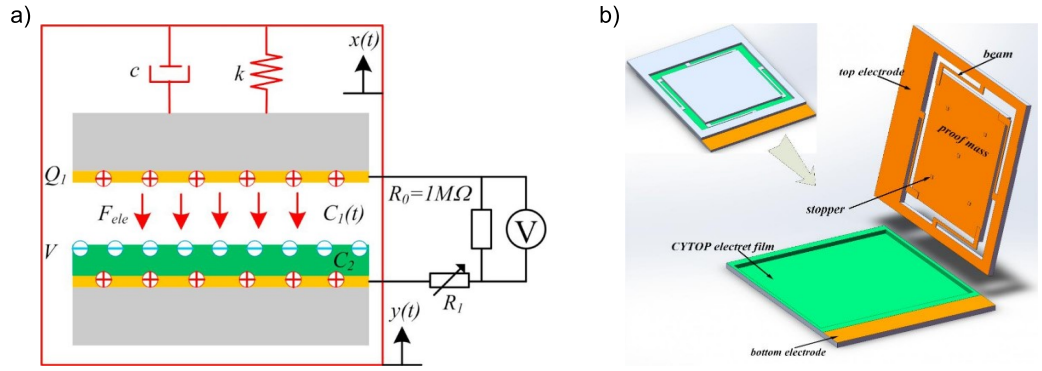

FIGURE 1.17: (a) Electrostatic transduction method for energy harvesting [Zha+18]; (b) 3D schematic of the electrostatic energy harvester [Zha+18]

Electromagnetic

Electromagnetic transducers use generally a coil placed within a magnetic field. When subjected to mechanical vibrations or movements, the coil experiences changes in magnetic flux, which induces an electromotive force and generates an electrical current. A schematic description of the electromagnetic transduction is proposed in Figure 1.18 (a). The most famous application of this method is the flashlight which is depicted in Figure 1.18 (b). In this design, shaking the flashlight causes the magnet to move through a solenoid coil. This motion induces an electric current within the coil, which, in turn, powers the illumination of a light-emitting diode (LED). Electromagnetic energy harvesters are particularly suitable for applications with moderate to high-frequency vibrations, making them valuable in different scenarios and also for small-scale applications. However, it poses challenges when integrating with MEMS (Micro Electro-Mechanical Systems) due to its relatively large size and the requirement of large displacements of the magnet to obtain significant energy [BO09]. Furthermore, these systems usually produce low-voltage outputs, around ten to hundreds of millivolts (mV), which makes designing the energy extraction unit for powering sensor nodes more complex [Lom20].

Thèse accessible à l'adresse : https://theses.insa-lyon.fr/publication/2024ISAL0017/these.pdf © [G. Taxil], [2024], INSA Lyon, tous droits réservés

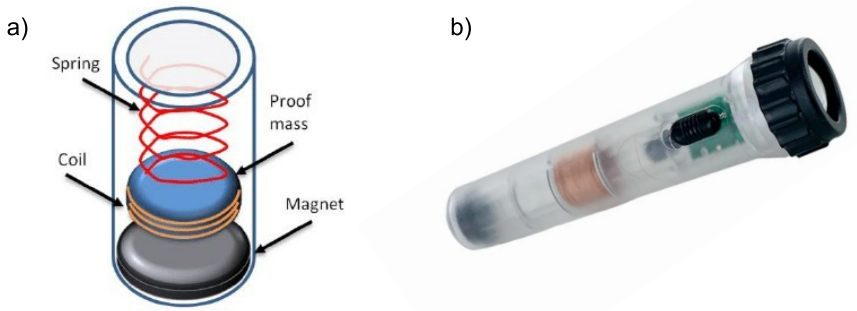

FIGURE 1.18: (a) Electromagnetic transduction method [AC98]; (b) Flashlight powered by an electromagnetic generator (https://www.arborsci.com)

Piezoelectric

Piezoelectric transducers, consists in using the direct piezoelectric effect which generate an electric charge when subjected to mechanical stress or deformation. Piezoelectric harvesters are made of piezoelectric elements strategically placed within a system that experiences mechanical movement or vibrations. As these materials deform or vibrate, they produce electrical potential differences across their surfaces, generating a usable electric current. There are two distinct ways of using piezoelectric materials. The first one involves directly attaching the piezoelectric material

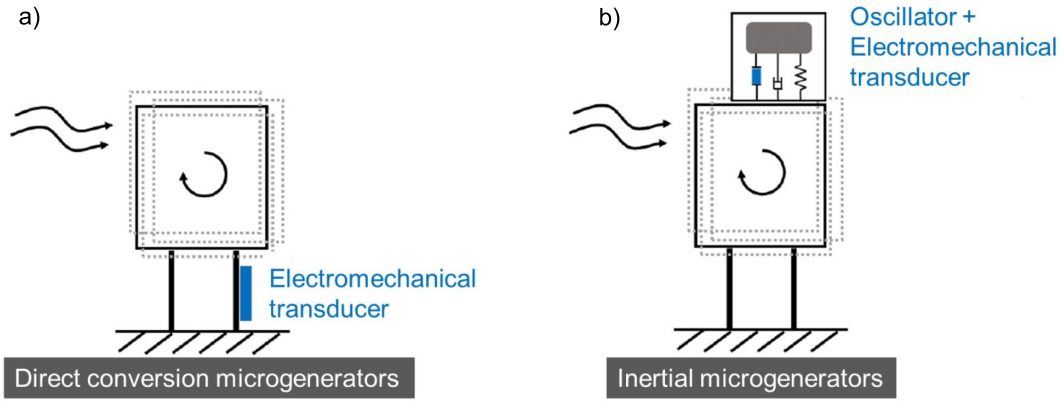

FIGURE 1.19: (a) A direct conversion microgenerator [Hug18]; (b) An inertial conversion microgenerator [Hug18]

to a host structure (direct conversion microgenerators) which results to a direct coupling. In the second approach, the piezoelectric element is connected to the structure through a secondary structure, creating an indirect coupling (inertial microgenerators) [Lal08]. This latter type of coupling allows for an independent design of the host structure and easier maintenance of the microgenerator, thus enabling an optimization of the system's response. Direct and indirect coupling will be more efficient in different situations. Indirect coupling is more adapted for fixed frequency

Thèse accessible à l'adresse : https://theses.insa-lyon.fr/publication/2024ISAL0017/these.pdf © [G. Taxil], [2024], INSA Lyon, tous droits réservés

application while direct coupling will be more adapted for broadband frequency applications [Hug18]. Piezoelectric energy harvesters are promising for their efficiency, compactness, and adaptability to a wide range of applications electronics. An illustration of microgenerators based on direct and inertial conversion are respectively depicted in Figure 1.19 (a) and (b).

In the rest of this manuscript, only piezoelectric transducers will be considered. More specifically, it will only be assured by ferroelectric materials. However, it was important to note that other transduction methods exist for energy harvesting and that it is also possible to combine these transducers to improve the output power [Lom20].

1.3.4 Structures for energy harvesting

Different structures with different geometries have been used in the frame of piezoelectric energy harvesting. These structures aim at improving the output power by different means. This section will be dedicated on presenting briefly some existing geometries that have been used in the literature.

Stack structure

One of the simplest structures in the research of energy harvesting from piezoelectric materials is the stack structure, it is illustrated in Figure 1.20. This geometry simply consists of multiple stacked piezoelectric structure containing more than two layers of wafer structure. This structure is capable of improving the current and voltage, and the working status is almost every time in 33-mode (stress and electric field applied in the same direction). It can be noted that the gain of energy of such transducers is not optimal due to the electromechanical coupling between the different layers. However, the simplicity of such structure and specifically for direct conversion microgenerators give a lot of advantages to the stack structure in a lot of situations [FGS08]. More details on this structure will be given in Chapter 4 where this structure was employed in one of our implemented devices.

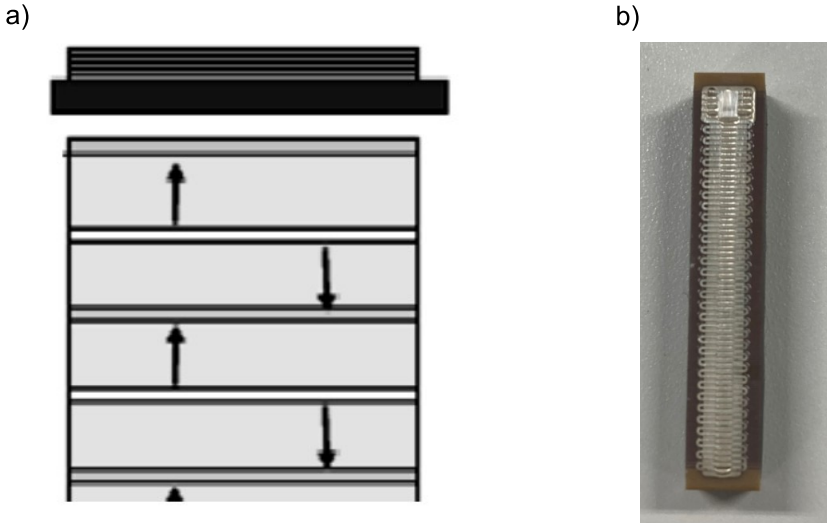

FIGURE 1.20: (a) A schematic illustration of a piezoelectric stack [Xu+18b]; (b) A photo of a piezoelectric stack

Thèse accessible à l'adresse : https://theses.insa-lyon.fr/publication/2024ISAL0017/these.pdf © [G. Taxil], [2024], INSA Lyon, tous droits réservés

Cantilever beam

A lot of works in energy harvesting employed a structure called “cantilever beam” [Fri+12; MJC09; Joh+06]. As illustrated in Figure 1.21. Piezoelectric cantilever beam is composed of a beam generally in steel or in aluminium. One or two piezoelectric layers (unimorph or bimorph) are fixed on the beam with a conductive adhesive. A block ("tipmass") is set at the end of the cantilever, which can increase the cantilever beam amplitude and adjust the frequency to increase the output power. The geometric configuration of cantilever structures is also a significant factor in enhancing the efficiency of energy harvesters. Rectangular-shaped cantilevers are widely employed in MEMS-based piezoelectric energy harvesting systems due to their ease of integration and their effectiveness in capturing energy from surrounding vibrations. However, different geometries exist (triangular, trapezoidal, etc) and have found their utility in other situations [GW08]. Due to its intrisic qualities, cantilever beam was used to develop another device in this work. More specifications on this structure will then be provided in Chapter 4.

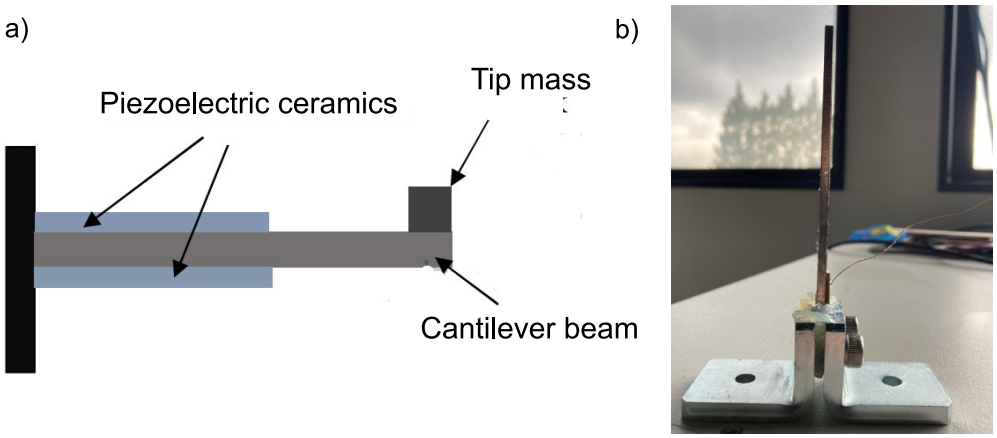

FIGURE 1.21: (a) A schematic illustration of a cantilever beam [Xu+18b]; (b) A photo of a cantilever beam (cf. Chapter 4)

Plucked method

One of the different piezoelectric energy harvester design, is called the plucked method. This energy harvester generator works for low frequency range (few Hz). It consists in a mass linked with a vibrating platform and secondary vibrating units composed of additional piezoelectric elements and vibrating beams fixed on one side. Ideally, when the initial impact effects on the platform, the mass attached on the mechanical energy transfer unit starts to vibrate in low frequency. The low vibration energy is then transferred to a much higher natural frequency vibration in the piezoelectric elements as the mass passes over and excites the piezoelectric beams [AKK21]. It can be noted that the excitation can be magnetically induced instead of employing mechanical impacts. An illustration of such method is given in Figure 1.22 (a).

Cymbal structure

Another promising design is called the cymbal structure. This geometry was developed in 90’s by the Pennsylvania state university to enhance the output power by his geometric form [DUN97]. This electric generator is composed by a thin piezoelectric

Thèse accessible à l'adresse : https://theses.insa-lyon.fr/publication/2024ISAL0017/these.pdf © [G. Taxil], [2024], INSA Lyon, tous droits réservés

disk with metal end cap on either side, as shown in Figure 1.22 (b). The different factor such as cymbal diameter, top diameter, and thickness of the end steel cap and the thickness of the piezoelectric material will determined the efficiency of the energy harvester.

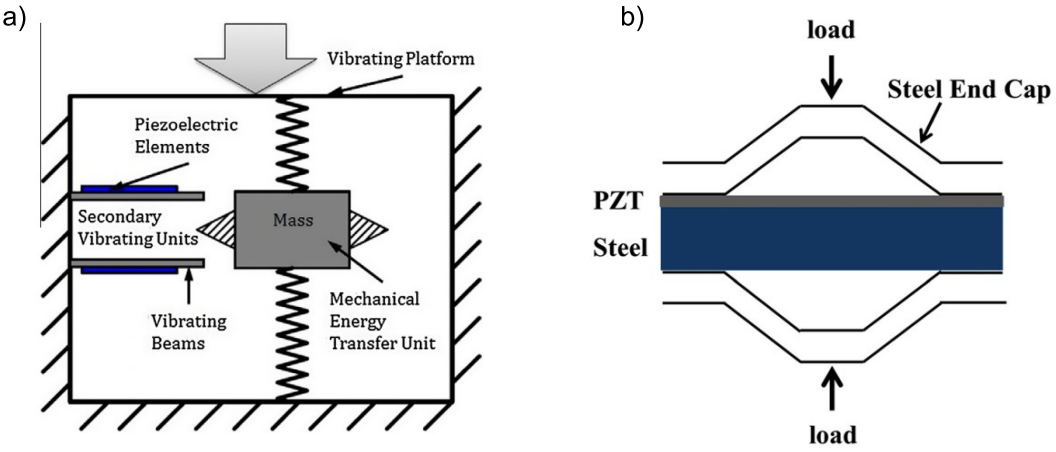

FIGURE 1.22: (a) The plucked method [LS14]; (b) An inertial conversion microgenerator using cymbal structure [SK21]

1.3.5 Non-resonant mechanical energy harvesting

As we have seen, in mechanical energy harvesting, the predominant focus in research lies on resonant devices that work with vibrating mechanical sources, as documented in various studies [BTW06; Mun+16; Cle+21; Yan+22a]. The typical output power of these microgenerators falls within the μW to mW range. In resonant energy harvesting, when the material is subjected to an imposed input force, the ultimate output power is limited by the product between the electromechanical coupling k^2 and the quality factor Q_m. Indeed when $k^2 Q_m >> \pi$, no better performance can be obtained, as it becomes independent of the piezoelectric material properties [Ste06; Lef+09]. As a result, in most mechanical energy harvesting systems, studies utilize the transducers within their linear range and tend to avoid the effects of non-linearities. However, this work aims to demonstrate the great potential of these non-linear transducer regimes for non-resonant mechanical energy harvesting. Non-resonant systems have received relatively less attention by the scientific community compared to resonant ones. The main challenge in this approach is to efficiently capture maximum energy from diverse mechanical sources. It is worth noting that there exists a large amount of sporadic mechanical energy inputs in our daily lives such as switches, footsteps, tire-road interactions and door openings [AAMF19; SVP16; Xu+18a]. All this energy sources have in common to be low frequency processes (<10Hz). Indeed, non-resonant energy harvesting approach is not really suitable for higher frequency.

There are a lot of demonstration made by companies on the feasibility of such an approach in the real environment. In order to scavenge foot step energy, in 2008, Sound Power Corp proposed a real harvester integrated in the floor of the Tokyo subway. Another application was the Sustainable Dance Floor in Rotterdam which developed a dance floor of a night club that harvested the energy induced by the

Thèse accessible à l'adresse : https://theses.insa-lyon.fr/publication/2024ISAL0017/these.pdf © [G. Taxil], [2024], INSA Lyon, tous droits réservés

steps of the dancers. Moreover, Enocean (ECO 200) proposes a fully functional energy converter for linear motion for possible applications such as miniaturized switches. An illustration of the experiment in Tokyo with the associated mechanism explanations is given in Figure 1.23.



FIGURE 1.23: Illustration of the Tokyo subway implementation [VK15]

Apart from foot steps energy scavenging, the scientific community focused on the potential energy from the force induced by the tire on road on asphalt pavement. Xiong carried out a field experiment utilizing piezoelectric prototypes with the aim of harvesting energy from road surfaces and reports an output power of 3.1mW [Xio14]. Roshani *et al*, employed piezoelectric disks of Lead zirconate titanate (PZT), spatially arranged them to optimize the output energy [Ros+16]. They also considered in their study the role of force and frequency on the output energy.

1.3.6 Thermodynamic cycles

Energy harvesting from low frequency or infrequent sources still suffer from the low energy involved. In this context, employing a thermodynamic cycle is a good solution due to the high energy conversion of such method. Employing thermodynamic cycle is a technique which have been largely employed in pyroelectric energy harvesting [OBB85; MKP12; Lhe+22]. However, the utilization of thermodynamic cycles in mechanical energy harvesting has been quite limited. Nevertheless, these types of cycles are a good alternative for energy harvesting from low-frequency sources (<10Hz) and especially for non-resonant mechanical energy harvesting applications.

Pyroelectric cycles

Pyroelectric energy harvesting typically employs closed thermodynamic cycles to maximize energy output. Various cycles have been utilized for pyroelectric energy harvesting [OBB85]. Notably, there is the Stirling cycle, which comprises two isothermal and two constant electric induction processes. Another promising cycle is the Olsen cycle which involves two isothermal and two constant electric field processes. The latter has been more investigated and has shown better prospective for energy harvesting [GPS08a; Lhe+22]. This cycle consists of starting with a lower temperature denoted as T_l and an initial electric field marked as E_i. An electric field is gradually applied until it reaches a final value, E_f (following the 1-2 path shown

Thèse accessible à l'adresse : https://theses.insa-lyon.fr/publication/2024ISAL0017/these.pdf © [G. Taxil], [2024], INSA Lyon, tous droits réservés

in Figure 1.27 (a)). Subsequently, the temperature is raised to a higher level, T_h (following the 2-3 path). Then, the electric field is reduced back to its initial level, E_i (3-4 path). Finally, the temperature is lowered back to its initial value, T_l (closing the cycle with the 4-1 path). Previous research studies have underscored the feasibility and potential future applications of pyroelectric energy harvesting through Olsen cycles [Han+19; Pan+18]. Olsen cycle involves thermodynamic cycles within the

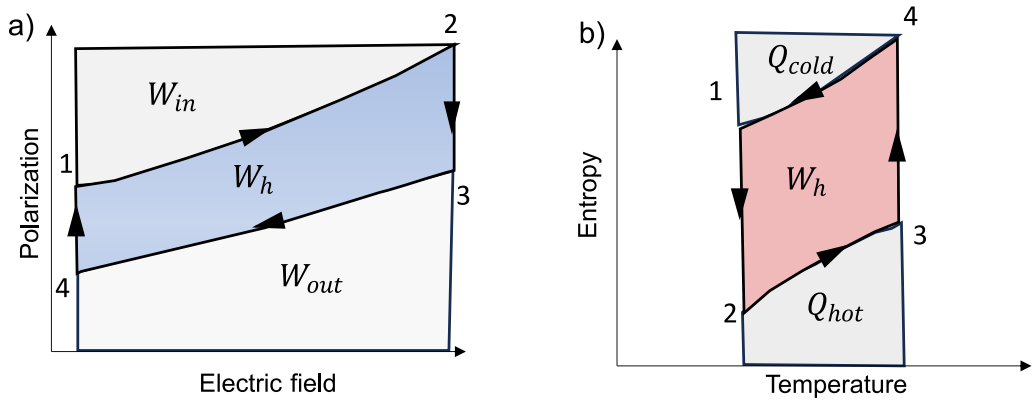

FIGURE 1.24: Illustration of an Olsen cycle (a) P-E cycle; (b) S-T cycle

polarization-electric field space and the entropy-temperature space as represented in Figure 1.27. In pyroelectric materials, the high relative dielectric permittivity $\kappa_r >> 1$ allows us to consider the polarization P as the conjugate variable of the electric field E. The harvested energy is given by the enclosed area of the cycle in Fig. 1.27. The harvested energy is generally expressed as:

$$W_h = \oint EdP \tag{1.18}$$

The Olsen cycle is a closed cycle and in such case, the following relationship holds:

$$W_h = \oint EdP = \oint PdE \tag{1.19}$$

For more convenience, the harvested energy will be only considered in the rest of this work as: $W_h = \oint PdE$. It can be observed that all the energy mentioned here primarily takes the form of electrical (W_e) and thermal energy (Q). The infinitesimal electrical work and heat transfer are given respectively by:

$$\delta W_e = EdP \tag{1.20}$$

$$\delta Q = TdS \tag{1.21}$$

From the first principle of thermodynamic, it is possible to derive the equation from the energy conservation equation:

$$\Delta U = 0 \tag{1.22}$$

which implies

$$Q_{hot} + Q_{cold} + W_{in} + W_{out} = 0 \tag{1.23}$$

where Q_{cold} is the heat given to the cold source (< 0), Q_{hot} is the heat quantity received from the hot source (> 0), W_{in} is the electrical work given to the system and W_{out} is the electrical work associated to the energy gained by the material. The harvested energy depending on the electrical work can be easily deduces from Figure

Thèse accessible à l'adresse : https://theses.insa-lyon.fr/publication/2024ISAL0017/these.pdf © [G. Taxil], [2024], INSA Lyon, tous droits réservés

1.27(a) and is given by:

$$W_h = W_{out} - W_{in} \tag{1.24}$$

Consequently, from the above relation and from Figure 1.27(b)

$$W_h = Q_{hot} + Q_{cold} \tag{1.25}$$

It can be seen that when the amount of heat removed from the hot source exceeds the heat released to the cold source, the difference in thermal energy corresponds to the energy that is transformed into electrical energy.

Figure 1.25 illustrates the different configurations of the polarization domains along the different steps of the cycle. The crystal starts from a random initial state which depends on its history. When applying the electric field (1-2 process), the polarization domains start to align within the electric field direction. This have for consequences that the polarization increase and at the contrary, the entropy decreases as the order in the material is higher. When increasing the temperature (2-3), the entropy will increase and conversely, the polarization will decrease due to the dipole disorder increment. Releasing the electric field (3-4) will have the effect to increase even more the entropy and decrease the polarization. The last cooling process will increase the polarization to close the cycle and the entropy will come back to its initial state. It is interesting to note that the two isothermal can be associated to the electrocaloric effect and the two isoelectric field processes to the pyrolectric effect.

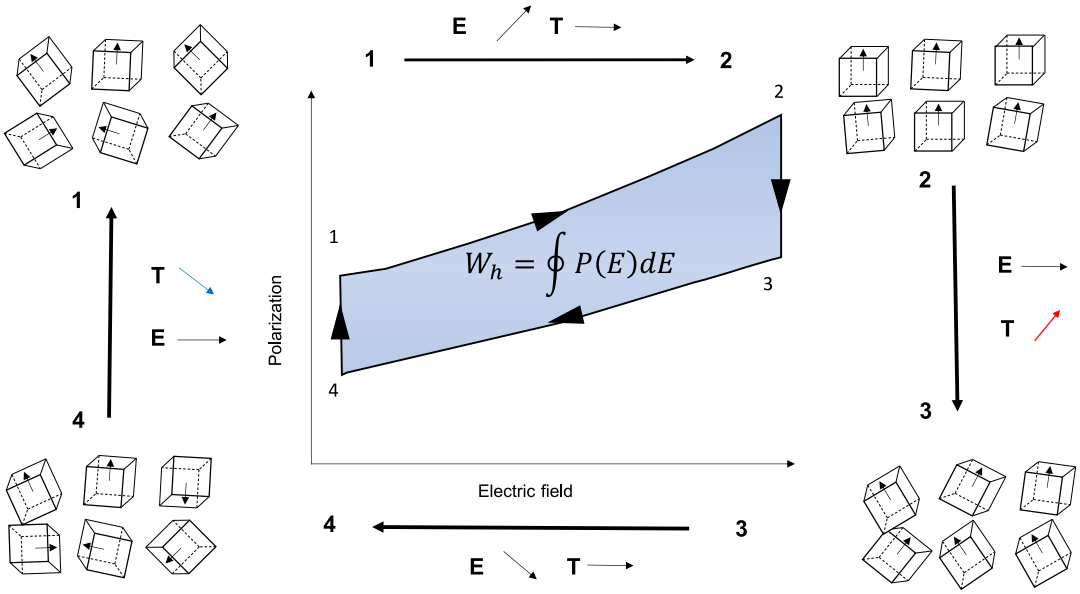

FIGURE 1.25: Evolution of the polarization during an Olsen cycle

Mechanical cycles

As detailed before, vibrational mechanical energy harvesting suffers of low output power. However, this inconveniences is solved by working at higher frequencies and in resonant conditions [BTW06; Mun+16]. On the other hand, non-resonant mechanical energy harvesting does not have such possibility. Hopefully, by working in lower frequency, it is then possible to employ thermodynamic cycles and exploit the non-linearities of the materials induced by the high applied stress and electric field compared to high frequency systems. When it comes to scavenge mechanical

Thèse accessible à l'adresse : https://theses.insa-lyon.fr/publication/2024ISAL0017/these.pdf © [G. Taxil], [2024], INSA Lyon, tous droits réservés

energy through a single force application, the goal is to maximize the conversion of the mechanical energy into electrical energy. To accomplish this objective effectively, utilizing a closed thermodynamic cycle is a good approach, given their high potential for energy conversion. The Ericsson cycle, which consists of two isoelectric and two isostress processes, is the equivalent of the Olsen cycle for mechanical energy harvesting and it has shown promising energy densities in PZT [PCV14a; PCV14b]. Instead of heating and cooling down, mechanical stress is applied to the material. One of the major difference with temperature is that the stress is a tensorial field. Depending on the stress direction and nature (uniaxial, biaxial, hydrostatic) the response of the ferrolectric material will be completely different. We will assume here that a compressive uniaxial stress (step, tire on road) is applied in the same direction than the electric field (33 mode). Like for pyroelectric energy harvesting and Olsen cycle, the harvested energy is given by the area of the polarization-electric field closed cycle Figure 1.26 (a). This time, the cycle is described in the polarization-electric field and in the strain-stress spaces. The associated energies with the cycle are in the form of electrical work (W_e) and mechanical work (W_m). δW_e and δW_m are respectively given by:

$$\delta W_e = EdP \tag{1.26}$$

$$\delta W_m = \sigma d\epsilon \tag{1.27}$$

It is again possible to derive from the energy conservation equation and from Figure

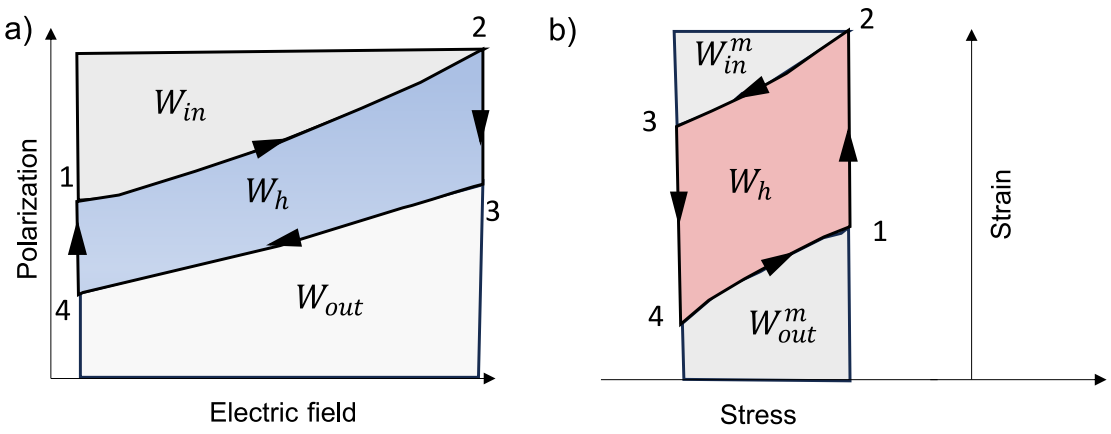

FIGURE 1.26: Illustration of an Ericsson cycle (a) P-E cycle; (b) $\epsilon - \sigma$ cycle

1.26(a) and (b) the harvested energy depending on the mechanical and the electrical works:

$$W_h = W_{out}^m - W_{in}^m \tag{1.28}$$

and

$$W_h = W_{out} - W_{in} \tag{1.29}$$

Here the two isolectric processes can be associated with the direct piezoelectric effect and the two isostress processes to the converse piezoelectric effect. One major advantage of using mechanical cycles instead of thermal one is the possibility to induce large stress variation much more rapidly than large temperature variation. Indeed, it is easier to implement for a real device large uniaxial stress variation than large temperature variation. Thus the potential depolarization is higher which means that the potential area of the cycle is larger and so the output energy. Like for Olsen cycle and pyroelectric energy harvesting and illustrated in Figure 1.25, the crystal starts

Thèse accessible à l'adresse : https://theses.insa-lyon.fr/publication/2024ISAL0017/these.pdf © [G. Taxil], [2024], INSA Lyon, tous droits réservés

from a random initial state depending on previous excitations. When the electric field is applied (1-2 process), the domains of polarization aligns within the electric field direction. This has the consequence of increasing the strain of the material and the polarization. Conversely, when the stress is applied (step 2-3), strain and polarization will decrease. Releasing the electric field (step 3-4) will further decrease the strain and the polarization. Finally, when the stress is released, it will increases polarization, completing the cycle, and returning the strain to its initial state.

In both non-resonant mechanical and pyroelectric energy harvesting using thermodynamic cycle, the goal is to have the largest cycle area to obtain the largest energy output possible. To achieve this, it is possible in both cases to apply a large electric field. Furthermore, it will be better in pyroelectric energy harvesting to have large temperature variation. Whereas, in mechanical energy harvesting, a large uniaxial stress will be better.

1.4 Context and objectives of the Ph.D

1.4.1 FIESTA Project

It is important to note that this present work was made in the frame of the collaborative FIESTA (Ferroelectric-ferroelectric transitions Induced by External STress for Applications in sensing and energy harvesting) project funded by the ANR (Agence Nationale de la Recherche), grant ANR-20-CE05-0026. This section will be dedicated to present the FIESTA project and its objectives as it was a guideline for this work.

The proliferation of wireless interconnected devices, particularly within the context of the Internet of Things (IoT), is demonstrating remarkable potential within the realm of communication in societies, including applications in smart cities and digital society. Projections suggest that over 75 billion connected devices will be in operation worldwide by 2025 [Dev], with an estimated economic value ranging from 4 trillion to 11 trillion of dollars [Iot]. These opportunities encompass global communication, sensing, and monitoring, which can enhance structural, product, and personal safety in areas such as buildings and transportation. Additionally, they can facilitate data collection across diverse environments, ultimately leading to improved quality of life and sustainable development. However, advancements in these domains, in addition to ethical considerations, are giving rise to numerous technical challenges, particularly at the device level.

In this context, FIESTA aims at enhancing small-scale energy harvesting and tunable acoustic filters by employing ferroelectric phase transitions. To reach this objective, FIESTA employs a transdisciplinary approach and conducts original scientific research related to societal challenges. The project encompasses all associated domains, from material science to practical applications, including mechanical and electrical aspects. FIESTA is primarily focused on turning what is conventionally considered a limitation (phase transitions in ferroelectrics) into an advantage, enabling the creation of bandgap filters and highly efficient microgenerators (a decade increase in performance [Ann+17]). The project objectives involve investigating these phase transitions and combining them with mechanical and electrical considerations to achieve globally optimized systems. The interfaces between each discipline are crucial in ensuring significant scientific advancements. In particular,

Thèse accessible à l'adresse : https://theses.insa-lyon.fr/publication/2024ISAL0017/these.pdf © [G. Taxil], [2024], INSA Lyon, tous droits réservés

the integration of intrinsic material nonlinearities with those induced by the electrical interface through the mechanical structure, leading to multiscale nonlinearities, is an innovative aspect of FIESTA. Another objective is to employ lead-free material which are actually mainly used in energy harvesting.

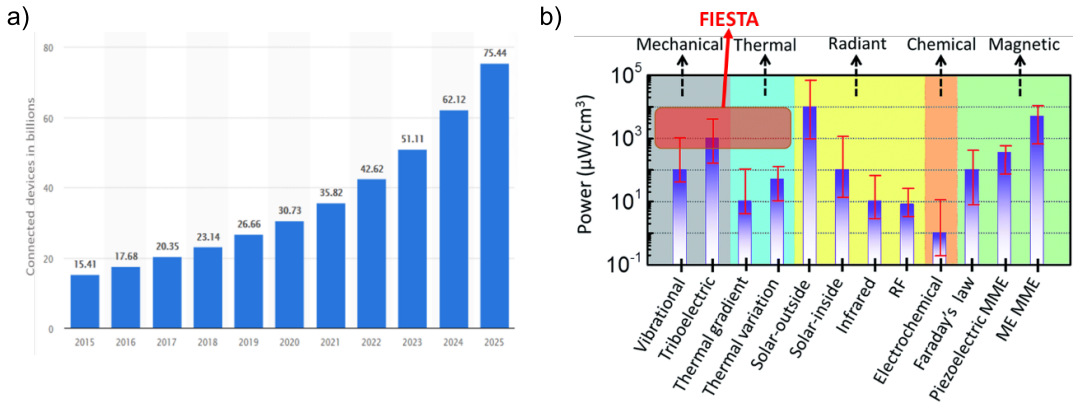

FIGURE 1.27: (a) Evolution of the number of connected devices with time [Dev]; (b) Energy harvesting comparison with FIESTA ambitions [Ann+17]

In the frame of this project, the work presented in this thesis was dedicated firstly to the modeling and characterization of ferroelectric materials. Another objective of this work was to proposed and developed an electromechanical structure implemented in a real device with the associate electrical interface. In parallel, the collaborators of this project worked on the elaboration of lead-free materials and the development of innovative electrical circuit dedicated to such applications.

1.4.2 Objectives of the thesis

As observed in the previous sections, energy harvesting has experienced substantial growth over the past two decades. The capability to power devices without relying on batteries, which encounter issues like self-discharge and challenging replacements in harsh conditions, has captured the attention of the scientific community. Furthermore, the impending ecological transition necessitates sustainable energy production, and energy harvesting can play a significant role in addressing this challenge. In the realm of mechanical energy harvesting, it has been shown that the majority of research focuses on resonant devices operating with vibrating mechanical sources and are limited to linear modes. However, there are numerous instances of sudden and random mechanical energy inputs in everyday life (such as switches, steps, tire-road interactions, door openings). In this chapter, we saw also that ferroelectric materials, a type of piezoelectric material, show great promise for such applications due to their remarkable properties. One distinctive feature of these materials is their ability to retain polarization even at zero electric field. Another intriguing aspect is their capacity to undergo phase transitions with changes in temperature, electric field, and stress.

In this context, the main goal of this thesis is to enhance energy harvesting by employing the non linearities of polarization induced by these phase transitions. To reach this objective, this work was divided in three part with their own objectives:

Thèse accessible à l'adresse : https://theses.insa-lyon.fr/publication/2024ISAL0017/these.pdf © [G. Taxil], [2024], INSA Lyon, tous droits réservés

- Identify the ideal thermodynamic conditions via modeling approach. To reach this objective, Landau-Devonshire theory is employed to model the phase transitions of ferroelectric materials depending on temperature, electric field, and stress. This allows predicting the optimal conditions for energy harvesting by employing thermodynamic cycle in both pyroelectric and mechanical energy harvesting.

- Experimentally identify the optimal thermodynamic conditions and associated phase transitions and confirmed by modeling results. For pyroelectric energy harvesting, a comparison of the results in the literature of the electrocaloric effect is made. For mechanical energy harvesting, a dedicated test-bench was developed for applying high uniaxial stress and high electric field to the materials and at the same time monitoring its temperature.

- Develop an electromechanical structure with the associated electrical interface able to reach the targeted stress and electric field. This objective is realised by development of a smart tile and a cantilever beam for switch applications. In both devices the stress applied was amplified to reach $\approx 100MPa$ and an electric field of $1.5kV/mm$ was applied. An electrical interface (Bennet doubler) is proposed for electrical interface and as a realistic solution for energy harvesting by employing Ericsson cycle.

1.4.3 Outline of the thesis

This thesis is dedicated to make profit of non-linearities of phase transitions to improve energy harvesting. In order to reach this objective, this thesis is divided in different parts, where each one deals with a different aspects of the problematic. First, Chapter 2 is dedicated to the modeling of ferroelectric single crystals for energy harvesting by employing Landau-Devonshire theory. Simulation of thermodynamic cycles is proposed for pyroelectric and mechanical energy harvesting. Different properties are investigated such as crystal orientation, optimal operating temperature and ideal FE-FE transitions. Then, Chapter 3 proposes an experimental characterization of ferroelectrics. The materials are tested under high stress, high electric field and different temperature. Different materials such as ceramics and single crystals with different orientations are experimentally tested. A comparison of their performances is made and their characterizations were performed to confirm modeling results of Chapter 2. After that, Chapter 4 proposed the development of devices operating with high electric field and high stress levels to reach the non-linearities identified in Chapter 2 and Chapter 3. The implementation is made for two devices, each one working with different piezoelectric mode (33 and 31 mode). An electrical interface is also proposed and demonstrates the possibility of a fully functional device. Finally, the Chapter 5 is dedicated to the perspectives and the conclusions of this work.

Thèse accessible à l'adresse : https://theses.insa-lyon.fr/publication/2024ISAL0017/these.pdf © [G. Taxil], [2024], INSA Lyon, tous droits réservés

Thèse accessible à l'adresse : https://theses.insa-lyon.fr/publication/2024ISAL0017/these.pdf © [G. Taxil], [2024], INSA Lyon, tous droits réservés

Chapter 2

Modeling for Pyroelectric and mechanical energy harvesting

In the precedent chapter, an overview of ferroelectric materials, their modeling and on the state of the art of pyroelectric and mechanical energy harvesting has been made. This work wants to utilize ferroelectric phase transitions for improving energy harvesting. This chapter is dedicated to link the modeling of ferroelectric materials with energy harvesting. To achieve this, an innovative way to employ Landau-Devonshire theory is proposed for modeling thermodynamic cycles.

In the first part of this chapter, the modeling is dedicated to simulate Olsen cycle for pyroelectric energy harvesting only. The modeling will investigate the optimal phase transitions of ferroelectric materials depending on crystal orientations. Electrocaloric effect in single crystals with different orientations is simulated and compared with results in the literature to confirm the modeling approach.

In the second part, the phenomenological approach will be used for mechanical energy harvesting. Ericsson cycles are simulated along with other ferroelectric properties with Landau-Devonshire theory for <001> oriented crystals. It is important to note that this part of the modeling of mechanical energy harvesting is strongly linked with Chapter. 3. Indeed some of the modeling results will be presented and conmparec with the experimental results in the next chapter.

Finally, the model will be extended to all the different crystal orientations. Different properties will be calculated such as piezoelectric coefficients and the harvested energy for different orientations. The difference between "low levels" and "high levels" energy harvesting will be discussed in the frame of the obtained results.

Thèse accessible à l'adresse : https://theses.insa-lyon.fr/publication/2024ISAL0017/these.pdf © [G. Taxil], [2024], INSA Lyon, tous droits réservés

2.1 Pyroelectric energy harvesting

The work presented in this section is inspired by the published article in Journal of Applied Physics [Tax+22]. The pursuit of sustainable energy sources has led significant interest in the field of pyroelectric energy harvesting. Pyroelectric materials possess a unique ability to generate electrical energy from temperature fluctuations, offering a promising avenue for renewable energy generation. Enhanced energy harvesting efficiency can be achieved through a precise understanding of the thermodynamic conditions within the target device. In this context, this section proposes to model ferrolectrics for pyroelectric energy scavenging and to identify their ideal phase transitions for energy harvesting applications.

2.1.1 Modeling of Olsen cycle

Previous experimental research efforts have looked for improving energy scavenging by employing phase transitions [GPS08b; GPS08c; Hof+15; Lhe+22]. However, few studies proposed to theoretically investigate the advantages of employing phase transitions for energy harvesting [SH20; Zhu+17]. Yet, none of these studies have investigated the potential of taking advantage of FE-FE phase transitions and the impact of crystal orientation. It can be observed that all these studies making profit of phase transitions of ferroelectric materials employed Olsen cycle. As detailed in Chapter. 1 Olsen cycle consists of applying and releasing electric field and temperature at different steps of the cycle. Past studies have highlighted the viability and potential future uses of pyroelectric energy harvesting through the utilization of Olsen cycles [Han+19; Pan+18]. Specifically, Hanrahan *et al* [Han+19], have successfully implemented Olsen cycles using a laser-based pyroelectric harvester, employing a square temperature variation and a triangular electric field evolution. For preliminary comparison and model evaluation in the simulations, this temporal evolution profile was employed. An illustration of a simulated Olsen cycle with the associated temporal evolution of the temperature and the electric field is given in Figure 2.1.

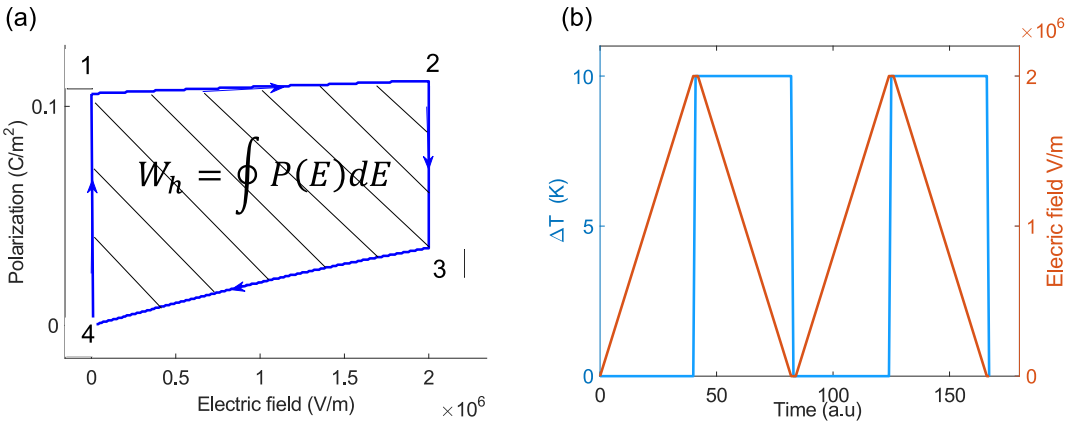

FIGURE 2.1: (a) Modeling of an Olsen cycle [Tax+22]; (b) Temporal evolution of the temperature and of the electric field [Tax+22]

It is worth highlighting that the selection of functions in an actual experiment has a direct influence on the resulting energy output due to time dependencies [Bha+14]. Nonetheless, the specific manner in which temperature and electric field evolve was not a critical factor in our modeling, as long as thermodynamic state changes occurred in a sequential fashion. Within our approach, when applying a positive electric field, we exclusively considered the positive polarization solution derived from

Thèse accessible à l'adresse : https://theses.insa-lyon.fr/publication/2024ISAL0017/these.pdf © [G. Taxil], [2024], INSA Lyon, tous droits réservés

the free energy. It is important to emphasize that the Landau-Devonshire theory operates independently of time, and all thermodynamic transitions are inherently reversible according to the model's assumptions. Furthermore, the model did not account for hysteresis effects or the frequency-dependent behavior of the material. The simulation was designed to represent a single Olsen cycle within a single ferroelectric domain, regardless of its size. Future research could assess how different waveforms and frequencies affect polarization and energy harvesting density. Additionally, an alternative approach suggested by Smith *et al* [SH20] involves introducing an electrical charge-discharge losses term into the output energy. Another possibility is to use a time-dependent Ginzburg-Landau (TDGL) model. Nevertheless, the approach is sufficient for the purpose of this work and remains largely unexplored for pyroelectric energy harvesting.

To ensure the practicality and relevance of the modeling approach, different materials were simulated with temperature variations and electric field easily achievable in real-world applications. The difference between the hot temperature (T_h) and the low temperature (T_l) was set to 10K ($T_h - T_l$) as it can be achieved within a reasonable time frame, as shown in previous studies [Sha+21]. The electric field variation spans from an initial value of $0kV/mm$ to a final value of $2kV/mm$. Within the context of a thermodynamic approach to energy harvesting, a thermodynamic path is modeled representing the ideal energy harvesting cycle, employing the Landau-Devonshire theory. For each combination of temperature and electric field values, the spontaneous polarization is determined, enabling the construction of the Olsen cycle in the P-E space as illustrated in Figure 2.1(a). The harvested energy corresponds to the hatched area within the P(E) cycle, and is expressed as detailed in Chapter 1 as:

$$W_h = \oint P(E)dE \tag{2.1}$$

The different theoretical aspects to model Olsen cycles for pyroelectric energy harvesting has been presented. The next step is to present the methodology to obtain the stable crystal state and the associated polarization solutions depending on the temperature, the applied electric field and the crystal orientation.

2.1.2 Model

The Landau-Devonshire theory has been extensively explored in the context of ferroelectrics [She+10; Ma+17; LCC05a], but has received relatively limited investigation for energy harvesting applications. In the previous chapter, the Landau theory theoretical background and concept has been introduced. This chapter will be dedicated to its direct application to examine thermodynamic cycles and ferroelectric phase diagrams using ferroelectric materials with different crystal orientations.

Chapter. 1 established that within the framework of the Landau-Devonshire theory, the free energy is formulated as a function of an order parameter and must exhibit symmetry with respect to a parent phase. Additionally, all other terms introduced into the free energy, typically referred to as second-order parameters, must also possess symmetry consistent with the parent phase, which, in this case, is the $m\bar{3}m$ (cubic) symmetry [Cao08a; Li+12]. The different contributions to the total free energy F are given by:

$$F = F_{lgd} + F_{elas} + F_{elec} + F_{grad} \tag{2.2}$$

Thèse accessible à l'adresse : https://theses.insa-lyon.fr/publication/2024ISAL0017/these.pdf © [G. Taxil], [2024], INSA Lyon, tous droits réservés

where, as detailed in Chapter. 1, F_{elas} and F_{grad} represent, respectively, the components contributing to the free energy arising from external stress and the diverse possible domain orientations within ferroelectric materials. On the other hand F_{lgd} and F_{elec} are respectively associated with the classical Landau-Devonsire free energy and the free energy resulting from an applied electric field. In the scope of this section, F_{elas} and F_{grad} will be neglected, as the crystal for pyroelectric energy harvesting is in stress free conditions, and when subjected to a sufficiently strong electric field, a single crystal can be regarded as existing in a single-domain state [CL07]. Consequently, our consideration is focused solely on F_{lgd} and F_{elec}. By performing a Legendre transformation, the total free enthalpy is expressed with respect to the cubic symmetry as:

$$\begin{aligned}\Delta G \;=\;& \alpha_1({P_1}^2+{P_2}^2+{P_3}^2)+\alpha_{11}({P_1}^4+{P_2}^4+{P_3}^4)\\ &+\alpha_{12}({P_1}^2{P_2}^2+{P_1}{P_3}^2+{P_2}^2{P_3}^2)+\alpha_{123}{P_1}^2{P_2}^2{P_3}^2\\ &+\alpha_{111}({P_1}^6+{P_2}^6+{P_3}^6)+\alpha_{112}({P_1}^2({P_2}^4+{P_3}^4)\\ &+{P_2}^2({P_1}^4+{P_3}^4)+{P_3}^2({P_1}^4+{P_2}^4))\\ &+\alpha_{1111}({P_1}^8+{P_2}^8+{P_3}^8)\\ &+\alpha_{1122}({P_1}^4{P_2}^4+{P_1}^4{P_3}^4+{P_2}^4{P_3}^4)\\ &+\alpha_{1123}({P_1}^4{P_2}^2{P_3}^2+{P_1}^2{P_2}^4{P_3}^2+{P_1}^2{P_2}^2{P_3}^4)\\ &+\alpha_{1112}({P_1}^6({P_2}^2+{P_3}^2)+{P_2}^6({P_1}^2+{P_3}^2)\\ &+{P_3}^6({P_1}^2+{P_2}^2))-E_1P_1-E_2P_2-E_3P_3\end{aligned} \tag{2.3}$$

It is sound to remind that E_i and P_i are the components of the spontaneous polarization in the cubic basis; α_{ij}, α_{ijkl}, α_{ijklmn} and $\alpha_{ijklmnop}$ are tensors which represent the different orders of the dielectric stiffness. In Landau-Devonshire theory, generally, only α_1 is temperature dependant even if some works proposed also a dependence of the higher order coefficients [Kim+18; LCC05b]. Here, only α_1 will be considered temperature dependent and has a different expression depending on the studied material [Wan+10a; Qiu+15]. The different expressions for barium titanate and PMN-30PT respectively are given by:

$$\alpha_1 = A_1 * [\coth(\tfrac{T_s}{T}) - \coth(\tfrac{T_s}{T_c})] \tag{2.4}$$

and

$$\alpha_1 = A_2 * (T - T_c) \tag{2.5}$$

where A_1 and A_2 are a constant dependant on the materials, while T_c represents the Curie temperature and T_s denotes the saturation temperature. The variation of α_{ij} with respect to T_s allows for the description of quantum effects that become important when T falls below T_s [Sal+07]. Determining this parameter for ferroelectric perovskites can poses a significant challenge so α_1 is much more frequently expressed as $\alpha_1 = C * (T - T_c)$.

By minimizing the free energy with respect to polarization, the stable ferroelectric state with its associated polarization can be established depending on applied temperature and electric field. In this study, three distinct ferroelectric phases were considered (rhombohedral, orthorhombic and tetragonal) for each material. An illustration of these ferroelectric states and their associated polarization configurations are presented in Table 2.1 and were visually depicted in Figure 1.7.

The approach involved the modeling of thermodynamic cycles, with a focus on selecting different low-temperature values to initiate these cycles. By varying the

Thèse accessible à l'adresse : https://theses.insa-lyon.fr/publication/2024ISAL0017/these.pdf © [G. Taxil], [2024], INSA Lyon, tous droits réservés

State	Polarization components	Number of configurations	Symmetry
Cubic	$(0,0,0)$	1	$m\bar{3}m$
Tetragonal	$(0,0,P)$	6	4mm
Orthorhombic	$(\frac{P}{\sqrt{2}},\frac{P}{\sqrt{2}},0)$	12	mm2
Rhombohedral	$(\frac{P}{\sqrt{3}},\frac{P}{\sqrt{3}},\frac{P}{\sqrt{3}})$	8	3m1

TABLE 2.1: Properties of the different ferroelectric phases

Parameter	$BaTiO_3$ [Wan+10a; He04]	PZN-4.5PT [Ham13; AFI88a]	PMN-30PT [Qiu+15; SPG07]	Units
T_s	160	0	0	K
T_c	390	423.75	390.1	K
α_1	$5*10^5*T_s$ $\times[\coth(\frac{T_s}{T})-\coth(\frac{T_s}{T_c})]$	$1.9*10^5$ $\times(T-T_c)$	$6.22*10^4$ $\times(T-T_c)$	$V.m.C^{-1}$
α_{11}	$-1.154*10^8$	$-1.35*10^7$	$-1*10^8$	$V.m^5.C^{-3}$
α_{12}	$6.530*10^8$	$8.05*10^7$	$2*10^8$	$V.m^5.C^{-3}$
α_{111}	$-2.106*10^9$	$2.75*10^8$	$2.5*10^9$	$V.m^9.C^{-5}$
α_{112}	$4.091*10^9$	$4.125*10^8$	$-3.5*10^9$	$V.m^9.C^{-5}$
α_{123}	$-6.688*10^9$	$-2.14*10^9$	$-9*10^9$	$V.m^9.C^{-5}$
α_{1111}	$7.590*10^{10}$	0	$1*10^{10}$	$V.m^{13}.C^{-7}$
α_{1122}	$-2.221*10^{10}$	0	$8.6*10^{10}$	$V.m^{13}.C^{-7}$
α_{1112}	$-2.193*10^{10}$	0	$1*10^{10}$	$V.m^{13}.C^{-7}$
α_{1123}	$2.416*10^{10}$	0	$6.8*10^{10}$	$V.m^{13}.C^{-7}$
ρ	6.02	8.31	8	$g.cm^{-3}$
C_p	406	200	350	$J.kg^{-1}.K^{-1}$

TABLE 2.2: List of Landau coefficients and physical properties [Tax+22]

initial temperature T_l, the goal is to identify the optimal range of temperature to enhance energy harvesting by using phase transitions. The selected ferrolectric materials are $BaTiO_3$, PZN-4.5PT, and PMN-30PT, as they are among the most extensively researched ferroelectric materials, with numerous sets of Landau coefficients available in the existing literature. In Table 2.2, a list of the parameters taken from the literature is given for all the studied ferroelectric materials.

Depending on the crystal orientation, different ferroelectric phase transitions can be of interest. In this part, only the <001>, <011>, and <111> crystallographic orientations will be considered. In every cases, the electric field is applied along the crystal cut direction, as illustrated in Figure 2.2.

Thèse accessible à l'adresse : https://theses.insa-lyon.fr/publication/2024ISAL0017/these.pdf © [G. Taxil], [2024], INSA Lyon, tous droits réservés

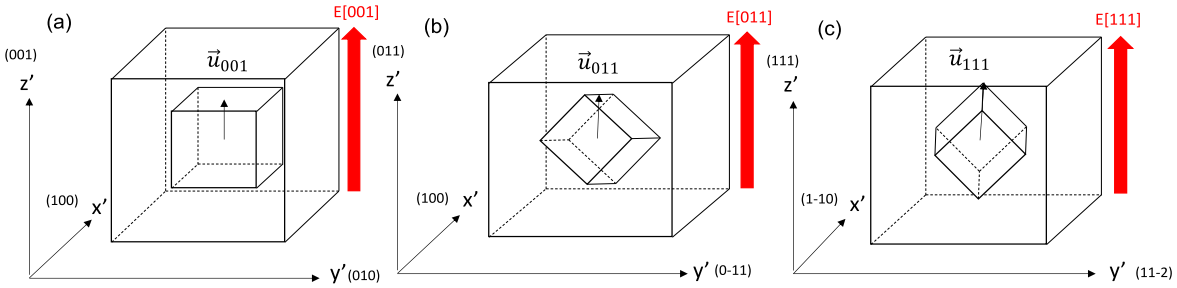

FIGURE 2.2: Illustration of the crystal in the different orientations with the associates projection vector and basis [Tax+22]. (a) <001> Orientation; (b) <011> orientation; (c) <111> orientation

.

It is worth noting that a symmetry transformation of the free energy is not required for <011> and <111> crystal orientations. In practical terms, polarization is measured by observing the change in current flowing through electrodes positioned on the faces aligned with the electric field direction. Consequently, the measured polarization represents a projection of the polarization vector along the electric field direction. Therefore, only the polarization vector has to be transformed via a matrix rotation [Zha+22; Guo+21]. The polarization P′ is defined in the laboratory reference frame (x', y', z'), whereas the polarization P is defined in the cubic coordinate system (x, y, z). This transformation results in the following relationship:

$$P_i' = A_{ij} P_j \tag{2.6}$$

$$A_{ij}^{<001>} = \begin{pmatrix} 1 & 0 & 0 \\ 0 & 1 & 0 \\ 0 & 0 & 1 \end{pmatrix}$$

$$A_{ij}^{<011>} = \begin{pmatrix} 1 & 0 & 0 \\ 0 & \frac{1}{\sqrt{2}} & \frac{-1}{\sqrt{2}} \\ 0 & \frac{1}{\sqrt{2}} & \frac{1}{\sqrt{2}} \end{pmatrix} \tag{2.7}$$

$$A_{ij}^{<111>} = \begin{pmatrix} \frac{1}{\sqrt{2}} & \frac{-1}{\sqrt{2}} & 0 \\ \frac{1}{\sqrt{6}} & \frac{1}{\sqrt{6}} & \frac{-2}{\sqrt{6}} \\ \frac{1}{\sqrt{3}} & \frac{1}{\sqrt{3}} & \frac{1}{\sqrt{3}} \end{pmatrix}$$

The electric field is assumed to be aligned with the z′ axis. Consequently, it is possible to establish the unit vectors $\vec{z'_{001}}$, $\vec{z'_{011}}$, and $\vec{z'_{111}}$, which allows keeping on using the free energy in cubic symmetry. The expression for polarization along the crystal z′ axis for various orientations can be defined as follows:

$$P_3'^{<001>} = \vec{P}.\vec{z'_{001}} \tag{2.8}$$

$$P_3'^{<011>} = \vec{P}.\vec{z'_{011}} \tag{2.9}$$

$$P_3'^{<111>} = \vec{P}.\vec{z'_{111}} \tag{2.10}$$

with respectively $\vec{z'_{001}} = (0, 0, 1)$, $\vec{z'_{011}} = (0, \frac{1}{\sqrt{2}}, \frac{1}{\sqrt{2}})$ and $\vec{z'_{111}} = (\frac{1}{\sqrt{3}}, \frac{1}{\sqrt{3}}, \frac{1}{\sqrt{3}})$

Thèse accessible à l'adresse : https://theses.insa-lyon.fr/publication/2024ISAL0017/these.pdf © [G. Taxil], [2024], INSA Lyon, tous droits réservés

2.1.3 Electrocaloric effect

In the previous part, the theoretical approach to simulate pyroelectric energy harvesting has been detailed. However, modeling Olsen cycle for different materials and crystal orientations still need to be confirmed. Validation of the approach via the electrocaloric effect is proposed here. Indeed, a lot of recent studies focused on first principle calculations and experimentally measured the electrocaloric effect (ECE) in different crystal orientations in $BaTiO_3$ and PMN-30PT [Chu+13; Mar+17; JH+15; Li+20a].

As it was briefly mentioned in the previous chapter, the electrocaloric effect can be regarded as the converse effect of pyrolectricity. More specifically, it corresponds to the temperature change and heat flow associated to the application of an electric field to the material as the entropy of the system is lowered. The electrocaloric effect (ECE) has received more attention in the last decade. The needing of micro-cooling devices at a small scale in important field such as electronic has attracted a lot of people to study ferroelectrics. One of the major attention paid on ECE studies is to achieve the largest ECE effect [Mis+06; Ye+14]. It was shown that the ECE activity was linked with phase transitions of ferroelectric materials [Zha+20]. Previous results obtained in the literature have shown that the ECE activity was more important close to the Curie temperature at the ferroelectric-paraelectric (FE-PA) transition [RC12]. This results are well understood due to the large variation of entropy and of the polarization at the Curie temperature. In the way to predict ECE of ferroelectric materials, different theoretical approach have been employed. The first principle calculations and Landau-Devonshire theory (the one considered here) are the mainly ones.

Is is possible to directly calculate the temperature variation associated to the ECE from the Landau free enthalpy [Wan+22b; Pir+11]. Indeed, the entropy S is given by the derivative of the Gibbs free energy ΔG with respect to the temperature T.

$$S = \frac{1}{\rho}\left(\frac{\partial \Delta G}{\partial T}\right)_E \tag{2.11}$$

where ρ is the density of the material. Since only α_1 is temperature dependant in the Gibbs free energy, inserting equation 2.3 in 2.11 it yields:

$$S = \frac{1}{\rho}\left(\frac{\partial \alpha_1}{\partial T}\right)_E P^2 \tag{2.12}$$

It is then possible to express the variation of entropy as follows:

$$\Delta S = \frac{1}{\rho}\left(\frac{\partial \alpha_1}{\partial T}\right)_E (P^2(E) - P^2(0)) \tag{2.13}$$

The associated temperature variation related to the ECE is then obtained as follows:

$$\Delta T_{ECE} = \frac{T}{\rho C_p}\left(\frac{\partial \alpha_1}{\partial T}\right)_E (P^2(E) - P^2(0)) \tag{2.14}$$

where C_p is the specific heat capacity.

However, in this section, the goal is to validate the approach of modeling Olsen cycle via Landau-Devonshire theory for different crystallographic orientations. Fortunately, it is possible to derive the electrocaloric effect based on the energy harvested [SPG07]. This chosen approach serves as a mean of validation of the energy

Thèse accessible à l'adresse : https://theses.insa-lyon.fr/publication/2024ISAL0017/these.pdf © [G. Taxil], [2024], INSA Lyon, tous droits réservés

obtained through the simulated Olsen cycle and is detailed below. Assuming the Maxwell relation:

$$(\frac{\partial P}{\partial T})_E = (\frac{\partial S}{\partial E})_T \tag{2.15}$$

allows expressing the heat flow of the electrocaloric effect, denoted as Q_{ECE}, as follows:

$$Q_{ECE} = T_h \int_{E_i}^{E_f} p dE \tag{2.16}$$

where, p is the pyroelectric coefficient and T_h the hot temperature. The converted energy could be expressed in terms of the pyroelectric coefficient as:

$$W_h = -(T_h - T_l) \int_{E_i}^{E_f} p dE \tag{2.17}$$

where T_l is the cold temperature. By substituting equation (2.17) into equation (2.16), the harvested energy can be expressed as:

$$W_h = -\eta_{carnot} Q_{ECE} \tag{2.18}$$

where, $\eta_{carnot} = \frac{T_h - T_l}{T_h}$ represents Carnot's efficiency. Finally, the temperature difference resulting from the electrocaloric effect is given by:

$$\Delta T_{ECE} = \frac{W_h}{\eta_{carnot} \rho C_p} \tag{2.19}$$

It can be noted that this equivalence between the harvested energy and the electrocaloric effect is dependent of the temperature variation $T_h - T_l$. A 10K difference was set as precised before. It is a range of temperature within it becomes possible to linearize the pyroelectric coefficient and express the converted energy W_h as a function of the heat flow Q_{ECE} [SPG07]. While this approximation offers a reasonable trend for the electrocaloric effect, it does not provide an accurate absolute value for the temperature variation of the electrocaloric effect due to its reliance on the chosen temperature variation $T_h - T_l$. Nevertheless, this approach allows to validate the Landau Devonshire methodology for modeling energy harvesting across different crystallographic orientations. In the context of this work, the most important aspect lies on the good predictions of the trend and the relative temperature variation obtained through the phenomenological approach, which correspond well with experimental results.

The simulation results for $BaTiO_3$ were compared with different studies. Particularly, Marathe *et al.* [Mar+17] utilized first-principle calculations to model the electrocaloric effect and conducted experimental measurements on barium titanate on different crystallographic orientations. The results, presented in Figure 2.3 agreed with both the experimental data and the results from first-principle calculations. Notably, a negative temperature variation in the <001> crystallographic direction of barium titanate was observed, occurring at the O-T transition at 270K, as depicted in Figure. 2.3(a). This "abnormal" electrocaloric effect is characteristic of specifics FE-FE transitions in particular crystal orientations and it seems that there are no studies that report this feature with Landau-Devonshire theory. This phenomena can only occurs when the polarization increases with the temperature ($\frac{\partial P}{\partial T} > 0$). Indeed, the projection of the polarization in the tetragonal phase is higher in <001> oriented crystal compared to the orthorhombic one. Then it gives the adequate conditions for

Thèse accessible à l'adresse : https://theses.insa-lyon.fr/publication/2024ISAL0017/these.pdf © [G. Taxil], [2024], INSA Lyon, tous droits réservés

the appearance of a negative ECE. Additionally, the <001> cut orientation induced a more pronounced temperature variation in barium titanate at the FE-PA transition compared to other orientations. This behavior agreed with both experimental observations and first-principle modeling. Furthermore, the results provide a pretty good estimation of the temperature variation of the electrocaloric effect [Mar+17; Li+20b].

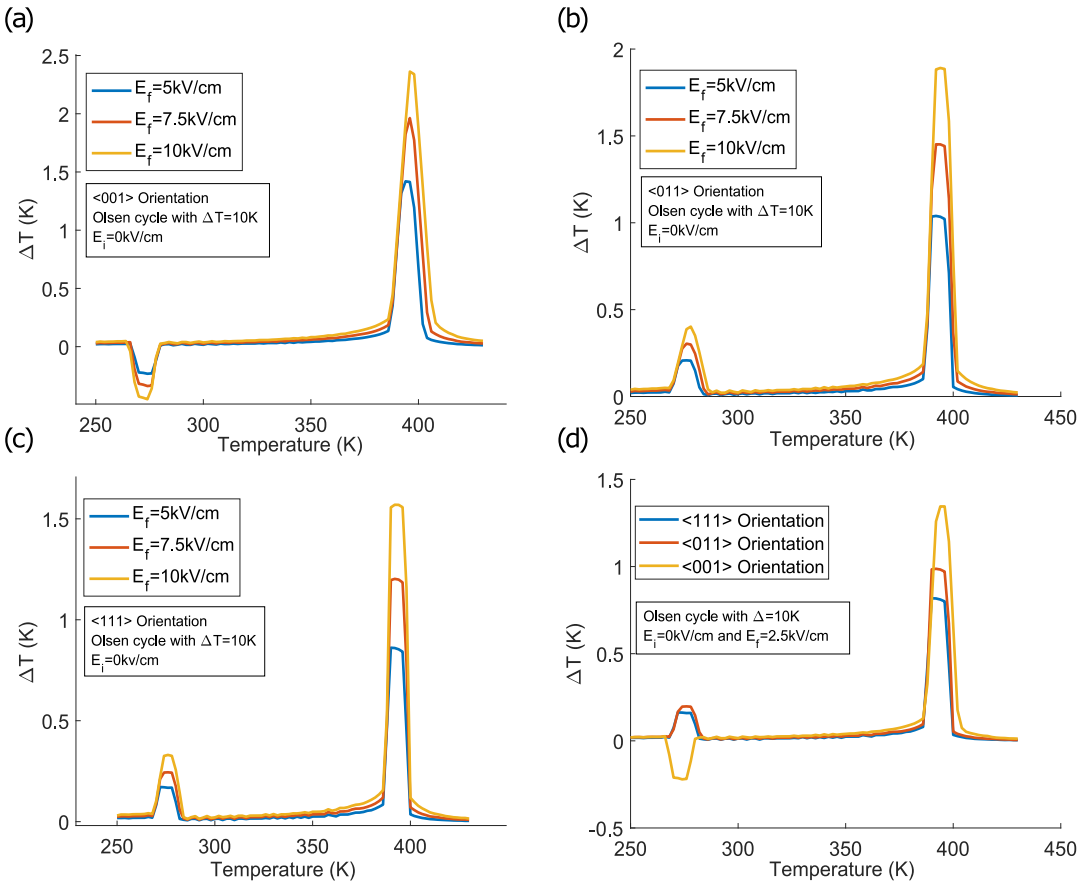

FIGURE 2.3: Electrocaloric effect for $BaTiO_3$ in function of the temperature for different applied electric fields [Tax+22]. (a) <001> orientation; (b) <011> orientation; (c) <111> orientation; (d) comparison between the three orientations.

The modeling results derived for PMN-30PT are consistent with experimental ones obtained from different crystal orientations [Li+20a; LG+12; Per+10]. Specifically, in the case of <001> cut crystals, a negative temperature variation is still evident, but this time it corresponds to the R-T transition, which occurs around 360K for PMN-30PT, as illustrated in Figure 2.4(a). This negative electrocaloric effect, similar to the O-T transition observed in barium titanate, can be attributed to the rise in polarization with temperature during specific FE-FE transitions in specific crystal orientations. In contrast to $BaTiO_3$ it is the <111> orientation for PMN-30PT that displays more favorable temperature variations at the FE-PA transition. This observation has been previously documented in scientific literature [Li+20a; BWQ15], providing experimental confirmation for the phenomenological approach, particularly within the context of a limited temperature variation range. Significantly, this approach offers predictions about whether specific FE-FE transitions will manifest negative or positive peaks in particular crystal orientations during phase transitions in ferroelectric materials. Consequently, these findings offer an explanation for the

Thèse accessible à l'adresse : https://theses.insa-lyon.fr/publication/2024ISAL0017/these.pdf © [G. Taxil], [2024], INSA Lyon, tous droits réservés

negative electrocaloric effect attributed to crystal orientation within the framework of the Landau-Devonshire theory.

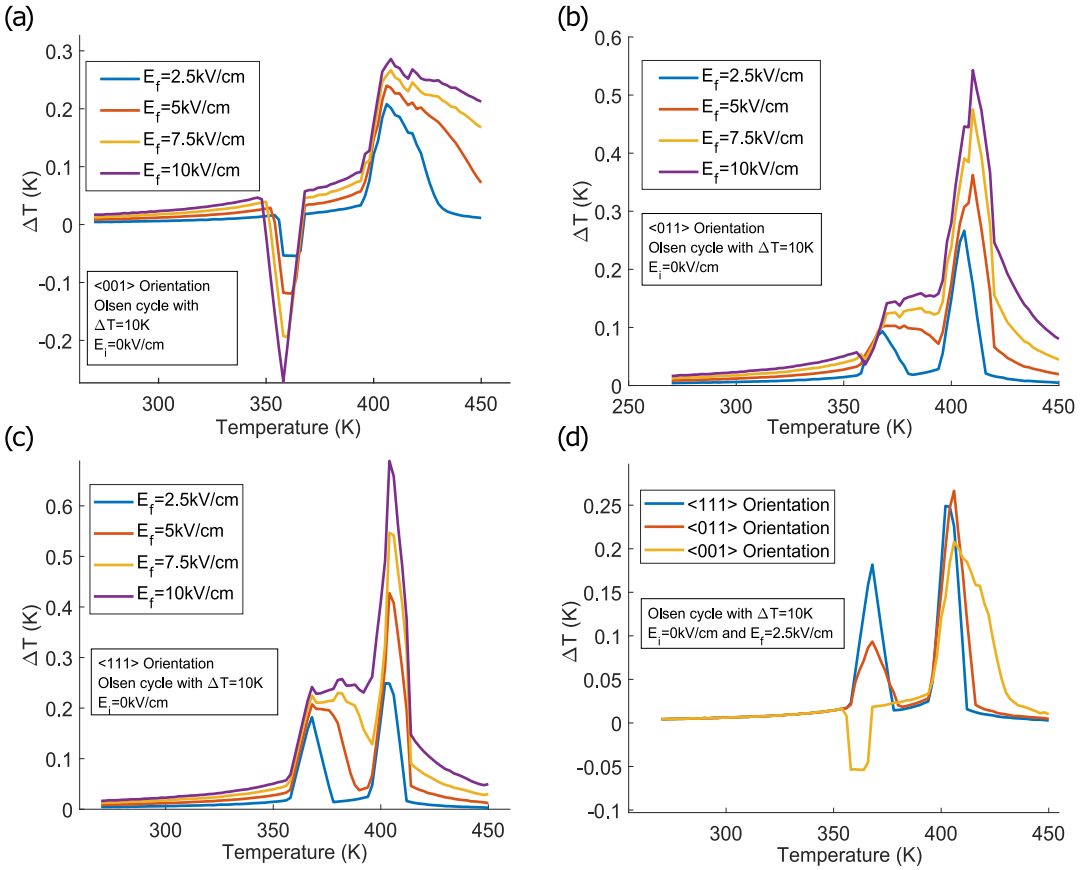

FIGURE 2.4: Electrocaloric effect for PMN-30PT in function of the temperature for different applied electric fields [Tax+22] (a) <001> orientation; (b) <011> orientation; (c) <111> orientation; (d) comparison between the three orientations.

Both materials exhibit electrocaloric temperature variations that evolve in a monotonic fashion as the electric field increases, with peaks shifting in response to the applied electric field. The direction of this temperature shift, whether positive or negative, depends on both the crystal orientation and the direction of the applied electric field. In Figure 2.3(a) and Figure 2.4(a), it can be observed that the negative electrocaloric peaks associated with FE-FE transitions shift in a negative direction with temperature for the <001> orientation of $BaTiO_3$ and PMN-30PT. These transitions correspond to the O-T and the R-T transitions. On the contrary, positive electrocaloric peaks are associated with a positive temperature shift as the electric field increases for all FE-FE transitions of <011> and <111> crystal orientations, as demonstrated in Figure 2.3(d) and Figure 2.4(d). Additionally, all orientations exhibit a positive shift for electrocaloric peaks associated with the FE-PA transition. This behavior arises from the fact that the electric field energetically favors the ferroelectric phase over the paraelectric phase as it contributes to asymmetry. Another noteworthy feature of both materials is that the maximum peak width is broader when the electric field is larger. This phenomenon is particularly evident in Figure 2.4(a) for the R-T transition at 370K. It is essential to note that this result comes from the equivalence drawn between the harvested energy and the electrocaloric effect

Thèse accessible à l'adresse : https://theses.insa-lyon.fr/publication/2024ISAL0017/these.pdf © [G. Taxil], [2024], INSA Lyon, tous droits réservés

and does not hold real significance for the electrocaloric effect itself. This underscores the limitation of the approximation presented in Equation 3.18, as an arbitrary temperature variation of 10K is used to model the Olsen cycle.

2.1.4 Energy harvesting

In the preceding part, the validity of the approach for modeling Olsen cycle has been confirmed through a comparison between the ECE (Electrocaloric Effect) results from existing literature and the simulation results. This section is now dedicated to employ the Landau-Devonshire theory for modeling Olsen cycle for energy harvesting. The targeted materials will still be PMN-30PT and $BaTiO_3$ with $< 001 >$,$< 011 >$ and $< 111 >$ orientations. The approach involves modeling harvested energy as a function of the low temperature, denoted as T_l. The temperature difference $\Delta T = T_h - T_l = 10K$ will be set as a constant, along with fixed electric field values of $E_i = 0kV/cm$ and $E_f = 2kV/mm$ (as illustrated in Figure 2.5(a),(d), and (g) and Figure 2.6(a),(d), and (g)). These settings allow us to determine the most effective temperature range for optimizing the output energy of pyroelectric materials through phase transitions. Different numerical values are assigned to represent various energy levels, and these numerical values correspond to specific thermodynamic cycles that are visually represented in $T - E$ phase diagrams (as shown in Figure 2.5(b),(e), and (h) and Figure 2.6(b),(e), and (h)). Furthermore, these associated cycles are graphically presented in the $P - E$ space (as depicted in Figure 2.5(c),(f), and (i) and Figure 2.6(c),(f), and (i)).

In the <001> orientation of PMN-30PT, as depicted in Figure 2.5(a),(b), and (c), a negative energy peak occurrs at $T_l = 346K$ for cycle n°1. This negative peak is related to the R-T transition, which takes place during the temperature variation at a constant electric field of $E_f = 2kV/mm$. When the electric field is reduced, the material returns to its initial rhombohedral state. These distinct phase transitions collectively result in an anticlockwise cycle in the high electric field region, leading to energy loss or minimal scavenged energy for practical applications.

For the <011> crystallographic orientation of PMN-30PT, as shown in Figure 2.5(d), (e), and (f), Cycle No. 1 also exhibits a negative peak occurring at a temperature of $T_l = 360K$. This observed negative peak is a consequence of the R-O transition. It is important to note that this transition takes place during the heating phase within the isoelectric process, resulting in an increase in polarization due to the favorable orientation of the orthorhombic state. Like for PMN-30PT with the <001> orientation, an anticlockwise cycle persists for high electric field. However, the energy loss experienced in this region is effectively balanced by a gained energy in the low electric field range, driven by successive O-R and R-T transitions.

The <111> cut direction, as illustrated in Figure 2.5(g), (h), and (i), present a positive energy peak occurring at a slightly lower temperature of $T_l = 366K$ in comparison to the R-T temperature transition at $E_i = 0kV/mm$. Cycle No. 1 in this orientation exhibits a fully clockwise direction, differing from the other orientations. The harvested energy in this case results from the occurrence of the R-T transition at the high temperature T_h when the electric field is released. This transition induces a rapid decrease in polarization, which in turn increases the area enclosed by the cycle, leading to an efficient energy harvesting. As the material cools down, the <111> PMN-30PT returns to its rhombohedral structure.

Thèse accessible à l'adresse : https://theses.insa-lyon.fr/publication/2024ISAL0017/these.pdf © [G. Taxil], [2024], INSA Lyon, tous droits réservés

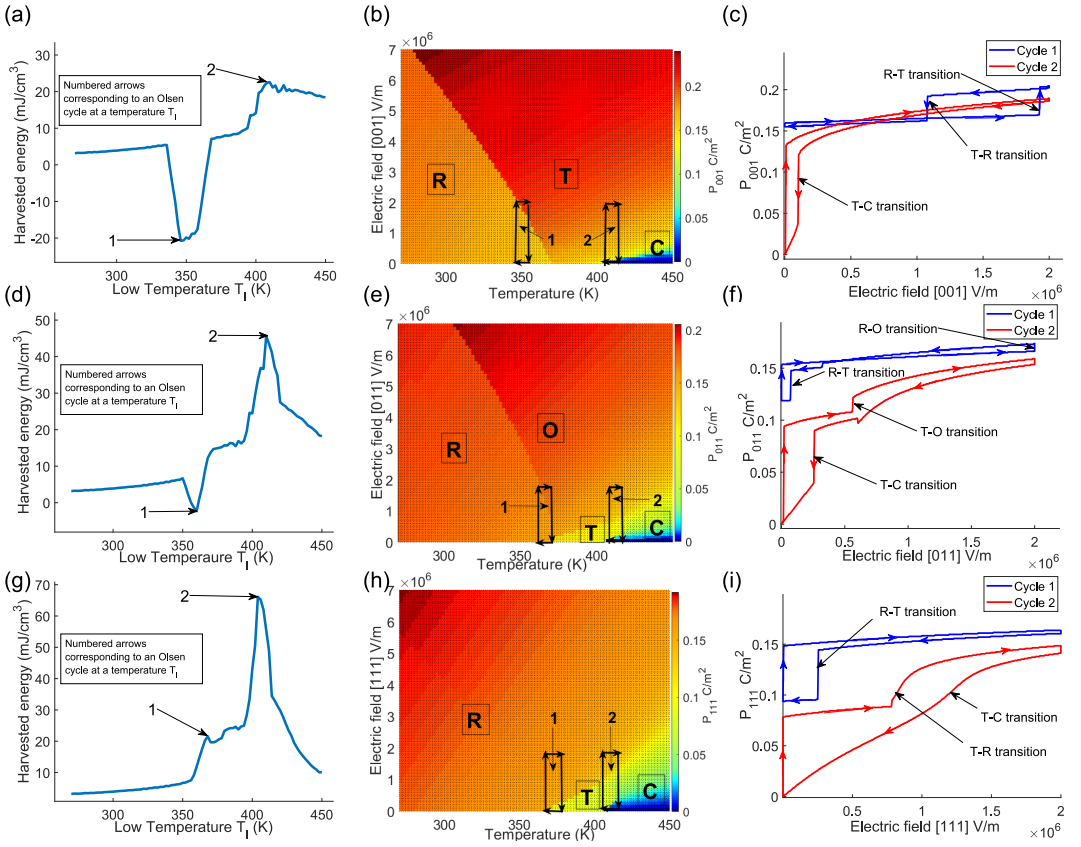

FIGURE 2.5: Harvested energy as a function of the working temperature T_l for PMN-30PT [Tax+22]. (a) <001> orientation; (d) <011> orientation; (g) <111> orientation. Temperature-Electric field phase diagram versus polarization for PMN-30PT. (b) <001> orientation; (e) <011> orientation; (h) <111> orientation. A plot of the associated P(E) cycles for PMN-30PT. (c) <001> orientation; (f) <011> orientation; (i) <111> orientation.

Considering the various orientations of PMN-30PT, Cycle No. 2 stands out as the most promising concerning energy gain, primarily because it takes advantage of the T-C transition, which leads to a more substantial variation in polarization at the Curie temperature. Across all orientations, initiating the cycle with T_l in close proximity to the Curie temperature T_c consistently results in an expanded thermodynamic cycle area. Notably, the <111> orientation outperforms others in terms of harvested energy. This superiority can be attributed to the T-C transition, which occurs at a higher electric field value for the <111> orientation. Interestingly, despite the <001> orientation having the highest polarization value for the tetragonal phase, it surprisingly yields the lowest energy output. This discrepancy arises from a significant shift in the Curie temperature T_c under the influence of the electric field, maintaining a ferroelectric state at high temperatures and low electric field conditions.

$BaTiO_3$ displays distinctive characteristics in different orientations. In the <001> orientation, as shown in Figure 2.6(a), (b), and (c), both the R-O and O-T transitions manifest negative energy peaks at temperatures of $T_l = 195K$ and $T_l = 269K$, respectively. Peak No. 2, associated with Cycle No. 2, is bigger than Peak No. 1. This behavior can be attributed to the substantial increase in polarization during the O-T

Thèse accessible à l'adresse : https://theses.insa-lyon.fr/publication/2024ISAL0017/these.pdf © [G. Taxil], [2024], INSA Lyon, tous droits réservés

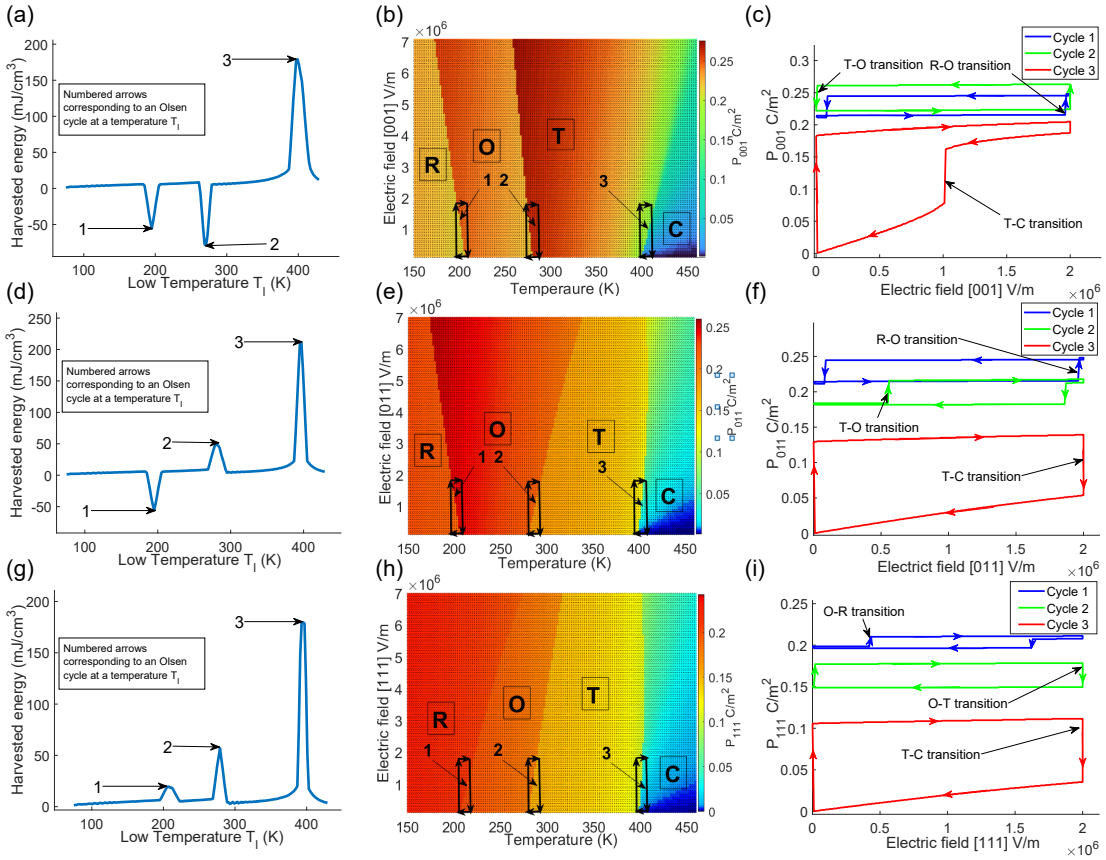

FIGURE 2.6: Harvested energy as a function of the working temperature T_l for $BaTiO_3$ [Tax+22]. (a) <001> orientation; (d) <011> orientation; (g) <111> orientation. Temperature-Electric field phase diagram versus polarization for $BaTiO_3$. (b) <001> orientation; (e) <011> orientation; (h) <111> orientation. A plot of the associated P(E) cycles for $BaTiO_3$. (c) <001> orientation; (f) <011> orientation; (i) <111> orientation.

transition compared to the R-O transition. Both transitions occur during the heating phase of the isoelectric process, and they both follow a counterclockwise rotation cycle.

For the <011> orientation, as shown in Figure 2.6(d), (e), and (f), Peak No. 1 and Cycle No. 1 at $T_l = 195K$ present a similar pattern to the <001> orientation. On the other hand, Cycle No. 2 at $T_l = 282K$ proves to be more favorable for energy harvesting. In this case, the O-T transition corresponds to a decrease in polarization. Furthermore, the optimal choice of low temperature, T_l, lies just before the O-T transition in the absence of an electric field.

For <111> oriented $BaTiO_3$, all FE-FE transitions are favorable and exhibit positive energy peaks. Both Cycle No. 1 and Cycle No. 2 have lower temperature values, respectively of, $T_l = 209K$ and $279K$. They are located just before the FE-FE transition at zero electric field. The energy density of Cycle No. 2 outperforms Cycle No. 1 due to the larger polarization variation induced by the O-T transition.

The area around the Curie temperature remains particularly attractive for pyroelectric energy energy scavenging in $BaTiO_3$ single crystals. The cycle n°3 for crystal

Thèse accessible à l'adresse : https://theses.insa-lyon.fr/publication/2024ISAL0017/these.pdf © [G. Taxil], [2024], INSA Lyon, tous droits réservés

cuts along <001> and <111> yields an energy density of $190mJ/cm^3$. Meanwhile, for the <011> orientation, this value is nearly $220mJ/cm^3$. Like for PMN-30PT, regardless of orientation, the energy peak of Cycle n°3 occurs at a low temperature T_l preceding the Curie temperature (T_c). In <001> oriented crystals, a more significant polarization variation is observed. However, the Curie temperature shifts more in response to an applied electric field unlike other orientations. This means that the shifting of T_c with respect to the electric field ($\frac{\partial T_c}{\partial E}$) is more pronounced for crystals oriented along the <001> direction. Consequently, the FE-PA transition does not occur during the heating process with a temperature variation of $10K$ at high electric field. This transition takes place solely when the electric field is low. In contrast, for crystal oriented along <011> and <111> directions, the FE-PA transition is possible during the heating process. However, it induces a smaller variation in polarization. Therefore, the overall area of the cycle, and consequently the energy harvested, represents a balance between the advantages of crystal orientation and of the Curie temperature shifting with electric field. The most favorable scenario will be a ferroelectric crystal oriented in the <001> direction with a minimal Curie temperature shift. Moreover, it can be noted that when the Curie temperature of a FE-FE transition shifts positively in response to an electric field, it results in a positive energy density, which is favorable to energy harvesting. Conversely, when this shift is negative, it leads to a negative energy density and an unfavorable temperature range for pyroelectric energy harvesting. Figure 2.7 provides an overview of the ideal phase transitions for the purpose of pyroelectric energy harvesting depending on their crystal orientations.

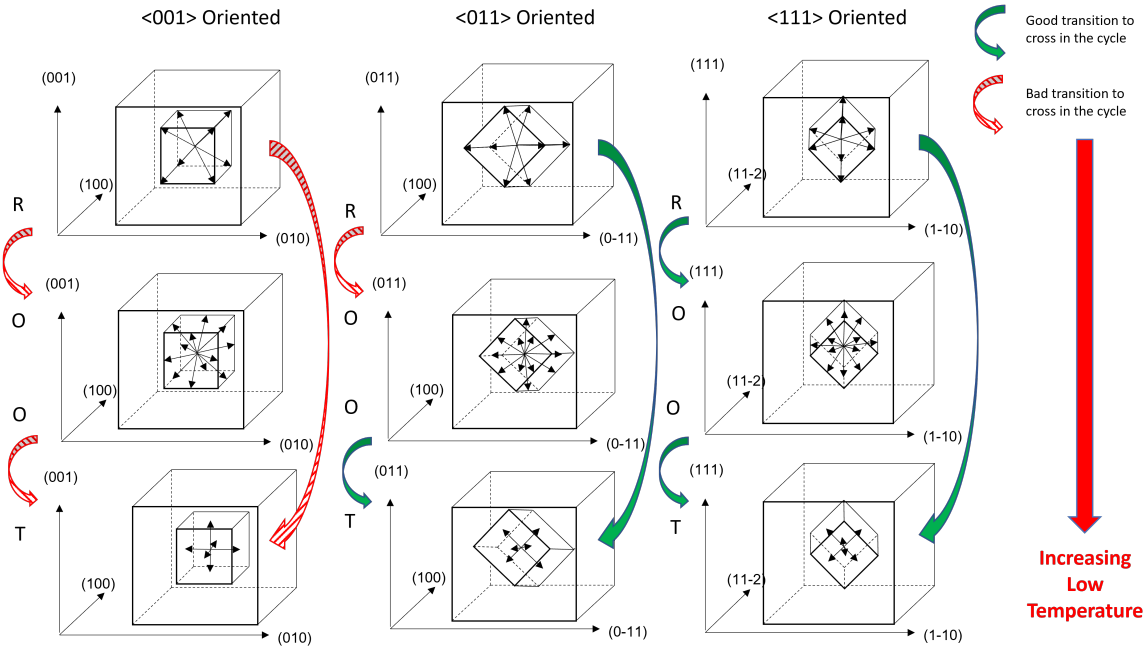

FIGURE 2.7: Illustration of the different phase transitions possible for different crystal orientations [Tax+22].

In order to give a comparison between the model and experimental datas, a graph illustrating the harvested energy as a function of temperature variation is presented in Figure 2.8. For this comparison, T_l has a constant value of 373K. The experiment was conducted by Khodayari *et al* [Kho+09a] using PZN-4.5PT crystals oriented along <011> with an electric field applied in the same direction. To obtain

Thèse accessible à l'adresse : https://theses.insa-lyon.fr/publication/2024ISAL0017/these.pdf © [G. Taxil], [2024], INSA Lyon, tous droits réservés

the Landau coefficients of PZN-4.5PT, a linear mixing law, utilizing coefficients from both PZN and PT as referenced in [AFI88a] was employed.

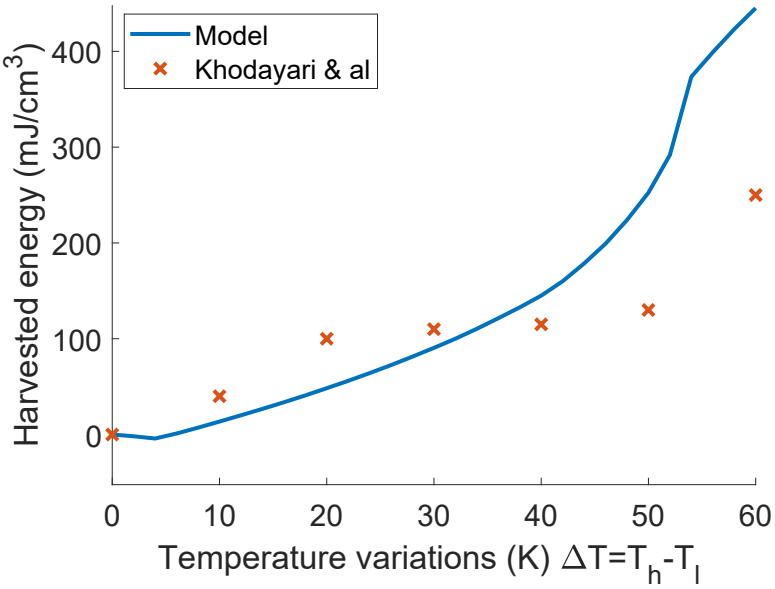

FIGURE 2.8: A plot of the harvested energy in function of the temperature variation $T_h - T_l$ for an Olsen cycle with $E_i = 0kV/mm$ and $E_f = 2kV/mm$ for a <011> oriented single crystal of PZN-4.5PT and an electric field applied in the [110] direction [Tax+22; Kho+09a].

One can observe that the model predictions for energy density closely align with the measured values. The overall curve trend is also consistent. Notably, a rapid increase in energy is evidenced for a temperature variation of $\Delta T = 60K$ in both curves, attributable to the FE-PA transition. Nevertheless, it is important to acknowledge that the fit is not flawless, and discrepancies arise that can be attributed to the presence of Polar Nano Regions (PNRs), particularly in the high-temperature range near the Burns temperature. These PNRs introduce additional contributions to the intrinsic polarization, as discussed in 1. Furthermore, the assumption of a single-domain crystal has been made, although real experiments involve multiple domains and present domain wall motions, which can alter the polarization response. However, a sufficiently high electric field has been applied, so that the hypothesis remains reasonably valid. Lastly, it is worth noting that the simulation does not account for electrical losses in the different Olsen cycle steps.

2.2 Mechanical energy harvesting

Mechanical energy harvesting is a sound solution to power devices without batteries. In non-resonnant mechanical energy harvesting, Ericsson cycle, equivalent to the Olsen cycle for pyroelectric energy harvesting, is a good alternative to increase energy efficiency of such an approach. Moreover, higher stress and electric field can be applied to the material and it is then possible to make profit of non-linearities of the polarization and enhance even more the harvested energy. The previous section dealt with the modeling to find optimal conditions for pyroelectric energy harvesting depending on various conditions such as the orientation of the crystal. This

Thèse accessible à l'adresse : https://theses.insa-lyon.fr/publication/2024ISAL0017/these.pdf © [G. Taxil], [2024], INSA Lyon, tous droits réservés

section will be devoted to the same purpose but for mechanical energy harvesting. It can be noted that this section will be connected with the next chapter as experimental characterizations were oriented to confirm the simulations. Moreover, it is important to note that this section is partly inspired by the published article in Acta Materialia [Tax+23]. In chapter 3, experimental results of Ericsson cycle on PMN-25PT and PZN-8PT <001> oriented samples will be provides along with the modeling results of these materials. This section will then as a first step introduce the approach for modeling Ericsson cycle in <001> oriented samples for comparison with the experimental campaign of next chapter. Finally, the modeling approach will be extended to all the orientations to generalize the approach.

2.2.1 Modeling of Ericsson cycle

In the previous chapter, it has been shown that mechanical energy harvesting from a single force application requires converting the largest part of the mechanical energy input into electrical one. Like for pyroelectric energy harvesting, closed thermodynamic cycles are a good alternative to this end, regardless of the practical implementation which will be the subject of Chapter 4. Here, Ericsson cycles are employed and consists of two isoelectric and two isostress processes (as detailed in chapter 1). Previous works have employed such cycles and reported especially high energy densities [PCV14a; PCV14b]. However, Ericsson cycle for mechanical energy harvesting has been much less explored compared to the Olsen cycle for pyroelectric energy harvesting. Concerning the modeling of such cycles, no research studies have been proposed so far to the best of our knowledge. Like for pyroelectric energy harvesting, a square variation of the stress and a triangular electric field functions were employed. This temporal evolution profile for the stress and the electric field are also quite realistic for possible devices as it will be shown in the next chapters. An illustration of an Ericsson cycle is given in Figure 2.9(a) along with the time evolution of the stress and the electric field in the simulations. As it was mentioned

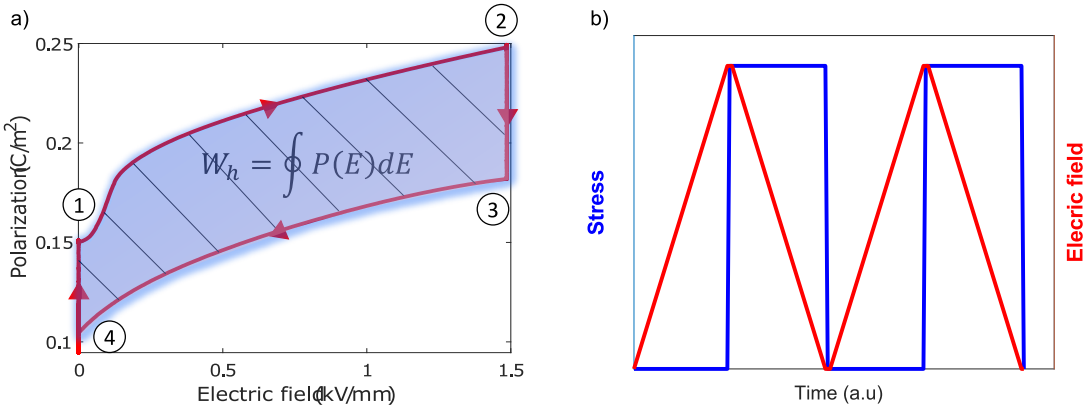

FIGURE 2.9: (a) Illustration of an Ericsson cycle [Tax+23]; (b) Temporal evolution of the stress and of the electric field

for Olsen cycles, in a real experiment, the temporal evolutions will have a direct influence on the output energies. [Bha+14]. However, in the Landau-Devonshire approach, no time dependency is considered. Thus, the time evolution profile is not important as long as the stress and the electric are applied successively and as the system is operating in quasi-static conditions. Like in the previous section, few assumptions were made. For instance, a single Ericsson cycle was simulated, a single

Thèse accessible à l'adresse : https://theses.insa-lyon.fr/publication/2024ISAL0017/these.pdf © [G. Taxil], [2024], INSA Lyon, tous droits réservés

ferroelectric domain was modeled and the frequency dependencies were not considered.

The modeling of the Ericsson cycle was made to predict experimental results of Chapter 3. Thus stress variations and applied electric field were chosen to be same than the achievable ones in the experimental test-bench. Moreover, such a range of stress and electric field are consistent with those that can be considered for real applicative devices. The stress was set to vary from 0 to 100MPa and the electric field from 0 to 1500kV/m. The spontaneous polarization is determined for every set of stress and electric field values, allowing the construction of the Ericsson cycle within the P-E space for each combination. It is important to note that the applied stress is a compressive unixial one. Moreover, the stress is applied in the same direction of the electric field (33-mode).

2.2.2 Model for <001> orientation

In order to study ferroelectric materials under stress, different studies proposed to employ Landau-Devonshire theory [Wan+10b; Bai+19; LWL16]. However, no report in the literature is found to model Ericsson cycle for mechanical energy harvesting via phenomenological approach. Compared to pyroelectric energy harvesting, the elastic contribution to the total free energy has to be added. The total free energy is expressed in the form of:

$$F = F_{lgd} + F_{elec} + F_{elas} \tag{2.20}$$

where, as it was mentioned before F_{elas}, F_{lgd} and F_{elec} represent respectively, the elastic contribution to the free energy, the classical Landau-Devonsire free energy and the free energy resulting from an applied electric field. The free enthalpy is again the appropriate thermodynamic potential as the electric field and the stress are the variables for the Ericsson cycle. The free enthalpy is expressed again by performing a Legendre transformation as follows.

$$\Delta G = F_{lgd} - E_i P_i - \frac{1}{2} s_{ijkl}\sigma_{ij}\sigma_{kl} - Q_{ijkl}\sigma_{ij}P_k P_l \tag{2.21}$$

where σ_{ij} represents the stress tensor, while s_{ijkl} and Q_{ijkl} correspond to the compliance and electrostrictive tensors, respectively. Considering the cubic symmetry, the free enthalpy can be expressed as follows:

$$\begin{aligned}
\Delta G \;=\; & \alpha_1({P_1}^2+{P_2}^2+{P_3}^2)+\alpha_{11}({P_1}^4+{P_2}^4+{P_3}^4)\\
& +\alpha_{12}({P_1}^2{P_2}^2+{P_1}{P_3}^2+{P_2}^2{P_3}^2)+\alpha_{123}{P_1}^2{P_2}^2{P_3}^2\\
& +\alpha_{111}({P_1}^6+{P_2}^6+{P_3}^6)+\alpha_{112}({P_1}^2({P_2}^4+{P_3}^4)\\
& +{P_2}^2({P_1}^4+{P_3}^4)+{P_3}^2({P_1}^4+{P_2}^4)+\alpha_{1111}({P_1}^8+{P_2}^8\\
& +{P_3}^8)+\alpha_{1122}({P_1}^4{P_2}^4+{P_1}^4{P_3}^4+{P_2}^4{P_3}^4)\\
& +\alpha_{1112}({P_1}^6({P_2}^2+{P_3}^2)+{P_2}^6({P_1}^2+{P_3}^2)\\
& +{P_3}^6({P_1}^2+{P_2}^2))+\alpha_{1123}({P_1}^4{P_2}^2{P_3}^2+{P_1}^2{P_2}^4{P_3}^2\\
& +{P_1}^2{P_2}^2{P_3}^4)-\tfrac{1}{2}s_{11}(\sigma_1^2+\sigma_2^2+\sigma_3^2)\\
& -s_{12}(\sigma_1\sigma_2+\sigma_1\sigma_3+\sigma_2\sigma_3)-\tfrac{1}{2}s_{44}(\sigma_4^2+\sigma_5^2+\sigma_6^2)\\
& -Q_{11}(\sigma_1P_1^2+\sigma_2P_2^2+\sigma_3P_3^2)-Q_{12}[\sigma_1(P_2^2+P_3^2)\\
& +\sigma_2(P_1^2+P_3^2)+\sigma_3(P_1^2+P_2^2)]-Q_{44}(\sigma_4P_2P_3+\sigma_5P_1P_3\\
& +\sigma_6P_1P_2)-E_1P_1-E_2P_2-E_3P_3
\end{aligned} \tag{2.22}$$

In this part, the electric field and the stress are considered to be applied in the $[001]_c$ direction. It has for consequence that a lot of terms of the free enthalpy vanish ($E_1 =$

Thèse accessible à l'adresse : https://theses.insa-lyon.fr/publication/2024ISAL0017/these.pdf © [G. Taxil], [2024], INSA Lyon, tous droits réservés

State	Polarization components	Number of configuration	Symmetry	Poled domain structure
Cubic <001>	$(0,0,0)$	1	$m\bar{3}m$	
Tetragonal <001>	$(0,0,P)$	6	4mm	1T
Orthorhombic <001>	$(\frac{P}{\sqrt{2}},\frac{P}{\sqrt{2}},0)$	12	mm2	4O
Rhombohedral <001>	$(\frac{P}{\sqrt{3}},\frac{P}{\sqrt{3}},\frac{P}{\sqrt{3}})$	8	3m1	4R

TABLE 2.3: Properties of the different ferroelectric phases [Tax+23]

$E_2 = 0$ and $\sigma_1 = \sigma_2 = 0$ and $\sigma_4 = \sigma_5 = \sigma_6 = 0$), and the expression is then reduced to:

$$\begin{aligned}\Delta G \;=\; & \alpha_1({P_1}^2+{P_2}^2+{P_3}^2)+\alpha_{11}({P_1}^4+{P_2}^4+{P_3}^4)\\ & +\alpha_{12}({P_1}^2{P_2}^2+{P_1}{P_3}^2+{P_2}^2{P_3}^2)+\alpha_{123}{P_1}^2{P_2}^2{P_3}^2\\ & +\alpha_{111}({P_1}^6+{P_2}^6+{P_3}^6)+\alpha_{112}\Big[{P_1}^2({P_2}^4+{P_3}^4)\\ & +{P_2}^2({P_1}^4+{P_3}^4)+{P_3}^2({P_1}^4+{P_2}^4)\Big]+\alpha_{1111}({P_1}^8+{P_2}^8\\ & +{P_3}^8)+\alpha_{1122}({P_1}^4{P_2}^4+{P_1}^4{P_3}^4+{P_2}^4{P_3}^4)\\ & +\alpha_{1112}\Big[{P_1}^6({P_2}^2+{P_3}^2)+{P_2}^6({P_1}^2+{P_3}^2)\\ & +{P_3}^6({P_1}^2+{P_2}^2)\Big]+\alpha_{1123}({P_1}^4{P_2}^2{P_3}^2+{P_1}^2{P_2}^4{P_3}^2\\ & +{P_1}^2{P_2}^2{P_3}^4)-\tfrac{1}{2}s_{11}\sigma_3^2-Q_{11}\sigma_3P_3^2-Q_{12}\sigma_3(P_1^2+P_2^2)-E_3P_3\end{aligned} \tag{2.23}$$

By minimizing the free enthalpy, it is then possible to get the corresponding polarization for each thermodynamic state. The electric field and stress along with their application directions, can lead to various phase configurations and even enable the creation of distinct engineered crystal structures. These characteristics for <001> oriented crystals are summarized in Table 2.3.

During the experiments, the polarization is determined by measuring the changes in the current passing through the samples. These crystals are oriented along the <001> direction, which means that the measured polarization corresponds to a projection along the z-axis (P_3). In the modeling process, the considered ferroelctric states were the tetragonal (T), orthorhombic (O), and rhombohedral (R) states, which are depicted in Figure 2.10 (a).

The monoclinic and triclinicic phases will not be taken into account due to the limitation to the sixth-order of the free energy for PZN-8PT [VC01]. When both electric field and stress are applied simultaneously, it becomes challenging to predict which crystal state the material will adopt. This is because the electric field tends to favor alignment along its direction of application, as shown in Figure 2.10 (b), while uniaxial stress tends to promote states perpendicular to its direction of application, as depicted in Figure 2.10 (c).

Therefore, modeling is employed here for its capability to forecast the crystal

Thèse accessible à l'adresse : https://theses.insa-lyon.fr/publication/2024ISAL0017/these.pdf © [G. Taxil], [2024], INSA Lyon, tous droits réservés

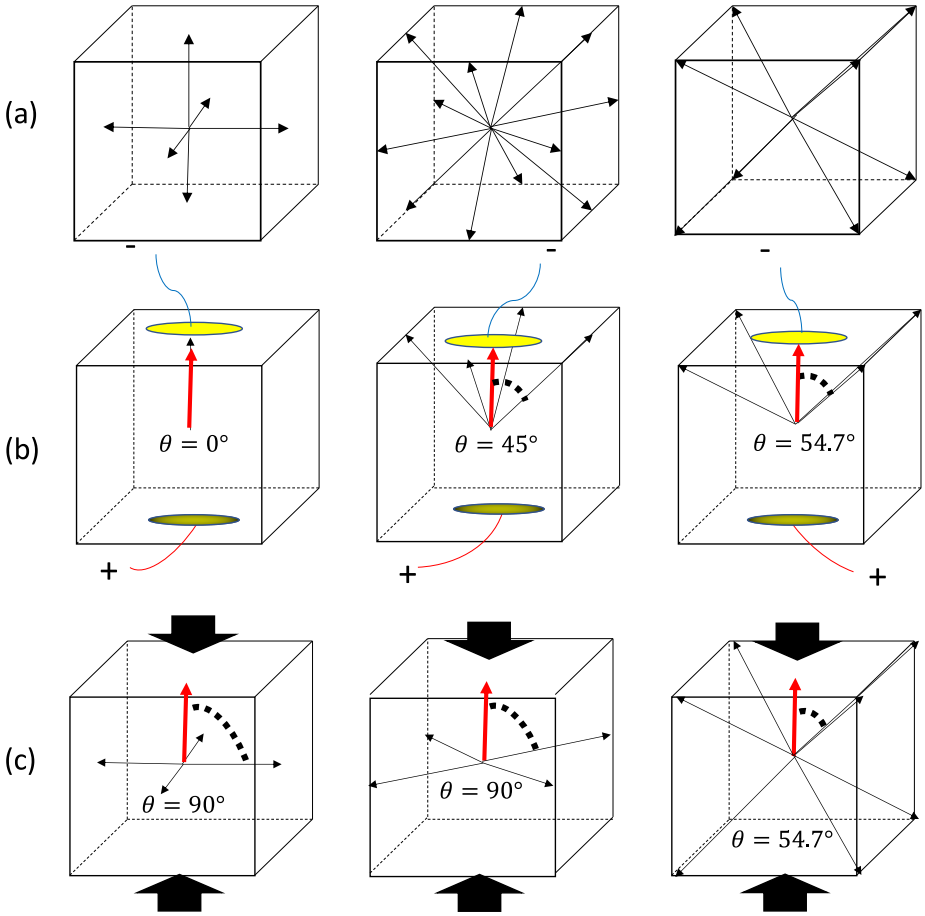

FIGURE 2.10: The different possible orientations of polarization for tetragonal, orthorhombic and rhombohedral (left to right) single crystals. (a) Possible configurations without applied electric field and stress; (b) Possible configurations when an electric field is applied; (c) Possible configurations when an uniaxial stress is applied. Red arrows represent the electric field and black ones the stress

state at each step of the Ericsson cycle. All the coefficients used in this modeling are outlined in Table 2.4. The phenomenological coefficients for PMN-25PT were sourced from [Qiu+15], while the coefficients for PZN-8PT were derived from a mixing law [HB20], expressed as $\alpha_1^{PZN-xPT} = x * \alpha_1^{PT} + (1-x) * \alpha_1^{PZN}$, as detailed in [AFI88b]. The phase diagram of $(1-x)PZN - xPT$ calculated with such an approach is depicted in Figure 2.11. It can be noted that these coefficients can also be experimentally determined by fitting them to the dielectric constants or the bipolar hysteresis loop, as described in [Lu+21; Zha+17].

It should be noted that certain approximations are made in the simulations. Like for pyroelectric energy harvesting, a single-domain crystal is assumed, which may not hold true in a real experiment. Nevertheless, as detailed before, this approximation is reasonably accurate under a sufficiently high electric field [CL07]. Additionally, hysteresis of the material is not taken into account, and the linear response of polarization to stress is significantly underestimated. For instance, simulations predict a piezoelectric coefficient of approximately $d_{33} \approx 10^2 pC/N$ while in PMN-25PT and PZN-8PT, it is around $d_{33} \approx 10^3 pC/N$ [Yos05; DDS06b]. Nonetheless, this modeling approach is well-suited for qualitatively predicting the optimal ferroelectric

Thèse accessible à l'adresse : https://theses.insa-lyon.fr/publication/2024ISAL0017/these.pdf © [G. Taxil], [2024], INSA Lyon, tous droits réservés

Parameter	PMN-25PT [Qiu+15]	PZN-8PT [AFI88b]	Units
T_c	366.9	432.8	K
α_1	$7.5 * 10^5$ $\times(T - T_c)$	$2.55 * 10^5$ $\times(T - T_c)$	$V.m.C^{-1}$
α_{11}	$-1 * 10^8$	$-3.75 * 10^7$	$V.m^5.C^{-3}$
α_{12}	$1 * 10^8$	$1.8 * 10^7$	$V.m^5.C^{-3}$
α_{111}	$1.1 * 10^9$	$1.79 * 10^8$	$V.m^9.C^{-5}$
α_{112}	$-3.5 * 10^9$	$3.63 * 10^8$	$V.m^9.C^{-5}$
α_{123}	$-4.8 * 10^9$	$-4.57 * 10^8$	$V.m^9.C^{-5}$
α_{1111}	$1 * 10^{10}$	0	$V.m^{13}.C^{-7}$
α_{1122}	$1 * 10^{10}$	0	$V.m^{13}.C^{-7}$
α_{1112}	$9.8 * 10^{10}$	0	$V.m^{13}.C^{-7}$
α_{1123}	$5.9 * 10^{10}$	0	$V.m^{13}.C^{-7}$
Q_{11}	0.055	0.098	$m^4.C^{-2}$
Q_{12}	-0.024	-0.035	$m^4.C^{-2}$
Q_{44}	0.021	0.034	$m^4.C^{-2}$
s_{11}	$52 * 10^{-12}$	$21.33 * 10^{-12}$	$N^{-2}.m^4$
s_{12}	$-18.9 * 10^{-12}$	$-2.68 * 10^{-12}$	$N^{-2}.m^4$
s_{44}	$14 * 10^{-12}$	$9.24 * 10^{-12}$	$N^{-2}.m^4$

TABLE 2.4: List of Landau coefficients and physical properties [Tax+23]

phase under specific working conditions and is primarily geared towards evaluating the non-linear response of the materials at high electric field and stress (where linear coefficients are meaningless).

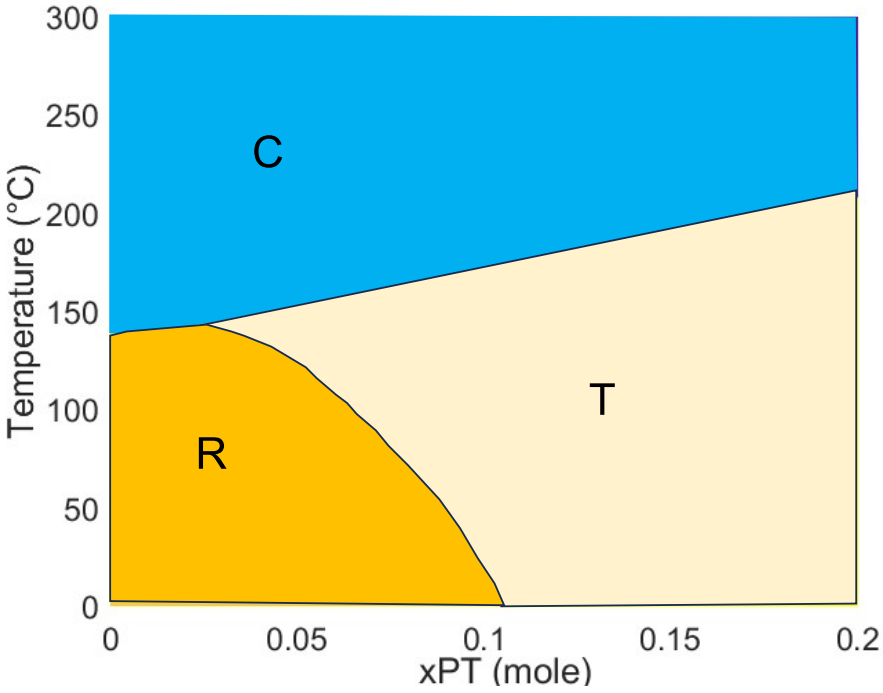

FIGURE 2.11: Simulated phase diagram of $(1 - x)PZN - xPT$

Thèse accessible à l'adresse : https://theses.insa-lyon.fr/publication/2024ISAL0017/these.pdf © [G. Taxil], [2024], INSA Lyon, tous droits réservés

The modeling results dedicated to PMN-25 and PZN-8PT <001> oriented crystals will be presented along with associated experimental results in Chapter 3, for the sake of clarity of the next chapter along with an easier comparison between model and experiments and to emphasize in the present chapter the underlying concepts.

2.3 Orientation in mechanical energy harvesting

2.3.1 Model

In the previous part, the approach for simulating an Ericsson cycle and ferroelectric crystals under uniaxial stress with a <001> cut direction has been presented. This part will be dedicated to generalize the approach for all the orientations of ferroelectric single crystals. To achieve this, two distinct basis have been used. The first one is the basis of the material (x, y, z) and the second one is the laboratory frame (x', y', z'). In the latter, the electric field and the unixial stress are applied along the (001) direction. An illustration of both basis are presented in Figure 2.12. With the same justification of precedent simulations, the measured polarization is the projection of the inner polarization along the z' axis of the laboratory frame. To operate this basis change, two rotation matrices were considered.

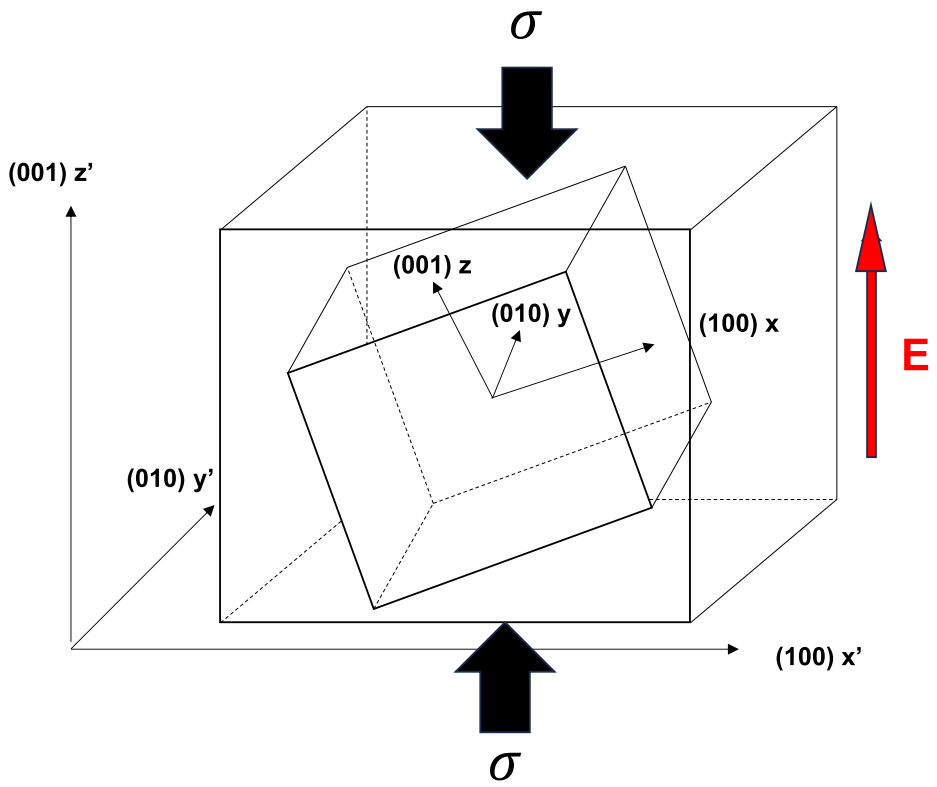

FIGURE 2.12: Illustration of the two basis and of the direction of the electric field and stress in these basis

The first matrix defines the rotation of an angle ϕ around the z axis and is given by:

$$R_z(\phi) = \begin{pmatrix} cos(\phi) & -sin(\phi) & 0 \\ sin(\phi) & cos(\phi) & 0 \\ 0 & 0 & 1 \end{pmatrix} \tag{2.24}$$

Thèse accessible à l'adresse : https://theses.insa-lyon.fr/publication/2024ISAL0017/these.pdf © [G. Taxil], [2024], INSA Lyon, tous droits réservés

The second one, defines the rotation of an angle θ around the x axis and it is expressed as:

$$R_x(\theta) = \begin{pmatrix} 1 & 0 & 0 \\ 0 & cos(\theta) & -sin(\theta) \\ 0 & sin(\theta) & cos(\theta) \end{pmatrix} \tag{2.25}$$

The total rotation matrix for the basis change is then given by:

$$A = R_z(\phi)R_x(\theta) = \begin{pmatrix} cos(\phi) & -sin(\phi)cos(\theta) & sin(\phi)sin(\theta) \\ sin(\phi) & cos(\phi)cos(\theta) & -cos(\phi)sin(\theta) \\ 0 & sin(\theta) & cos(\theta) \end{pmatrix} \tag{2.26}$$

It is important to note that the rotation matrix A will also be in some cases written in tensorial notation as $\lambda_{ij} = cos(e_i, e'_i)$. Here e_i and e'_i are respectively the components of the unit vectors of the material basis and of the laboratory frame.

The originality of this approach is to consider other crystal orientations by changing only the basis of the applied electric field and of the applied stress to the materials frame. In the material frame the electric field is expressed as:

$$E_i = \lambda_{ij}E'_j \text{ or } E = AE' \tag{2.27}$$

The stress in this basis is then given by:

$$\sigma_{ij} = \lambda_{ik}\lambda_{jl}\sigma'_{kl} \text{ or } \sigma = A\sigma' A^\top \tag{2.28}$$

As explained previously, in the laboratory frame, the electric field and the uniaxial stress are applied in the z direction, which implies:

$$E' = \begin{pmatrix} 0 \\ 0 \\ E'_3 \end{pmatrix} \text{ and } \sigma' = \begin{pmatrix} 0 & 0 & 0 \\ 0 & 0 & 0 \\ 0 & 0 & \sigma'_{33} \end{pmatrix} \tag{2.29}$$

After that, the free enthalpy in the material basis is given in tensorial notation as:

$$\begin{aligned} \Delta G \quad = \quad & \alpha_{ij}P_iP_j + \alpha_{ijkl}P_iP_jP_kP_l + \alpha_{ijklmn}P_iP_jP_kP_lP_mP_n + \alpha_{ijklmnop}P_iP_jP_kP_lP_mP_nP_oP_p \\ & -\tfrac{1}{2}s_{ijkl}\sigma_{ij}\sigma_{kl} - Q_{ijkl}\sigma_{ij}P_kP_l - E_iP_i \end{aligned} \tag{2.30}$$

Thus, by minimizing for each orientations the free energy with respect to the polarization in the material frame ($\frac{\partial \Delta G}{\partial P} = 0$), the polarization vector in the material basis can be calculated. The measured polarization is then given in the laboratory frame as:

$$P' = A^\top P \tag{2.31}$$

The measured polarization is then expressed as:

$$P'_3 = \vec{P'}.\vec{e'_z} \tag{2.32}$$

It can be noted again that in a real experiment, the measured polarization corresponds to the projection along the applied electric field direction. Thus, only the z' component of polarization is considered in the modeling. The model was first tested on barium titanate as this material has been largely investigated experimentally and theoretically. Furthermore, it undergoes successive phase transitions (R-O, O-T and T-C) with temperature. The component of polarization P'_3 depending on the angle θ

Thèse accessible à l'adresse : https://theses.insa-lyon.fr/publication/2024ISAL0017/these.pdf © [G. Taxil], [2024], INSA Lyon, tous droits réservés

and ϕ at different temperature are presented in a 3D plot in Figure 2.13(a), (b) and (c). It appeared that for each selected temperature, $BaTiO_3$ presents a different crystal phase symmetry. The results obtained emphasize that the measured polarization in the laboratory frame will be higher with a cut direction along the spontaneous direction as shown in Figure 2.13(d). For instance, at 320K, the crystal presents a tetragonal symmetry, thus, the measured polarization in the laboratory frame will adopt this symmetry

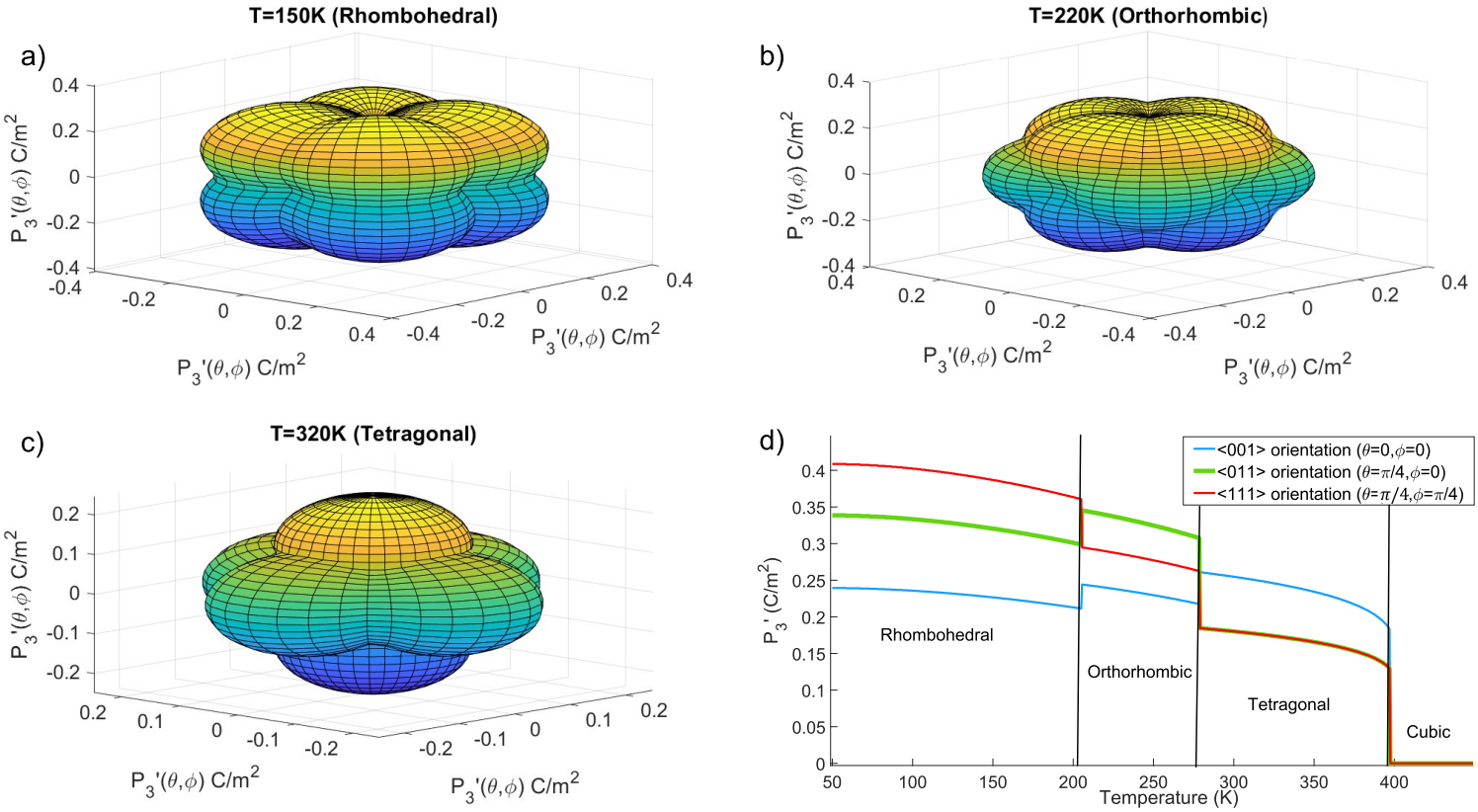

FIGURE 2.13: 3D plot of the polarization P_3' in different orientations of $BaTiO_3$ (a) At 150K; (b) At 220K; (c) At 320K; (d) P_3' in particular crystal orientaions in function of the temperature

2.3.2 Piezoelectric coefficicient

In the previous part, the approach to describe the materials with different crystal orientations in the frame of the Landau-Devonshire theory has been introduced. This part will be devoted to the calculation of different physical quantities, and particularly to the piezoelectric coefficients which are usually used in energy harvesting to compare the different efficiencies of piezoelectric materials. First, the dielectric susceptibility has to be derived from the free enthalpy. All the quantities were calculated in the material basis (x,y,z) and rotated afterwards in the laboratory frame. The dielectric stiffness is given by:

$$\xi ij = \frac{\partial^2 \Delta G}{\partial P_i \partial P_j} \tag{2.33}$$

Thèse accessible à l'adresse : https://theses.insa-lyon.fr/publication/2024ISAL0017/these.pdf © [G. Taxil], [2024], INSA Lyon, tous droits réservés

and the susceptibility is obtained with

$$\chi_{ij} = \epsilon_0(\xi_{ij})^{-1} \tag{2.34}$$

Subsequently, the piezoelectric coefficients can be determined by the equation:

$$g_{ijk} = \frac{\partial^2 \Delta G}{\partial P_i \partial \sigma_{jk}} \tag{2.35}$$

The Voigt notation was abandoned to facilitate the tensor calculation and rotation between the basis. The off diagonal stress tensor terms follow then these relations:$\sigma_4 = 2\sigma_{23}$, $\sigma_5 = 2\sigma_{13}$ and $\sigma_6 = 2\sigma_{12}$. Thereafter, to calculate all these tensors in the material basis, the piezoelectric and the susceptibility tensors were rotated in the laboratory frame:

$$\chi'_{ij} = \lambda_{ik}\lambda_{jl}\chi_{kl} \tag{2.36}$$

and

$$g'_{ijk} = \lambda_{im}\lambda_{jn}\lambda_{ko}g_{mno} \tag{2.37}$$

The d'_{ijk} tensor in the laboratory frame is then given by:

$$d'_{ijk} = \chi'_{im}g'_{mjk} \tag{2.38}$$

Initially, the modeling was performed on barium titanate and compared with different results obtained in the literature. The coefficients used for barium titanate were the same as referenced in Table 2.2. Figure 2.14(a), (b) and (c) provide the calculated piezoelectric coefficient d'_{33} in the laboratory frame for different orientations. Similar shape for the different orientation of the d_{33} of $BaTiO_3$ have been previously reported and well agreed with the simulation [DBS02; Dav+07]. It could be observed that the maximum of the piezoelectric coefficients are not along the spontaneous polarization direction. This behavior for barium titanate and other ferroelectric materials is explained as a direct consequence of the close presence of a phase transition and of the crystal anisotropy, reflecting the crystal lattice behavior [DBS02]. This characteristics explained the use of domain engineered crystals to make profit of this enhanced properties in particular orientations with particular lattice symmetries. In Figure 2.14(d), the d_{33}, d_{31} and d_{15} piezoelectric coefficients of <001> oriented $BaTiO_3$ are plotted as function of the temperature. The results were compared to the one obtained by Acosta *et al* [Aco+17]. The results again are in agreements and different aspects can be notified. Firstly, the different piezoelectric coefficients present different peaks corresponding to the different phase transitions (FE-FE, FE-FA). The highest d_{33}, d_{31} and d_{15} values for a crystal cut along the $[001]_c$ direction are obtained close to the R-O transition. It can be observed that the piezoelectric coefficients vary largely whether the temperature is close or not to a transition. Moreover, it can be noted that the d_{31} exhibits a very low value in the orthorhombic phase and does not displays a peak at the O-T transition.

The modeling results for orientation dependence have been confirmed through the piezoelectric coefficients assessments. In the following part, the simulation approach is proposed to establish a comparison between the orientation influence on high level energy harvesting by employing Ericsson cycle and low level energy harvesting via piezoelectric coefficients calculation for PMN-30PT single crystals.

Thèse accessible à l'adresse : https://theses.insa-lyon.fr/publication/2024ISAL0017/these.pdf © [G. Taxil], [2024], INSA Lyon, tous droits réservés

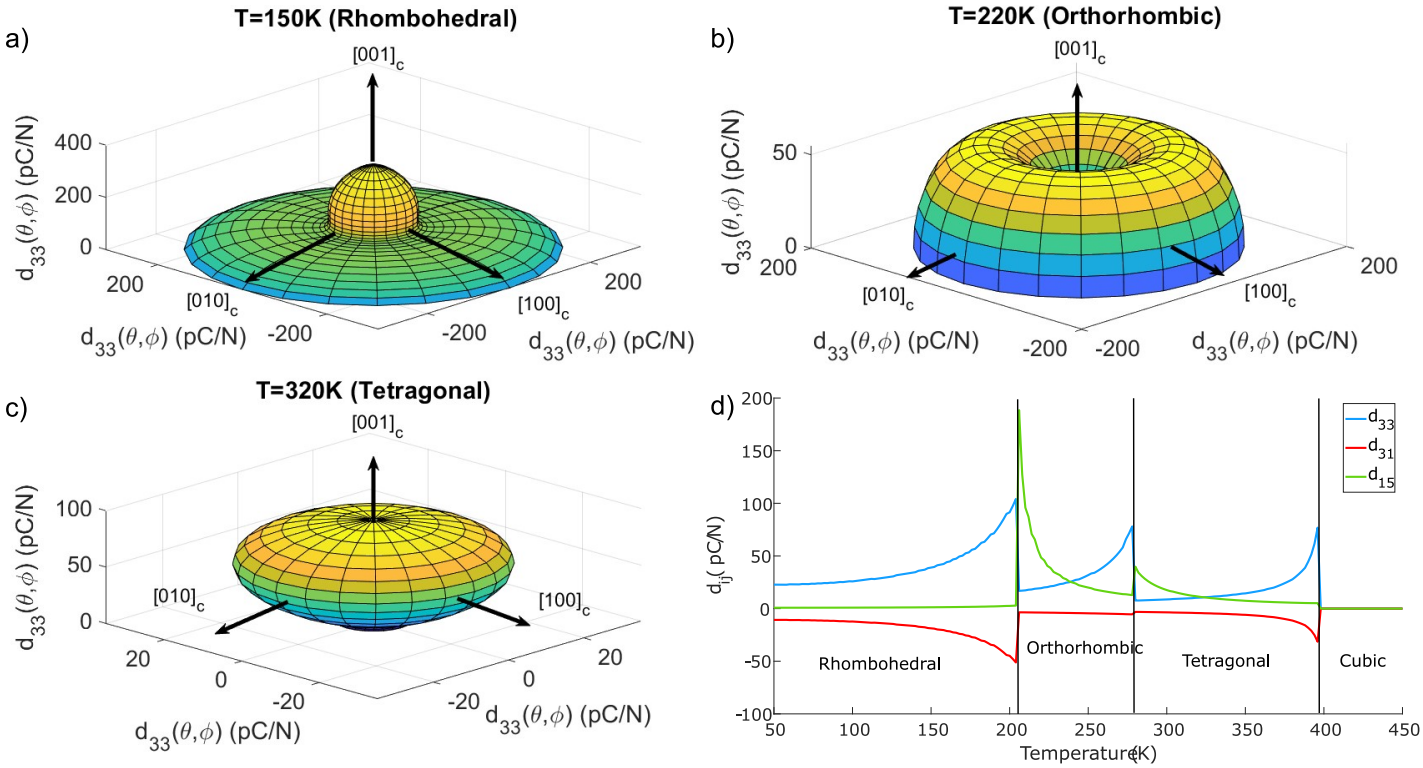

FIGURE 2.14: 3D plot of the d_{33} in different orientations of $BaTiO_3$ (a) At 150K; (b) At 220K; (c) At 320K; (d) Different piezoelectric coefficients in function of the temperature

2.3.3 Low level vs High level energy harvesting

In the previous part, the modeling of piezoelectric coefficients has been conducted and it showed the large anisotropy of piezoelectric coefficients depending on the crystal orientations. In the frame of energy harvesting, people generally want to employ materials with the largest piezoelectric coefficients. Indeed, the output voltage is linearly dependant of the piezoelectric coefficients. However, when applying large uniaxial stress, non linearities occurs and the piezolectric coefficient symmetry should not be necessarily respected. The modeling was performed on PMN-30PT single crystals. This choice was motivated by the commercial availability of PMN-30PT single crystals samples with <001>, <011> and <111> orientations. Experimental characterization of these samples is still ongoing but some preliminary results will be elaborated upon in Chapter 3.

For the modeling, Ericsson cycle were simulated with a similar approach used for <001> oriented crystals. With the same justifications than the previous part, the stress was adjusted to range from 0 to 100 MPa, while the electric field was controlled within the range of 0 to 1500 kV/m. The distinction in this modeling approach was based on the utilization of varying angles θ and ϕ for the application of both electric field and stress. The direction of application of the compressive uniaxial stress and of the electric field was still along the $[001]_c$ in the laboratory frame. The measured polarization is as exposed before obtained through the projection along the z direction of the laboratory basis. The Landau coefficients employed for PMN-30PT were identical to the one employed in the section dedicated to pyroelctric energy harvesting (cf. Table 2.2). The simulation were performed for two different temperatures of

Thèse accessible à l'adresse : https://theses.insa-lyon.fr/publication/2024ISAL0017/these.pdf © [G. Taxil], [2024], INSA Lyon, tous droits réservés

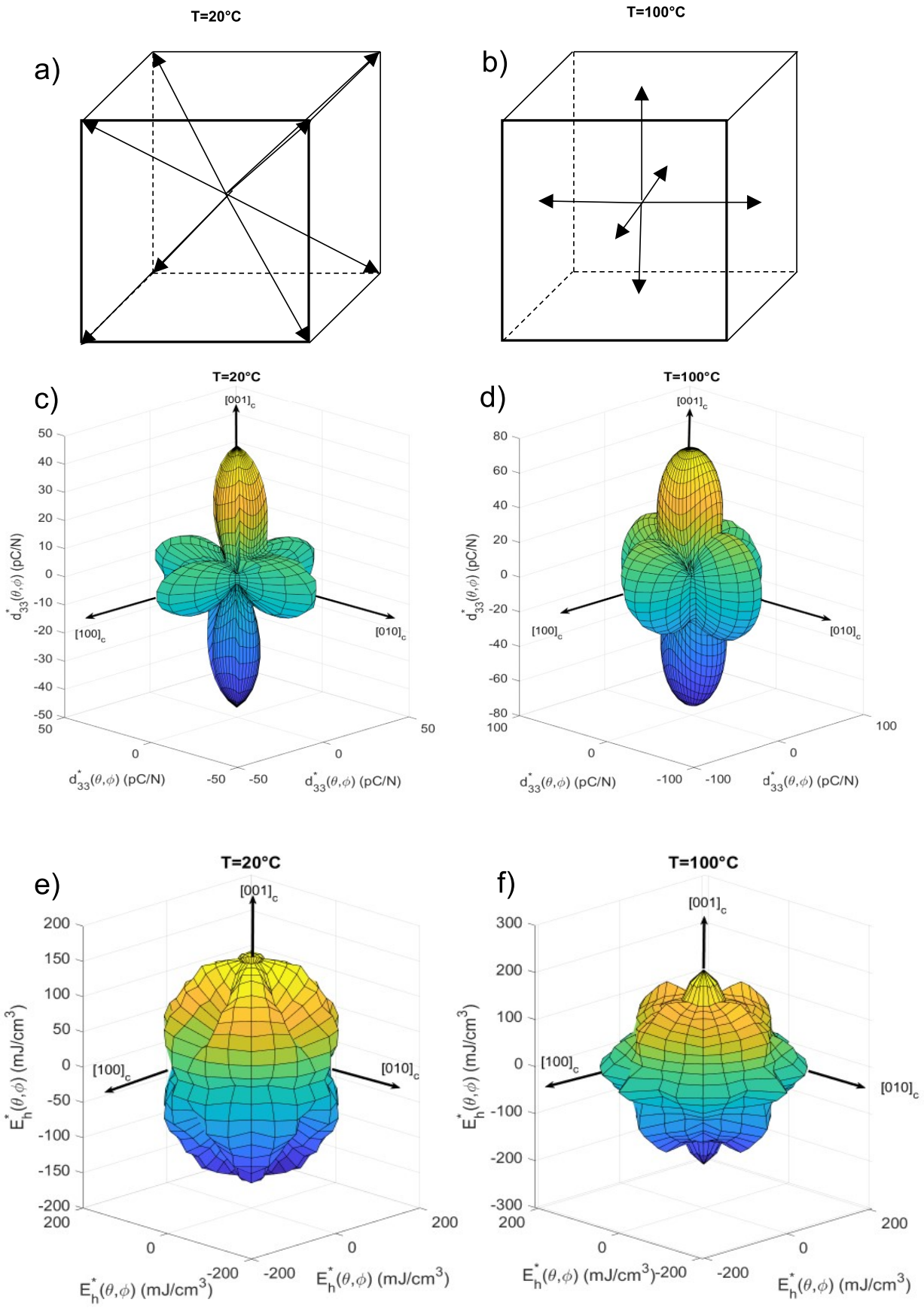

FIGURE 2.15: Illustration of the crystal symmetries of PMN-30PT (a) At 20°C; (b) At 100°C; 3D plot of the d_{33} in different orientations of PMN-30PT (c) At 20°C; (b) At 100°C; 3D plot of the harvested energy via Ericsson cycle in 33-mode in different orientations of PMN-30PT (e) At 20°C; (f) At 100°C

Thèse accessible à l'adresse : https://theses.insa-lyon.fr/publication/2024ISAL0017/these.pdf © [G. Taxil], [2024], INSA Lyon, tous droits réservés

20°C and 100°C. At 20°C, PMN-30PT presents a rhombohedral symmetry while at 100°C it has a tetragonal crystal symmetry. These two crystal phases are illustrated respectively in Figure 2.15 (a) and (b).

In Figure 2.15 (c) and (d), the d_{33} piezoelectric coefficients at respectively 20°C and 100°C of PMN-30PT for different orientations are provided. Various distinct characteristics can be observed, including the fact that 4R domain engineered crystals display the highest piezoelectricity. Indeed, the maximum of the piezoelectric coefficients are along the six tetragonal directions within the rhombohedral symmetry. This reflects that operating along the spontaneous polarization is not profitable for energy harvesting in such a configuration. This particularity was already noticed in the previous chapter as large heterogeneity between d_{33} piezoelectric coefficients was reported for different crystal orientations (cf. Table 1.2).

On the other hand, Figure 2.15(e) and (f) gives the harvested energy at respectively 20°C and 100°C calculated from the enclosed area of the Ericsson cycle for different angles θ and ϕ. A largely different symmetry is exhibited by the harvested energy. Indeed, the scavenged energy is much more homogeneous depending on the crystal orientation. Working along the spontaneous polarization here seems to provide the best output energy. This is explained by larger polarization variation by applying high uniaxial stress along the spontaneous polarization direction. However, it required applying sufficiently high unixial stress to force the material to adopt an in-plane ferroelectric state.

The modeling results indicates that very different symmetry are displayed between the piezoelectric coefficients and the harvested energy. This emphasizes the large differences existing between energy harvesting under low levels and high level of stress and electric field. These differences are explained by the non-linearities and phase configuration change induced by high stress and electric field. Taking advantage of such non-linearities for non-resonant mechanical energy harvesting can be a very profitable solution. Thus, understanding the polarization mechanisms when performing Ericsson cycle and identifying the response of ferroelectric materials under high applied stress and electric field for energy harvesting is essential.

2.4 Summary

This chapter was dedicated to set a theoretical framework in the context of energy harvesting under extreme conditions through thermodynamic cycles. To this end, the Landau-Devonshire theory was considerd. The first section focused on pyroelectric energy harvesting via Olsen cycles and investigated the optimal FE-FE transitions depending on three different crystal orientations. To confirm the modeling approach, calculation of the electrocaloric effect has been made and successfully compared to previous results in the literature. Another noteworthy side aspect for ECE was to elucidate the negative electrocaloric peaks by establishing a connection between the harvested energy and the electrocaloric effect. It appeared for energy harvesting that depending on the crystal orientations, different FE-FE transitions will be favorable for energy harvesting, whereas other transitions will not be profitable and corresponds to the ones displaying a negative ECE. In all the modeling results, the FE-PA transition maximizes the output energy, which is not surprising considering the large polarization variation occuring at the Curie temperature. Nonetheless,

Thèse accessible à l'adresse : https://theses.insa-lyon.fr/publication/2024ISAL0017/these.pdf © [G. Taxil], [2024], INSA Lyon, tous droits réservés

taking advantage of FE-FE transitions could serve as a viable alternative to enhance energy harvesting with materials presenting a too high Curie temperature (around 100°C).

Then, the next section of this chapter focused on the modeling of Ericsson cycles for mechanical energy harvesting. The modeling approach for Ericsson cycles was first introduced. The theoretical context and all the assumptions made to simulate PMN-25PT and PZN-8PT single crystals with <001> orientation has been introduced. All the simulation results on these materials will be provided along with the experimental results performed on these materials in Chapter 3 for a more qualitative discussion and conclusion.

Finally, the modeling was extended to all the different crystallographic orientations. To achieve this, two coordinate systems were introduced and the different calculations were detailed to express different physical properties and particularly the piezoelectric coefficient. A comparison between high level energy harvesting via Ericsson cycle and low level one through piezoelectric coefficient was made. It appears that the symmetries are very different in both cases. Particularly, under high electric field and uniaxial stress, the energy harvested is much more homogeneous. This emphasizes the particularity of energy harvesting in non-resonant condition with extreme conditions which contradicts approach using 4R domain engineered crystals in such conditions. Indeed, using non-linearities and phase transitions induce unique behavior and it can be more profitable to operate along the spontaneous polarization direction. These results will be discussed in more detail in the next chapter as some experimental results tend to corroborate such conclusions.

Thèse accessible à l'adresse : https://theses.insa-lyon.fr/publication/2024ISAL0017/these.pdf © [G. Taxil], [2024], INSA Lyon, tous droits réservés

Chapter 3

Experimental characterization

In this chapter, the objectives are to provide an experimental characterization of ferroelectric materials under large uniaxial stress, large applied electric field and various temperatures and to compare associated results with outputs of the theoretical framework presented in Chapter 2. Their abilities to convert mechanical energy to electrical one is evaluated in the context of non-resonant energy harvesting as well.

In the first section, the chapter will be dedicated to the presentation of the experimental methods and the experimental test-bench employed for the characterization. Different details will be given on the materials employed along with the measurement setup.

Following this part, a section dedicated on evaluating the energy conversion abilities of various ferroelectric materials including ceramics and single crystals is proposed. Ericsson cycles are employed and the materials are compared at different stress levels. Moreover the ultimate energy conversion abilities of different electroactive materials are evaluated and discussed.

Then, only single crystals of PMN-25PT and PZN-8PT cut along the $[001]_c$ direction are experimentally assessed. Large stress and high electric field are tested on the materials. The results are compared with theoretical predictions using the modeling approach developed in Chapter 2. Ericsson cycles estimated by the descending curves of bipolar hysteresis loops are also tested and the energy converted is assessed but this time at different operating temperature. Again, the results are discussed in the frame of the simulation results

Finallly, a small part will be dedicated to the experimental characterization under high uniaxial stress and high electric field of <111> oriented PMN-30PT. However, it is important to note that experimental measurements are still ongoing and this part of the study is not complete yet. The results will be again discussed in the frame of the modeling results obtained in Chapter 2.

Thèse accessible à l'adresse : https://theses.insa-lyon.fr/publication/2024ISAL0017/these.pdf © [G. Taxil], [2024], INSA Lyon, tous droits réservés

3.1 Experimental methods

The previous chapter dealt with the modeling of ferroelectric materials under extreme conditions for possible practical applications. Another main objectives of this work is to experimentally characterize different ferrolectric materials and their energy conversion abilities and confront the results with the simulation predictions. A test-bench able to reach high stress levels, high electric field and different temperatures was designed. In this framework, this section is devoted to present this experimental test-bench along with other practical details.

3.1.1 Samples

The properties of ferroelectric materials vary significantly depending on which specific material is under consideration. Thus, different ferroelectric ceramics and singles crystals have been investigated. The different samples along with their associated properties given by the suppliers or found in the literature are all highlighted in Table 3.1.

Materials	C203	C6	C9	PMN-25PT <001> [Pot+11; MTI05]	PZN-8PT <001>	PMN-15 [Pan+00; Ren+02]
Coupling factor k_{33}	0.71	0.76	0.69	0.91-0.95	0.94	0.6
Dielectric constant $\kappa_{33}^T \times \epsilon_0$	1450	2130	6640	5450	7700	24,000
Piezoelectric coefficient $d_{33}(pC/N)$	325	427	718	1540-2060	2890	700 Peak value

TABLE 3.1: Properties of the different ferroelectric materials at room temperature [Tun+22]

It is worth observing that the PMN 15 electrostrictive ceramic displays an exceptionally high dielectric constant. This distinct characteristic can be attributed to the ferroelectric-to-paraelectric (FE-PA) transition that occurs at approximately 15°C. Consequently, the measured value corresponds to a peak since the measurement was conducted at room temperature. The PMN 15 ceramics were purchased from TRS Technologioes, State College, PA, USA. These ceramics presents a disk shape with a diameter of $10mm$ and a thickness of $1mm$ with silver electrodes deposited upon the surfaces. $Pb[Zr_xTi_{1-x}]O_3$ (PZT) C203, C6 and C9, which are also qualified respectively of hard, medium and soft ceramics, were purchased from Fuji Ceramics Corporation, Fujinomiya, Japan. All the samples displayed a $6 \times 6mm^2$ surface and a thickness of $1mm$. PMN-25PT and PZN-8PT $\langle 001 \rangle$-oriented single crystals were respectively obtained from Otsuka Corporation, Japan, and Microfine Materials Technologies, Singapore. Both samples were polarized along the $[001]_c$ direction and had a thickness of 1 mm. Their surface dimensions were $6 \times 6mm^2$ for PMN-25PT and $2.5 \times 2.5mm^2$ for PZN-8PT. An illustration of all the samples is given in Figure 3.1. The samples were cut by using a dicing machine DISCO DAD3240. After cutting, The samples were electrically poled by immersing them in a silicone oil bath and employing the field cooling method [Kou+08]. These samples were gradually heated to their specific target temperatures (200°C, 180°C, 130°C, 90°C, and 150°C for PZT C203, C6, C9, PMN-25PT, and PZN-8PT, respectively). An electric field of 3 kV/mm

Thèse accessible à l'adresse : https://theses.insa-lyon.fr/publication/2024ISAL0017/these.pdf © [G. Taxil], [2024], INSA Lyon, tous droits réservés

was applied for 30 minutes while cooling down the samples. When the room temperature was reached, the electric field and then the samples were removed. However, it is important to note that this poling method was not necessary for all the samples. Indeed, the coercive fields of the tested materials were sufficiently low. Thus, an Ericsson cycles or a bipolar cycle measurements at room temperature could also act as a poling process. Nevertheless, this process was necessary for PZT C203 ceramics which present a high coercive field (more than 1kV/mm). Moreover, for some materials the ratio Electric field/Coercive field is not sufficiently high at room temperature. Then, the material could be in a partially depolarized state, which would degrade the piezoelectric properties of the material.

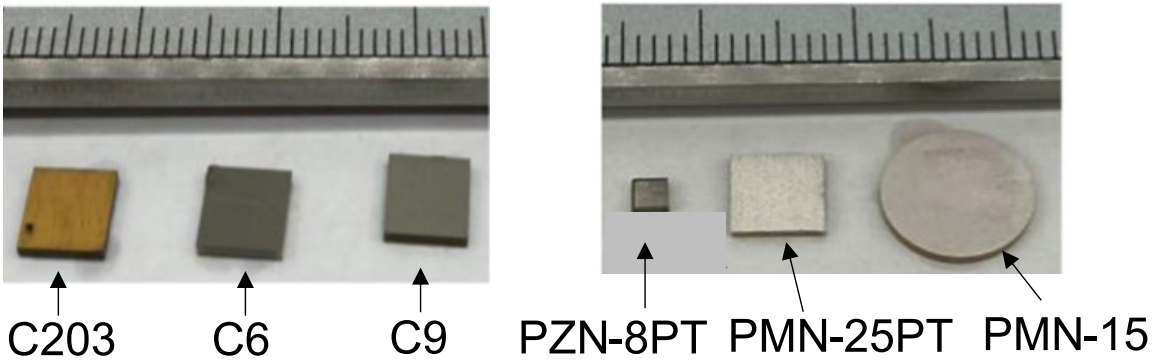

FIGURE 3.1: Image of all the tested samples [Tun+22]

It is worth noting that some crystals present segregation during particular crystal growth methods. Consequently, the precise composition of the material is uncertain. This is the case for PMN-25PT which is generally synthesized by the Bridgman crystal growth method which can induce segregation [Yin+99]. It is however possible to check the composition by performing a dielectric permittivity vs. temperature characterization. Thus, the composition of PMN-25PT was checked by associating the peaks of the dielectric constant to the R-T and the T-C transitions as shown in Figure 3.2. These measurements were not conducted for PZN-8PT because the crystal growth method (flux-grown crystals [Kob+97]) does not induce segregation during the elaboration process.

3.1.2 Test-bench

As mentioned before, the experimental test-bench was designed for applying high uniaxial compressive stress and high electric field, while monitoring the temperature of the sample. The application of the high uniaxial stress on the samples was achieved using a Shimadzu® AGS-X series compression test machine. With this machine, the force has to be specified by the user. The uniaxial compressive stress σ_3 applied to the materials is then deduced with the simple following relation:

$$\sigma_3 = \frac{F}{S} \tag{3.1}$$

where F is the applied force with the machine and S is the surface of the sample. To apply the electric field, a Tektronix® AFG1022 arbitrary function generator and a Trek® 10/10B-HS high voltage amplifier were employed. The electric field applied to the material E_3 is then given by:

$$E_3 = \frac{V}{e} \tag{3.2}$$

Thèse accessible à l'adresse : https://theses.insa-lyon.fr/publication/2024ISAL0017/these.pdf © [G. Taxil], [2024], INSA Lyon, tous droits réservés

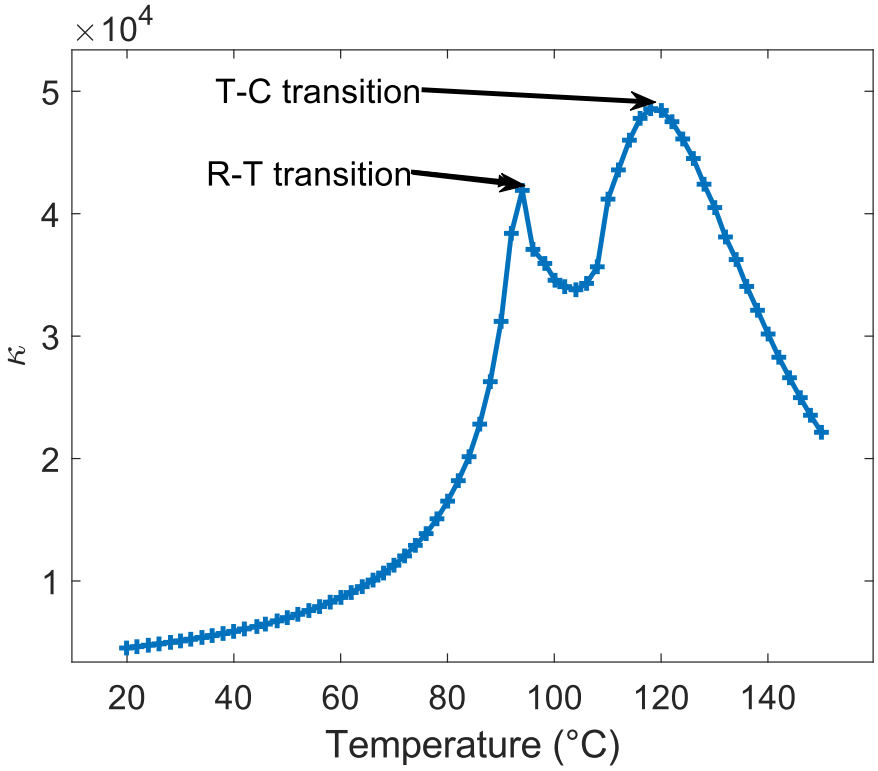

FIGURE 3.2: Dielectric permittivity as a function of the temperature of PMN-25PT

where V is the applied voltage to the faces of the sample and e is the thickness of the sample. The sample were sandwiched between two ceramic plates with gold sputtered electrodes on their surfaces. Samples were immersed in a silicon oil bath to apply the electric field and avoid electrical breakdown. A schematic illustration along with a photo of the experimental test-bench is given in Figure 3.3 (a) and (b).

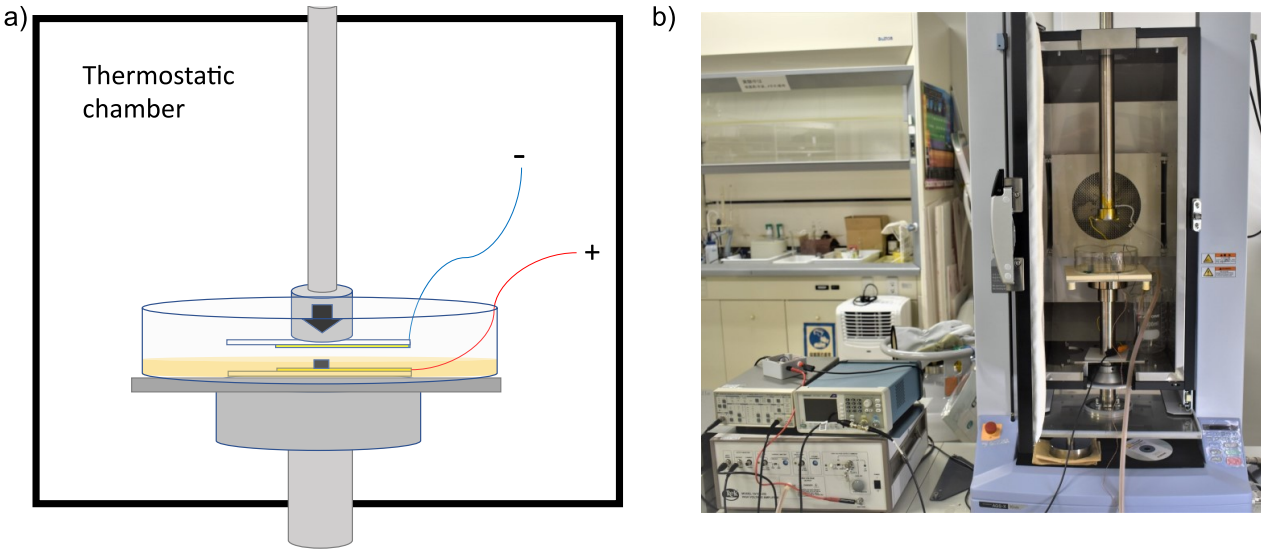

FIGURE 3.3: (a) Schematic illustration of the test-bench [Tax+23]; (b) Photo of the test-bench [Tax+23]

The current through the samples was monitored by using a low-noise current

Thèse accessible à l'adresse : https://theses.insa-lyon.fr/publication/2024ISAL0017/these.pdf © [G. Taxil], [2024], INSA Lyon, tous droits réservés

amplifier (Stanford research®, Sunnyvale, CA, United States of America). As detailed in the previous chapters, the polarization P_3 can be deduced from the total current flowing through the samples via the following relations:

$$Q = \int I(t)dt \tag{3.3}$$

$$P_3 = \frac{Q}{S} \tag{3.4}$$

where I is the measured current and Q is the charge integrate from the current. The silicon oil bath also allowed regulating the temperature of the sample which was monitored using a Shimadzu® TCE-N300A thermostatic chamber. The temperature was measured using a thermocouple immersed inside the silicon oil bath. Finally, all the signals were recorded using a Data Acquisition System (Dewesoft Krypton 8LV, Slovenia). A schematic illustration of the test-bench along with the acquisition system is given in Figure 3.4.

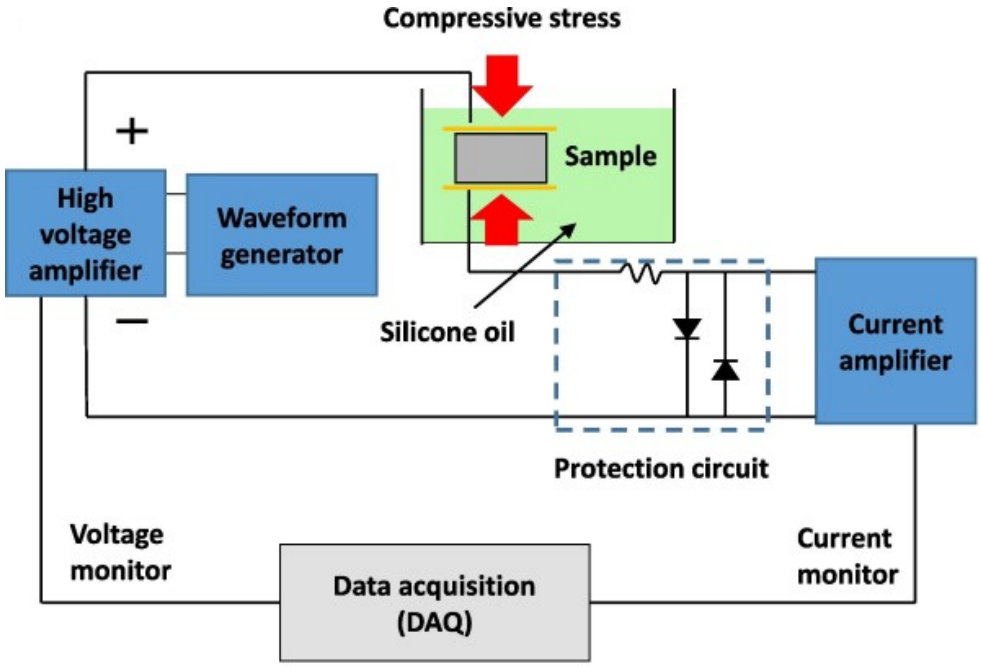

FIGURE 3.4: Schematic diagram of the measurement system [Tun+22]

3.1.3 Ericsson cycles and bipolar hysteresis loops

Electromechanical conversion abilities of the considered ferroelectric materials were evaluated by different means. The harvested energy can be derived from two bipolar hysteresis curves. With this method the first bipolar loop is made at zero stress level and the second one is made under uniaxial stress. The converted energy is then estimated by the enclosed area formed by the two remnant polarization and the two saturation polarization as shown in Figure 3.5(a). The other possibility is to make the real Ericsson cycle and perform the successive steps of the Ericsson cycle (cf. Chapter 1 and 2) as illustrated in Figure 3.5(b). It is worth noting that there are some distinctions in the evaluation of harvested energy when comparing the bipolar descending curves with real Ericsson cycles. In the latter, hysteresis losses occur as a result of the sample repolarization during the 1-2 process (electric field

Thèse accessible à l'adresse : https://theses.insa-lyon.fr/publication/2024ISAL0017/these.pdf © [G. Taxil], [2024], INSA Lyon, tous droits réservés

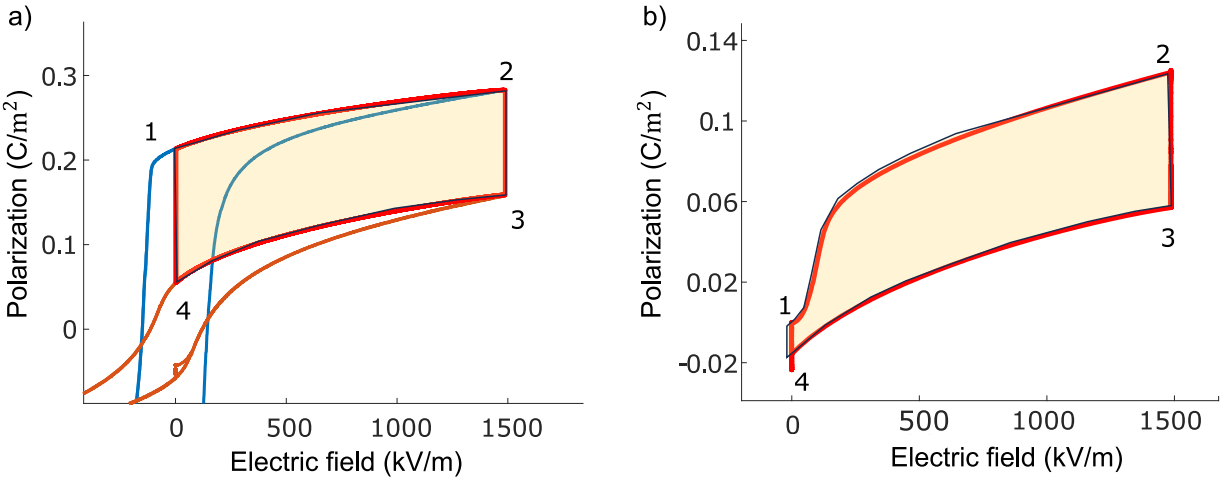

FIGURE 3.5: (a) Estimation of the Ericsson cycle from the bipolar hysteresis loops; (b) Real Ericsson cycle

application). Both methods have their own advantages, for instance, real Ericsson cycles have the advantage to be more representative of the potential area in a real implementation. However, it suffers from DC current losses which can be important during the stress applications. On the other hand, Ericsson cycles estimated from the bipolar hysteresis curves has the advantages to limit the DC current losses. Furthermore, the Ericsson cycles modeled with Landau–Devonshire corresponds to these descending curves of bipolar loops. It is then more convenient, to understand properly the polarization mechanisms and the phase transitions involved, to employ the bipolar hysteresis curves. Nevertheless, the drawback is an overestimation the energy possibly harvested in real devices. In this chapter, these two methods will be employed for calculating the harvested energy. If the characterization is devoted to understand the inherent mechanisms and compared with the model predictions, then, the bipolar curves will be used. Conversely, actual Ericsson cycles will be used to compare materials and assess the feasibility of real-world implementation.

For bipolar hysteresis curves, the voltage function had a sinusoidal shape with a frequency of 0.5 or $1Hz$. It appears that the response of the materials did not change in such a frequency range. Moreover, this work does not aims at investigating frequency dependencies. The electric field was set to vary from $-1500kV/m$ to $1500kV/m$ and different uniaxial compressive stresses were tested. The voltage function and the associated current for two bipolar hysteresis curves performed at 0 and 100MPa is given in Figure 3.6(a) and (b).

Concerning real Ericsson cycle, a trapezoidal waveform was employed for the applied voltage and the applied force. The electric field varied from $0kV/m$ to $1500kV/m$. Only compressive stresses of 30 and $100MPa$ were tested for real Ericsson cycles. The waveform of the applied voltage and force for a real Ericsson cycle with successive steps along with the corresponding current is presented in Figure 3.6(c) and (d).

It can be noted, that a restriction on the electric field strength was imposed to prevent dielectric breakdown, despite the successful application of higher electric fields to single crystals in prior studies [PS97b]. A safety limit of 1500 kV/m was set for practical and achievable values, considering potential engineering applications

Thèse accessible à l'adresse : https://theses.insa-lyon.fr/publication/2024ISAL0017/these.pdf © [G. Taxil], [2024], INSA Lyon, tous droits réservés

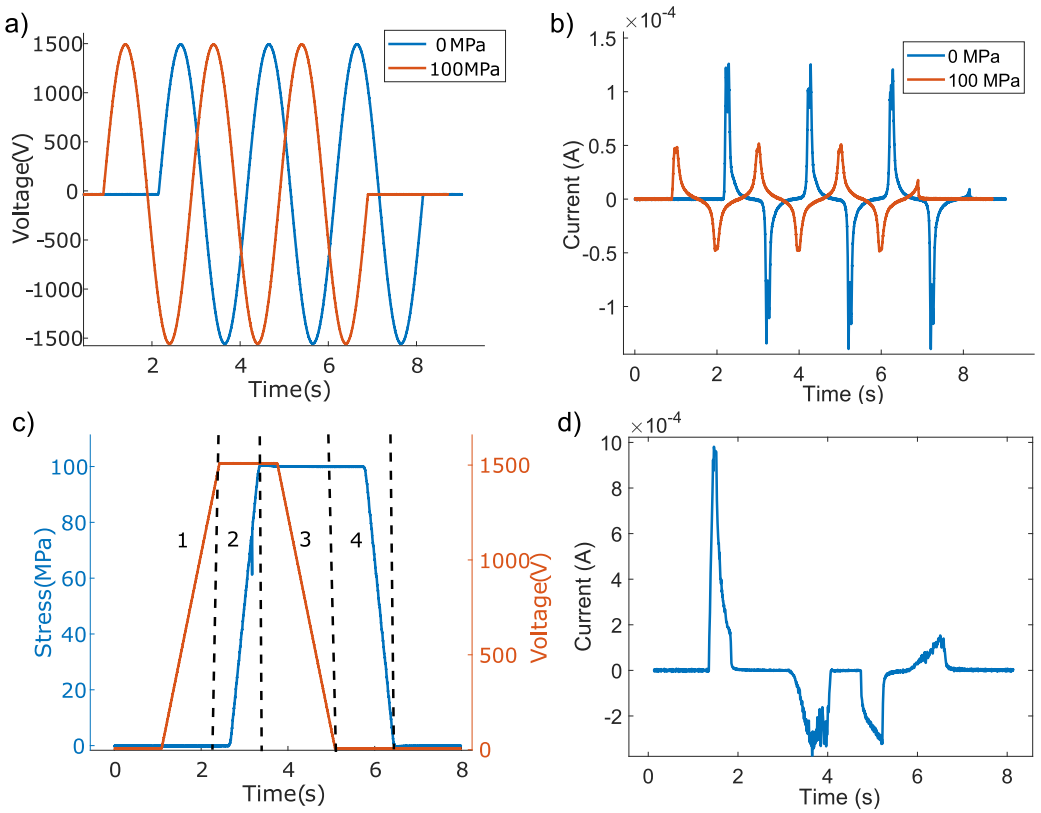

FIGURE 3.6: (a) Voltage function for bipolar hysteresis loop; (b) Associated current; (c) Voltage and stress function for real Ericsson cycle; (d) Associated current

in the future. Moreover, the stress was limited to 100MPa for similar reason. Indeed, again the limitation was set to avoid breaking of the samples and for possible future engineering devices. It can be noted again that it is possible to applied higher uniaxial stress to ferroelectric materials [PCV14a].

3.2 Material comparisons

The previous section dealt with the presentation of the experimental test-bench and the experimental conditions. This experimental setup was developed to assess energy conversion under extreme conditions of ferroelectric materials and to exploit the non-linearities induced by such high levels. In this upcoming part, the experimental results of real Ericsson cycles and their resulting energy densities will be presented for various materials and different uniaxial stress levels. One of the main objectives of this study is to assess the ultimate energy conversion of ferroelectric materials for energy harvesting applications. The test bench and subsequent comparison between various materials in section 3.2 was part of the FIESTA collaborative project and done mostly by Dr Nguyen Thanh Tung, postdoctoral researcher working at ELyTMaX. In the frame of the thesis, the analysis of the tendencies have been further deepened thanks to the model introduced in Chapter 2, as shown in sections 3.3 and 3.4. For the sake of completeness and to give to the reader an overview of the ferroelectric materials properties, section 3.2 will describe the main results from the comparison between materials, and taken from [Tun+22].

Thèse accessible à l'adresse : https://theses.insa-lyon.fr/publication/2024ISAL0017/these.pdf © [G. Taxil], [2024], INSA Lyon, tous droits réservés

3.2.1 Results

Energy conversion performance by employing real Ericsson cycle was first investigated at an intermediate stress level of 30MPa. These cycles for PZT C203, C6, C9, PMN-25PT, PZN-8PT, and PMN15 are presented in Figure 3.7. It can be noted that

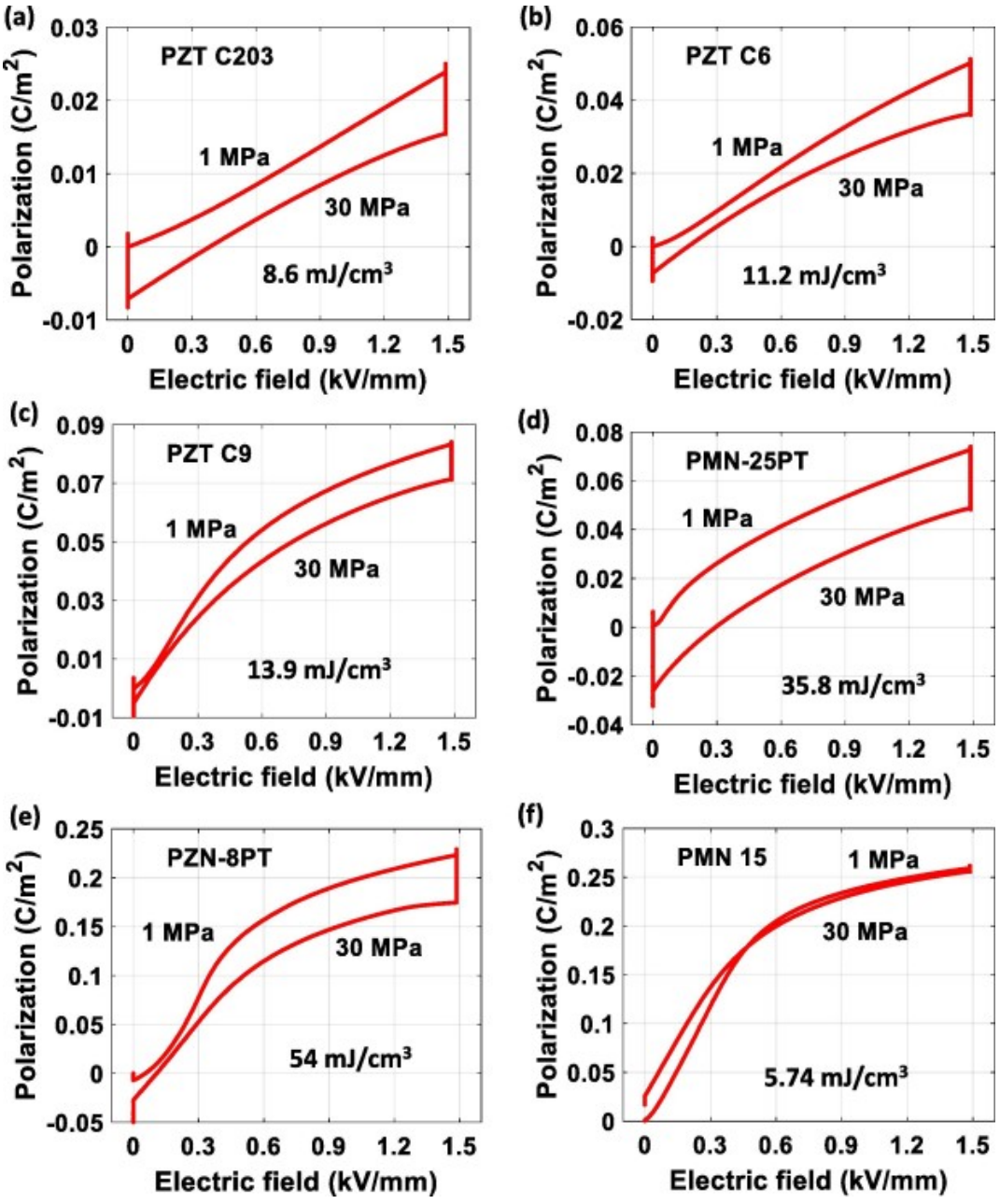

FIGURE 3.7: Real Ericsson cycles under intermediate levels of stress for different materials [Tun+22]. (a) PZT C203; (b) PZT C6; (c) PZT C9; (d) PMN-25PT; (e) PZN-8PT; (f) PMN 15

a low compressive stress of $1MPa$ was applied during the electric field application and the releasing of the stress (1-2 and 4-1 processes). This was to ensure the electrical contact between the ceramic plates and the sample surfaces. Different energy densities are reported for the different materials. The hard, medium and soft PZT ceramics (C203, C6 and C9 respectively) present energy densities around $10mJ/cm^3$. However, it can be observed that their energy densities increase slightly from the

Thèse accessible à l'adresse : https://theses.insa-lyon.fr/publication/2024ISAL0017/these.pdf © [G. Taxil], [2024], INSA Lyon, tous droits réservés

harder to the softer ceramic. This emphasizes their d_{33} hierarchies as it was reported in Table 3.1. Concerning PMN-25PT and PZN-8PT <001>-oriented crystals, they display much higher energy densities of respectively $35.8 mJ/cm^3$ and $54 mJ/cm^3$. PMN15 presents a very low energy gain of only $5.74 mJ/cm^3$ explained by the paraelectric state of this material at room temperature.

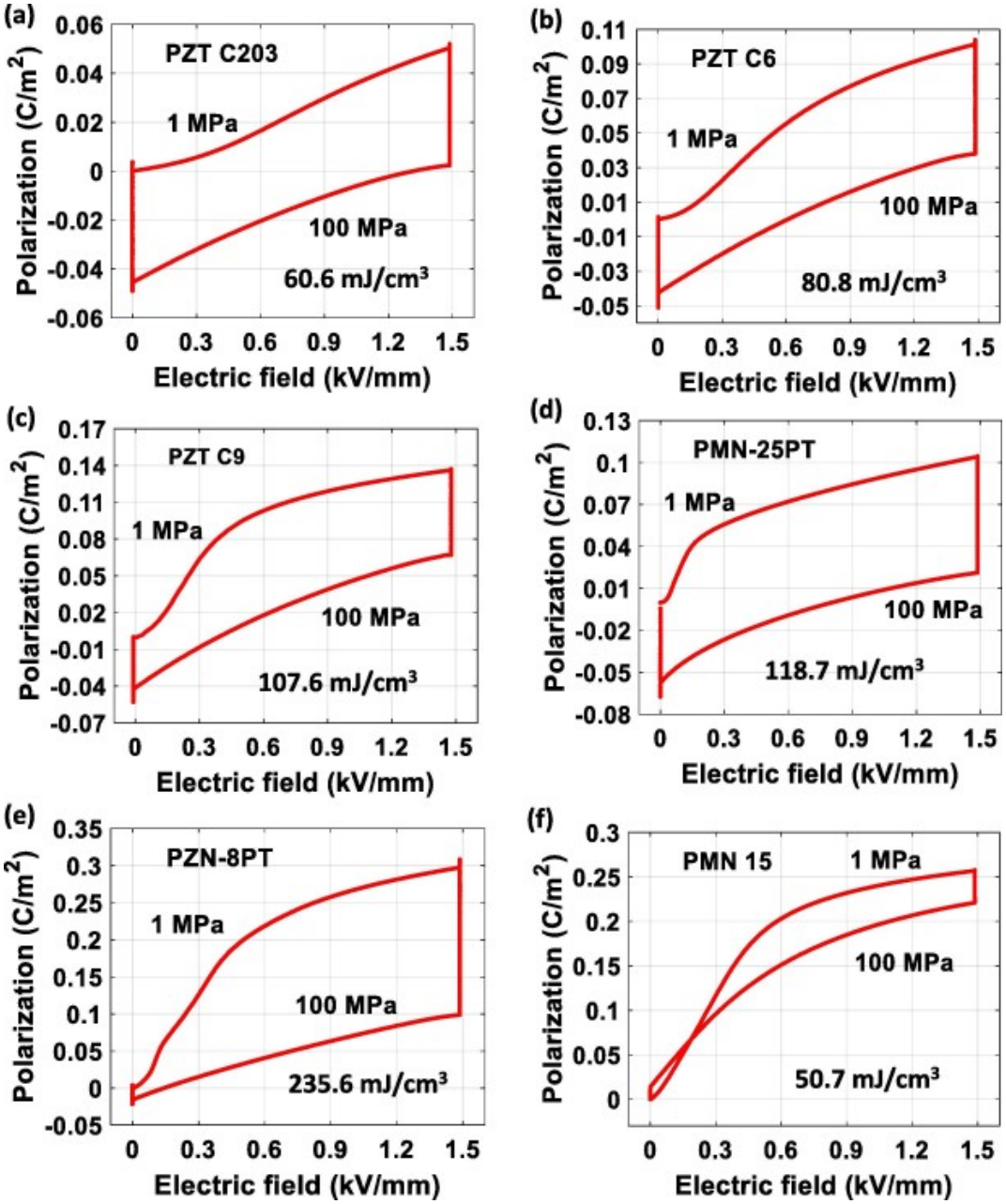

FIGURE 3.8: Real Ericsson cycles under high levels of stress for different materials [Tun+22]. (a) PZT C203; (b) PZT C6; (c) PZT C9; (d) PMN-25PT; (e) PZN-8PT; (f) PMN 15

After that, higher stress level of $100 MPa$ was tested on the materials and the results are presented in Figure 3.8. The energy density was lower for the hard PZT C203, higher for the medium PZT C6, and significantly higher for the soft PZT C9 (60,6, 80.8 and $107.6 mJ/cm^3$). For the ferroelectric single crystals, PMN-25PT presents almost a similar output energy than PZT-C9 which was unexpected results

Thèse accessible à l'adresse : https://theses.insa-lyon.fr/publication/2024ISAL0017/these.pdf © [G. Taxil], [2024], INSA Lyon, tous droits réservés

considering their d_{33} differences. However, PZN-8PT exhibits an exceptional energy density of $235.5 mJ/cm^3$ which highlights unique polarization mechanisms. In the case of the paraelectric phase material, the energy density of PMN 15 was lower than that of the ferroelectric phase materials with an energy density of only $50.7 mJ/cm^3$.

Moreover, tests were made with significantly reduced levels of mechanical stress and electric field. By constraining the electric field to 100 V/mm and the mechanical stress to 1 MPa, it is acceptable to consider only the linear response with stress and electric field of the material. With such assumptions, it is possible to express the energy density as follows:

$$W_h = d_{33}\sigma_3 E_3 \tag{3.5}$$

Then, it was possible to obtain a quite accurate value of the d_{33} of the tested materials (cf. Table 3.1). A comparison between the energy densities obtained with Ericsson cycle at $30 MPa$ and $100 MPa$, and from the d_{33} measurements for all the tested materials, is proposed respectively in Figure 3.9(a), (b) and (c). The energy densities for these samples at lower levels exhibited the same trend as observed at intermediate levels. However, energy densities, of Ericsson cycles at 100MPa display a slightly different trend. Indeed, it seems that all the different materials except PZN-8PT converge on similar energy densities. This change of trend is explained by non-linearities induced by the high uniaxial stress and will be discussed in the next part of this chapter.

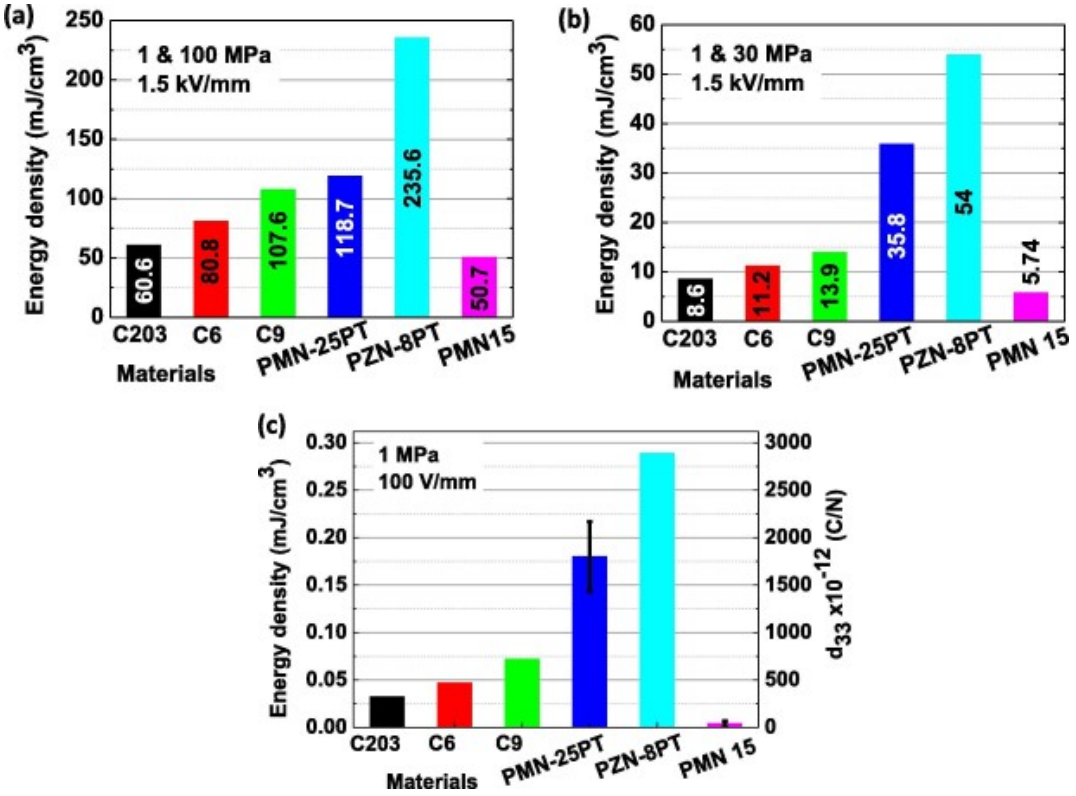

FIGURE 3.9: Different materials with their associated energy densities under different levels (a) high levels; (b) Intermediate levels; (c) Low levels.

Thèse accessible à l'adresse : https://theses.insa-lyon.fr/publication/2024ISAL0017/these.pdf © [G. Taxil], [2024], INSA Lyon, tous droits réservés

3.2.2 Discussion

Energy harvesting involving low excitation levels of piezoelectric materials is typically evaluated by considering the linear properties of the materials. Indeed the output energy density is solely dependant on the d_{33} as it was reported in Figure 3.9(c). In the case of Ericsson cycles used for electromechanical energy conversion, the output energy will be the results of more complex phenomena when sufficient electric field and stress are applied. In the results reported here, the ranking of the materials followed their d_{33} values at low and even intermediate levels (Figure 3.9(b) and (c)). However, at higher electric field and mechanical stress levels, the output energies converged due to polarization saturation, which primarily depended on the dipole moment and dipole density. For instance, in low-level energy harvesting, the energy ratio between PZT C9 and PMN-25PT was determined by their d_{33} ratio, which was approximately 2.2 times larger for PMN-25PT. However, for energy cycles involving 100 MPa and 1.5 kV/mm, this ratio decreased to around 1.1. However, PZN-8PT displays a unique behavior and did not follow this trend. This, particularity is explained by phase transition induced by the applied stress in the $2-3$ process. At room temperature, PZN-8PT <001>-oriented crystal presents a rhombohedral symmetry corresponding to a 4R domain engineered crystal. When the electric field is applied in the $2-3$ process, the crystal is poled and reach its saturation polarization. The uniaxial stress applied in the $2-3$ process will induce an in plane phase configuration which can be either tetragonal or orthorhombic. This phase transition will results in a large polarization variation and so a wider area of the cycle which corresponds to higher energy density. A schematic illustration of the polarization mechanisms along the cycle exhibited by PZN-8PT is given in Figure 3.10.

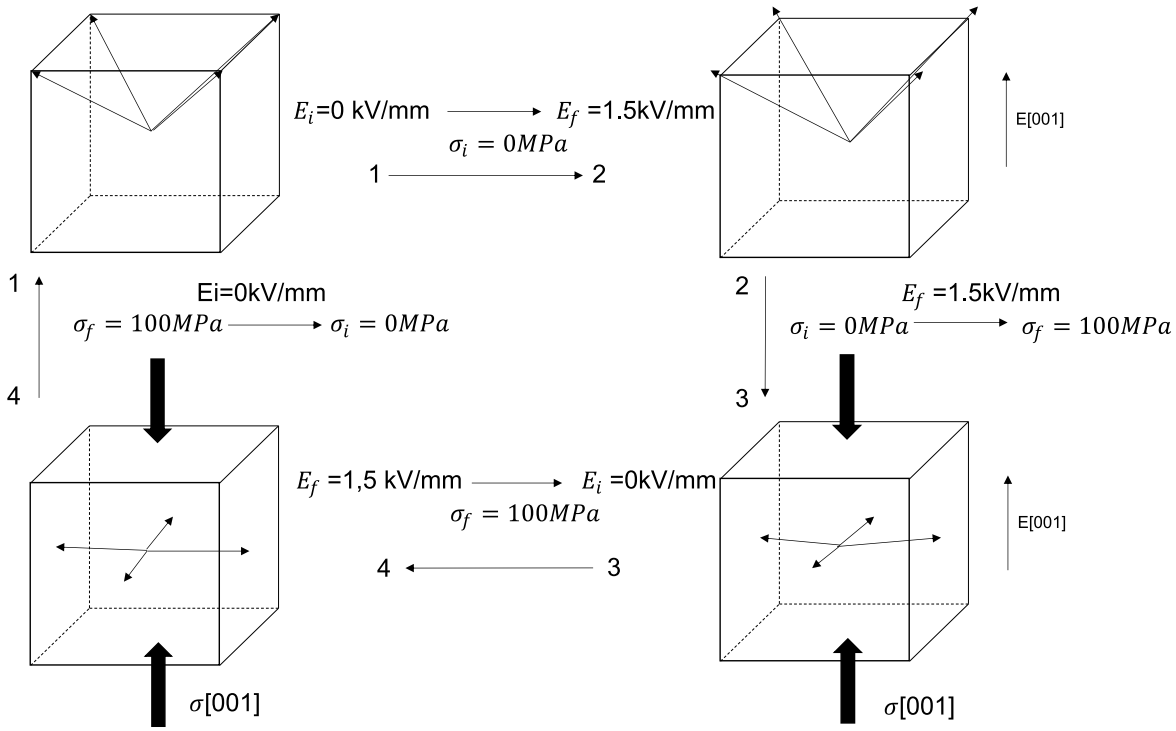

FIGURE 3.10: Polarization mechanisms during an Ericsson cycle under high levels for PZN-8PT

Thèse accessible à l'adresse : https://theses.insa-lyon.fr/publication/2024ISAL0017/these.pdf © [G. Taxil], [2024], INSA Lyon, tous droits réservés

The spontaneous polarization among ferroelectric materials, typically ranges from 0.15 to 0.4 C/m^2 [Dam98; Won+08]. However, it becomes apparent that if the electric field were sufficiently high to fully saturate the material and the mechanical stress were large enough to completely depolarize it, the resulting converted energy would be fairly similar across all materials. However, in this work, both the electric field and mechanical stress were not sufficient to reach these ideal conditions. This leads to a ranking of materials in terms of converted energy, varying by a factor of four, from the lowest to the highest. This ranking was particularly pronounced with the phase transitions induced by the mechanical stress. It is simple to estimate that with an applied electric field value of 1.5 kV/mm and a saturation polarization of 0.4 C/m^2, the maximum attainable energy density would be $600mJ/cm^3$. However, the experimental results ranged from 50 mJ/cm^3 to 236 mJ/cm^3 at 100MPa. The latter represents nonetheless 40% of the ultimate energy density.

As detailed in the previous section, the limitation of the electric field was motivated by safety reasons and by possible future realistic devices. However it can be noted that the output energy was linked with the chosen electric field in the Ericsson cycle. Indeed, doubling the electric field would approximately double the energy density. The constraint on the electric field was intrinsically tied to the dielectric strengths of the materials. The dielectric strength is correlated with the likelihood of encountering defects in ceramics and single crystals. For bulk ceramics, typical values range from 5 kV/mm to 15 kV/mm [Hae99; GM59; Yan+04] which can be even higher for single crystals [PS97b]. Then the electric field limit of 1.5 kV/mm could potentially be increased up to 3 to 10 times higher for particular materials. However this could lead to a significant reduction in fatigue life [HLO05] which is something to avoid for real applications. Particularly, with devices designed that aim at replace the use of batteries.

When it comes to the limit in terms of mechanical stress, the concurrent application of an electric field and stress has the potential to induce premature fatigue, even with stress levels as low as 100 MPa [MK94]. Furthermore, increasing the stress will not be efficient when passing a certain threshold corresponding to the required stress for depolarizing the sample. This threshold was already reached with stress as low as 100MPa for PZN-8PT.

As a result, in this study, the electric field was restricted to 1.5 kV/mm, and the stress was set at 100 MPa. Conducting more comprehensive analyses will be required to investigate the upper limits of various materials. Nevertheless, the significant disparities in energy density among the tested materials highlight the importance of material selection for specific applications and the interest of polarization non-linearities for energy harvesting.

3.3 <001> oriented crystals investigation

The previous section investigated the electromechanical energy conversion potential of various ferroelectric materials. The non-linearities induced by applied stress have shown to be very attractive for energy harvesting. PMN-25PT and particularly PZN-8PT cut along their $[001]_c$ direction displayed the most outstanding properties in terms of energy density. This section propose to investigate more these highly piezoelectric perovskites single crystals. The modeling approach for mechanical

Thèse accessible à l'adresse : https://theses.insa-lyon.fr/publication/2024ISAL0017/these.pdf © [G. Taxil], [2024], INSA Lyon, tous droits réservés

energy harvesting presented in Chapter 2 along with experimental measurements is performed to understand the ideal inherent polarization mechanisms for energy harvesting application via Ericsson cycles. It can be noted that this work is inspired by the article published in Acta Materialia [Tax+23].

3.3.1 Polarization under stress

PMN-25PT and PZN-8PT were initially subjected to various static stress levels (ranging from 0 to 100 MPa). Bipolar loops were measured at room temperature with electric fields spanning from -1500 kV/m to 1500 kV/m, all at a frequency of 1 Hz. Results are depicted in Figure 3.11(a) and (b). With the same justifications as in the previous section, the electric field was again limited to 1500kV/m. The input voltage consisted of a sinusoidal signal with three cycles as it was illustrated in Figure 3.6(a). It is worth observing that the first bipolar hysteresis loop does not consistently coincide at 0 V/mm. This phenomenon arises from the repolarization process occurring at the start of the first cycle, given that the initial polarization state depends on the material's history. For data analysis, only cycles 2 and 3 were considered due to their independence from this repolarization process.

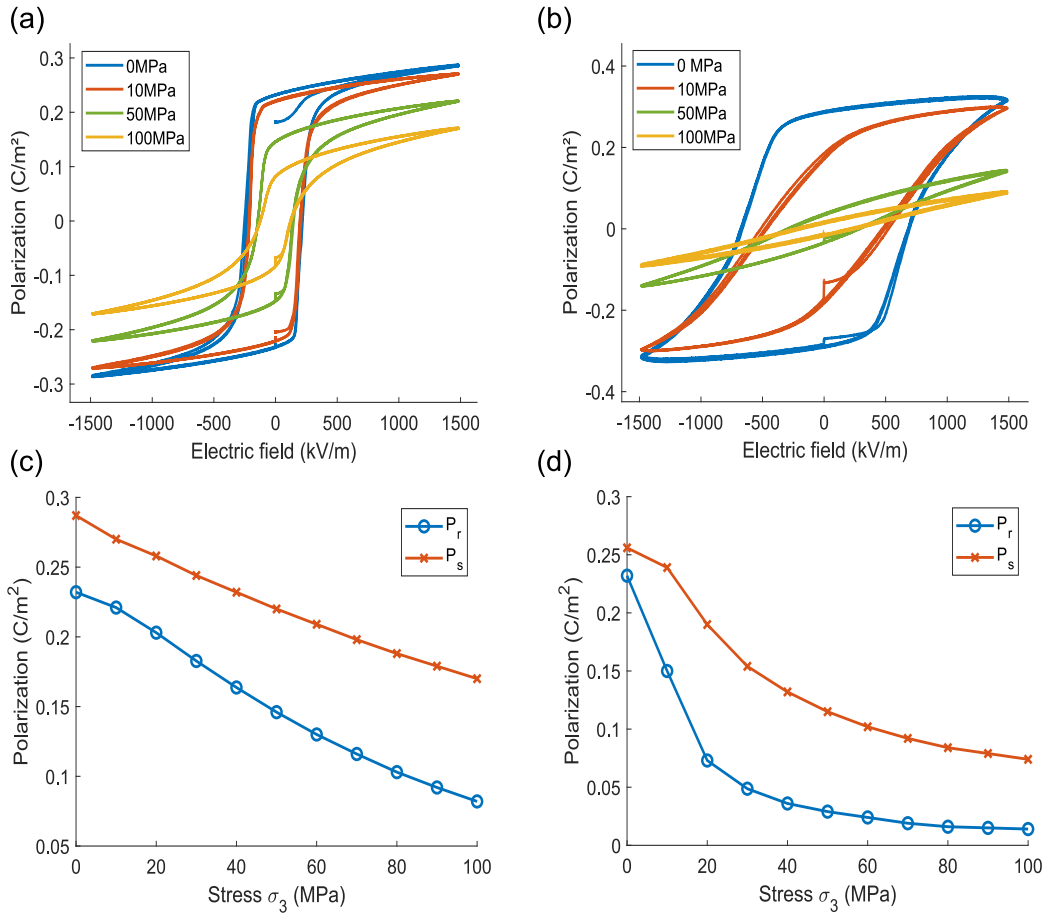

FIGURE 3.11: Bipolar hysteresis loops under different uniaxial stress [Tax+23]; (a) PMN-25PT (b) PZN-8PT. Remnant and saturation polarization under different uniaxial stress [Tax+23]; (c) PMN-25PT; (d) PZN-8PT.

Thèse accessible à l'adresse : https://theses.insa-lyon.fr/publication/2024ISAL0017/these.pdf © [G. Taxil], [2024], INSA Lyon, tous droits réservés

The associated remnant and saturation polarization as functions of uniaxial stress are presented in Figure 3.11(c) and (d). In both PMN-25PT and PZN-8PT, the coercive field (E_c) decreases with increasing applied stress. This phenomenon is well-documented and has been observed previously [Xue+15; WZL08]. The variation in polarization of both materials with applied stress exhibits distinct behaviors. Specifically, PMN-25PT demonstrates a linear response of remnant and saturation polarizations with applied stress, which implied a constant d_{33} response to stress. However, for PZN-8PT, the polarization response under and without an applied electric field is highly nonlinear for uniaxial stress in the 0-40 MPa range and becomes quasi-linear in the 40-100 MPa range. The significant non-linearity within the 0-40 MPa range indicates that d_{33} is not constant with stress. Defining d_{33} as a piezoelectric coefficient here is complicated because the large polarization variations originate from in-plane polarization switching.

3.3.2 Polarization vs temperature

The crystals were also investigated at different temperature from 20°C to 140°C. Bipolar hysteresis loops were performed under stress free conditions with identical electric field limits at different temperature as shown in Figure 3.12 (a) and (b). The remnant and saturation polarizations depending on all the tested temperatures are represented in Figure 3.12(c) and (d). It can be observed for PMN-25PT that the coercive field declines with increasing temperature, which is typically associated with an increase of piezoelectric properties [Yan+22b]. This phenomenon is well

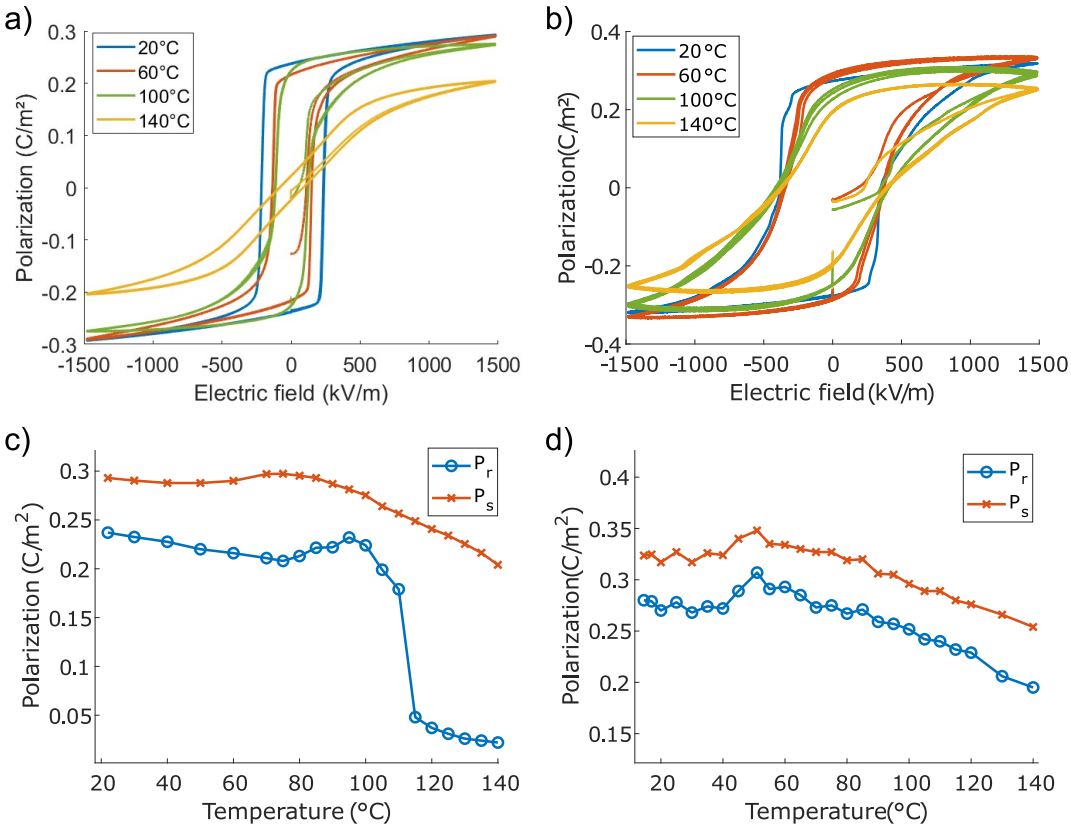

FIGURE 3.12: Bipolar hysteresis loops under different temperatures; (a) PMN-25PT (b) PZN-8PT. Remnant and saturation polarization under different temperatures; (c) PMN-25PT; (d) PZN-8PT.

Thèse accessible à l'adresse : https://theses.insa-lyon.fr/publication/2024ISAL0017/these.pdf © [G. Taxil], [2024], INSA Lyon, tous droits réservés

explained by the reduction of the energy barrier at elevated temperatures, allowing domains to reorient with a lower electric field. However, PZN-8PT displayed a distinct behavior, with E_c remaining constant from 20 to 140°C. Additionally, it is worth noting that dielectric losses increased at higher temperatures. The remnant and saturation polarization evolve differently with temperature in both crystals. For PMN-25PT, both P_r and P_s decrease from 20°C to respectively 80°C and 70°C where a polarization increase is then observed. This is explained by the R-T transition and its associated polarization augmentation in <001> oriented crystals. The polarization under electric field (P_s) transits more easily due to the application of the electric field in the $[001]_c$ direction (T phase direction) and was already reported [Li+20a]. After that, the remnant polarization exhibited a sharp decrease at the FE-PA transition, occurring at approximately 110°C. However the crystal under electric field remained ferrolectric and presents a slight decrease from 80°C to 140°C.

Concerning PZN-8PT, P_r and P_s have the same trend at all temperatures. From 20°C to 50°C, the polarizations remain constants. After that, the R-T transition occurs resulting in a polarization increase. Finally, both polarizations decrease slowly until 140°C without transiting from the ferroelectric to the paraelectric as T_c =160°C in PZN-8PT.

3.3.3 Polarization under different thermodynamic conditions

To have a deeper understanding of the materials response and identify the most effective polarization mechanisms for energy harvesting, experimental results for the polarization component P_3 are presented in relation to the applied electric field E_3 and uniaxial stress σ_3 for the <001> PMN-25PT single crystal at various temperatures. These results are depicted in Figure 3.13 (a), (c), and (e), while their corresponding simulated phase diagrams using Landau-Devonshire theory are shown in Figure 3.13 (b), (d), and (f).

At room temperature, experimental results (Figure 3.13 (a)) reveal a flat polarization surface, indicating a fully linear response of the material to the applied stress and electric field. PMN-25PT at this temperature exhibits a rhombohedral (R) phase, consistent with the theoretical model predictions. However, the simulation suggests an in-plane switching of polarization perpendicular to E_3, denoted as T$\perp$, under high stress and low electric field. However, this behavior was not observed experimentally as a higher uniaxial stress was required to induce such a transition.

At 50°C, the material still maintains its rhombohedral phase. The modeling predicts a phase transition from rhombohedral to an in-plane phase, either tetragonal or orthorhombic. This transformation is observed in Figure 3.13 (c), with a nonlinear response of polarization within the region defined by electric fields from 0 to 500 kV/m and stresses from 50 to 100 MPa, corresponding to low electric field and high stress conditions. This result corresponds with prior reports in the literature for $(1-x)$PMN $-$ xPT [WZL08; MLL04; MLL05].

As the temperature increases from 20°C to 50°C, both experimental and simulated results indicate a decrease in spontaneous polarization due to rising entropy, inducing disorder. However, from 50°C to 80°C, both measurements and calculations show an increase in spontaneous polarization. This suggests the emergence of a tetragonal phase in place of the rhombohedral phase. In particular, the z-projection

Thèse accessible à l'adresse : https://theses.insa-lyon.fr/publication/2024ISAL0017/these.pdf © [G. Taxil], [2024], INSA Lyon, tous droits réservés

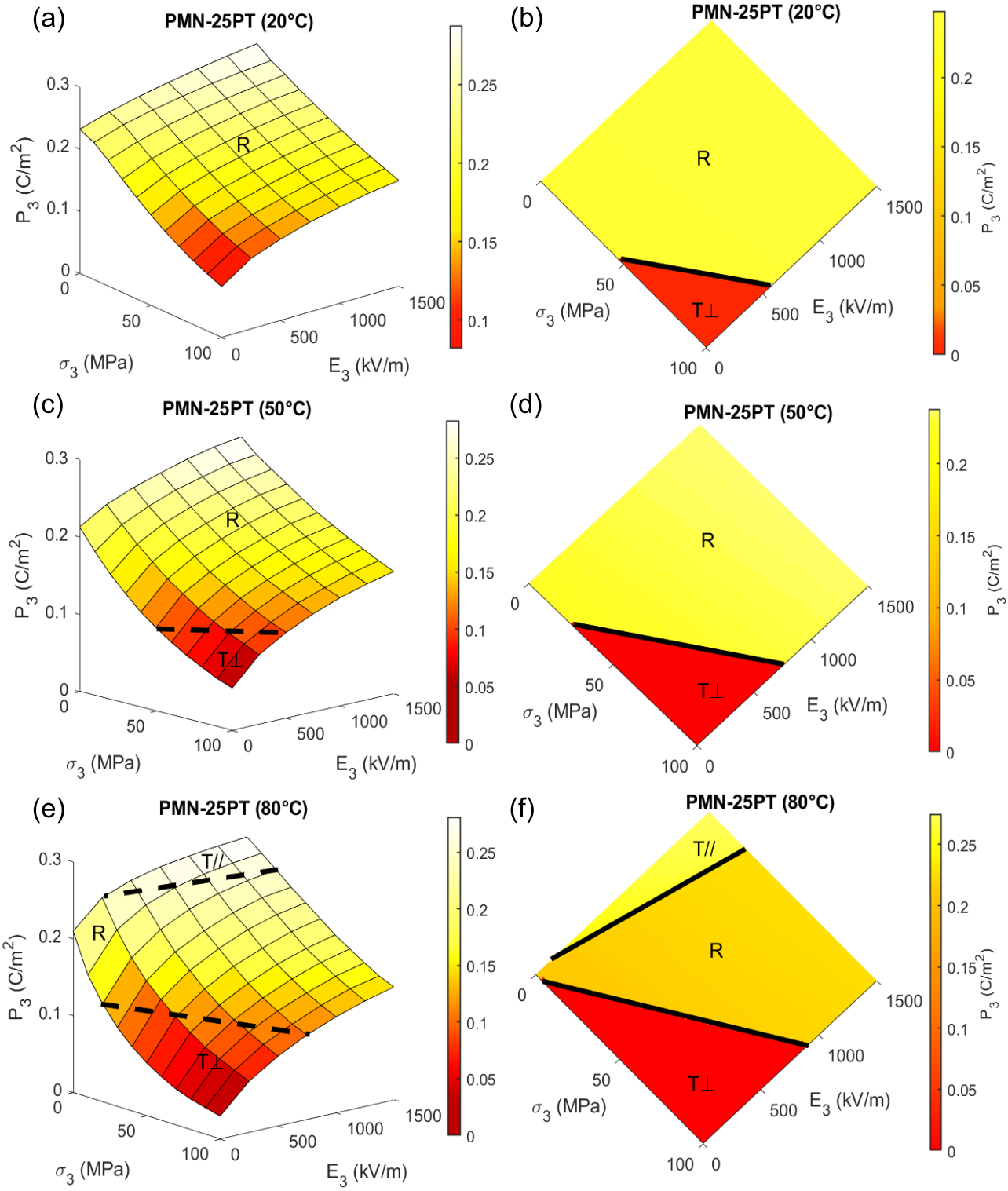

FIGURE 3.13: Plot of the component of polarization P_3 depending of uniaxial stress σ_3 and electric field E_3 for PMN-25PT [Tax+23]. (a) Experiment at 20°C; (b) Modeling at 20°C; (c) Experiment at 50°C; (d) Modeling at 50°C; (e) Experiment at 80°C; (f) Modeling at 80°C.

Thèse accessible à l'adresse : https://theses.insa-lyon.fr/publication/2024ISAL0017/these.pdf © [G. Taxil], [2024], INSA Lyon, tous droits réservés

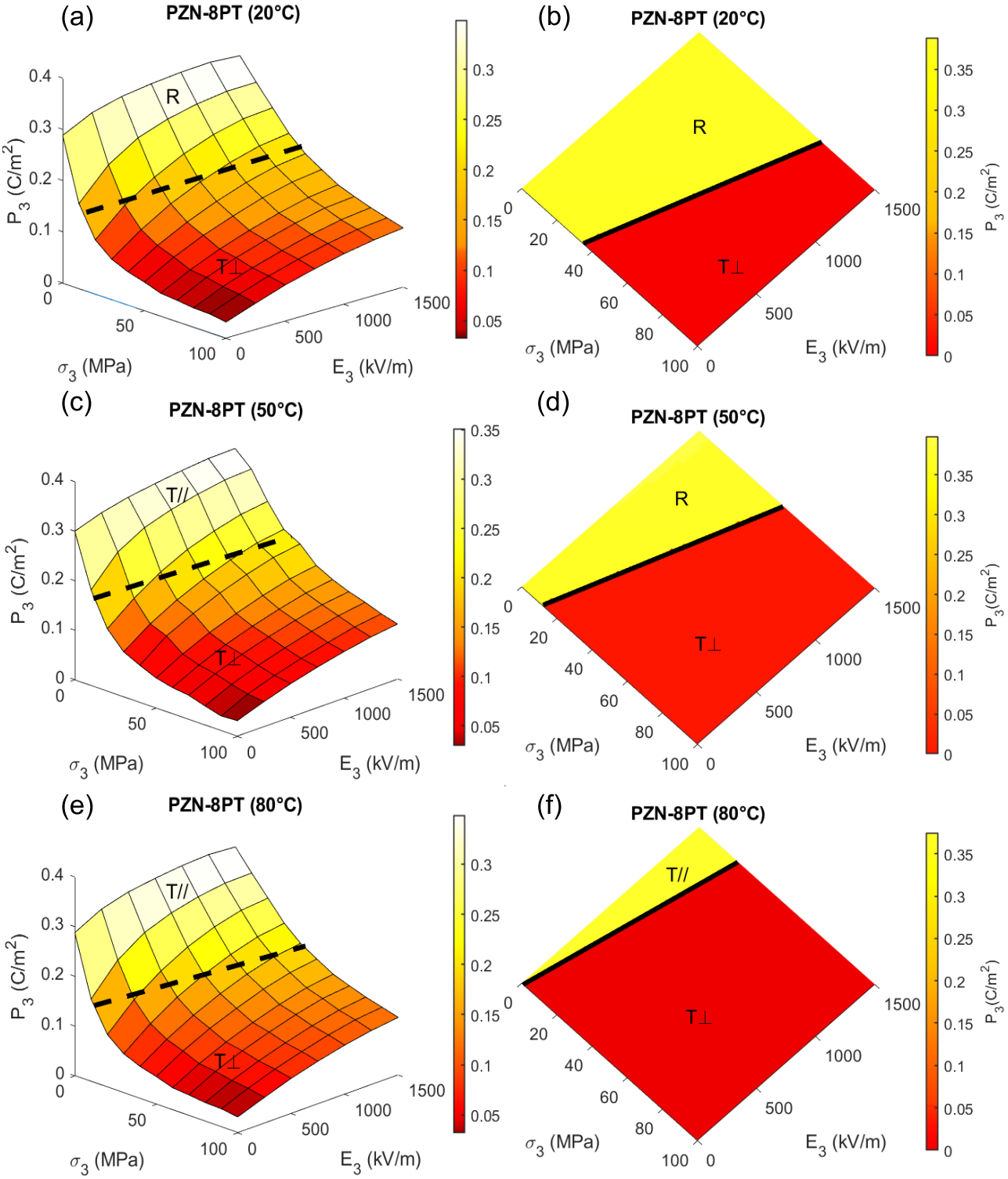

FIGURE 3.14: Plot of the component of polarization P_3 depending of uniaxial stress σ_3 and electric field E_3 for PZN-8PT [Tax+23]. (a) Experiment at 20°C; (b) Modeling at 20°C; (c) Experiment at 50°C; (d) Modeling at 50°C; (e) Experiment at 80°C; (f) Modeling at 80°C.

Thèse accessible à l'adresse : https://theses.insa-lyon.fr/publication/2024ISAL0017/these.pdf © [G. Taxil], [2024], INSA Lyon, tous droits réservés

of polarization is measured and calculated in the cubic basis, given that the crystal is oriented along <001>. Therefore, the polarization projection is higher for the tetragonal phase since its spontaneous polarization aligns with the $[001]_c$ direction ($[111]_c$ for the rhombohedral phase).

The measured polarization at 80°C exhibits a significant increase in the 0 to 500 kV/m range compared to the 500 to 1500 kV/m range in Figure 3.13 (e). This implies a rhombohedral-to-tetragonal transition with the electric field, a phenomenon previously observed and predicted [MLL05; Li+20a; Kim+22]. This R-T transition is further confirmed by the Landau-Devonshire theory, where it emerges under the application of the electric field at low stress and is denoted as T// (polarization aligns with the electric field) in Figure 3.13 (f). Under high stress and low electric field, both experimental and simulated results still present a 90° switching of polarization. The region where the polarization is in-plane appears to expand from 50°C to 80°C in the experimental data. This temperature-dependent shift in the polarization adopting a phase perpendicular to the applied electric field direction is also predicted by the calculations. Consequently, PMN-25PT undergoes a transition with increasing temperature, evolving from a pure linear regime of polarization response to stress and electric field to a more complex behavior with the emergence of the T// phase and in-plane phases (T⊥).

Similar investigations were conducted on PZN-8PT single crystal at different temperatures under high uniaxial stress σ_3 and electric field E_3, as illustrated in Figure 3.15. It displayed a different response in terms of the polarization projection P_3 compared to PMN-25PT. At 20°C, a strong non-linear response of polarization was observed under low stress, ranging from 0 to 50 MPa, and even under high applied electric fields, as shown in Figure 3.15(a). From 50 to 100 MPa, polarization exhibited a linear variation with electric field and stress. This linear behavior can be attributed to a transverse dielectric response of the material in the $[001]_c$ direction, as the spontaneous polarization switched to a 90° ferroelectric state. Theoretical calculations presented in Figure 3.15(b) predicted a rhombohedral-to-tetragonal (R-T) transition with an in-plane orientation of the polarization under high stress and agreed well with the experimental results.

Interestingly, there was no significant change in the response of PZN-8PT with temperature. Experimental curves remained quite similar between 20°C and 50°C (Figure 3.15 (a) and (c)). However, literature [DDS06a] and experiment results suggest that the material is in a tetragonal state at 50°C, as indicated by the slightly higher remnant polarization at 0 MPa compared to that at 20°C, which is typical of R-T transitions in <001> oriented crystals. The modeling results, on the other hand, indicated that the crystal remained in a rhombohedral state, as the R-T transition was predicted to occur at 60°C with the Landau coefficients used.

Similarly to PMN-25PT, the simulation suggested an easing of in-plane domain switching with increasing temperature (Figure 3.15 (d)). When examining the characterization results at 80°C, it was evident that the response of PZN-8PT with stress and electric field remained largely unchanged with temperature. Experimental curves for PZN-8PT at different temperatures were nearly identical (Figure 3.15 (a), (c), and (e)). The spontaneous polarization at 80°C exhibited a slight decrease compared to 50°C, attributable to increased disorder. The model suggested that the material was

Thèse accessible à l'adresse : https://theses.insa-lyon.fr/publication/2024ISAL0017/these.pdf © [G. Taxil], [2024], INSA Lyon, tous droits réservés

in a tetragonal state and switched out to a perpendicular tetragonal state with low applied stress, regardless of the applied electric field.

3.3.4 Operating temperature for energy harvesting

The investigation initially focused on the polarization dependence with uniaxial stress, electric field, and temperature, which plays a crucial role in determining the energy harvesting capabilities. Subsequently, the energy conversion of PMN-25PT and PZN-8PT single crystals was assessed using Ericsson cycles. The assessment of energy harvesting capabilities was carried out by analyzing the descending curves of bipolar loops at 0 and 100 MPa, as previously discussed. It is worth noting that there are discrepancies between the evaluation of harvested energy using the descending curves of bipolar loops and real Ericsson cycles. However, it is important to clarify that the modeled Ericsson cycles based on Landau-Devonshire theory correspond with these descending curves of bipolar loops. Therefore, the term "Ericsson cycle" will refer to the cycle enclosed within the descending curves of bipolar loops.

This evaluation was performed at different operating temperatures while maintaining consistent Ericsson cycle conditions, including stress ranging from 0 to 100 MPa and an electric field spanning from 0 to 1500 kV/m. The bipolar hysteresis curves at 0 and 100 MPa, along with their associated Ericsson cycles, are presented for both PMN-25PT and PZN-8PT at various temperatures in Figure 3.15. Then, corresponding energy density is provided depending on the operating temperature of the cycle based on experimental and simulated results using Landau-Devonshire approach (Figure 3.16).

The energy density of PMN-25PT (Figure 3.16 (a) and (b)) exhibits an ascending trend from room temperature to 80°C, which corresponds to the rhombohedral-tetragonal (R-T) transition temperature. Within this temperature range, the energy density increases from 210 mJ/cm^3 to 260 mJ/cm^3. This elevation in energy density for PMN-25PT can be attributed to the easier switching of 90° domains with stress as the temperature rises, as observed in Figure 3.13. These in-plane switches of polarization result in a more significant variation in polarization with increasing stress, thereby expanding the cycle area (and the harvested energy). Modeling predicts a more substantial increase in harvested energy at 60°C due to the appearance of the tetragonal phase when a sufficient electric field is applied. This increase is barely visible in the experimental curve, with a slightly more pronounced rise in energy around 70°C. The maximum energy density is observed at 80°C in both the experimental data and the modeling, coinciding with the transition to a fully tetragonal phase in the material. In the tetragonal phase, the remnant polarization is maximized for <001>-oriented crystals, leading to the greatest possible polarization variation during in-plane switching and, consequently, the highest energy density at the R-T transition. Afterwards, the energy density remains nearly constant experimentally from 80°C to 100°C and from 80°C to 115°C in the modeling. This behavior results from the compensation of two phenomena. Firstly, the drop in spontaneous polarization, driven by increased entropy, results in reduced polarization variations, leading to a decrease in harvested energy. However, the facilitation of in-plane polarization states under stress with rising temperature mitigates this effect, resulting in a nearly constant evolution of energy density within this temperature range. In the final temperature range, from 110°C to 140°C, there is a significant decrease in energy density, declining from 250 mJ/cm^3 to 110 mJ/cm^3. This decrease is attributed to the

Thèse accessible à l'adresse : https://theses.insa-lyon.fr/publication/2024ISAL0017/these.pdf © [G. Taxil], [2024], INSA Lyon, tous droits réservés

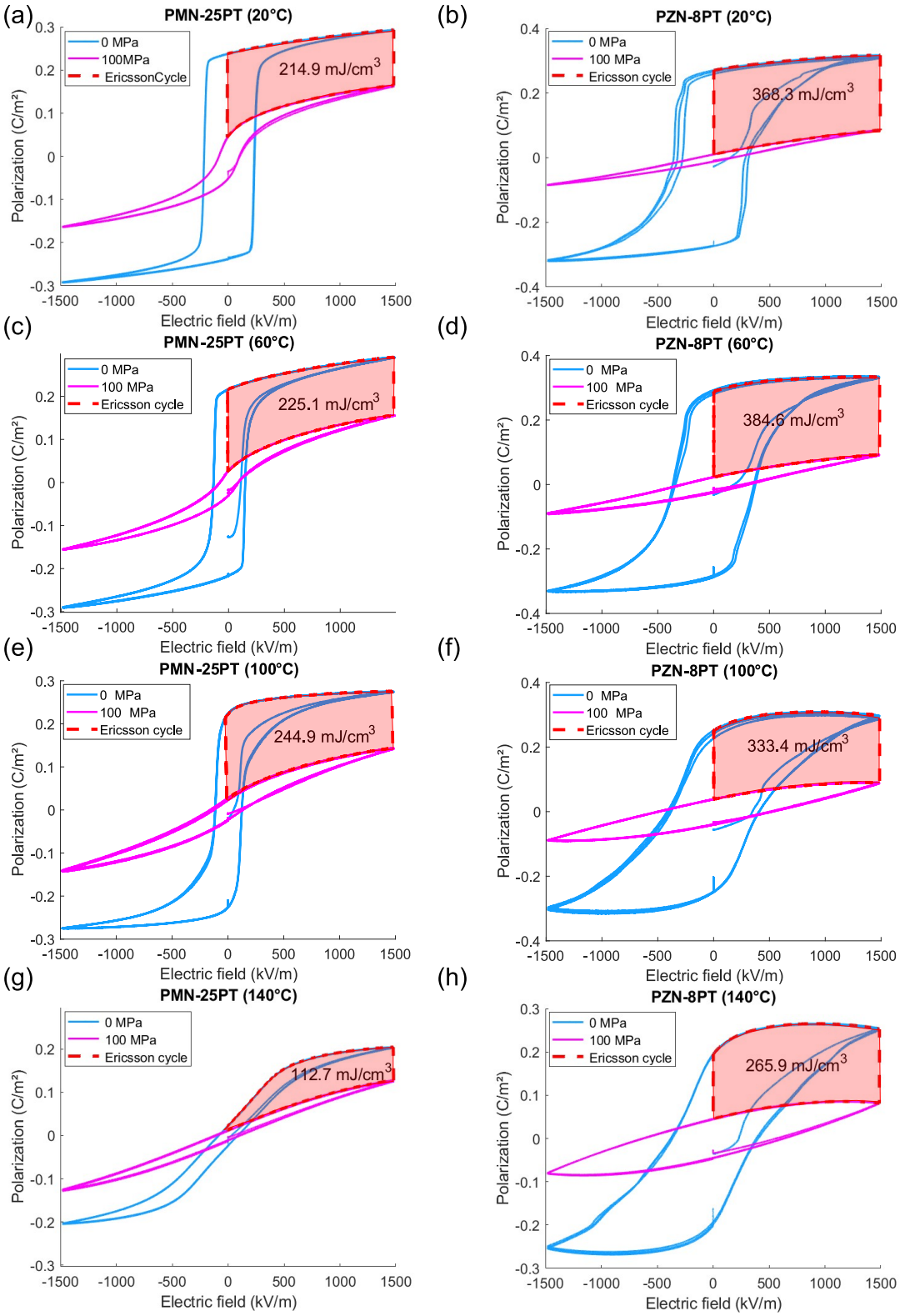

FIGURE 3.15: Bipolar loops of PMN-25PT and PZN-8PT with their associated Ericcson cycle at different temperature [Tax+23]. (a) PMN-25PT at 20°C; (b) PZN-8PT at 20°C; (c) PMN-25PT at 60°C; (d) PZN-8PT at 60°C; (e) PMN-25PT at 100°C; (f) PZN-8PT at 100°C ; (g) PMN-25PT at 140°C; (h) PZN-8PT at 140°C.

Thèse accessible à l'adresse : https://theses.insa-lyon.fr/publication/2024ISAL0017/these.pdf © [G. Taxil], [2024], INSA Lyon, tous droits réservés

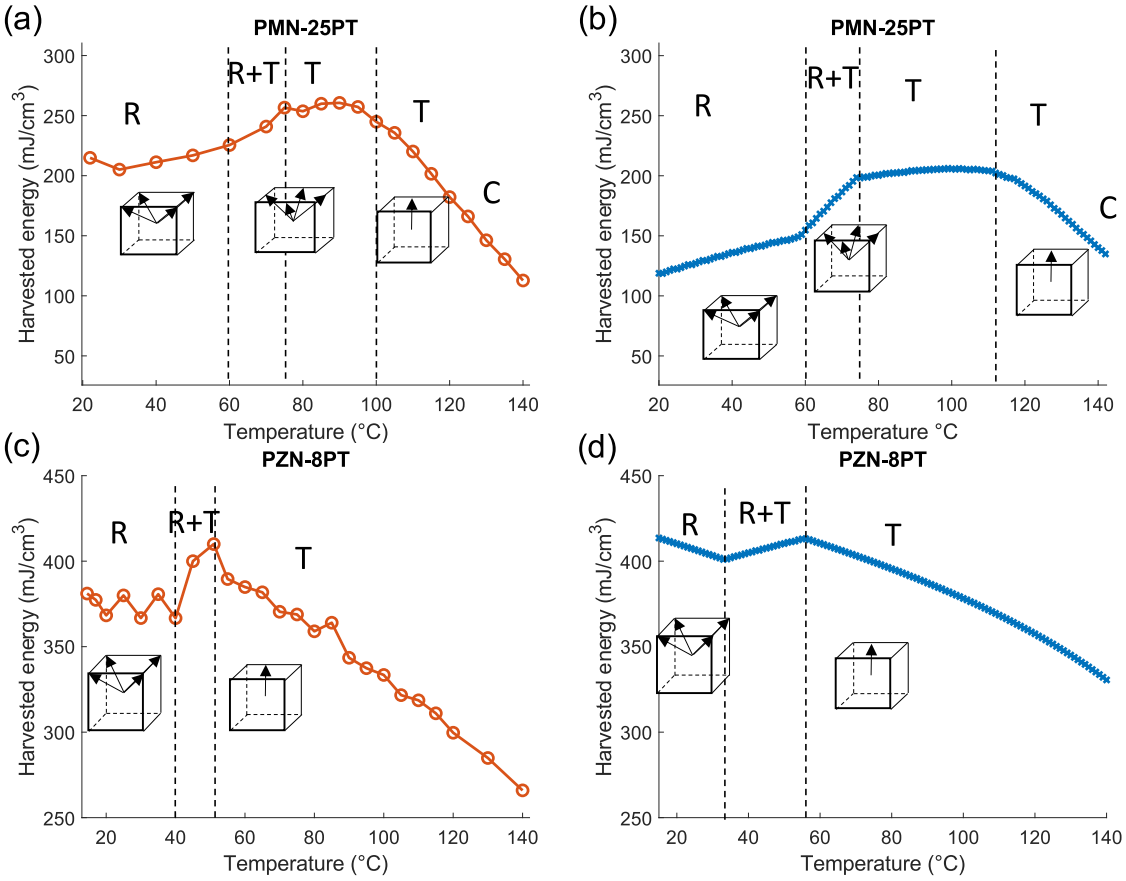

FIGURE 3.16: Plot of the energy density depending of the temperature of work of the cycle [Tax+23]. (a) Experiment for PMN-25PT; (b) Modeling for PMN-25PT; (c) Experiment for PZN-8PT; (d) Modeling for PZN-8PT.

reduction in polarization as the material crosses the ferroelectric-paraelectric transition of PMN-25PT. A Curie temperature of 110°C has been measured and reported previously [Zha+05; Per+13]. The modeling predicts a similar trend for PMN-25PT but for slightly higher temperatures.

Regarding PZN-8PT (Figure 3.16 (c) and (d)), it is important to note that its energy density is approximately twice than that of PMN-25PT, as it was reported in the previous section. PZN-8PT exhibits a distinct trend with changing temperature compared to PMN-25PT. Experimental results indicate a nearly constant energy harvested of approximately 375 mJ/cm^3 from 20°C to 40°C. Afterward, energy density increases from 40°C until 55°C, where it reaches a peak of 410 mJ/cm^3. This upward trend is also observed in simulations and, like PMN-25PT, it originates from the R-T transition under an electric field, which increases the spontaneous polarization. However, in simulations, for the 20-40°C temperature range, a decrease in harvested energy is reported due to the reduction of polarization in the rhombohedral phase as the operating temperature rises. Strangely, this decrease was not observed in experimental results, where the energy density remained nearly constant. The exact reasons for this discrepancy are still unclear. Similar to PMN-25PT, energy conversion is maximized at the R-T transition due to the same underlying reasons. Notably, the maximum energy density of 410 mJ/cm^3 is exceptionally high. It appears that no previous work has reported such a high energy conversion with these levels of

Thèse accessible à l'adresse : https://theses.insa-lyon.fr/publication/2024ISAL0017/these.pdf © [G. Taxil], [2024], INSA Lyon, tous droits réservés

electric field and uniaxial stress. However, the work of [PCV14a; PCV14b] can be noted, where the authors achieved higher energy conversion ($\approx 500 mJ/cm^3$) with the Ericsson cycle but at much higher stress levels (approximately 400 MPa) and electric field levels (approximately 2000 to 6000 kV/m). After 55°C, both the model and experiments showed a declining trend in energy density until 140°C. This decline is again explained by the reduction of spontaneous polarization as disorder and entropy increase with temperature. It is worth noting that the experimental curve exhibits a faster rate of decay compared to the theoretical one. This difference could be attributed to the more pronounced dielectric losses at higher temperatures for PZN-8PT, as observed in Figure 3.15 (a),(d),(f), and (h).

Both materials exhibit different polarization mechanisms involved in the various steps of the Ericsson cycle. These mechanisms evolve with temperature and account for the distinct trends in the cycle's performance and their energy density values. For PMN-25PT, an illustration of the evolution of polarization during the different Ericsson cycle processes is provided in Figure 3.17(a) and (b) at 20°C and 60°C, respectively.

At 20°C, the crystal remains rhombohedral throughout all the steps. The material response is purely linear with applied stress and electric field, resulting in a lack of substantial non-linearities. Consequently, the output energy does not exhibit outstanding performance. At 60°C, PMN-25PT displays a much more complex behavior. The crystal starts in a rhombohedral state and transits to a tetragonal phase with the application of an electric field. Applying uniaxial stress at high electric field still does not induce in-plane switching of polarization. However, this switching becomes possible at lower electric field levels, leading to increased polarization variation and, consequently, higher harvested energy.

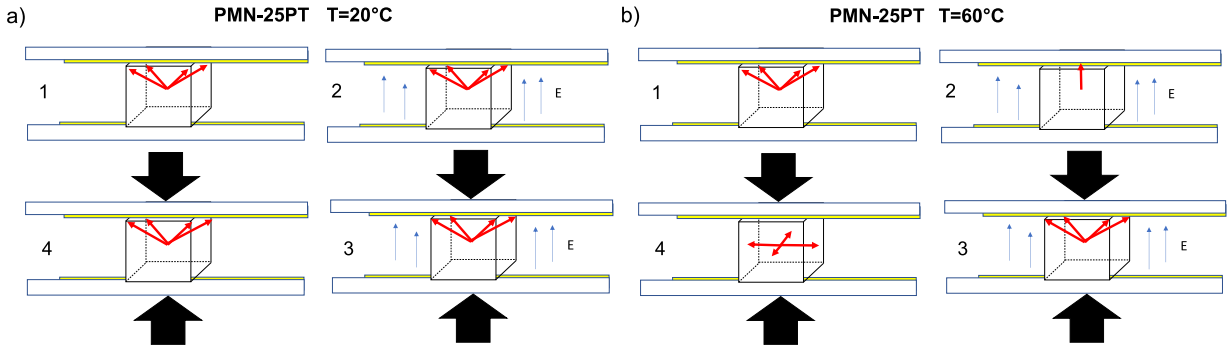

FIGURE 3.17: Schematic illustration of the polarization mechanisms during an Ericsson cycle for PMN-25PT; (a) At 20°C; (b) At 60°C.

Regarding PZN-8PT, this crystal exhibits different behavior compared to PMN-25PT. The illustration for PZN-8PT at 20°C and 60°C is respectively provided in Figure 3.18(a) and (b). At 20°C, the crystal remains rhombohedral during the 1-2 process. However, when uniaxial stress is applied, the material adopts an in-plane phase even at high electric field. The non-linearities induced by these 90° switching explain the especially high output energy in PZN-8PT <001> oriented single crystals. At a temperature of 60°C, PZN-8PT is fully tetragonal, as the R-T transition occurs around 50°C. The in-plane switching occurs again at high electric field, and the energy density is still especially high at this temperature, where dielectric losses

Thèse accessible à l'adresse : https://theses.insa-lyon.fr/publication/2024ISAL0017/these.pdf © [G. Taxil], [2024], INSA Lyon, tous droits réservés

are low.

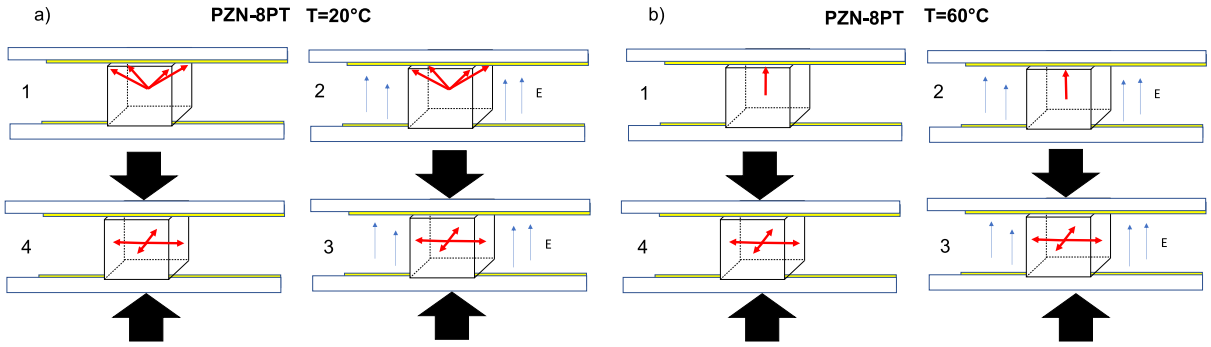

FIGURE 3.18: Schematic illustration of the polarization mechanisms during an Ericsson cycle for PZN-8PT; (a) At 20°C; (b) At 60°C.

The different results suggest that optimal operating temperature occurs when the crystal transits to a fully tetragonal state. This observation may hold true for all <001> oriented ferroelectric crystals when subjected to sufficient uniaxial compressive stress, enabling in-plane switching. These 90° switchings induce more significant polarization variations along the spontaneous polarization direction. An interesting aspect of these ferroelectric relaxors is the potential to tailor the ferroelectric-to-ferroelectric (FE-FE) temperature transition by adjusting the mixing proportions. This, aspect could be employed for future engineering applications and enhance the harvested energy.

3.4 <111> PMN-30PT

In this section, few results on the experimental characterization of PMN-30PT with a cut along the $[111]_c$ direction will be presented. However, this work is still in progress, and additional data will be necessary to properly finish this study. As it was previously mentioned, the d_{33} piezoelectric coefficient of 4R <001> oriented crystals is largely superior to the one of 1R <111> oriented crystals. The results of the previous section showed that the optimal operating temperature for Ericsson was not necessarily equivalent to the one optimizing the d_{33}. Moreover, in chapter 2, the simulated piezoelectric coefficients present a large anisotropy depending on the orientation. However, when Ericsson cycles were simulated, the harvested energy was much more homogeneous depending on the crystal orientation. This section will then presents the energy characterization of <111> oriented crystal for mechanical energy harvesting. The results will be compared to those obtained from PMN-25PT <001> oriented crystals and the simulation results of Chapter 2.

PMN-30PT <111>-oriented crystals were purchased from MSE Supplies. The surface of the sample was originally of $10 \times 10mm^2$. Samples were cut with a dicing machine DISCO DAD3240 and feature a surface of $5 \times 5mm^2$. The sample thickness was $0.5mm$ so the applied voltage was divided by two compared to the previous samples which displayed a 1mm thickness. Gold sputtered electrodes were deposited on the surfaces and samples were poled via bipolar hysteresis curve. The

Thèse accessible à l'adresse : https://theses.insa-lyon.fr/publication/2024ISAL0017/these.pdf © [G. Taxil], [2024], INSA Lyon, tous droits réservés

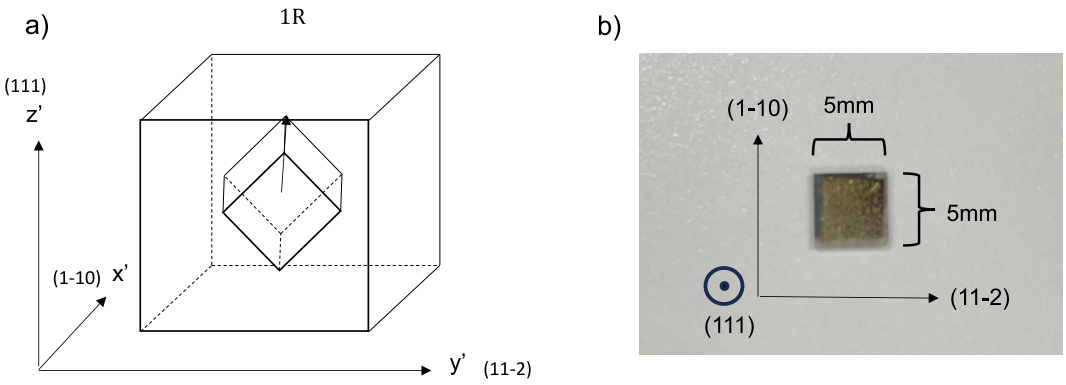

FIGURE 3.19: (a) Illustration of a 1R domain engineered crystal; (b) Photo of a sample of PMN-30PT <111>-oriented crystals.

experimental test-bench and methods were similar to the previous experimental investigations presented in the past section. An illustration of the 1R engineered domain along with a photo of the PMN-28PT sample are given in Figure 3.19 (a) and (b)

This experiment has been solely conducted at room temperature. Bipolar hysteresis curves ranging from $-1500kV/m$ to $1500kV/m$ at different level of stress were first evaluated as shown in Figure 3.20 (a). PMN-30PT with a <111> orientation displays a larger spontaneous polarization at 20°C compared to <001>-oriented crystals. Indeed, at 20°C the crystal exhibits a rhombohedral symmetry with a spontaneous polarization along the $[111]_c$ direction. Consequently, the polarization projection is higher in 1R crystals. This difference of remnant polarization between <001> and <111> oriented crystals is given by a factor $\sqrt{3}$ which corresponds to the projection of the polarization vector. It can also be noted that the coercive field is larger for <111> PMN-30PT ($Ec \approx 500kV/m$) compared to <001> PMN-25PT ($Ec \approx 200kV/m$)

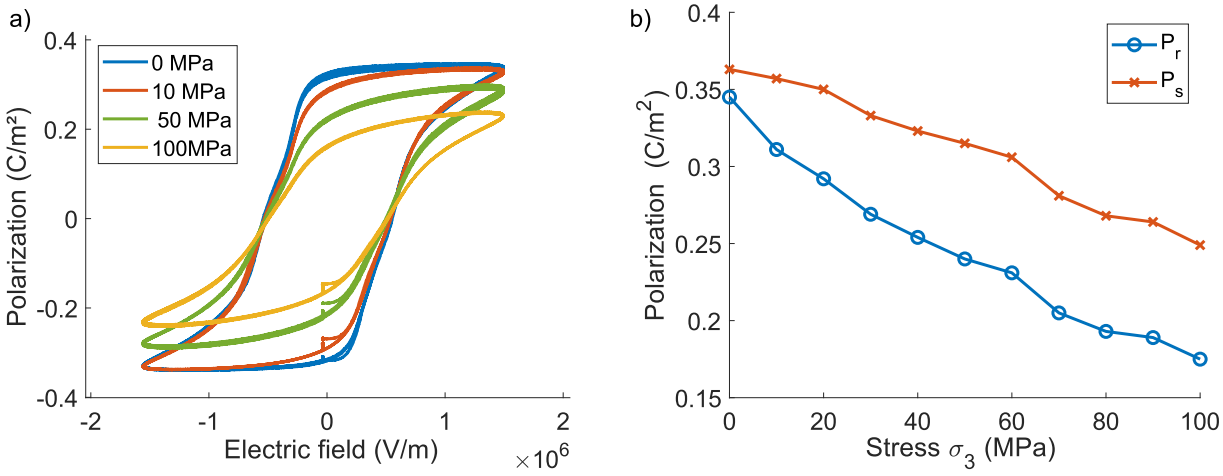

FIGURE 3.20: (a) Bipolar hysteresis loops under different uniaxial stress for PMN-30PT <111>-oriented crystal; (b) Remnant and saturation polarization under different uniaxial stress for PMN-30PT <111>-oriented crystal.

The remnant and the saturation polarizations under different uniaxal compressive stress are plotted in Figure 3.20(b). Like for PMN-25PT with a <001> orientation, P_r and P_s vary relatively linearly with applied stress. It can be observed that both

Thèse accessible à l'adresse : https://theses.insa-lyon.fr/publication/2024ISAL0017/these.pdf © [G. Taxil], [2024], INSA Lyon, tous droits réservés

polarizations exhibit a slightly non-linear variation around 60 and 80MPa which can be explained by a transition between a rhombohedral to a monoclinic phase. Such transition will induces a soft polarization variation as the polarization will not be in an in-plane state. However it is complicated to ensure of the occurrence of this transition and further experiments should be necessary to affirm it.

The energy densities via Ericsson cycles were then evaluated for <111> PMN-30PT. Again the Ericsson cycles were assumed to correspond to the descending curves of the bipolar hysteresis loops. This choice was motivated by the previous experimental campaign on <001>-oriented crystal and by the correspondence between the modeling approach via Landau-Devonshire theory and such descending curves. An illustration at room temperature of an estimated Ercisson cycle between 0 and $1500 kV/m$ and 0 and $100 MPa$ is given in Figure 3.21(a). In Figure 3.21(b), the harvested energy is given depending on different levels of applied stress for <001> PMN-25PT and <111> PMN-30PT. The two curves follow similar trend and almost identical values of energy density are obtained for all the different level of stress. It can be noted that at 10MPa, almost no output energy is obtained for <111>-oriented crystals compared to the <001> orientation. However, except from this point, the output energy values remain practically similar for higher stress levels. The fact that <111> and <001> orientations exhibit similar energy densities is quite surprising as the d_{33} for both orientations is very different. Indeed, the d_{33} for <001> oriented PMN-25PT is around ten times superior compared to the <111> orientation as it was reported in Table 1.2 and 3.1. However, it is worth remarking that the composition of PT were not exactly the same between the <001> orientation and the <111> ones. This can leads to some differences when comparing both materials responses. Nonetheless, the compositions are sufficiently close to establish a first comparison in terms of energy outputs.

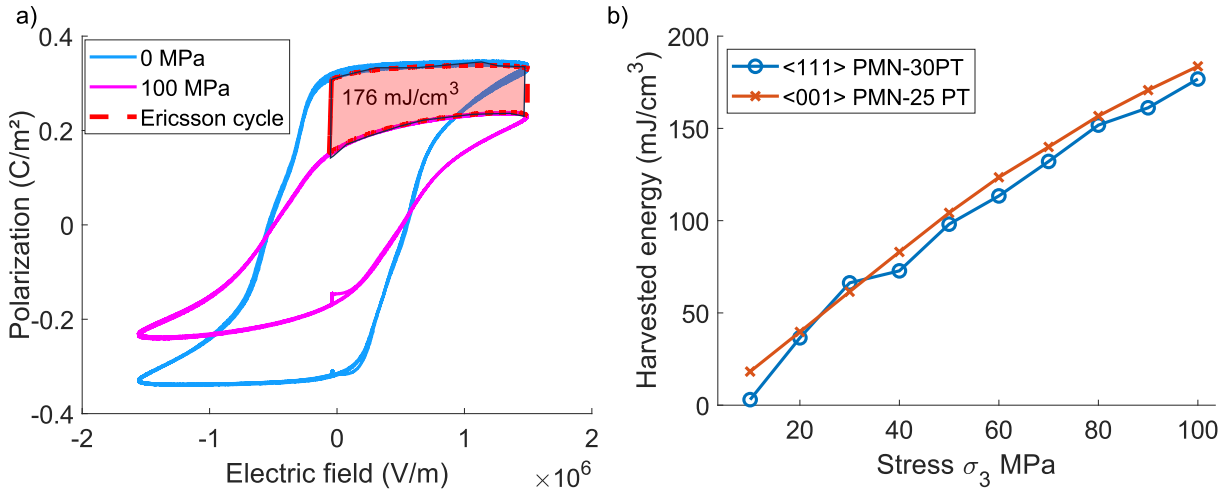

FIGURE 3.21: (a) Bipolar hysteresis loops of PMN-30PT <111>-oriented crystal with an associated Ericcson cycle at 100MPa; (b) Energy density as a function of applied stress for <001> PMN-25PT and <111> PMN-30PT.

The experimental and modeling results for the harvested energy at room temperature for Ericsson cycle with applied electric field ranging from 0 to $1500 kV/m$ and stress from 0 to $100 MPa$ are given for <001> PMN-25PT and <111> PMN-30PT

Thèse accessible à l'adresse : https://theses.insa-lyon.fr/publication/2024ISAL0017/these.pdf © [G. Taxil], [2024], INSA Lyon, tous droits réservés

in Figure 3.22(a). It can be seen that the modeling results for <001> PMN-25PT and <111> PMN-30PT are almost identical. The <111> orientation displays a slightly higher energy density of $145 mJ/cm^3$ compared to the <001> orientation which exhibits an energy density of $130 mJ/cm^3$. These differences are explained because the modeling predicts in-plane switching for low electric and high applied stress as it was shown in Figure. 3.13(b). Thus, larger polarization is induced in <111> oriented crystals and then larger harvested energy. The experimental results for both orientations display also similar energy outputs as it was reported in Figure 3.20. However, the converted energies for the <001> and the <111> orientation are higher compared to the modeling results with respectively an energy of $176 mJ/cm^3$ and $183 mJ/cm^3$. These differences can be explained by the low piezoelectric coefficients predicted by the phenomenological approach compared to the measured ones. These differences of piezoelectric coefficients between modeling and experiment can be observed in Figure 3.22 and was previously mentioned in this chapter.

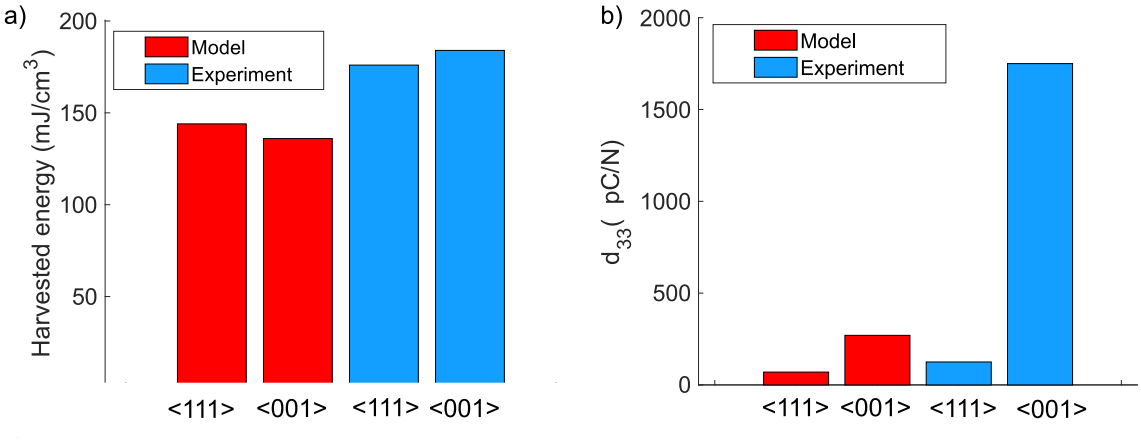

FIGURE 3.22: (a) histogram of the modeling and the experimental results of the energy harvested for an Ericsson cycle at 100MPa for <001> PMN-25PT and <111> PMN-30PT; (b) histogram of the modeling and experimental results of the d_{33} piezoelectric coeffificient for <001> PMN-25PT and <111> PMN-30PT

In Figure 3.22(b), the piezoelectric coefficients, specifically the d_{33}, is presented. These coefficients have been determined using the Landau-Devonshire theory and have also been experimentally measured for crystals oriented along <001> and <111> directions. As previously discussed, there is a significant contrast in the absolute values of the modeled and experimental results for the d_{33} coefficient. Nevertheless, the relative variation in d_{33} between the <001> and <111> crystal orientations is more consistent when comparing the simulation predictions with the experimental findings. These outcomes underscore the material differences in symmetry and response when considering high-level energy harvesting using Ericsson cycle versus low-level energy harvesting.

3.5 Summary

The primary focus of this chapter was to present the characterization results on ferroelectric materials when subjected to high electric field, high uniaxial stress, and varying temperatures and to compare these results with modeling predictions. Initially, we introduced the ferroelectric materials under investigation, along with a

Thèse accessible à l'adresse : https://theses.insa-lyon.fr/publication/2024ISAL0017/these.pdf © [G. Taxil], [2024], INSA Lyon, tous droits réservés

brief overview of some of their key properties. Subsequently, an overview of the experimental test setup was provided , highlighting the various techniques and procedures employed to carry out Ericsson cycle on these materials.

Then, the study focused on assessing the electromechanical energy conversion efficiency of different ferroelectric materials, such as hard PZT C203 ceramic, medium PZT C6 ceramic, soft PZT C9 ceramic, PMN 15 paraelectric ceramic as well as PMN-25PT and PZN-8PT single crystals. The characterizations were conducted at room temperature by performing real Ericsson cycle with successive steps under two distinct levels of compressive stress – intermediate (30 MPa) and high (100 MPa) – along with an electric field of 1500 kV/m. PZN-8PT <001>-oriented crystals demonstrated the highest potential for energy conversion, achieving an energy density of 235.6 mJ/cm^3 explained by non-linearties induced by the high compressive stress. Nevertheless, when exposed to high electric field and stress conditions, the energy conversion performance of PZT C9 ceramic was similar to PMN-25PT single crystal which displayed an energy density of 118.7 mJ/cm^3. This, result showed that under high levels, the energy density of the materials converges, emphasizing the differences between low level and high level energy harvesting.

After that, the work targeted solely PZN-8PT and PMN-25PT <001>-oriented crystals. This choice was driven by the desire to gain a deeper comprehension of how to leverage phase transitions and the associated polarization mechanisms in the context of high-level energy harvesting. Moreover, this investigation allowed applying the model developed in Chapter 2 on such crystals for a better comprehension on the material responses. The model was confronted to the experimental results on different levels of stress, electric field and temperature. Both experimental and theoretical results agreed well. Specifically, in-plane switching of polarization was reported in PZN-8PT at all considered temperatures and even under high electric field when subjected to compressive stress. For PMN-25PT, this in-plane switching occured but in more specific conditions (high temperature and low electric field), which was also predicted by the simulations. The ideal operating temperature for Ericsson cycle was determined for both crystals. The results pointed out the fact that the optimal performance is attained at the temperature at which the crystal becomes fully tetragonal. This observation has the potential to be extrapolated to all <001> oriented ferroelectric crystals under conditions of significant stress, allowing for in-plane switching. In fact, a more substantial variation in polarization is achievable with increased uniaxial stress along the direction of spontaneous polarization. Thus, the results under high stress conditions suggest that operating in alignment with the polarization direction produces the highest energy densities, which contradicts the conclusions drawn in domain-engineered crystals.

The experimental investigation focused also on <111>-oriented PMN-30PT which displays a rhombohedral structure with a polarization along the $[111]_c$ direction at 20°C. As it was reported, the value of the d_{33} piezoelectric coefficients of the <001> orientation is almost 10 times superior to the <111> orientation in PMN-30PT at room temperature. However, the experiments and the simulations of Ericsson cycles under high stress and electric field showed that they exhibited similar energy levels. These results reinforce the unique features of high levels mechanical energy harvesting compared to low levels ones. However, further experiments should be performed at different temperature and under different applied uniaxial stress to confirm these results.

Thèse accessible à l'adresse : https://theses.insa-lyon.fr/publication/2024ISAL0017/these.pdf © [G. Taxil], [2024], INSA Lyon, tous droits réservés

Considering, all the different results of this chapter, making profit of non-linearities induced by in-plane switching is very beneficial for mechanical energy harvesting. Moreover, it seems that if a sufficient uniaxial stress is applied to the material and it allows the polarization to switch in-plane even under the application of an electric field. Then, all the energy density of the materials should converge and no big differences in terms of energy density should be observed between the materials.

Thèse accessible à l'adresse : https://theses.insa-lyon.fr/publication/2024ISAL0017/these.pdf © [G. Taxil], [2024], INSA Lyon, tous droits réservés

Chapter 4

Device implementation

The previous chapters enlightened the potential of exploiting non-linear behaviors induced by stress and electric field in ferroelectric materials, particularly within the context of non-resonant mechanical energy harvesting. In such scenarios, the mechanical design of an energy harvesting device needs to be tailored to the mechanical source, ensuring that the mechanical stress is sufficiently high to maximize energy conversion.

This chapter aims at implementing real applicative devices with the conditions of stress and electric field previously considered in the modeling (Chapter 2) and the characterization of ferroelectric materials (Chapter 3). The main objective is to made profit of the non-linearities largely discussed in this manuscript for demonstrating their potential for energy harvesting.

In the first section, the work will focus on the presentation of a fully developed functional smart tile. This device operates in 33-mode as in the previous experimental test-bench and modeling. The elaboration of such a device will be first presented, then the experimental methods will be provided. After that, the characterization results will be given. Finally, an electrical interface is proposed with the associated characterization results.

In the second section, the development of an additional device based on a cantilever beam is given for potential applications such as switches. This device has for particularity to operate in 31-mode compared to the previous one. The work will primarily focus on the test-bench presentation and the fabrication methods of the cantilever. Then, analytical and finite element modeling will be introduced to establish the effective tensile stress in the material based on the beam displacement. Finally, the different characterization results will be presented.

Thèse accessible à l'adresse : https://theses.insa-lyon.fr/publication/2024ISAL0017/these.pdf © [G. Taxil], [2024], INSA Lyon, tous droits réservés

4.1 Smart tile

The development of a device was a logical extension of this research. Various challenges must be addressed to achieve a fully functional device, including ensuring an adequate supply of active materials and implementing a suitable electrical interface for extracting the energy. Here, a smart tile based on a force amplification mechanism is employed with the explicit aim of operating in the nonlinear regime. The objective is then to unlock the potential for ultra-high energy conversion density. This section draws inspiration, in part, from the article previously published in Smart Materials and Structures [Seb+23].

4.1.1 Design and fabrication

The mechanical system was designed with the aim of transforming an initial input force into the necessary mechanical stress applied to several piezoelectric ceramic plates. PZT stacks were then selected for maximizing the total amount of active material while still being compatible with forces in the range of hundreds of Newtons. To attain stress levels around $\approx 100MPa$ (which are necessary to induce significant depolarization under stress), the cross-sectional area was maintained to less than 1 cm^2, and a force amplification mechanism was developed. A piezoelectric stack was chosen for this purpose because it offers several advantages. It comprises numerous piezoelectric plates electrically connected in parallel and mechanically connected in series. As previously noted by Ling *et al.* [Lin+22], this configuration also enables the effective utilization of the 33-mode instead of operating in 31-mode, which displays a piezoelectric coefficient less important (d_{33} is 2 to 3 times the d_{31}). The input mechanical force was enhanced thanks to a lever amplification system, which is represented on a schematic illustration in Figure 4.1. This device was composed of 3 piezoelectric stacks electrically connected in parallel and mechanically in series.

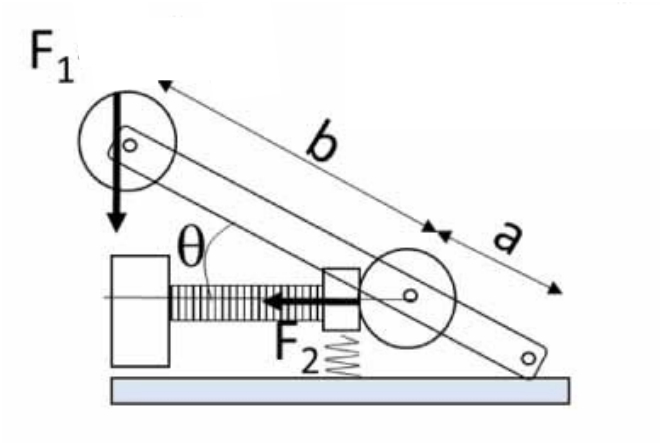

FIGURE 4.1: Schematic of the mechanical amplification system [Seb+23].

The dimensions of the different parts of the tile were chosen to target the desired stress with a input force equivalent to a human stepping on the device. It is possible to express the equivalent force applied to the piezoelectric stacks depending on the input force as follows:

$$F_2 = \beta F_1 = \frac{a+b}{atan(\theta)} F_1 \tag{4.1}$$

Thèse accessible à l'adresse : https://theses.insa-lyon.fr/publication/2024ISAL0017/these.pdf © [G. Taxil], [2024], INSA Lyon, tous droits réservés

where F_1 and F_2 are respectively the input force and the force applied to the piezoelectric stacks. a,b and θ denote respectively different distances and the angle formed between the lever and the bases as shown in Figure 4.1. It can be noted that θ vary when stepping on the device. Nevertheless, it was approximated to remain constant throughout the process due to its extremely low variations. Finally β represents the mechanical amplification ratio.

All the different mechanical parts were purchased from Misumi or were 3D printed in ABS with a FlashForge Dreamer printer. For transmitting the stress between the different piezoelectric elements, linear shafts were employed with a length of $30mm$ and a diameter of $12mm$. These linear shafts were put inside linear ball bearings featuring a length of $28mm$ and an inner and outer diameters of respectively $12mm$ and $19mm$. Finally, the linear shafts were inserted in circular holes of $20mm$ within blocks made of steel with dimensions of $54 \times 25 \times 30mm^3$. All these different parts are illustrated in Figure 4.2 (a).

After that, the 3 different blocks were fixed on a steel plate of $80 \times 300mm^2$ with a thickness of $6mm$ as shown in Figure 4.2(b). Another steel block without holes was added and fixed on the extremity of the plate to stop the PZT stacks when the force was applied, inducing uniaxial stress in the PZT stacks. Finally, 3D printed ABS piezoelectric supports were inserted between the steel blocks to align the stacks with the linear shafts.

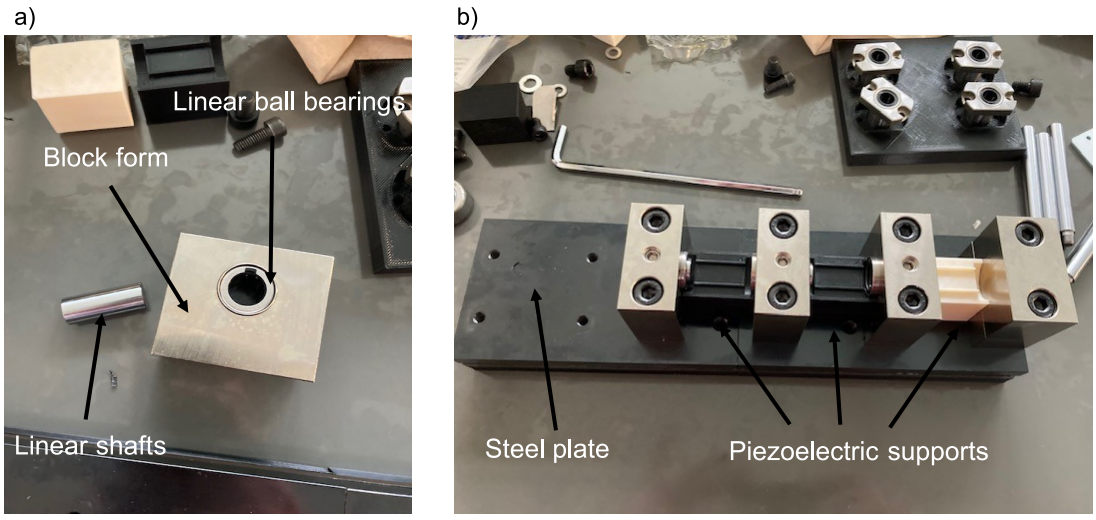

FIGURE 4.2: Fabrication steps of the device

The lever was assembled with the different components as depicted in Figure 4.3(a). The lever is composed of two steel links which determine the lengths a and b of equation 4.1 and illustrated in 4.1. With the selected links a and b were respectively of $90mm$ and $40mm$. the two steel links were bound by different steel rods with a diameter of $10mm$ inserted in the associated holes of the steel links. Finally rotating guides allow the lever to rotate in order to applied the force on the linear shaft via a horizontal contact roll (Figure 4.3(a)).

Then, the lever was fixed on the steel plate as shown in Figure 4.3(b). 4 vertical linear shafts with a length of $84mm$ and a diameter of $10mm$ were screwed on the base steel plate and a mounting plate was added to rigidify the structure as shown

Thèse accessible à l'adresse : https://theses.insa-lyon.fr/publication/2024ISAL0017/these.pdf © [G. Taxil], [2024], INSA Lyon, tous droits réservés

in Figure 4.3(c). The 4 vertical linear shafts were then inserted in 4 linear ball bearings that were fixed to an ABS plate on which one can step on as illustrated in Figure 4.5(a) and (b). This device was a proof of concept and different components can be

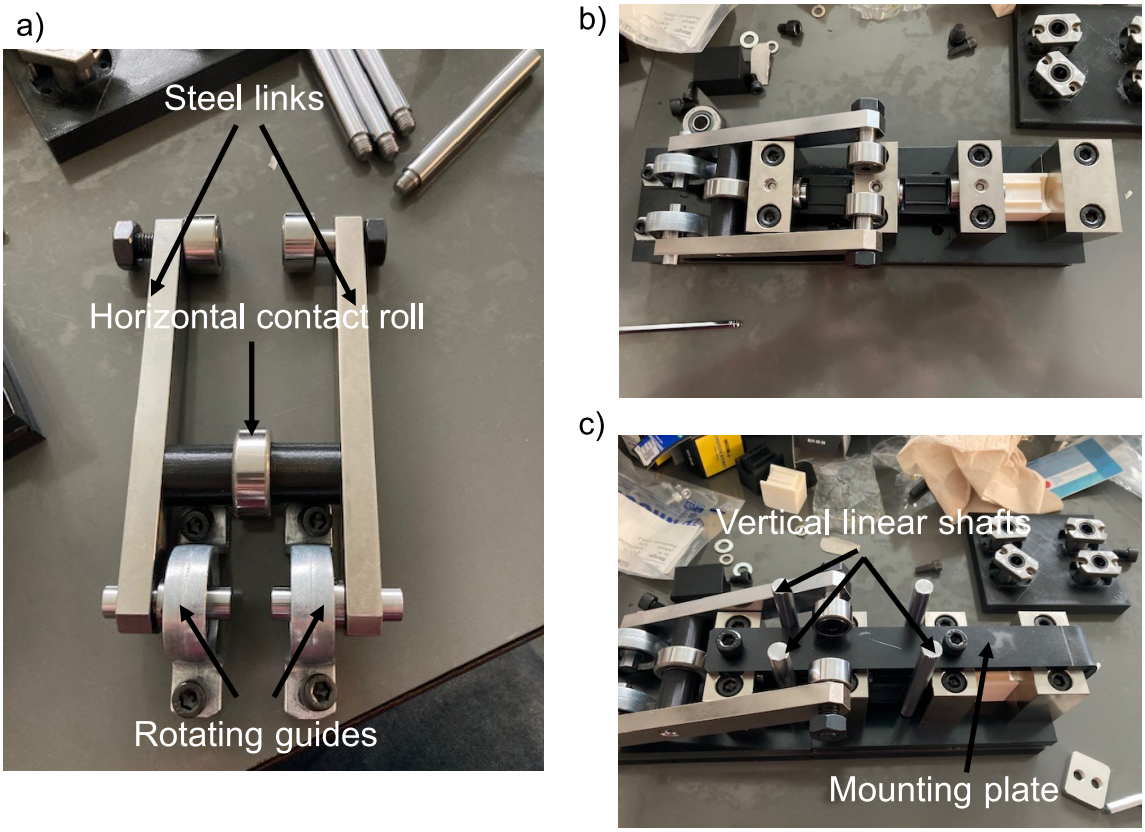

FIGURE 4.3: Fabrication steps of the device

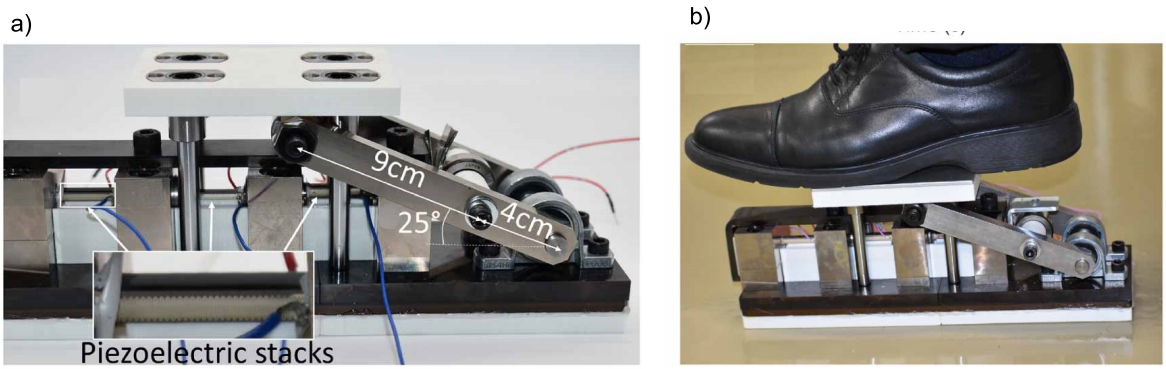

FIGURE 4.4: (a) Photograph of device, with piezoelectric stacks mechanically assembled in series. The force is applied vertically on the top white plate, which is converted into a larger horizontal force squeezing the piezoelectric stacks [Seb+23]; Photograph of the device when stepping on it [Seb+23].

modified to enhance the portability and reduce the volume of the device. Additionally, the components can be adapted to achieve the desired stress for other uses like for road pavements. With the dimension selected and illustrated in Figure 4.5(a) ($b = 90mm$,$a = 40mm$ and $\theta = 25°$), it yields to a mechanical force amplification factor $\beta \approx 7$. Considering a human of $70kg$ stepping on the device, the total force F_2

Thèse accessible à l'adresse : https://theses.insa-lyon.fr/publication/2024ISAL0017/these.pdf © [G. Taxil], [2024], INSA Lyon, tous droits réservés

applied to the three PZT stacks is then around $4900N$. The stack surface was around $27mm^2$ which result in an applied uniaxial stress in the range of 100-200MPa.

4.1.2 Experimental methods

The piezoelectric stack actuator chosen for this study was the B58004M4030A020 model manufactured by TDK in Munich, Germany. For more information on the ferroelectric response under stress of a similar piezoelectric stack, the reader can refer to the details provided in [Est+17]. This actuator comprised approximately 430 layers of soft PZT, each with a thickness of $70\mu m$, and these layers are interconnected with electrodes. The overall length of the actuator measured $30mm$, with a surface of $5.2 \times 5.2mm^2$.

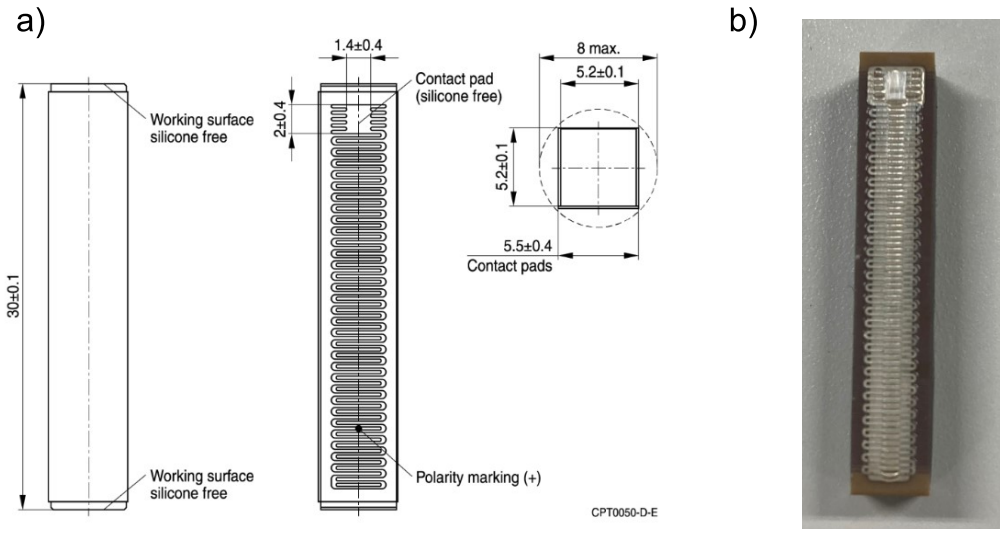

FIGURE 4.5: (a) Piezoelectric stack illustration taken from "Digikey" (https://www.digikey.com); (b) Photo of the piezoelectric stack.

Before implementing the PZT stack in the device, characterization of the piezoelectric materials in their ferroelectric state without any applied stress and under compressive stress was performed. This assessment was carried out using a similar setup as presented in Chapter 3. The samples were first tested on the compression testing machine (Shimadzu AGS-X, Japan), which applied a predetermined static force to the piezoelectric material. The sample electrodes were connected to a high-voltage amplifier (AIE Inc., Trek 10/10BHS, USA), and controlled by a function generator (Tektronix AFG1022, USA). The current was monitored using a current amplifier (Stanford Research®, USA), connected in series with an input resistance of 1Ω. The polarization was again determined by integrating the current over time. All the signals were captured and recorded using a Data Acquisition System (Dewesoft Krypton 8LV, Slovenia). Bipolar hysteresis curves at different stress levels and real Ericsson cycles were performed in similar way than the protocole described in Chapter 3. However, higher applied electric field could be reached based on the voltage range advertised by the company. The highest applied voltage was of $180V$ which corresponds to an electric field around $2.6kV/mm$. An electric field of $1.5kV/mm$ corresponding to a voltage of $105V$ was also tested to compare with the previous material characterizations.

Thèse accessible à l'adresse : https://theses.insa-lyon.fr/publication/2024ISAL0017/these.pdf © [G. Taxil], [2024], INSA Lyon, tous droits réservés

As exposed in the previous part, the prototype was constructed using tailor-made mechanical components. Ericsson cycles, were realised with similar conditions as described previously with the materials within the structure. Uniaxial stress was applied thanks to the compression machine but also by stepping on the tile for testing the device in real conditions. An illustration of the voltage evolution with the associated current are depicted in Figure 4.6(a) when performing an Ericsson cycle while stepping on the device. The prototype also incorporated a displacement sensor (Panasonic HG-C1100-P, Kadoma, Japan) to keep track of the displacement of the contact frame. This allowed the measurement of the mechanical work performed by the external mechanical source. The displacement for the same Ericsson cycle and its different processes is shown in Figure 4.6(b). Interestingly, the displacement induced by the applied voltage (converse piezoelectric effect) can be observed clearly, denoting the high electromechanical coupling. This also reflects the especially high electric field applied to the material as a significant displacement was measured.

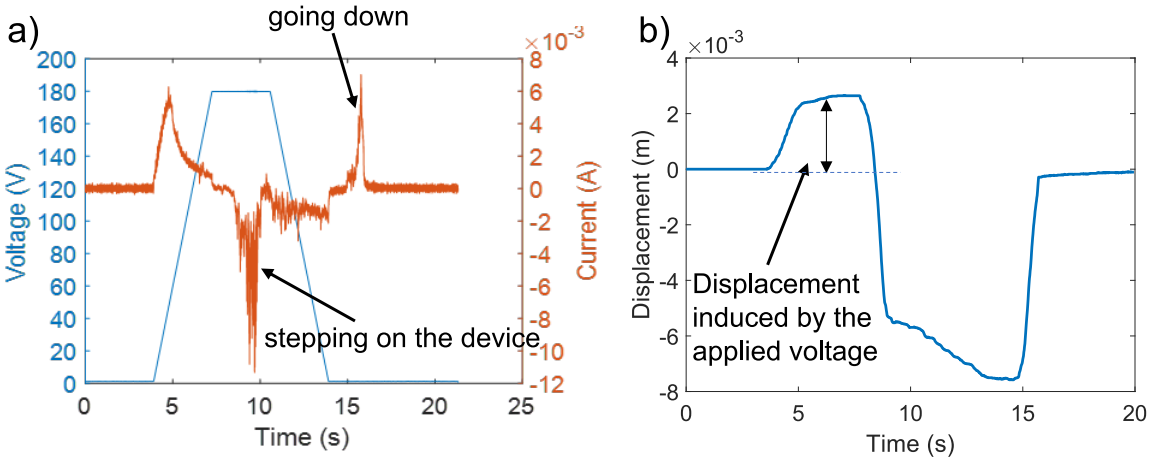

FIGURE 4.6: (a) Voltage and current as a function of time when performing an Ericsson cycle by stepping on the device; (b) Displacement as a function of time when performing an Ericsson cycle by stepping on the device.

4.1.3 Characterization results

The PZT stacks were initially subjected to characterization tests under static stress and bipolar voltage excitation. Figure 4.7(a) illustrates the polarization as a function of the electric field at static stress levels of 1MPa and 100MPa. A noticeable alteration in the hysteresis cycle shape, consistent with previous findings [Unr+19; PCV14c], was observed. Based on the bipolar cycles, a method for estimating real Ericsson cycles as in [Tun+22] was employed. A maximum energy conversion density of $210 mJ/cm^3$ was thus estimated (indicated by the blue dashed line in Figure 4.7). In a subsequent experiment, the real Ericsson cycles were applied to the piezoelectric stack actuator, using similar waveforms for the stress and the electric field as in Figure 3.6(c). The stress levels were sufficiently high to induce irreversible polarization changes, and the Ericsson cycles were systematically executed three times successively. The third cycle was then employed to calculate the energy density conversion, defined by the enclosed area within the polarization cycle. The Ericsson cycles were performed according to three different scenarios, for different sets

Thèse accessible à l'adresse : https://theses.insa-lyon.fr/publication/2024ISAL0017/these.pdf © [G. Taxil], [2024], INSA Lyon, tous droits réservés

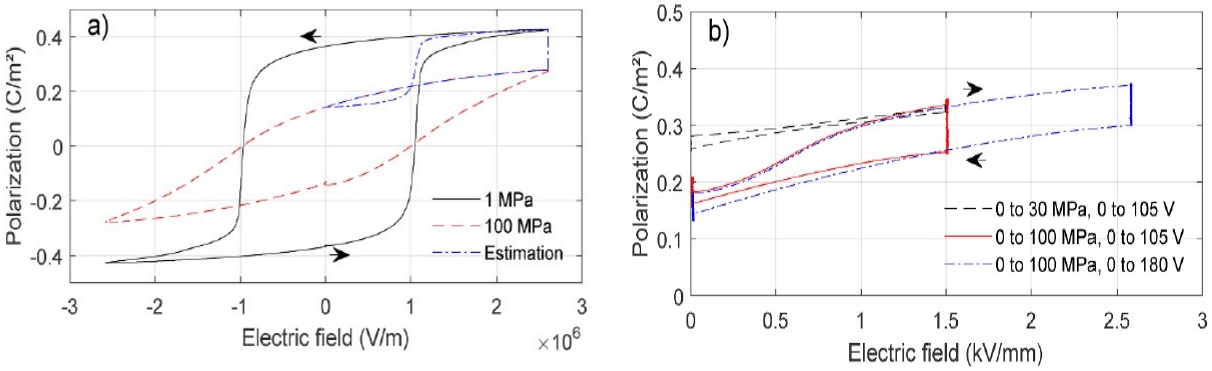

FIGURE 4.7: (a) Bipolar cycles at 1 MPa and 100 MPa on a piezoelectric stack, with the estimated Ericsson cycle area in blue dotted line [Seb+23]; (b) Ericsson unipolar cycles on a piezoelectric stack [Seb+23].

of mechanical stress and electric field magnitudes. The resulting polarization versus electric field are displayed in Figure 4.7(b). All the resulting energy densities reported in Table 4.1 are consistent with the results of the previous chapter. Indeed, similar values were obtained for soft PZT under similar stress and electric field conditions as test N°1 and N°2.

Test	Electric field (kV/mm)	Mechanical stress (MPa)	Converted energy density (mJ/cm^3)	Energy converted by the stack (mJ)
N°1	1.5	30	13.9	11.3
N°2	1.5	100	74.5	60.4
N°3	2.6	100	163	132

TABLE 4.1: Different tests and their corresponding energies

After that, the PZT stacks were characterized within the mechanical structure. Ericsson cycles were tested under different input forces, spanning from 100N to 700N, and applied voltage from 0 to 180V. The charge-voltage (Q-V) cycles were similar to the polarization versus electric field cycles previously characterised on the single stack. Consistently with the high-level systemic approach of this Chapter, the Q-V space is used here to obtain directly the converted energy from the enclosed area instead of the converted energy density obtained from P-E cycles. Figure 4.8 displays the Ericsson cycles for each tested force. It can be observed that at 100N as shown in Figure 4.8(a), the energy absorbed by the voltage amplifier is negative, revealing an energy transfer from the amplifier to the piezoeletric stacks. This means that the voltage application costs more energy than the energy gain from the mechanical force input. The cycles under higher forces all exhibit positive energies and reach an output energy as high as $828 mJ/cycle$ for 700N (Figure 4.8(g)).

Figure 4.9 depicts the converted output energy and the stored mechanical energy depending on the applied forces. The mechanical energy was considered as it is the reservoir from which the converted electrical energy is partially derived. Across

Thèse accessible à l'adresse : https://theses.insa-lyon.fr/publication/2024ISAL0017/these.pdf © [G. Taxil], [2024], INSA Lyon, tous droits réservés

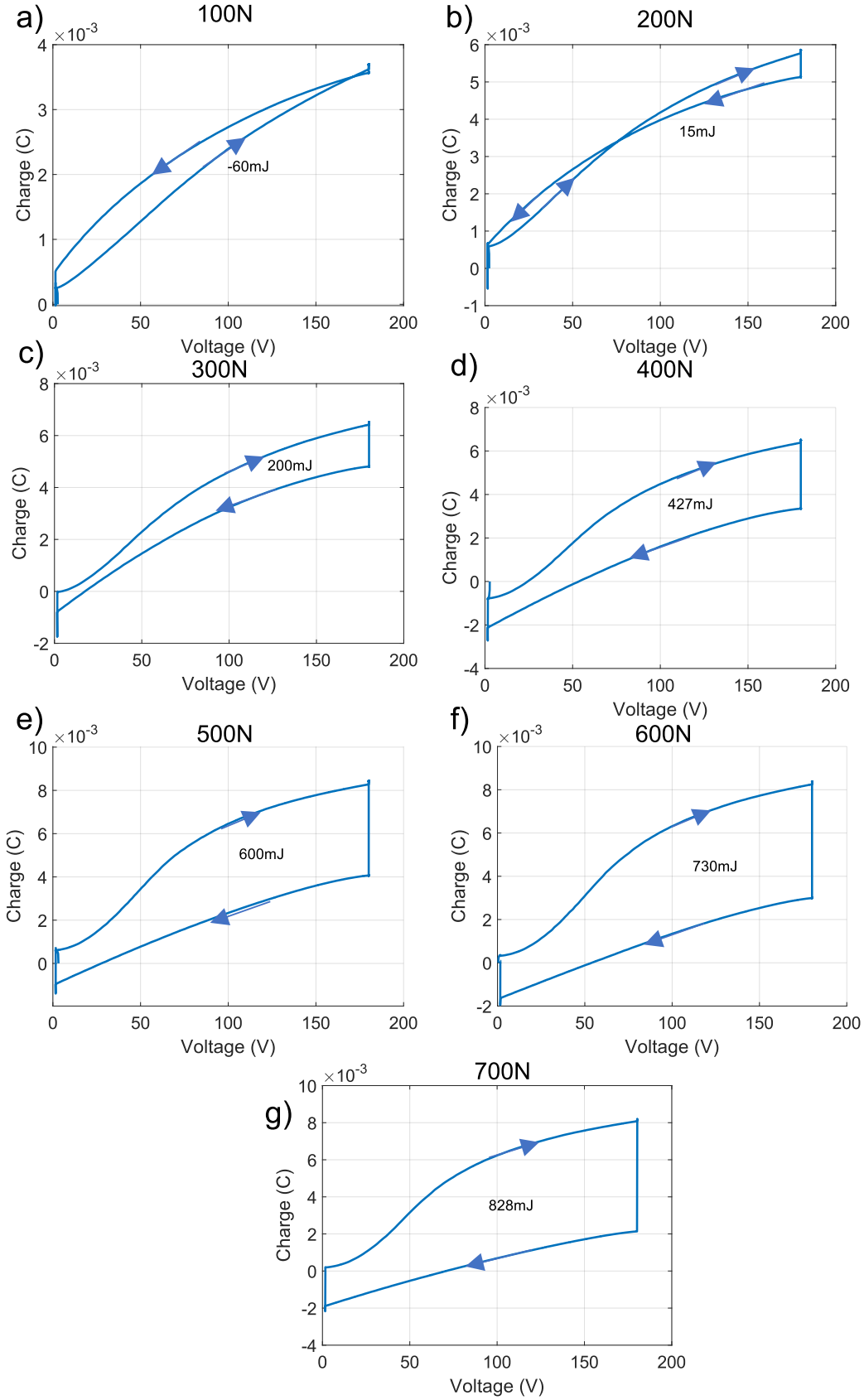

FIGURE 4.8: Ericsson cycles performed on the tile; (a) 100N; (b) 200N; (c) 300N; (d) 400N; (e) 500N; (f) 600N; (g) 700N

Thèse accessible à l'adresse : https://theses.insa-lyon.fr/publication/2024ISAL0017/these.pdf © [G. Taxil], [2024], INSA Lyon, tous droits réservés

all tested force scenarios, it became apparent that the maximum stored mechanical energy substantially surpassed the amount converted to electrical energy. This difference originates from the higher mechanical stiffness of the piezoelectric stacks in contrast to the lever system. Consequently, the lever system stored a greater amount of energy compared to the PZT stacks. Since only the latter could be converted into electrical energy, ultimately, just a few percents of the maximum stored mechanical energy could be harnessed. The choice to place the 3 stacks in a series configuration was chosen for optimizing the ratio of convertible energy to the total stored mechanical energy. Indeed, this allows a greater proportion of mechanical energy to be stored within the piezoelectric transducers in comparison to the lever system due to the reduction of the mechanical stiffness of the piezoelectric stack with such a configuration.

Both the mechanical energy and the converted energy display a significant increase in the 100 to 500N range. From 500 to 700N, this regime change to a slight increase of both energies. The results show that this device is interesting with input forces as low as 300N which is a small input force for a human step. This design enabled the achievement of a substantially high mechanical stress, reaching up to 170 MPa, and consequently leading to a especially high output energy. This emphasizes the interest of such systems for non-resonant mechanical energy harvesting.

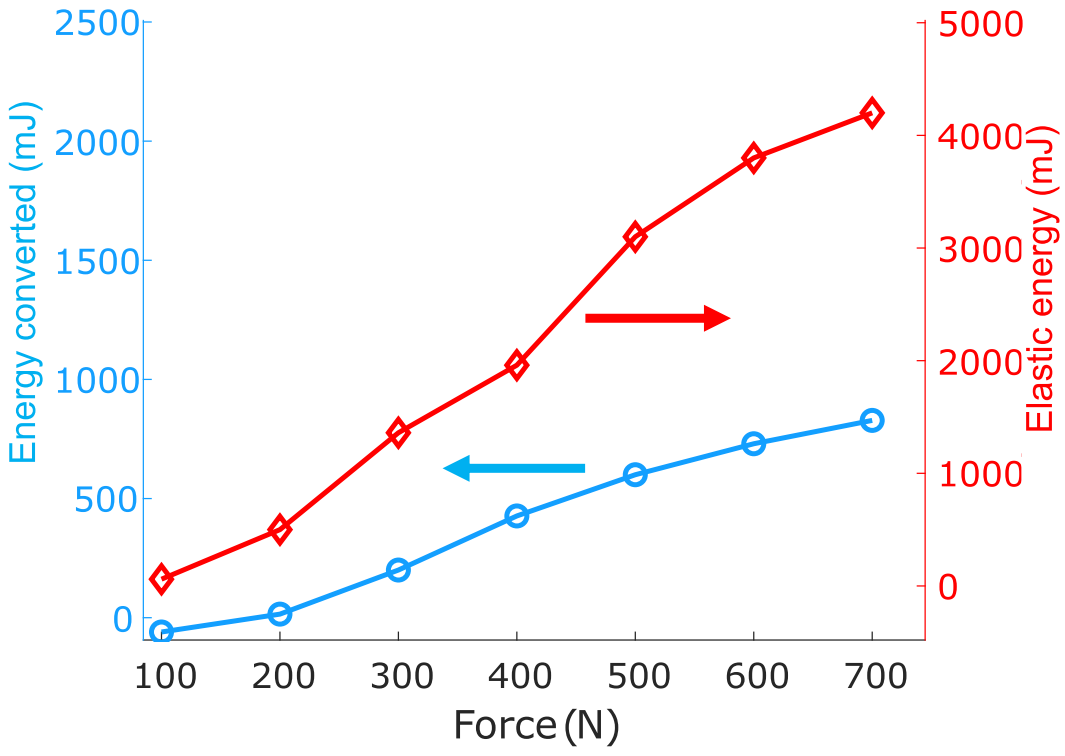

FIGURE 4.9: Stored mechanical energy (red curve) and converted energy (blue curve) as a function of the input force

In a subsequent experiment, force application involving physical stepping on the upper plateau of the device is illustrated in Figure 4.5(b). External voltage control, as employed in other Ericsson cycle experiments, was utilized. It is important to note that the precise timeline of force application was not regulated and displayed a more rapid rise compared to the controlled compression testing equipment. This however

Thèse accessible à l'adresse : https://theses.insa-lyon.fr/publication/2024ISAL0017/these.pdf © [G. Taxil], [2024], INSA Lyon, tous droits réservés

did not significantly impaired the operation of the system. Figure 4.6(a) and (b) illustrate respectively the resulting current-time profile, and displacement-time for a force of 700 N. The current profile exhibited three distinct peaks: a positive peak during voltage increase, corresponding to the charging of the electrical capacitance of the piezoelectric ceramic; a negative peak upon applying force, indicating depolarization due to the mechanical stress and electromechanical conversion through piezoelectric effect; and a negative peak during voltage decrease, relating the discharge of the piezoelectric capacitance. With a force of 700 N, the experimentally measured converted energy reached a value as high as 776mJ per step, whereas a 500 N force resulted in an energy of 578mJ. These two Ericsson cycles realised with the stepping on the device are presented in Figure 4.10. It can be noted that the output energy with the real steps are slightly lower compared to the test with the compression machine at equivalent force. These differences of energies are explained by the current saturation when stepping on the device. This saturation can be observed in figure 4.10(a) and (b) and reduces the polarization variation in the 2-3 process.

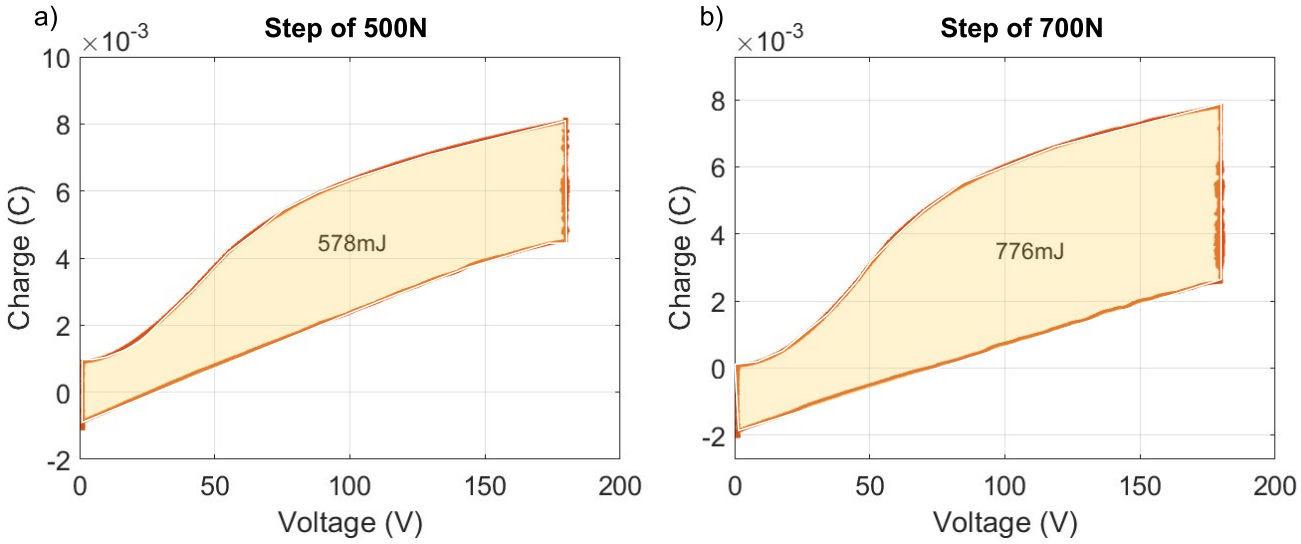

FIGURE 4.10: Ericsson cycles with a true step; (a) 500N; (b) 700N.

4.1.4 Electrical interface

All the prior results focused on Ericsson cycles, which, in practical implementation, could be difficult to achieve due to their dependence on a fully controllable voltage source. Such an approach indeed consumes excessive energy when operating independently, thereby compromising the overall energy balance of the device. In this work, the objective was to create a fully operational and realistic prototype which can function independently. The key consideration in selecting the most suitable interface lied on establishing a viable fully passive system while enabling the utilization of extensive energy cycles in the Q-V space. Specifically, although Ericsson cycles exhibited the greatest area for a given maximum voltage (or electric field), a significant drawback in their realistic application is the substantial depolarization they induced. Consequently, it is necessary to limit the cycle to maintain remnant polarization, resulting in a pseudo-rectangular cycle as shown in figure 4.11(b).

Thèse accessible à l'adresse : https://theses.insa-lyon.fr/publication/2024ISAL0017/these.pdf © [G. Taxil], [2024], INSA Lyon, tous droits réservés

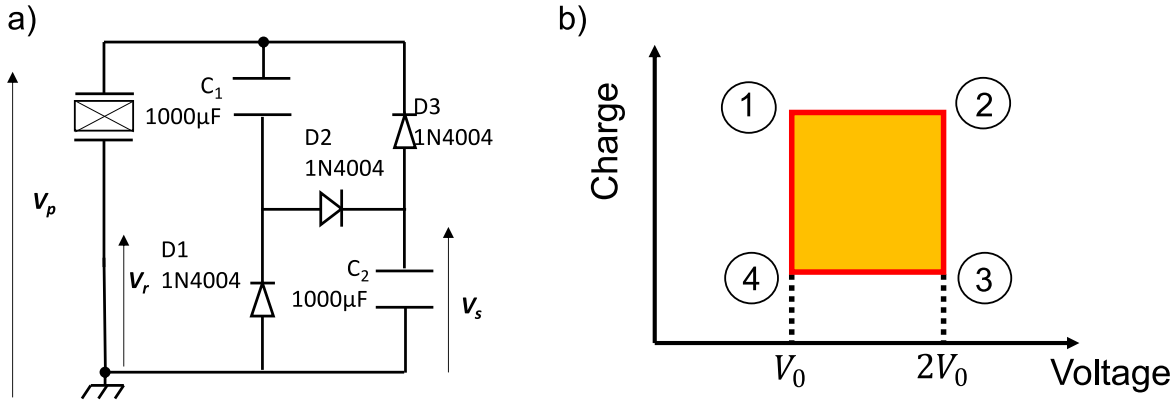

FIGURE 4.11: (a) Bennet doubler electrical circuit; (b) Bennet doubler associated Q-V cycle.

Considering these aspects, the chosen interface was an electrical adaptation of the Bennet doubler [QD11], which incorporated three diodes 1N4004 and two storage capacitors of $1000\mu F$ (depicted in Figure 4.11(a)). The Bennet doubler, through the sequential operation of diodes operating with only one DC source (denoted storage capacitance thereafter), allows the use of a single source that is besides refilled by an energy greater than the provided one. This ensures the feasibility and practicality of the microgenerator. Specifically, the charging process involves a parallel configuration of the voltage source and the buffer and storage capacitances as illustrated in Figure 4.12(a). On the other hand the discharge harvesting process consists of a series connection of the buffer capacitance and the storage capacitance as showns in Figure 4.12(b). This arrangement results in the ferroelectric material being exposed to a voltage that is successively one and twice the value of the voltage of the storage capacitance.

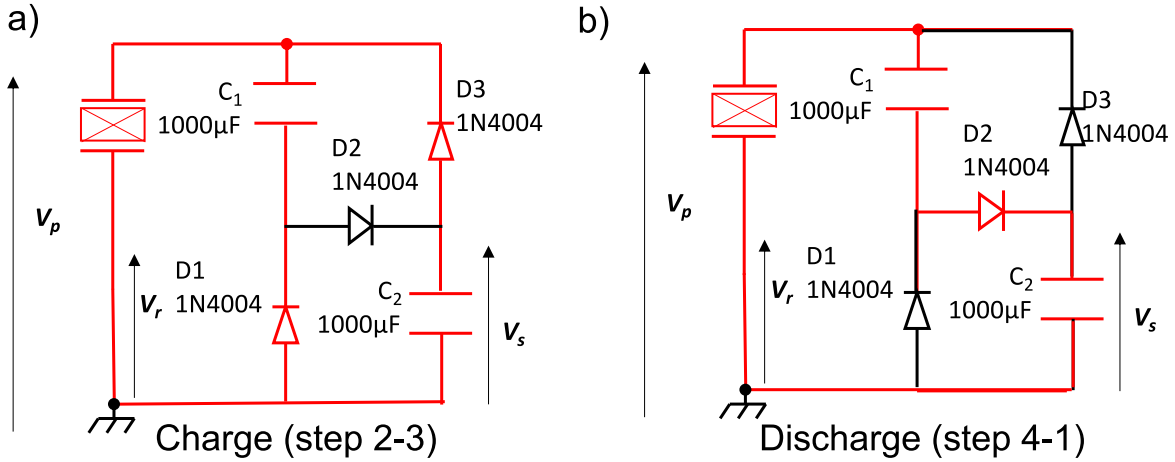

FIGURE 4.12: (a) Equivalent electrical circuit during the charging process; (b) Equivalent electrical circuit during the discharging process

In this work, an innovative application of the Bennet doubler is therefore introduced. While traditional applications of this circuit are for electrostatic devices, based solely on capacitance variation of the transducer, this study incorporated piezoelectric elements into the circuit, enabling the generation of charges. This passive

Thèse accessible à l'adresse : https://theses.insa-lyon.fr/publication/2024ISAL0017/these.pdf © [G. Taxil], [2024], INSA Lyon, tous droits réservés

transduction system eliminated the need for a voltage source and allowed for the operation of a self-starting and energetically self-contained system. In this setup, the conventional voltage source is replaced by a $1000\mu F$ storage capacitor, resulting in a fully passive circuit. This led to the spontaneous appearance of energy cycles that charged the storage capacitor, thus leading to an increase in voltage and a larger area within the cycle [QD11]. Numerous enhancements could potentially be employed to finaly tune the device and achieve a charge versus voltage behavior that aligns closely with the real Ericsson cycle, then maximizing the enclosed area [Lef+14].

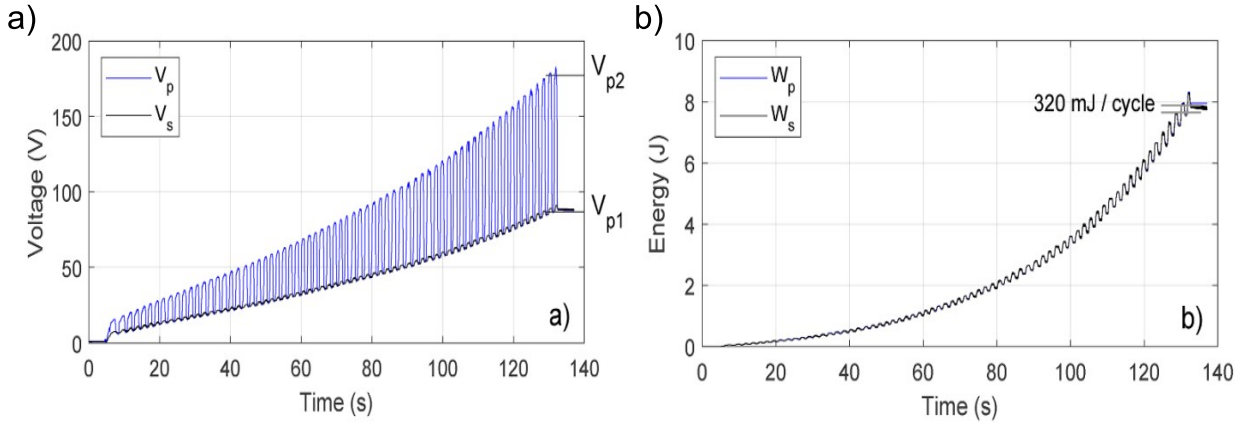

FIGURE 4.13: (a) Piezoelectric voltage as a function time [Seb+23]; (b) Associated stored energy as a function of time [Seb+23]

In the experiment, when a force was applied to the PZT stacks from an initial voltage V_{p1}, the circuit remained open until the voltage reached $V_{p2} = 2V_{p1}$. This was followed by a discharge at a constant voltage. Upon releasing the force, the voltage decreased at a constant charge until it reached the lower voltage V_{p1}. Then, the charge increased slightly beyond the initial value. Repeating these cycles gradually increased the starting voltage V_{p1} and the area enclosed within the cycle (Figure 4.13).

The interface was set up with the piezoelectric stacks connected in parallel, and a series of 50 steps force applications at 700N were applied, starting from a completely discharged state. As a result of the piezoelectricity of the active elements, the initial voltage increased when the force was applied, initiating a series of gradual charges of the buffer and storage capacitors. From this measurement, the electrical power was integrated over time to calculate the electrical work W_p of the PZT stacks, which is expressed as:

$$W_p(t0) = \int_0^{t0} V_p(t)I(t)dt. \tag{4.2}$$

where V_p is the measured voltage across the PZT stacks and I is the measured outgoing current. It is also possible to obtain the total stored electrical energy in the capacitors W_s as:

$$W_s(t) = \tfrac{1}{2}(C_1 + C_2)V_s(t)^2. \tag{4.3}$$

where C_1 and C_2 are the value of the two capacitors and V_s is the voltage source. The voltage signals over time are displayed in Figure 4.13(a). The minimum piezoelectric voltage value over one cycle followed the storage capacitor ones and reached twice the value when the force was applied. The stored energy in the materials and in the storage capacitor is illustrated in Figure 4.13(b). A nearly quadratic increase

Thèse accessible à l'adresse : https://theses.insa-lyon.fr/publication/2024ISAL0017/these.pdf © [G. Taxil], [2024], INSA Lyon, tous droits réservés

of energy with time was observed, suggesting that a higher starting voltage V_{p1} was preferable for increasing the output energy. However, the dielectric strength of the piezoelectric elements set a limit of 180 V, as recommended by the manufacturer. Thus, the cycles were terminated when the voltage reached this limit. Consequently, in the last cycle, the storage capacitors were charged at 90 V, and the voltage of the PZT stacks ranged then between 90 V and 180 V. In such a scenario, the energy per cycle reached 320 mJ per cycle, which is approximately 40% of the ultimate convertible energy obtained using real Ericsson cycle.

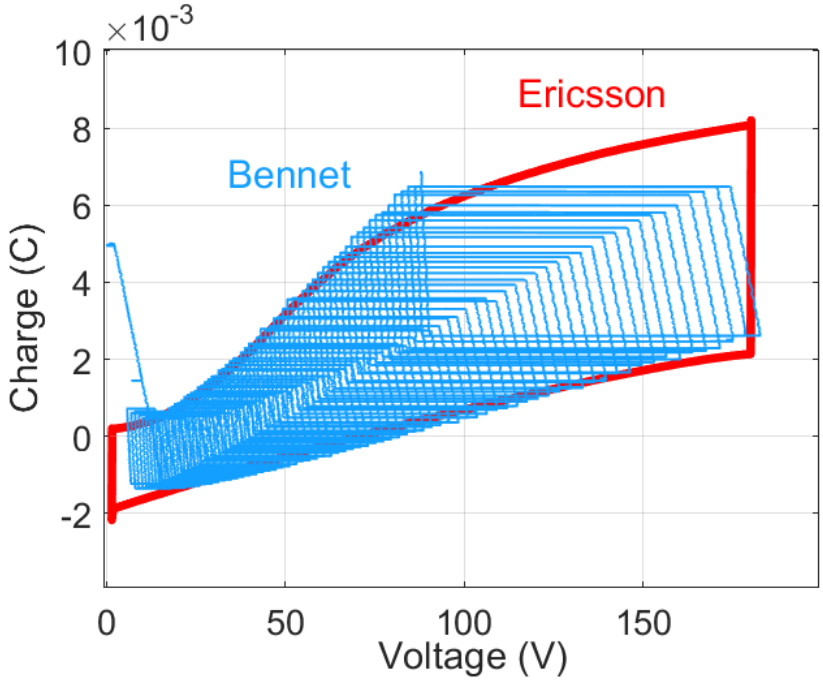

FIGURE 4.14: Charge vs voltage using Ericsson cycle (red line) and Bennet doubler (blue line) at 700N.

Interestingly, the Bennet doubler cycles shapes (Figure 4.14) outfitted those of the Ericsson cycles. Initially, it was expected that the top-left and bottom-right angles of the Bennet doubler cycles would align with the Q-V curves observed during Ericsson cycle measurements. However, this was not the case as it can be observed in the experimental results in Figure 4.11. This behavior is interpreted in terms of irreversible depolarization induced by the appied stress. When performing an Ericsson cycle, the charging curve started from zero, and the initial part of the curve corresponded to the repolarization process, from a partially depolarized state. However, the Bennet doubler did not yield a return at a zero voltage value, resulting in a lower depoling. Therefore, the equivalent charging branch corresponds to a different first-order reversal curve, characterized by a higher polarization value. Consequently, the Bennet doubler cycles were higher than expected, reaching about 40% of the real Ericsson cycle.

4.1.5 Comparison with the state of the art

The different results obtained with this device are valuable for non-resonnant energy harvesting and it is interesting to compare the obtained energy values with prior studies. Firstly, Qian *et al.* [QXZ19] introduced a frame amplification system

Thèse accessible à l'adresse : https://theses.insa-lyon.fr/publication/2024ISAL0017/these.pdf © [G. Taxil], [2024], INSA Lyon, tous droits réservés

for harvesting energy from footsteps. They achieved an output power of 11mW at 1Hz, employing a 500N force that led to a peak-to-peak displacement of 4mm. Similarly, Chen *et al.* [CSS20] proposed an amplification system designed for traffic roads. By applying an initial step force of 1333N, which induced a 2.5 mm deflection, they were able to obtain an output energy of 121mJ per cycle, representing around 6% of the mechanical energy input.

In this work, the force amplification was combined with Ericsson cycles, which were subsequently facilitated using a Bennet doubler electrical interface. This innovative approach allowed us to harness the benefits of non-linear dielectric behavior. While it may not match the energy density of Ericsson cycles, the Bennet doubler provides nonetheless an impressive value of 320 mJ per cycle (equivalent to 320 mW at 1 Hz), nearly 40% of the output achieved via Ericsson cycle. This was accomplished with a force input of 700N and a displacement of 12mm. When compared to the results presented in [QXZ19] and [CSS20], our device demonstrated significantly higher output energy and improved efficiency. This superiority can be primarily attributed to the non-linearities induced by the high electric field and high stress levels.

References	Frequency (Hz)	Piezoelectric volume (m^3)	Output energy per cycle
Choi *et al.* [Cho+06]	13970	2.12×10^{-14}	72pJ
Jeon *et al.* [Jeo+05]	13900	2.12×10^{-14}	72pJ
Muralt *et al.* [Mur+09]	855	6.4×10^{-13}	1.6nJ
Shen *et al.* [She+09]	183.8	1.32×10^{-12}	1.7nJ
Fang *et al.* [Fan+06]	608	1.96×10^{-12}	3.6nJ
Shen *et al.* [She+08]	461.15	1.28×10^{-12}	4.7nJ
Lee *et al.* [Lee+09]	255.9	3.75×10^{-11}	8.2nJ
Moromoto *et al.* [Mor+10]	126	2.14×10^{-10}	42nJ
Song *et al.* [Son+16]	10	3.47×10^{-6}	$18\mu J$
Elfrink *et al.* [Elf+09]	572	4.04×10^{-12}	110nJ
Ericka *et al.* [Eri+05]	2580	2.82×10^{-8}	700nJ
Minazara *et al.* [Min+06]	1710	2.82×10^{-8}	990nJ
Chen *et al.* [Che+13]	113	2.40×10^{-7}	1 μJ
Guyomar *et al.* [GSK11]	277	1.00×10^{-8}	14μJ
Wang *et al.* [Wan+12]	150	9.82×10^{-8}	163μJ
Qian *et al.* [QXZ19]	1	1.27×10^{-5}	11mJ
Wang *et al.* [Wan+22a]	10	7.63×10^{-6}	51mJ
Chen *et al.* [CSS20]	1	1.58×10^{-6}	120mJ
This work	**1**	2.43×10^{-6}	**320mJ**

TABLE 4.2: Examples of energy harvesting prototypes, with their piezoelectric elements volume, and the output energy per cycle [Seb+23].

To provide a more comprehensive perspective, a comparative analysis of various works related to piezoelectric energy harvesting, encompassing both dynamic and static regimes, is provided in Table 4.2. It is essential to note that the prototypes significantly vary in terms of their geometries, operating conditions, working frequencies, and mechanical energy inputs. Nevertheless, this comparative approach

Thèse accessible à l'adresse : https://theses.insa-lyon.fr/publication/2024ISAL0017/these.pdf © [G. Taxil], [2024], INSA Lyon, tous droits réservés

helps evaluating the overall potential for energy harvesting, considering both the input mechanical energy and the part that is converted and harvested as electrical energy. While each data point may need a specific investigation for a detailed analysis, the main objective is to discern a general trend. In Figure 4.15, a plot of the output energy per cycle against the volume of the piezoelectric elements along with the overall trend is given. A similar plot based this time on the output energy against the volume of the employed devices is given in Figure 4.16. The distinct data points represent a spectrum of input mechanical energies and frequencies, rendering direct point-to-point comparisons complicated. Nonetheless, a general pattern emerges, which provides an indication of the attainable output energy depending on the volumes of the piezoelectric material and of the device.

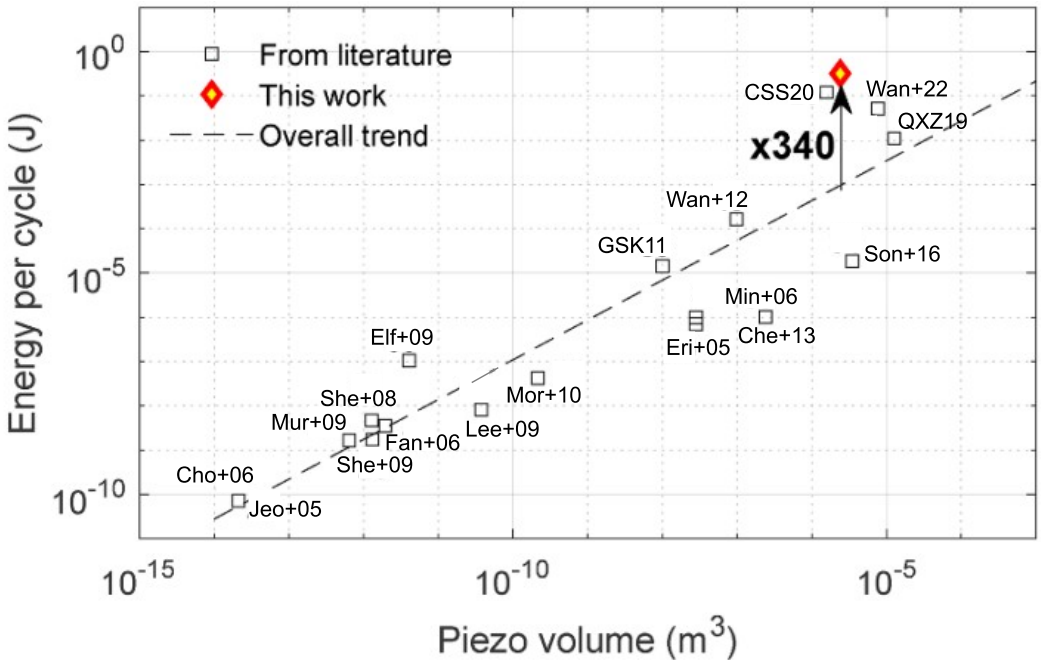

FIGURE 4.15: General trend of the output energy of piezoelectric energy harvesting devices, as a function of the volume of the piezoelectric elements [Seb+23].

It is noteworthy that nano and micro devices with a piezoelectric volumes less than $10^{-}11m^3$ exhibited relatively higher energy density, surpassing the general trend. However, it is important to mention that these devices may not consistently supply sufficient energy for direct utilization in powering sensors or similar applications. For instance, devices falling within the millimeter to centimeter size range with piezo volumes ranging from 10^{-11} to $10^{-8}m^3$ typically exhibit performance below the expected trend. In contrast, macroscopic devices (piezo volumes exceeding $10^{-8}m^3$) incorporating force amplification and stacked piezoelectrics piezo, outperform the expected trend due to their higher input mechanical energy density. In this work, the Bennet doubler allowed to harness nonlinear electrical behavior combined with force amplification. This integration yielded significantly higher output energy, reaching levels up to two orders of magnitude greater than the established trends. Furthermore, considering that Ericsson cycles achieved an output energy two to three times higher than the Bennet doubler interface, there exists potential for further enhancements with innovative electrical circuits.

Thèse accessible à l'adresse : https://theses.insa-lyon.fr/publication/2024ISAL0017/these.pdf © [G. Taxil], [2024], INSA Lyon, tous droits réservés

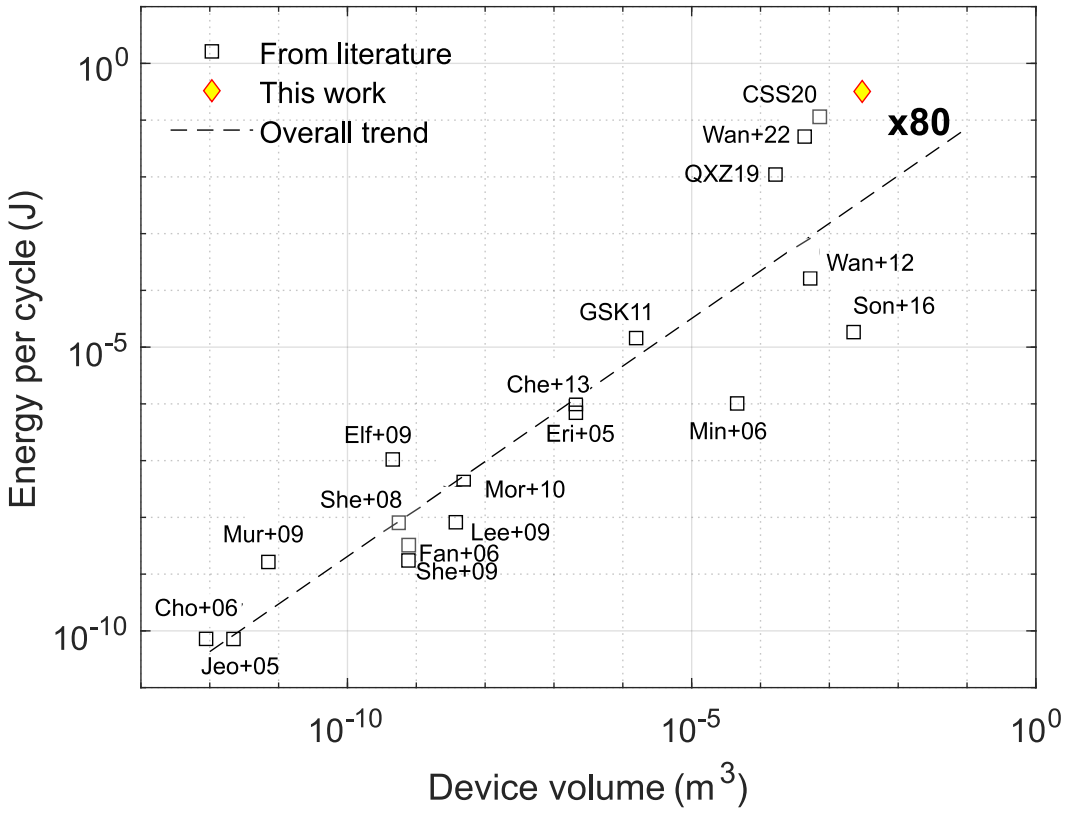

FIGURE 4.16: General trend of the output energy of piezoelectric energy harvesting systems, as a function of the volume of the devices.

4.2 Device based on a cantilever

In the previous section, a device operating in 33-mode was proposed as a solution for non-resonant energy harvesting. Employed high stress and high electric field allowed to reach outstanding energies per cycle compared to the state of the art. The proposed application targeted input forces in the hundred of Newtons such as human steps. In this section, the objective is to develop again a device working at high levels conditions. However, the goal was to operate in 31-mode for energy sources in the order of the tens of Newton such as forces induced by finger when activating a switch and to operate at a smaller scale compared to the tile. Moreover, implementing some of the materials characterized in Chapter 3 such as single crystals to reach ultra high energy density is one of the objectives of this section. Despite having generally a d_{33} ≈2 or 3 times the d_{31}, the objective with the device presented in this section was to reach similar energy density compared to the 33-mode thanks to in-plane domain switching induced by tensile stress.

Thèse accessible à l'adresse : https://theses.insa-lyon.fr/publication/2024ISAL0017/these.pdf © [G. Taxil], [2024], INSA Lyon, tous droits réservés

4.2.1 Device fabrication and methods

The mechanical device had for objectives to reach high stress levels and high electric field to perform Ericsson cycles in 31-mode but this time with smaller force inputs and smaller dimensions. A cantilever beam-based design was chosen as it allows operating in 31-mode while reach high tensile stress with a small input force and integration potential. The dimensions of the system were carefully selected as the induced stress in the material strongly depends on it. Analytical calculations and finite elements modeling were employed to this end and will be presented later in this section. In this part the fabrication processes along with the experimental methods are provided.

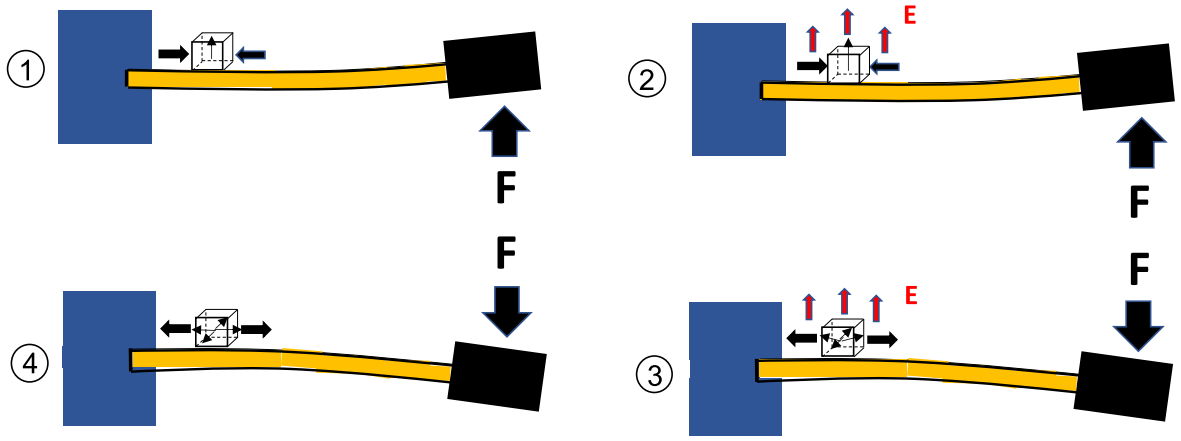

FIGURE 4.17: Schematic illustration of an idealized Ericsson cycle with a cantilever beam.

In the previous Chapters, the potential of in-plane switching induced by applied stress has been highlighted. The development of this cantilever was then motivated in order to control the polarization with both compressive and tensile stresses during the different Ericsson cycle processes. Indeed, previous studies considered mechanically poled ferroelectric materials thanks to compressive stress on the lateral direction [Kan+23; KCH22]. This mechanical poling increases the polarization, which is of great interest as larger polarization variations are possible through in-plane switching with tensile stress [MLL04]. The idealized 4 steps of the Ericsson cycle in 31-mode are illustrated in Figure 4.17. With such cycles, the material is electrically and mechanically poled (1-2 process) with a positive force applied at the tip of the beam. After that the materials is depolarized thanks to a negative force, which induces a tensile stress (2-3 process). Then, the material is further depolarized with the release of the electric field (3-4 process) with the negative force still applied. Finally the cycle is closed by coming back to the initially poled state.

Applying a large stress and electric field with such a small device can be challenging and one system geometry was finally selected as illustrated in Figure 4.18. The different elaboration methods will now be provided to build the cantilever. The choice of the beam material was very important and should have a sufficient yield stress to stay in the elastic limit when the force was applied, as large deflection are required to reach tens to hundreds of MPa. The dimensions were also crucial as the induced stress strongly depends on them. Different beam materials and geometries were tested and will be discussed later. The final device was made of carbon steel

Thèse accessible à l'adresse : https://theses.insa-lyon.fr/publication/2024ISAL0017/these.pdf © [G. Taxil], [2024], INSA Lyon, tous droits réservés

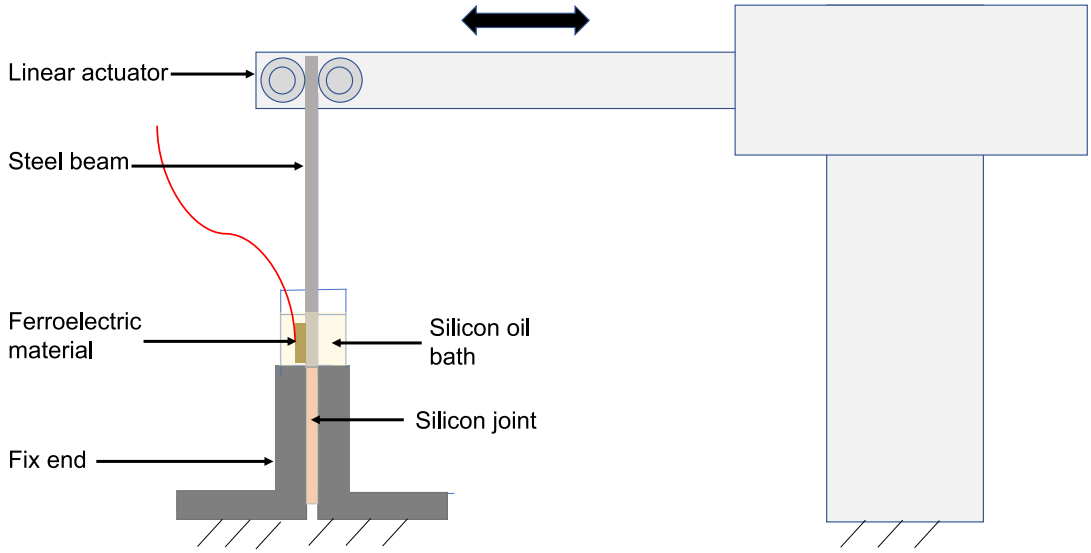

FIGURE 4.18: Schematic illustration of the desired device.

with a dimension of $3mm \times 10mm \times 100mm$. A photo of the selected beam is provided in Figure 4.19.

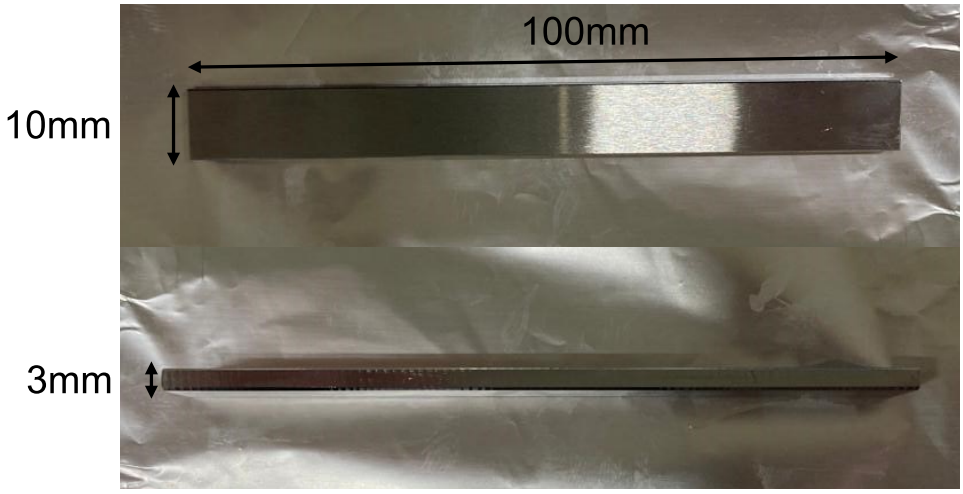

FIGURE 4.19: Photographs of the beam steel.

A specific glue was essential to strongly bond the materials to the beam. In order to resist at stresses superior to 100MPa, a mix of A (epoxy main agent) and B (amine curing agent) constituent of adhesive EP-340 from Kyowa was selected as shown in Figure 4.20(a). A mixture of 4:1 of agents A and B was prepared (Figure 4.20(b)) and were put in a vacuum chamber to remove bubbles that can affect the bonding. After that, a thin layer of adhesive was deposited on the beam and the ferroelectric materials were deposited on it as shown in Figure 4.21(a). After the sample deposition, the glue was dried for 24 hours at room temperature. Then, an electrical wire was bonded on the top surface of the samples thanks to a silver conductive paste. The silver paste was dried for one hour at 100°C as illustrated in Figure 4.21(b).

The cantilever was clamped between two pieces of steel (fixed end in Figure 4.18) thanks to two bolts. A polycarbonate tube with a diameter of 15mm and a length of

Thèse accessible à l'adresse : https://theses.insa-lyon.fr/publication/2024ISAL0017/these.pdf © [G. Taxil], [2024], INSA Lyon, tous droits réservés

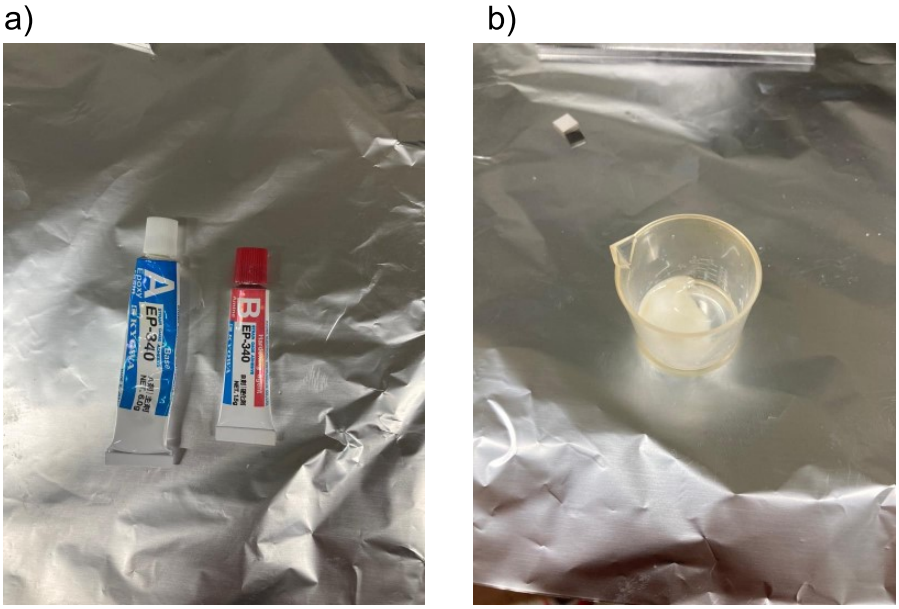

FIGURE 4.20: Photographs of the epoxy glue and the associated mixture.

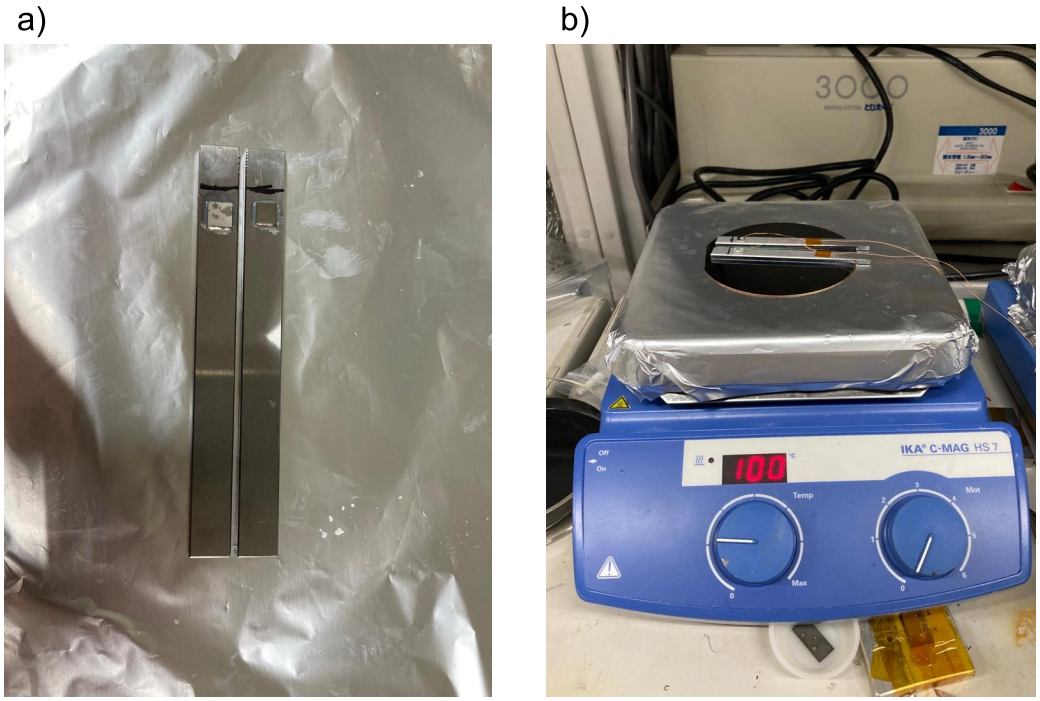

FIGURE 4.21: Different steps for the bonding of the materials on the beam.

20mm was fixed thanks to a Shin-Etsu RTV KE-45T silicon joint to build the silicon oil bath. Moreover, The volume between the two fixed ends was filled with the same silicon joint to avoid leakage. The full electromechanical cantilever with a zoom on the silicon oil bath is depicted in Figure 4.22(a). The cantilever was then fixed on the test-bench and electrically connected as illustrated in Figure 4.22(b).

Different materials were bonded on the cantilever substrate and it was decided to used similar ones that have been characterized in Chapter 3 in 33-mode. Thus, PZT

Thèse accessible à l'adresse : https://theses.insa-lyon.fr/publication/2024ISAL0017/these.pdf © [G. Taxil], [2024], INSA Lyon, tous droits réservés

C6 (medium), PZT C9 (soft) ceramics ($6 \times 6 \times 1mm^3$) and PZN-8PT <001> oriented crystals ($5 \times 5 \times 1mm^3$) were purchased again from Fuji Ceramics Corporation, Fujinomiya, Japan and Microfine Materials Technologies, Singapore, respectively. All the materials had the same properties as described in the previous chapter. It can be noted that for PZN-8PT single crystals, the lateral orientations were important to be distinguished in 31-mode compared to 33-mode as the d_{31} piezoelectric coefficient depends on it. PZN-8PT with lateral crystal directions of <100> and <010> as well as <110> and <1-10> were then tested.

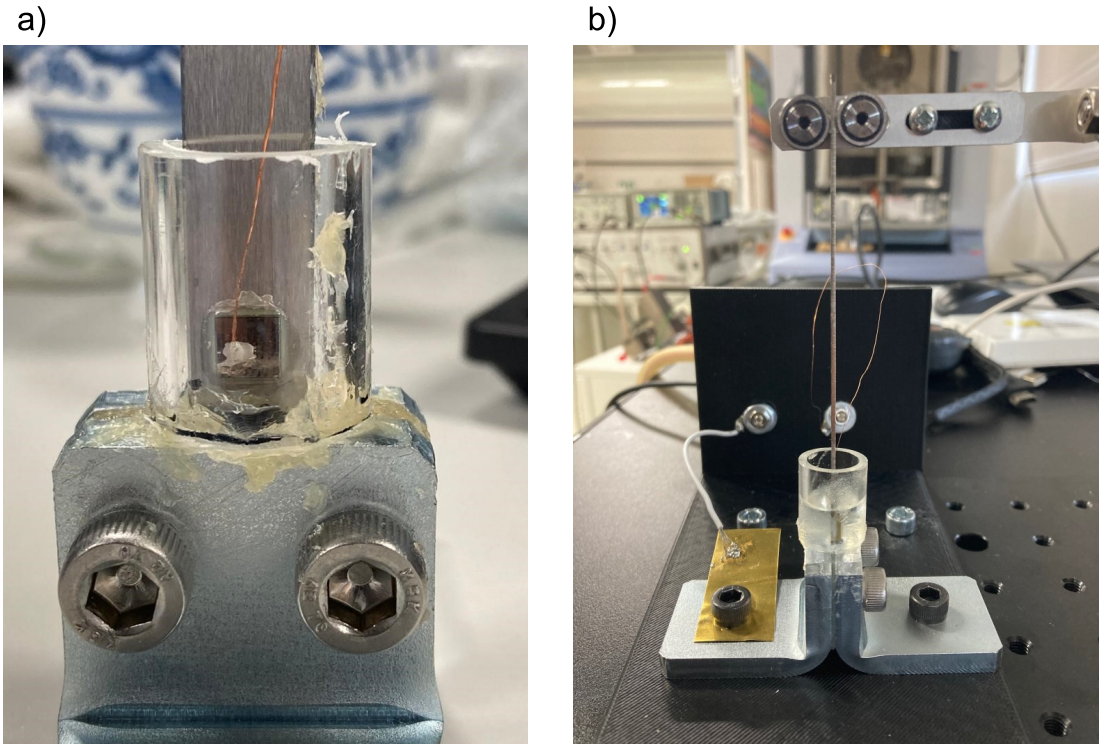

FIGURE 4.22: Photographs of the full electromechanical cantilever beams mounted on the test-bench

The test-bench was similar to the characterization of Chapter 3. Again a Tektronix® AFG1022 arbitrary function generator, a Trek® 10/10B-HS high voltage amplifier and a low-noise current amplifier (Stanford research®, Sunnyvale, CA, United States of America) was employed. A linear actuator RSD112 purchased from Misumi was used to monitor the deflection of the beam with a possible applied force ranging from 0 to 100N. Finally, a laser Panasonic HG-C1100-P sensor was employed to measure the displacement of the actuator. A photo of the global experimental test-bench for the cantilever based device is provided in figure 4.23.

To evaluate the energy conversion of this device, different characterization tests were performed. As in Chapter 3, real Ericsson cycles at different stress levels were performed. The applied electric field ranged again from 0 to 1500kV/m and the deflection varied from +4 to -4mm. The equivalent tensile stress was determined from analytical and finite elements simulations and will be presented in the next part. The temporal profile of the voltage, the force and the displacement for a real Ericsson cycle at 1500kV/m and with a beam deflection of 4mm is given in Figure 4.24.

Thèse accessible à l'adresse : https://theses.insa-lyon.fr/publication/2024ISAL0017/these.pdf © [G. Taxil], [2024], INSA Lyon, tous droits réservés

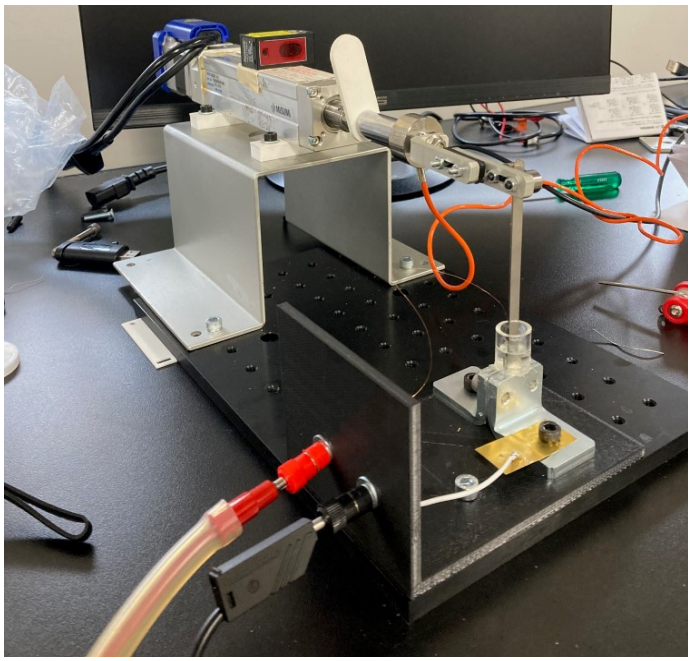

FIGURE 4.23: Photo of the test-bench

Bipolar hysteresis loops were also performed with an applied electric field ranging from -1500 to 1500kV/mm and with fixed deflections from -4 to 4mm. The voltage waveform for the bipolar hysteresis loops were similar to Chapter 3 displaying a sinusoidal profile with a frequency of 1Hz.

4.2.2 Modeling for stress evaluation

Assessing the tensile and the compressive stresses in the ferreoelectric material depending on the beam deflection is essential to have a good comparison with the previous results of this study. The stress evaluation was ensured analytically via Euler-Bernoulli beam theory and with finite elements simulations.

Analytical stress evaluation

Euler–Bernoulli beam theory, commonly known as engineer beam theory or classical beam theory, is a simplified framework that originates from linear elasticity theory. It is employed to estimate how beams carry loads and deflect. This theory is particularly suitable for cases where beams encounter lateral loads, and the resulting deflections are of a modest scale. Some conditions have to be respected to use the Euler-Bernoulli beam theory [NZ17] and the following prerequisites should be observed to ensure the highest accuracy of the final analytical modeling:

- The beam length to thickness ratio is greater than 10 [HM+10].
- The ratio between the beam length and its width is greater than 2 [Vil+13].
- The piezoelectric material length is much greater than its thickness [KSS16].

All these assumptions are respected with our device. However, the third hypothesis is perhaps not fully satisfied as the ratios between the piezoelectric lengths and their thickness are only 5 or 6 depending on the considered samples.

Thèse accessible à l'adresse : https://theses.insa-lyon.fr/publication/2024ISAL0017/these.pdf © [G. Taxil], [2024], INSA Lyon, tous droits réservés

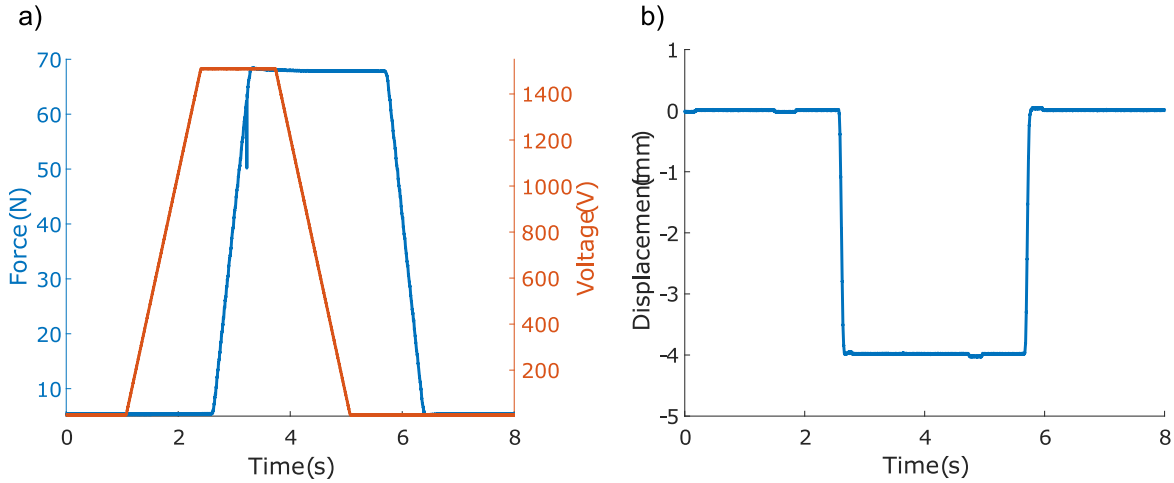

FIGURE 4.24: (a) Force and voltage as a function of time for an Ericsson cycle with a beam deflection of 4mm; (b) Associated measured displacement.

In static condition, it is possible to express the deflection of beam w as:

$$\frac{d^2w}{dx^2} = -\frac{M(x)}{Y_b I(x)} \tag{4.4}$$

where M is the bending moment, I is the moment of inertia and Y_b is the Young modulus of the beam. It is possible to express the bending moment as:

$$M(x) = FL(1 - \tfrac{x}{L}) \tag{4.5}$$

The calculation of the moment of inertia $I(x)$ requires finding the neutral line y_m of the beam for $a < x < a + L_p$ (it is in the middle of the beam elsewhere). An illustration of beam with the piezoelectric material and the different quantities is shown in Figure 4.25. The new neutral line in the active zone (part with the piezoelectric element) y_m is given by:

$$y_m = \frac{\sum A_i f_i y_i}{\sum A_i f_i} = \frac{y_0 l_p e + y_p e_p l_p \frac{Y_p}{Y_b}}{e l_p + e_p l_p \frac{Y_p}{Y_b}} \tag{4.6}$$

where A_i is the area of the ith material and f_i is a transformation factor based on the ratio of the Young modulus of the piezoelectric material and the beam. All the other quantities are distances represented in Figure 4.25(a) and (b). Finally the new neutral line is given by:

$$y_m = \frac{\frac{e^2}{2} + (e + \frac{e_p}{2}) e_p \frac{Y_p}{Y_b}}{e + e_p \frac{Y_p}{Y_b}} \tag{4.7}$$

It is then possible to express the product of the moment of inertia with the Young modulus in the different regions:

- $EI(x) = \frac{2}{3} e_p l_p Y_b y_m^3$ for $a < x < a + L_p$
- $EI(x) = \frac{2}{3} e_p l_p Y_b (\frac{e}{2})^3$ elsewhere

Thèse accessible à l'adresse : https://theses.insa-lyon.fr/publication/2024ISAL0017/these.pdf © [G. Taxil], [2024], INSA Lyon, tous droits réservés

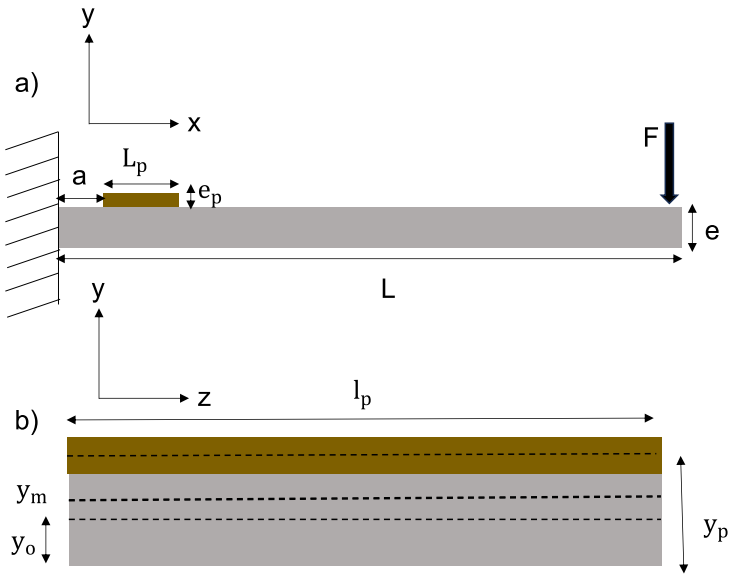

FIGURE 4.25: Schematic illustration of the beam and the piezoelectric material with different associated dimensions.

The beam deflection can be obtained by performing a double integration and by inserting equation (4.5) and the moment of inertia depending on the x value in equation (4.4), which yields.

$$w(x) = \int \int \frac{M(x)}{Y_b I(x)} dxdx \tag{4.8}$$

However, the calculation aimed at determining the stress and it which is expressed as:

$$\sigma = -yY_b \frac{d^2w}{dx^2} \tag{4.9}$$

and yields after insertion in equation (4.8):

$$\sigma = -\frac{M(x)}{I(x)}(y - y_m)n \tag{4.10}$$

where $n = \frac{Y_p}{Y_b}$ in the piezoelectric material and $n = 1$ in the beam. Table 4.3 gives all the different dimensions and properties of the device and then employed in the modeling.

Parameter	Value	Description
a	2mm	Distance between the fixed part and the piezo
l	10mm	Width of the beam
l_p	5 or 6mm	Width of the piezo (PZN-8PT or PZT C9)
e	3mm	Thickness of the beam
e_p	1mm	Thickness of the piezo
L	900mm	Length of the beam
L_p	5 or 6mm	Length of the piezo (PZN-8PT or PZT C9)
y_0	1.5mm	Neutral line of the beam
y_p	3.5mm	Neutral line of the piezo
Y_b	200GPa	Young modulus of the beam
Y_p	20 [Ami+07] or 50GPa [TFT02]	Young modulus of the piezo (PZN-8PT or PZT C9)

TABLE 4.3: Properties and dimensions of the piezoelectric materials and the steel beam.

Thèse accessible à l'adresse : https://theses.insa-lyon.fr/publication/2024ISAL0017/these.pdf © [G. Taxil], [2024], INSA Lyon, tous droits réservés

The measured force in the experiment was used to determine the stress and its heterogeneity in the material. The results of the calculated stress for PZT ceramics with an input force of 63N (corresponding to the measured one on the beam for a deflection of 4mm) is given in Figure 4.26.

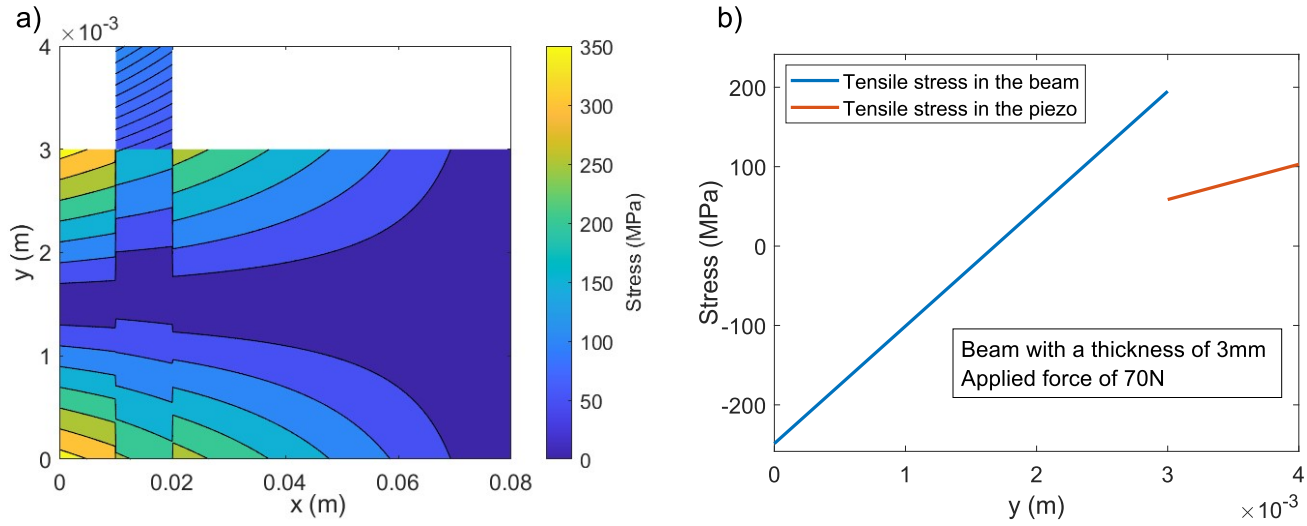

FIGURE 4.26: (a) Calculated stresses as a function of x (longitudinal direction) and y (thickness direction) for a beam deflection of 4mm; (b) Calculated stress in the beam and in the material as a function of y for a beam deflection of 4mm at x=15mm.

The simulations showed that the stress is not homogeneous in the beam and in the material. The average tensile stress in the piezoelectric material was around 80MPa. This deflection was the maximum reached in the experiment as most of the samples broke beyond this stress. Indeed, the calculated stress was already superior to tensile strength measurements for PZT reported in the literature [TOY93]. Before using a 3mm thickness of the beam, a 1mm one was employed, which revealed after simulations that the stress heterogeneity was too important in the material and induced cracking. One can note that at the distance x where the piezoelectric material is located, the stress profile changes as the neutral line is shifted upward (Figure 4.26(a)) as detailed in the calculations. Interestingly, a jump of stress can be observed in Figure 4.26(b) and its amplitude depends of the Young modulus ratio of the two materials.

Finite elements modeling

Finite elements simulations were also performed to have a better confirmation of the calculated stress in the ferrolectric material depending on the applied force or deflection. COMSOL Multiphysics was employed with similar conditions and dimensions than the experiments and analytical simulations. The different modules of COMSOL employed were "Solid Mechanics", "Electrostatics" and "Multiphysics" for the piezoelectric coupling. The chosen boundary conditions were representative of the experiment. Indeed, the part embedded in the fixed part was set as "Fixed constraint" and at the other extremity of the beam, an "Edge load" similar to the ones measured experimentally was set.

Thèse accessible à l'adresse : https://theses.insa-lyon.fr/publication/2024ISAL0017/these.pdf © [G. Taxil], [2024], INSA Lyon, tous droits réservés

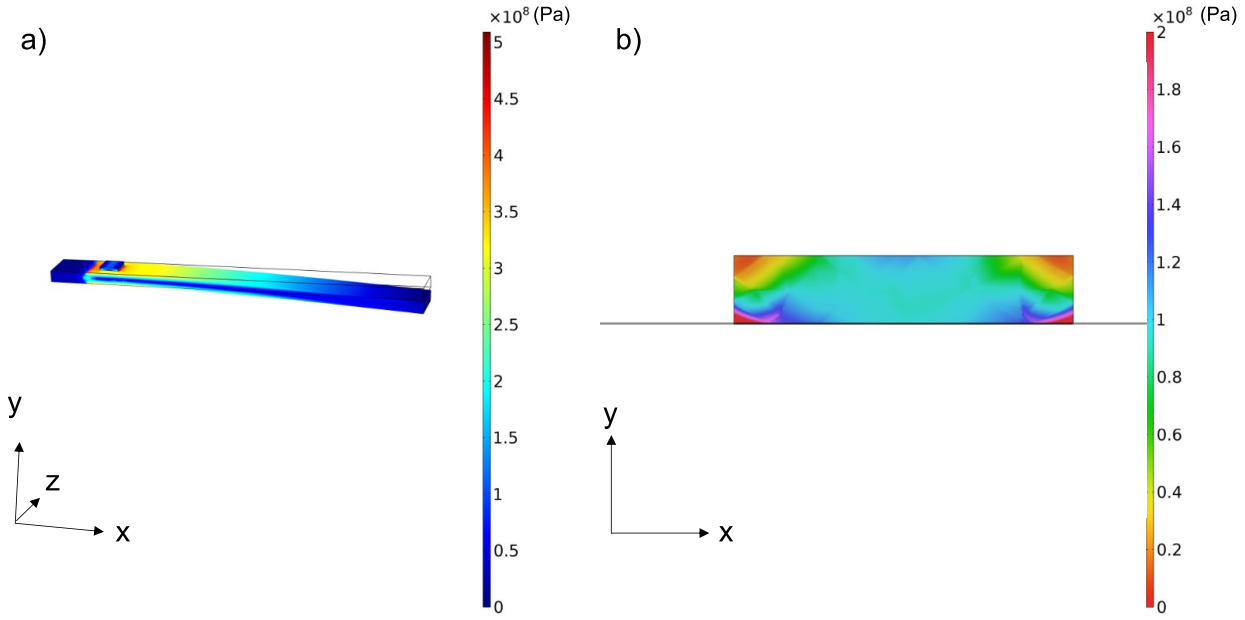

FIGURE 4.27: (a) Finite elements simulation of the Von Mises stress distribution in the global device for a beam deflection of 4mm; (b) Finite elements simulation of the Von Mises stress distribution in a slice in the xy plane of the piezoelectric material for a deflection of 4mm.

The Von Mises stress was then calculated with these initial conditions and the stress distribution in the beam and in the piezoelectric material is given in Figure 4.27(a). The analytical and finite elements simulations agreed well for the stress distribution in the beam reaching both $\approx 400MPa$ close to the fixed part for an input force of 63N. Concerning the stress distribution in the material, a slice in the xy plane with the associated values of the Von Mises stresses were simulated as shown in Figure 4.27(b). It can be noted that at the edges of the materials, finite elements calculations predict large stress heterogeneity due to boundaries effect compared to analytical calculations. However, if neglecting the boundary effect, the stress distribution was very similar to the stress predictions presented in Figure 4.26. Indeed, the average stress in this slice of material was found to be of 90MPa while it was of 80MPa for the Euler-Bernoulli beam theory.

4.2.3 Experimental results and discussion

Bipolar hysteresis loops were first tested on the ferroelectric materials with negative and positive deflections applied to the beam. This allowed to firstly characterize the response of the materials with compression and tensile stresses as well as applied electric field. It is important to note that a positive deflection corresponds here to a tensile stress, which should induce a depolarization. Conversely, a negative deflection is associated to a compressive stress which tends to increase the polarization [MLL04]. PZT-C9 were firstly investigated and the associated bipolar hysteresis curves are given in Figure 4.28.

In Figure 4.28(a) the applied deflection to the beam of 4mm was assessed in terms of tensile stress ($\approx 80MPa$) thanks to the analytical and finite element simulations presented previously. The bipolar hysteresis curve for PZT C9 at 0mm was similar

Thèse accessible à l'adresse : https://theses.insa-lyon.fr/publication/2024ISAL0017/these.pdf © [G. Taxil], [2024], INSA Lyon, tous droits réservés

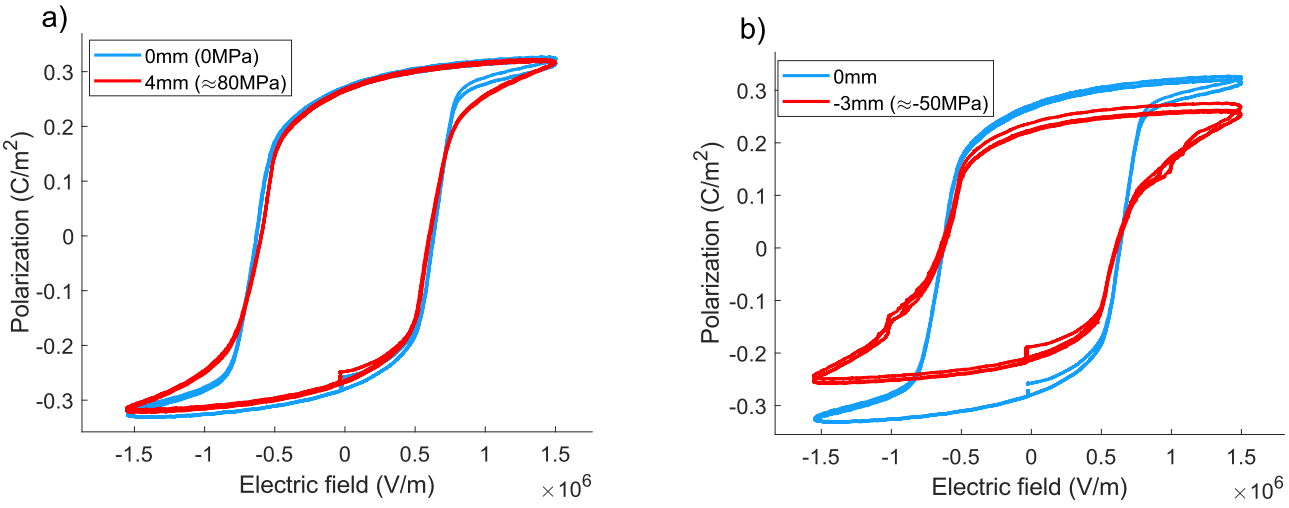

FIGURE 4.28: (a) Bipolar hysteresis curves of PZT C9 under tensile stress; (b) Bipolar hysteresis curves of PZT C9 under compressive stress

to the one obtained in Chapter 3. It can be observed that the coercive field remains constant with the applied tensile stress, which is different compared to the results in 33-mode where a decrease of the coercive field with the applied stress was observed. The induced depolarization with stress was not as high as expected. Indeed, it can be found in the literature that the piezoelectric coefficient d_{31} of soft PZT is around $\approx 300pC/N$. With levels of stress around 90MPa, the induced linear variation of polarization in 31-mode is given in a first approximation by $\Delta P_3 = d_{31}\sigma_{11}$, which give here a polarization variation around $\approx 0.03C/m^2$. However, the experimental results gave a polarization variation lesser than $0.007C/m^2$. Unfortunately, applied higher stress levels was not possible due to the materials breaking with higher deflections.

The bipolar hysteresis curve measurements under a compressive stress is illustrated in Figure 4.28(b). A large depolarization can be observed with a deflection of only -3mm ($\approx 50MPa$). However, this depolarization originates from the degradation of the material. It was observed experimentally that the materials broke and were degraded more easily under compressive in plane stress. Moreover, by applying a compressive stress, an increase of polarization was expected and desired for energy harvesting applications. Consequently, it was chosen to not pursue the investigation under compressive stress (negative deflection) as the response was not interesting for energy harvesting applications and due to the limitation of available materials.

Bipolar curves were also performed on PZN-8PT with orientations of respectively [100]L_p, [010]l_p and [001]e_p as shown in Figure 4.29. In this experiment, a first bipolar hysteresis loop was measured at 0mm (blue curve), then a similar hysteresis curve with this time a deflection of 2mm (tensile stress) was recorded (purple curve). Subsequently, a second measurement was made at 0mm after the stress application (red curve).

The first curve at 0mm displayed identical remnant and saturation polarization

Thèse accessible à l'adresse : https://theses.insa-lyon.fr/publication/2024ISAL0017/these.pdf © [G. Taxil], [2024], INSA Lyon, tous droits réservés

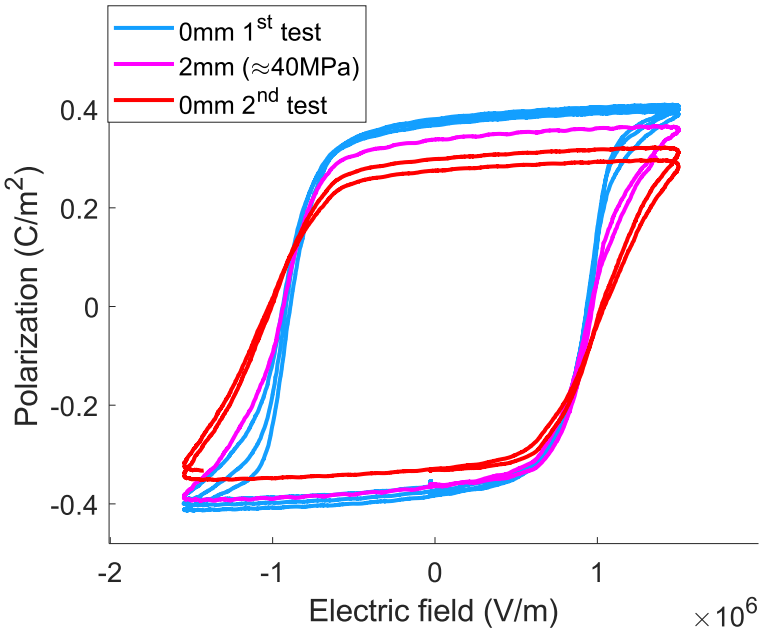

FIGURE 4.29: Bipolar hysteresis curves of PZN-8PT ([100] and [010] lateral crystal directions) under tensile stress

to the ones measured in 33-mode. However, the coercive field exhibits higher values compared to the results obtained in Chapter 3 as $E_c \approx 1kV/mm$ here while it was previously measured around $\approx 0.5kV/mm$. With a beam deflection of 2mm associated to a calculated stress of 40MPa, the performed bipolar hysteresis curve presents a depolarization of $\approx 0.05C/m^2$. This depolarization was consistent with a $d_{31} \approx -1000pC/N$, which is close to the reported ones [Sha+07]. However, it is not clear if the material response with tensile stress was due to pure intrinsic piezoelectric response or due to the degradation of the material. Indeed, the second test performed at 0mm just after the measurement with the 2mm deflection displayed a even more depolarized state, which certainly indicates a cracking or degradation of the materials. This behavior was also observed on the other tested materials and as the numbers of ferroelectric ceramics and single crystals was limited, it was decided to stop bipolar hysteresis curve measurements and to performed the real Ericsson cycles.

Real Ericsson cycles with an electric field ranging from 0 to 1500kV/mm and for different beam deflections were performed on PZN-8PT single crystals with again [100]L_p, [010]l_p and [100]e_p crystal directions. The cycles with their associated energy densities for beam deflections of 2 and 4mm are respectively given in Figure 4.30(a) and (b).

For a deflection of 2mm (Figure 4.30(a)), a negative energy density of $-26mJ/cm^3$ was obtained. This negative energy is associated with an anti-clockwise cycle rotation and means that the electrical energy required to apply the electric field is superior to the one restituted by the material which originates from the depolarization process. By increasing the deflection to 4mm (Figure 4.30(b)), the lost energy decreased and was reported to be $-14mJ/cm^3$. This reduction of lost energy with larger deflection is due to higher piezoelectric response thanks to higher applied stress. Then, the electrical work provided by the ferroelectric material increases and

Thèse accessible à l'adresse : https://theses.insa-lyon.fr/publication/2024ISAL0017/these.pdf © [G. Taxil], [2024], INSA Lyon, tous droits réservés

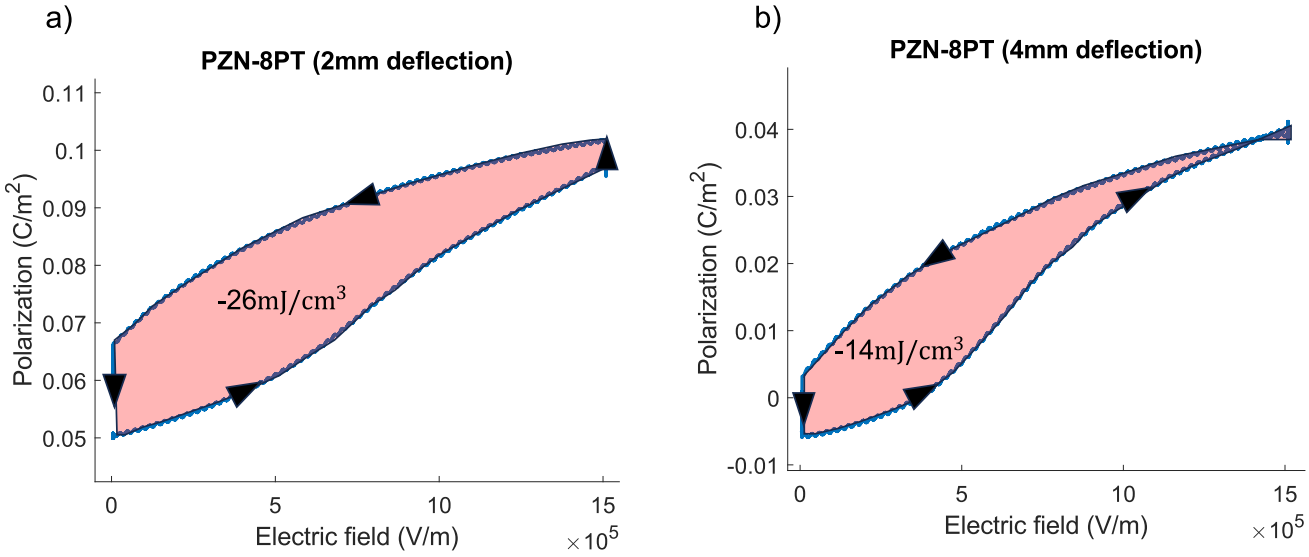

FIGURE 4.30: Bipolar Real Ericsson cycles on PZN-8PT ([100] and [010] lateral crystal directions) under different beam deflections. (a) 2mm; (b) 4mm.

almost reach the electrical work given to the system. However, this work is devoted to energy harvesting and instead, lost energy was obtained here, even at stress levels around 90MPa. A negative energy output was not expected ant it emphasizes the unique material responses in 31-mode and particularly, when the materials are bonded to a beam and subjected to high tensile stress and high electric field. It can be noted that all the materials displayed similar negative Ericsson cycles. Thus, it was decided to stop performing Ericsson cycles and try to test the materials response differently.

The third investigation aimed at having a better comprehension of such low piezoelectric response by measuring the electrical response for different oscillating beam deflections. The deflections were set to vary from 0 to 4mm and the oscillations were repeated several times to check if the piezoelectric response was lowered by repeated cycles. The corresponding force was measured and is presented in Figure 4.31(a). The associated variation of polarization was also measured and no degradation of the piezoelectricity was detected by repeating the cycles as shown in Figure 4.31(b). As it can be expected, the force and the polarization variation increased when the beam deflections were larger.

PZT C9 (soft) ceramics as well as PZN-8PT with lateral directions of respectively [100]L_p, [010]l_p and [110]L_p, [1-10]l_p and with electrodes in both crystal deposited in the [001]e_p directions were tested. For the different materials, the variation of polarization is plotted in Figure 4.32(a) as a function of the beam deflection. It can be observed that polarization variations evolve linearly for all the tested materials. However, the variations of polarization were not equivalent between the materials, which emphasizes their difference in terms of d_{31} piezoelectric coefficients. Particularly, PZN-8PT samples with lateral crystal directions of [110]L_p and [1-10]l_p exhibit a better response compared to PZT ceramic and the other lateral orientation of PZN-8PT single crystal.

The piezoelectric coefficients d_{31} were fitted from the experimental results to

Thèse accessible à l'adresse : https://theses.insa-lyon.fr/publication/2024ISAL0017/these.pdf © [G. Taxil], [2024], INSA Lyon, tous droits réservés

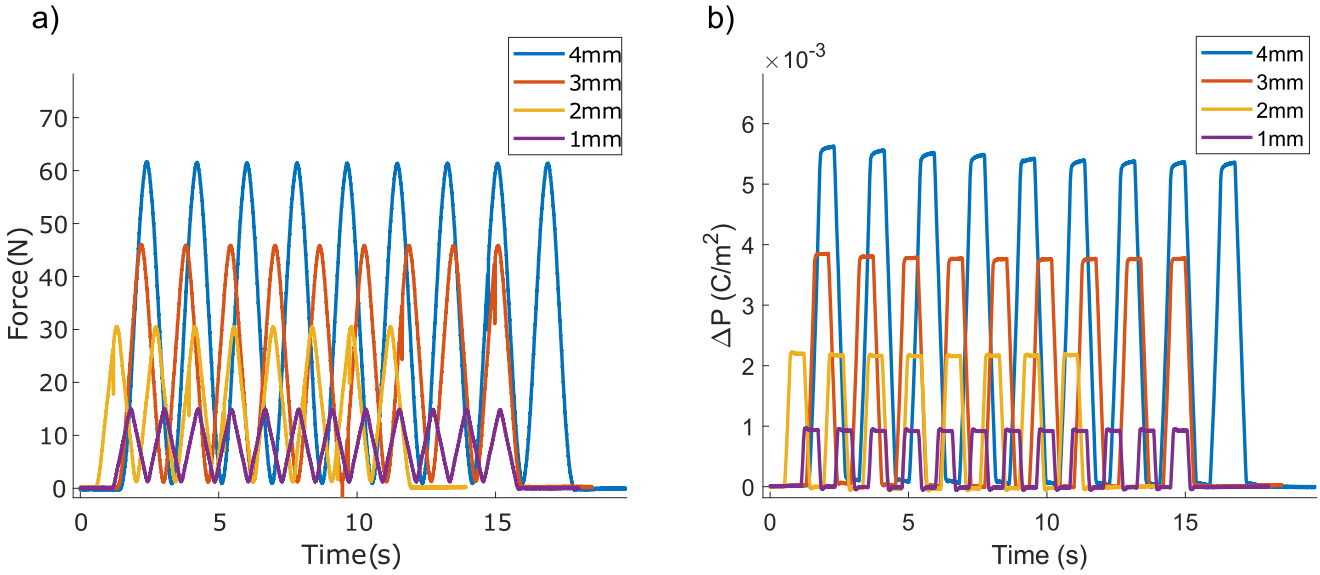

FIGURE 4.31: (a) Oscillating forces as a function of time for different beam deflections; (b) Associated variation of polarizations as a function of time for different beam deflections

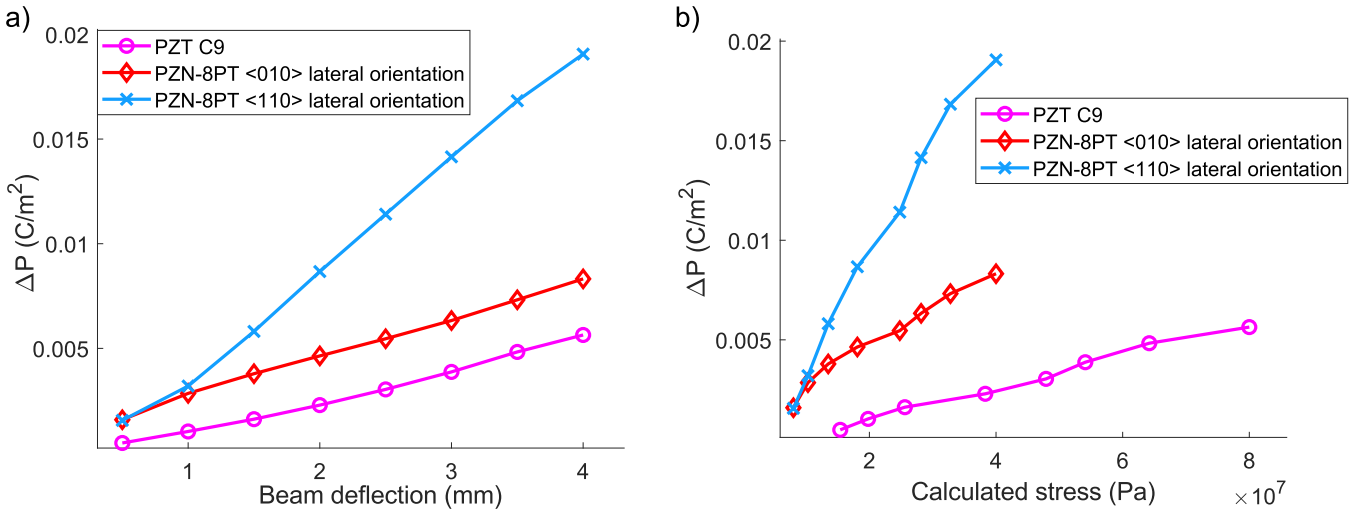

FIGURE 4.32: (a) Polarization variations as a function of the beam deflections (b) Polarization variations as a function of the associated calculated tensile stresses.

have a better comparison with literature results and understanding of the materials response. The tensile stresses were then calculated via finite elements and analytical modeling from the measured forces. It is important to note that the calculated stress for the same beam deflections are different depending on the materials due to the difference in their Young modulus. It was then possible to estimate the d_{31} piezoelectric coefficients for each materials by doing a linear fitting of the polarization variation with respect to the calculated tensile stress. The estimated d_{31} for PZT C9 was $\approx -79pC/N$, which is almost 3 times less than the coefficients reported in the literature [KC98; Li+02]. In parallel, the d_{31} piezoelectric coefficient of PZT C9 was determined without bonding the sample by analyzing the electrical impedance of the resonator at various frequencies as detailed in [**IEEE**]. The obtained d_{31} aligned with values found in existing literature, affirming that the observed low d_{31} value

Thèse accessible à l'adresse : https://theses.insa-lyon.fr/publication/2024ISAL0017/these.pdf © [G. Taxil], [2024], INSA Lyon, tous droits réservés

did not stem from deteriorated samples. For PZN-8PT single crystals with [100]L_p and [010]l_p lateral crystal directions, a d_{31} of only $-210pC/N$ was measured, which is very surprising as it was reported to be around $-1000pC/N$ in previous studies [ŠEN03; Sha+07]. For lateral orientations [110]L_p and [1-10]l_p in PZN-8PT single crystals, the d_{31} piezoelectric coefficient was estimated to be of $\approx -547pC/N$. It is difficult to find previous studies that report the d_{31} of PZN-8PT with these particular crystal orientations. The difference of performance between the two crystal cuts of PZN-8PT remains unclear. However, a higher piezoelectric activity with [110]L_p and [1-10]l_p lateral crystal direction is the main hypothesis to explain such differences.

Concerning the low value of the piezoelectric coefficients obtained when comparing with the literature, different reasons have been potentially identified. Firstly, the stress distribution is not homogeneous in the material and only a fraction of the volume of material participate to the piezoelectric activity. Indeed, as it was observed in Figure 4.27(b), some part at the edges of the material are under low tensile stress. Another possibility lies in the epoxy glue which potentially does not transmits very well the induced strain of the steel beam to the piezoelectric material. Indeed, COMSOL simulations have indicated that the transmitted stress to the material significantly varied based on the thickness of the epoxy glue as shown in Figure 4.33. This outcome underscores the crucial nature of the bonding process, as the response of the material undergoes significant changes with variations in the thickness of the deposited glue. Additionally, if the glue experiences plastic deformation under substantial stress, it can also lead to a highly degraded response.

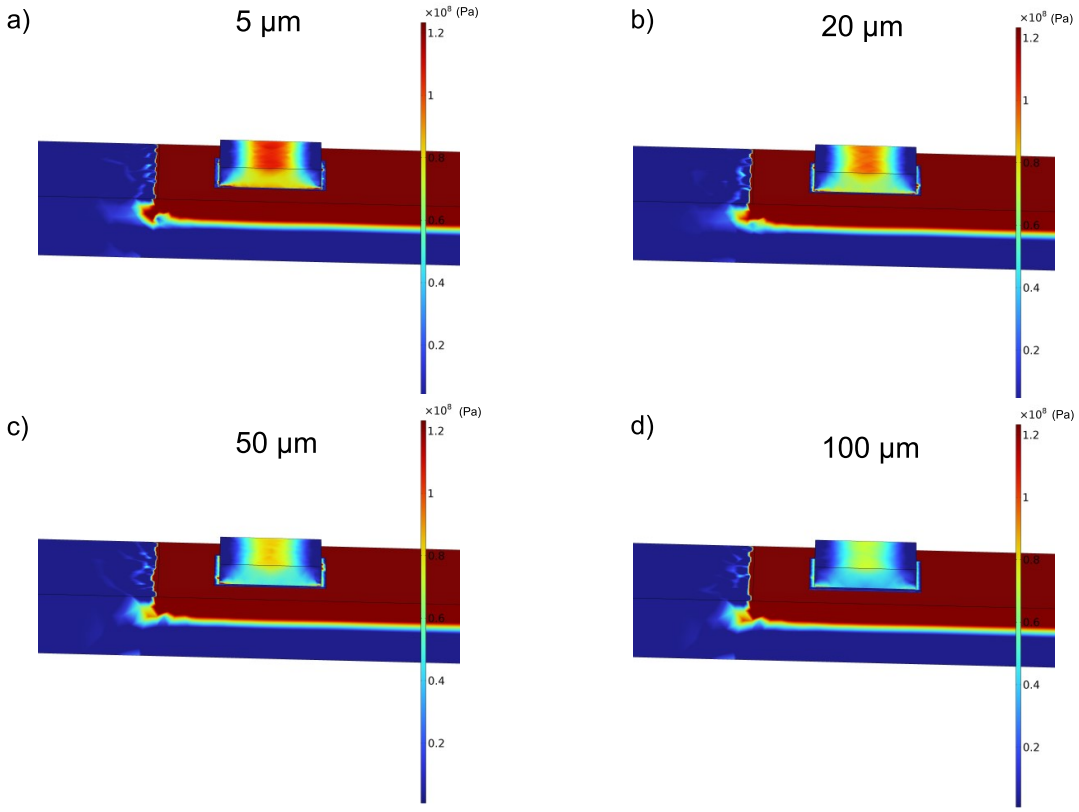

FIGURE 4.33: Finite elements simulation of the Von Mises stress distribution for a beam deflection of 4mm with different thicknesses of epoxy glue. (a) 5 μm; (b) 20 μm; (c) 50 μm; (d) 100 μm.

Thèse accessible à l'adresse : https://theses.insa-lyon.fr/publication/2024ISAL0017/these.pdf © [G. Taxil], [2024], INSA Lyon, tous droits réservés

With simple linear elasticity calculation, it appeared also that if the Poisson ratio of the steel is superior to the Poisson ratio of the piezoelectric material, it will tend to reduce the tensile stress in the piezoelectric material as a compressive stress along direction 2 will appear. However, this aspect is difficult to assess due to the discrepancies of the elastic compliance coefficient s_{12} found in the literature. Moreover, it is difficult to find this coefficient for particular crystal cuts of PZN-8PT in the literature.

All these considerations could be the bases of future works to better understand the response of ferroelectric materials when they are bonded on a substrate and subjected to high tensile stress and high electric field. It will be also interesting for future works to develop a design for high levels energy harvesting working in 31-mode but without bonding the material. Indeed, the results obtained in this work indicated so far that operating in 31-mode with a cantilever under high level of stress and electric field is not suitable for energy harvesting.

4.3 Summary

As a last step towards the use of ferroelectric material under extreme conditions for energy harvesting. This chapter focused primarily on presenting a smart tile device operating in 33-mode working with high electric field and high levels of stress thanks to a lever amplification system. A large volume of piezoelectric materials was successfully implemented in the device to enhance the output energy. Some fabrication steps of such a smart tile with the associated dimensions of the key pieces was presented. A description of the materials (PZT stacks) employed for this device along with the experimental methods for the characterization of the materials outside or within the device was also provided.

After that, this section was devoted to present the characterization results performed on the device. Ericsson cycles under various input forces were first tested on the device and the output energy at 700N was as high as 800mJ per cycle. Ericsson cycles with true steps of 500N and 700N were also realised on the tile and gave similar output energy to the ones obtained with the compression machine. Then, as synchronization of the different steps of the Ericsson cycle can be complicated for real applications, a fully passive electrical interface based on the Bennet Doubler was proposed. This simple electrical circuit composed of capacitors and diodes allowed to operate in the Q-V space with a voltage ranging from one time to two times the voltage source. Surprisingly the Bennet doubler cycle shapes outfitted those of the Ericsson cycles as some of the hysteresis of the materials can be avoided when the materials is depolarized under high voltage. The converted energy per cycle with the Bennet doubler was around 40% of the one obtained with the Ericsson cycles, which is still an important amount of energy. The output energy per cycle was finally compared to the state of the art. It appeared that our results stand out to previous work, particularly when comparing the energy per cycle with respect to the piezoelectric volume where our work was over two decades compared to the general trend.

In the second section and with in minds the investigation of the integrability of the concept, a cantilever based device working again under high electric field and

Thèse accessible à l'adresse : https://theses.insa-lyon.fr/publication/2024ISAL0017/these.pdf © [G. Taxil], [2024], INSA Lyon, tous droits réservés

high stress levels was presented. However, this device had the particularity to operate in 31-mode, which was not yet explored in this work. This device had the advantage of being able to implement the different materials and particularly single crystals which have been characterized previously in 33-mode. The elaboration processes of the cantilever beams was again provided with the key steps and parameters. The different experimental methods have been given along with the presentation of the experimental test-bench. Then, an analytical model based on the Euler Bernoulli beam theory was proposed to establish the stress in the ferroelectric materials depending on the applied force. In parallel, finite element simulations were performed to better confirm the predicted stresses.

Then, the experimental characterization of beams featuring PZT C9 ceramics and PZN-8PT single crystals with different lateral crystal directions was presented. Bipolar hysteresis curves under different beam deflections were investigated. It appeared that the induced polarization variation were very low. Moreover, degradation of the materials was observed, particularly with negative deflection (compression). It was then decided to abandon the application of compressive stresses to increase the polarization and to stop experiments with bipolar hysteresis loops.

Subsequently, real Ericsson cycles were tested to check the energy densities related to conversion abilities of the materials. The results were not successful as negative energy output was obtained. This indicated that 31-mode with cantilever beam is not suitable for energy harvesting under high levels as the required stress for materials depolarization is beyond their tensile strengths. In a final experiment, the d_{31} coefficients of the materials were characterized and it appeared that the estimated coefficients were largely inferior than the reported ones in the literature. The fundamental mechanisms of such behavior is still unclear and different possibility have been mentioned. The negative energy outputs exhibited by Ericsson cycles is surely linked to this low piezoelectric response and the unique physics of bonded materials under such extreme conditions.

The different devices presented in this Chapter emphasized that the 33-mode with the smart tile works exceptionally well when performing Ericsson cycles under high levels of stress and electric field. On the contrary, the 31-mode with the cantilever based device displays very poor potential for energy harvesting in such conditions. However, further investigations are required to fully exclude the 31-mode and one particular investigation would consider the fact to avoid using a passive substrate.

Thèse accessible à l'adresse : https://theses.insa-lyon.fr/publication/2024ISAL0017/these.pdf © [G. Taxil], [2024], INSA Lyon, tous droits réservés

Chapter 5

Conclusion and perspectives

5.1 Thesis summary

This work focused on non resonnant mechanical energy harvesting. As detailed, this approach is a good solution for random intermittent (e.g., pulsed) mechanical energy sources such as steps and tire on roads. This method is of particular interest with the actual requirements to have clean electrical generation and in the context of interconnected devices. The major issue with this approach is the low output energy. Therefore, scavenge the most energy as possibe per cycle is essential for realistic applications. This work, by considering different aspects such as the material properties, the electromechanical structure and the electrical interface aimed at enhancing the energy conversion capabilities of ferroelectric materials. Particularly, an innovative approach was to make profit of the non-linearities of polarization induced by applying high electric field and high stress to the ferroelectric materials, which was the main objective of this work.

This work encompassed diverse aspects, ranging from the fundamental characteristics of ferroelectric materials to the design of energy harvesting devices. The first chapter was then dedicated to introduce the various concepts involved in this work. Ferroelectric materials with their unique properties have been first devised. Then, the theoretical background for describing ferroelectricity and its phase transitions was presented. It was particularly important in the frame of this work as the Landau-Devonshire theory has been employed to model the material responses. The work also delved into presenting the unique features of ferrolectric relaxors $(1-x)PMN-xPT$ and $(1-\mathrm{x})\mathrm{PZN}-\mathrm{xPT}$, particularly close to their Morphotropic Phase Boundaries (MPB) where they exhibit outstanding properties. After that, Chapter 1 focused on the introduction of energy harvesting and its different scopes of applications. Specific attention was dedicated to the state of the art in mechanical energy harvesting and particularly to non resonant microgenerators as this thesis aimed at improve these systems. The different techniques existing to optimize such an approach were explored and particularly thermodynamic cycles, which allowed extracting larger energy in low frequency applications. After introducing all the necessary theoretical background of this thesis, the ANR FIESTA research project was presented highlighting that this work was conducted within the framework of this collaborative project. In this context, the introduction ended by presenting the different objectives and the outline of this work.

Understanding and predicting the nonlinearities of polarization with phase transitions was essential for this work. With such an objective, Chapter 2 focused largely on modeling thermodynamic cycles via Landau-Devonshire theory. The investigation was firstly dedicated to pyroelectric energy conversion. The novelty of this

Thèse accessible à l'adresse : https://theses.insa-lyon.fr/publication/2024ISAL0017/these.pdf © [G. Taxil], [2024], INSA Lyon, tous droits réservés

work was to employ phenomenological theory to model Olsen cycles in different crystal orientations. To validate the approach, an equivalence between the electrocaloric effect (ECE) and the harvested energy was made. The obtained results were compared to existing experimental results of the ECE in particular crystal orientations as a lot of works can be found in the literature. Simulation results agreed well and particularly, a negative ECE was observed for <001> oriented crystals at the R-T transition for PMN-30PT and at the O-T transition for barium titanate. This work, to the best knowledge of the author, is the first to explain such a behavior using a phenomenological approach. For pyroelectric energy harvesting, it appeared that various ferroelectric-ferroelectric (FE-FE) transitions yield different outcomes based on crystal orientations. Some transitions proved to be favorable for energy harvesting, while others, indicated by a negative ECE, are less profitable. Notably, across all modeled scenarios, the ferroelectric-paraelectric (FE-PA) transition consistently maximizes output energy. This result is unsurprising, given the substantial polarization variation occurring at the Curie temperature. Nevertheless, leveraging FE-FE transitions could present a viable alternative for enhancing energy harvesting in materials characterized by excessively high Curie temperatures (approximately 100°C). Modeling of Ericsson cycles for mechanical energy harvesting was then presented. The modeling approach for the cycles was initially introduced, outlining the theoretical framework and assumptions employed in simulating PMN-25PT and PZN-8PT single crystals with <001> orientation for comparison with the experimental reults of Chapter 3. Moreover, the modeling scope was expanded to encompass various crystallographic orientations. This extension involved introducing two coordinate systems and providing detailed explanations of the calculations used to express various physical properties, with a specific focus on the piezoelectric coefficients. A comparative analysis was conducted between high-level energy harvesting using the Ericsson cycle and low-level harvesting through the piezoelectric coefficient. Notably, the symmetries exhibited significant differences in both cases. Particularly under high electric field and uniaxial stress, the harvested energy demonstrated a more homogeneous distribution. This highlights the distinctive nature of energy harvesting under non-resonant conditions and extreme circumstances, challenging the conventional approach of using 4R domain-engineered crystals in such scenarios. The utilization of nonlinearities and phase transitions introduces unique behaviors, suggesting that operating along the spontaneous polarization direction could be more advantageous.

Then, Chapter 3 presented the characterization results of ferroelectric materials under conditions of high electric field and high uniaxial stress, and varying temperatures. Initially, the work focused to assessing the electromechanical energy conversion efficiency of different ferroelectric materials, including hard PZT C203 ceramic, medium PZT C6 ceramic, soft PZT C9 ceramic, PMN 15 paraelectric ceramic, as well as PMN-25PT and PZN-8PT single crystals. Characterizations were performed at room temperature by executing real Ericsson cycles with successive steps under two distinct levels of compressive stress-intermediate (30 MPa) and high (100 MPa)-accompanied by an electric field of 1500 kV/m. Notably, PZN-8PT <001>-oriented crystals exhibited the highest potential for energy conversion, achieving an energy density of 235.6 mJ/cm^3 attributed to nonlinearities induced by the high compressive stress. However, under high electric field and stress conditions, the energy conversion performance of PZT C9 ceramic was comparable to that of PMN-25PT single crystal, displaying an energy density of 118.7 mJ/cm^3. This result underscores the

Thèse accessible à l'adresse : https://theses.insa-lyon.fr/publication/2024ISAL0017/these.pdf © [G. Taxil], [2024], INSA Lyon, tous droits réservés

convergence of material energy density under high levels, and highlighted differences between low-level and high-level energy harvesting. The subsequent phase of the work focused solely on PZN-8PT and PMN-25PT <001>-oriented crystals. This deliberate choice aimed to deepen understanding of how to leverage phase transitions and associated polarization mechanisms in the context of high-level energy harvesting. Furthermore, this investigation facilitated the application of the model developed in Chapter 2 to gain better insights into material responses. Experimental and theoretical results aligned well, with in-plane switching of polarization reported in PZN-8PT at all considered temperatures, even under high electric field when subjected to compressive stress. For PMN-25PT, such in-plane switching occurred under specific conditions (high temperature and low electric field), in line with predictions from simulations. The optimal operating temperature for the Ericsson cycle was determined for both crystals, emphasizing peak performance when the crystal becomes fully tetragonal. This observation holds potential for extrapolation to all <001> oriented ferroelectric crystals under conditions of significant stress, allowing in-plane switching. Under high stress conditions, operating in alignment with the polarization direction was found to produce the highest energy densities, contradicting conclusions drawn from domain-engineered crystals. The experimental investigation was also extended to <111>-oriented PMN-30PT, exhibiting a rhombohedral structure with polarization along the [111]$_c$ direction at 20°C. Despite the almost tenfold superiority of the $d33$ piezoelectric coefficients of the <001> orientation compared to the <111> orientation in PMN-30PT at room temperature, experiments and simulations of Ericsson cycles under high stress and electric field revealed similar energy levels. These results emphasized again the distinctive characteristics of high-level mechanical energy harvesting compared to low-level scenarios, though further experiments at different temperatures and under varying uniaxial stress are needed to confirm these findings.

To finalize the demonstration of the interest of ferroelectric materials under extreme conditions for energy harvesting, the last chapter was then dedicated to implement these materials in real devices. Primarily, it focused on introducing a smart tile device operating in 33-mode under high electric field and substantial levels of stress, facilitated by a lever amplification system. A significant volume of piezoelectric materials was successfully integrated into the device to enhance the output energy. The fabrication steps of this smart tile, including the dimensions of key components, were presented. Following this, the section delved into presenting the characterization results obtained from the device. Ericsson cycles under various input forces were conducted, revealing an impressive output energy of up to 800mJ per cycle at 700N. Ericsson cycles with true steps of 500N and 700N were also performed on the tile, yielding similar output energy to those obtained with the compression machine. Recognizing the potential complexity of synchronizing different steps in real applications, a fully passive electrical interface based on the Bennet Doubler was proposed. This simple electrical circuit, comprising capacitors and diodes, allowed operation in the Q-V space with a voltage ranging from one to two times the voltage source value. Surprisingly, the Bennet doubler cycle shapes outperformed those of the Ericsson cycles thanks to lower hysteresis losses. With approximately 40% of the converted energy per cycle compared to the Ericsson cycles, the Bennet doubler exhibits a significant amount of scavenged energy. The output energy per cycle was then compared to the state of the art, revealing that the results surpassed previous works, especially when considering energy per cycle relative to the piezoelectric volume. In the subsequent section, with in mind the developement of

Thèse accessible à l'adresse : https://theses.insa-lyon.fr/publication/2024ISAL0017/these.pdf © [G. Taxil], [2024], INSA Lyon, tous droits réservés

a more integrated device, a cantilever-based device designed to operate under high electric field and stress levels was introduced. This device operated in 31-mode, an aspect not previously explored in this work. One notable advantage of this device was its capability to incorporate various materials, particularly single crystals characterized earlier in 33-mode. The fabrication processes of the cantilever beams were elucidated, highlighting key steps and parameters. Comprehensive details on experimental methods were provided, and an analytical model based on the Euler-Bernoulli beam theory was introduced to determine stress in ferroelectric materials based on the applied force. Additionally, finite element simulations were conducted to validate the predicted stresses. The experimental characterization of beams featuring PZT C9 ceramics and PZN-8PT single crystals with different lateral crystal directions was then presented. Bipolar hysteresis curves under various beam deflections were investigated, revealing minimal induced polarization variations and material degradation, especially under negative deflection (compression). Real Ericsson cycles were conducted to assess the energy densities associated with the materials conversion capabilities. However, the results were not successful, indicating a negative energy output. This suggested that 31-mode with a cantilever beam is unsuitable for energy harvesting under high levels, as the required stress for material depolarization exceeds their tensile strengths. In a final experiment, the d_{31} coefficients of the materials were characterized, revealing values much lower than those reported in the literature. The underlying mechanisms of this behavior still remain unclear, with various possibilities mentioned. The negative energy outputs observed in Ericsson cycles are undoubtedly linked to this low piezoelectric response and the unique physics of bonded materials under extreme conditions.

To conclude, by considering the modeling, the characterization and the implementation of ferroelectric materials, this work enlightened their unique potential of ultra-high energy conversion when they are subjected to sufficient levels of stress and electric field. The nonlinearities of polarization induced by these conditions, conventionnaly considered as counter-productive, have been demonstrated as an effective solution for devices operating in non-resonant conditions. However, future works could aimed at improving different aspects of this thesis.

5.2 Perspectives

This thesis considered different ways to improve the converted energy of ferroelectric materials in non-resonnant conditions. Certain aspects examined in this work could undergo further exploration, while potential avenues not addressed in this research could serve as the foundation for future investigations. A non-exhaustive list of these possibilities will be provided for possibly continue this work:

- Concerning the modeling of ferroelectric materials for energy harvesting, further investigations could add a Ginzburg term to the free energy to take into account extrinsic contributions. Indeed, only a single ferrorelectric domain was examined in the simulations and adding domains and their interactions can modify the material response.
- Enhancing the applied stress and the electric field for the Ericsson cycles in 33-mode could allow observing the convergence of the energy densities between all the materials and will permit to increase even more the harvested energy per cycle reported in this work.

Thèse accessible à l'adresse : https://theses.insa-lyon.fr/publication/2024ISAL0017/these.pdf © [G. Taxil], [2024], INSA Lyon, tous droits réservés

- Developing a new electrical interface could be another possibility. Indeed, despite having the advantage to be a fully passive circuit, the Bennet Doubler allowed to scavenge only 40% of the Ericsson cycle. Then, future studies could develop a new electrical circuit, possibly derived from the Bennet doubler, such as cascaded Bennet circuits to adjust the voltage ratio and then fit more the Ericsson cycle in the Q-V space.
- Utilizing Ericsson cycles with tensile stress and compressive stresscould be another avenue. It has been shown that it is possible to mechanically pole ferroelectric materials. Therefore, future studies could made profit of alternating positive and negative stress to the materials to avoid some of the hysteresis in the 1-2 process (application of the electric at the constant low stress level) of the Ericsson cycle. This could further enhance the energy converted per cycle.
- Designing a device that could efficiently work in 31-mode. Indeed, the cantilever beam-based device developed in this work was not efficient for energy harvesting under high levels with Ericsson cycles. However, the 31-mode is not to exclude if a new device design permits avoiding the bonding of the material. Further investigations could focus then on developing such a device.

Thèse accessible à l'adresse : https://theses.insa-lyon.fr/publication/2024ISAL0017/these.pdf © [G. Taxil], [2024], INSA Lyon, tous droits réservés

Thèse accessible à l'adresse : https://theses.insa-lyon.fr/publication/2024ISAL0017/these.pdf © [G. Taxil], [2024], INSA Lyon, tous droits réservés

Publications

Peer reviewed articles

- **Gaspard Taxil**, Mickaël Lallart, Benjamin Ducharne, Tung Thanh Nguyen, Hiroki Kuwano, Takahito Ono and Gaël Sebald, "Modeling of Olsen cycle for pyroelectric energy harvesting and assessment of abnormal electrocaloric effect in ferroelectric single crystals", Journal of Applied physics, 132 (2022) 144101
- **Gaspard Taxil**, Gaël Sebald, Tung Thanh Nguyen, Benjamin Ducharne, Hung Hoang Nguyen, Takahito Ono, Hiroki Kuwano and Mickaël Lallart, "Stress and electric field induced phase transitions for ultra high energy conversion in ferroelectrics", Acta Materialia, 261 (2023) 119367
- **Gaspard Taxil**, Mickaël Lallart, Hung Hoang Nguyen, Benjamin Ducharne, Hiroki Kuwano, Takahito Ono and Gaël Sebald, "Anisotropy breaking in high level piezoelectric energy harvesting", Scripta Materialia (Under review)
- Tung Thanh Nguyen, **Gaspard Taxil**, Hung Hoang Nguyen, Benjamin Ducharne, Mickaël Lallart, Elie Lefeuvre, Hiroki Kuwano and Gaël Sebald, "Ultimate electromechanical energy conversion performance and energy storage capacity of ferroelectric materials under high excitation levels", Applied energy, 326 (2022) 119984
- Gaël Sebald, Tung Thanh Nguyen, **Gaspard Taxil**, Benjamin Ducharne, Jhordan Chavez, Takahito Ono, Hiroki Kuwano, Elie Lefeuvre and Mickaël Lallart, "Piezoelectric small scale generator: towards near-Joule output energy generation", Smart Materials and Structures, 32 (2023) 085009

International conference presentations

- **Gaspard Taxil**, Mickaël Lallart, Benjamin Ducharne, Tung Thanh Nguyen, Hiroki Kuwano, Takahito Ono and Gaël Sebald, "Modeling of Olsen cycle for pyroelectric energy harvesting and assessment of abnormal electrocaloric effect in ferroelectric single crystals", International Workshop on Piezoelectric Materials and Applications in Actuators (Online 24-26 October 2022)
- **Gaspard Taxil**, Gaël Sebald, Tung Thanh Nguyen, Benjamin Ducharne, Takahito Ono , Hung Hoang Nguyen, Hiroki Kuwano and Mickaël Lallart, "Ferroelectric Materials and Their Phase Transitions for Energy Harvesting", International Symposium on Applications of Ferroelectrics (Cleveland, USA, 23-27 July 2023)

Thèse accessible à l'adresse : https://theses.insa-lyon.fr/publication/2024ISAL0017/these.pdf © [G. Taxil], [2024], INSA Lyon, tous droits réservés

- **Gaspard Taxil**, Gaël Sebald, Benjamin Ducharne, Tung Thanh Nguyen, Hung Hoang Nguyen, Takahito Ono, Hiroki Kuwano and Mickaël Lallart, "Characterization and Implementation of Piezoelectric Energy Harvesting under Ultra-high Levels", International Conference on Advanced Electromaterials 2023 (Jeju, South Korea, 31 October-3 November 2023)

Workshop presentations

- **Gaspard Taxil**, Mickaël Lallart, Gaël Sebald, Elie Lefeuvre, Benjamin Ducharne, Merieme Ouhabaz, Hiroki Kuwano, Tung Thanh Nguyen, "Modeling ferroelectric phase transitions for energy harvesting", ELyT Workshop (Online 21-25 June 2021)
- **Gaspard Taxil**, Mickaël Lallart, Benjamin Ducharne, Tung Thanh Nguyen, Hiroki Kuwano, Takahito Ono and Gaël Sebald, "Modeling of Olsen cycle for pyroelectric energy harvesting and assessment of abnormal electrocaloric effect in ferroelectric single crystals", ELyT Workshop (Lyon, France, 16-18 November 2022)

Poster presentations

- **Gaspard Taxil**, Gaël Sebald, Benjamin Ducharne, Tung Thanh Nguyen, Takahito Ono, Hung Hoang Nguyen, Hiroki Kuwano and Mickaël Lallart, "Phase transition in ferroelectric single crystals for ultra high energy harvesting ", Journées Nationales sur la Récupération et le Stockage de l'Energie 2023 (Paris, France, 12-13 June 2023)

Thèse accessible à l'adresse : https://theses.insa-lyon.fr/publication/2024ISAL0017/these.pdf © [G. Taxil], [2024], INSA Lyon, tous droits réservés

Acknowledgements

This doctoral thesis was conducted in collaboration between INSA Lyon and Tohoku University, and I express my gratitude to all those who contributed in any way to the completion of this work.

First and foremost, I extend my heartfelt thanks to Professor Mickaël Lallart, who chose to place trust in me for this academic journey and consistently provided unwavering support. His invaluable guidance throughout my thesis was crucial to the development of this manuscript.

I am also deeply appreciative of Professor Takahito Ono for graciously hosting me at Tohoku University and for his kindness. His expertise and support played a pivotal role in the success of this project.

I extend my acknowledgment to Professor Gaël Sebald for welcoming me to ELyTMaX and engaging in fruitful scientific discussions. These interactions served as a significant source of motivation, contributing to the understanding and realization of this work.

I express my gratitude to Dr. Benjamin Ducharne for assisting me throughout the completion of this project. His support has been invaluable, and I appreciate not only his guidance as a supervisor but also his role as a wonderful friend.

I deeply thank Professor Hiroki Kuwano for warmly welcoming me into his laboratory, establishing my comfort from the outset, and providing invaluable guidance throughout my research.

I would like like to express my gratitude to all the members of the ANR FIESTA project, with special thanks to Ausrine, Elie, and Alexis for the valuable advices and very nice moments we shared during our time together in South Korea and Sendai.

I sincerely thank all the individuals at LGEF, INSA Lyon, for their kindness and the wonderful moments we experienced together. A special appreciation goes to the PhD students Amaury, Giulia, Leopold, and Elliott for the enjoyable times we shared. I am grateful to Yuanyuan for always being available to lend assistance, Omar for being directly a nice friend, Foamie for your kindness, and Guilhem for consistently bringing positivity with your good mood. I also extend my gratitude to all the permanent staff, with special mention to Professor Claude Richard for consistently being kind to me. Fred, in your unique way, I had many pleasant moments. Evelyne, thank you for always being helpful and, at the same time, very kind.

In my stay in Sendai, I would like to thank all the members of ELyTMaX, of Ono's laboratory and Kuwano's laboratory. I want to have a particular thanks to Sylvain and Kostas for the nice coffee discussions, Sayaka for your help on the Japanese bureaucracy and the nice karaoke ! Jean-Yves for always been interested in my work and having been super nice with me. Hung san for your huge help and your transfer of knowledge, Toda-sensei for always being nice and curious about my work. Matsuda-san for managing my registration and your help. Ou-san for the nice moments. On a broader note, I extend my appreciation to all the wonderful individuals I encountered in Sendai. A special mention goes to Vilma, Taisei-san, and Tani-san

Thèse accessible à l'adresse : https://theses.insa-lyon.fr/publication/2024ISAL0017/these.pdf © [G. Taxil], [2024], INSA Lyon, tous droits réservés

for the delightful party we shared. I want to acknowledge Suzuki-san for his exceptional bartending skills and express gratitude to Takuya for being the most outstanding and funny chef.

I would like to offer special thanks to my friends from Briançon for their constant presence and the incredible times we've shared throughout the years. My grandmother for the hospitality in Lyon and her cook skills. Gratitude is extended to all my sisters, my brother, and my parents for their unwavering support and constant presence in my life.

A heartfelt thank you goes to Giulia for your contribution in your way to the success of this work and for the amazing years we've spent together in Japan, as well as for the years to come.

Finally, I extend my apologies and wish to express gratitude to anyone inadvertently omitted from my acknowledgments.

...

Thèse accessible à l'adresse : https://theses.insa-lyon.fr/publication/2024ISAL0017/these.pdf © [G. Taxil], [2024], INSA Lyon, tous droits réservés

Bibliography

[AAMF19] Saifuddin Ahmad, Muhammad Abdul Mujeebu, and Mohd. Ahmadullah Farooqi. "Energy harvesting from pavements and roadways: A comprehensive review of technologies, materials, and challenges". In: *International Journal of Energy Research* 43 (2019), pp. 1974–2015.

[AC98] R. Amirtharajah and A.P. Chandrakasan. "Self-powered signal processing using vibration-based power generation". In: *IEEE Journal of Solid-State Circuits* 33 (1998), pp. 687–695.

[Aco+17] Matias Acosta et al. "BaTiO3-based piezoelectrics: Fundamentals, current status, and perspectives". In: *Applied Physics Reviews* 4 (2017).

[AFI88a] Kazuhide Abe, Osamu Furukawa, and Hiroshi Imagawa. In: *Ferroelectrics* 87 (1988), p. 55.

[AFI88b] Kazuhide Abe, Osamu Furukawa, and Hiroshi Imagawa. "Calculations concerning the phase diagram, dielectric constant and lattice parameters for the $Pb(Zn_{1/3}Nb_{2/3})O_3 - PbTiO_3$ solid solution". In: *Ferroelectrics* 87 (1988), pp. 55–64.

[AKK21] Muhammad Masood Ahmad, Nadia Masood Khan, and Farid Ullah Khan. "Review of frequency up-conversion vibration energy harvesters using impact and plucking mechanism". In: *International Journal of Energy Research* 45.11 (2021), pp. 15609–15645.

[Ami+07] Ahmed Amin et al. "Mechanical and thermal transitions in morphotropic PZN-PT and PMN-PT single crystals and their implication for sound projectors". In: *IEEE transactions on ultrasonics, ferroelectrics, and frequency control* 54 (2007), pp. 1090–1095.

[Ann+17] Venkateswarlu Annapureddy et al. "Magnetic energy harvesting with magnetoelectrics: an emerging technology for self-powered autonomous systems". In: *Sustainable Energy Fuels* 1 (2017), pp. 2039–2052.

[AYH14] Abdessattar Abdelkefi, Zhimiao Yan, and Muhammad R Hajj. "Performance analysis of galloping-based piezoaeroelastic energy harvesters with different cross-section geometries". In: *Journal of Intelligent Material Systems and Structures* 25 (2014), pp. 246–256.

[Bai+19] Gang Bai et al. "Large negative piezocaloric effect: Uniaxial stress effect". In: *Solid State Communications* 291 (2019), pp. 11–14.

[Bar+00] Y. Barad et al. "Composition, temperature, and crystal orientation dependence of the linear electro-optic properties of Pb(Zn1/3Nb2/3)O3–PbTiO3 single crystals". In: *Applied Physics Letters* 77 (2000), pp. 1247–1249.

[BD83] Gerald Burns and F. H. Dacol. "Crystalline ferroelectrics with glassy polarization behavior". In: *Phys. Rev. B* 28 (1983), pp. 2527–2530.

[Bha+14] Bikram Bhatia et al. In: *Journal of Applied Physics* 116 (2014), p. 194509.

Thèse accessible à l'adresse : https://theses.insa-lyon.fr/publication/2024ISAL0017/these.pdf © [G. Taxil], [2024], INSA Lyon, tous droits réservés

[BO09] Stephen P Beeby and Terence O'Donnell. "Electromagnetic energy harvesting". In: *Energy Harvesting Technologies* (2009), pp. 129–161.

[Bov+04] Viktor Bovtun et al. "Central-peak components and polar soft mode in relaxor PbMg1/3Nb2/3O3 crystals". In: *Ferroelectrics* 298 (2004), pp. 23–30.

[Bow+14] Chris R Bowen et al. "Pyroelectric materials and devices for energy harvesting applications". In: *Energy & Environmental Science* 7 (2014), pp. 3836–3856.

[BTW06] S P Beeby, M J Tudor, and N M White. "Energy harvesting vibration sources for microsystems applications". In: *Measurement Science and Technology* 17 (2006), R175.

[BWQ15] Yang Bai, De Wei, and Li-Jie Qiao. In: *Applied Physics Letters* 107 (2015), p. 192904.

[Cao08a] Wenwu Cao. "Constructing Landau-Ginzburg-Devonshire Type Models for Ferroelectric Systems Based on Symmetry". In: *Ferroelectrics* 375 (2008), pp. 28–39.

[Cao08b] Wenwu Cao. "Constructing Landau-Ginzburg-Devonshire Type Models for Ferroelectric Systems Based on Symmetry". In: *Ferroelectrics* 375 (Dec. 2008), pp. 28–39. DOI: 10.1080/00150190802437845.

[Che+13] Guangzhu Chen et al. "Development and experiments of a micro piezoelectric vibration energy storage device". In: *Mechanical Systems and Signal Processing* 40 (2013), pp. 377–384.

[Cho+06] WJ Choi et al. "Energy harvesting MEMS device based on thin film piezoelectric cantilevers". In: *Journal of Electroceramics* 17 (2006), pp. 543–548.

[Chu+13] Rami Chukka et al. In: *AIP Advances* 3 (2013), p. 072118.

[CL07] Premi Chandra and Peter Littlewood. "A Landau Primer for Ferroelectrics". In: vol. 105. 2007, pp. 69–116.

[Cle+21] Giacomo Clementi et al. "$LiNbO_3$ films – A low-cost alternative lead-free piezoelectric material for vibrational energy harvesters". In: *Mechanical Systems and Signal Processing* 149 (2021), p. 107171.

[Coh92] Ronald E Cohen. "Origin of ferroelectricity in perovskite oxides". In: *Nature* 358 (1992), pp. 136–138.

[CSS20] Cheng Chen, Amir Sharafi, and Jian-Qiao Sun. "A high density piezoelectric energy harvesting device from highway traffic–Design analysis and laboratory validation". In: *Applied Energy* 269 (2020), p. 115073.

[Dam05] Dragan Damjanovic. "Contributions to the Piezoelectric Effect in Ferroelectric Single Crystals and Ceramics". In: *Journal of the American Ceramic Society* 88 (2005), pp. 2663–2676.

[Dam98] Dragan Damjanovic. "Ferroelectric, dielectric and piezoelectric properties of ferroelectric thin films and ceramics". In: *Reports on progress in physics* 61 (1998), p. 1267.

[Dav06] Matthew Davis. "Phase transitions, anisotropy and domain engineering the piezoelectric properties of relaxor-ferroelectric single crystals". PhD thesis. 2006.

Thèse accessible à l'adresse : https://theses.insa-lyon.fr/publication/2024ISAL0017/these.pdf © [G. Taxil], [2024], INSA Lyon, tous droits réservés

[Dav07] Matthew Davis. "Picturing the elephant: Giant piezoelectric activity and the monoclinic phases of relaxor-ferroelectric single crystals". In: *Journal of Electroceramics* 19 (2007), pp. 25–47.

[Dav+07] Matthew Davis et al. "Rotator and extender ferroelectrics: Importance of the shear coefficient to the piezoelectric properties of domain-engineered crystals and ceramics". In: *Journal of Applied Physics* 101 (2007).

[DBS02] Dragan Damjanovic, Franziska Brem, and Nava Setter. "Crystal orientation dependence of the piezoelectric d 33 coefficient in tetragonal BaTiO 3 as a function of temperature". In: *Applied physics letters* 80 (2002), pp. 652–654.

[DDS06a] Matthew Davis, Dragan Damjanovic, and Nava Setter. "Electric-field-, temperature-, and stress-induced phase transitions in relaxor ferroelectric single crystals". In: *Phys. Rev. B* 73 (2006), p. 014115.

[DDS06b] Matthew Davis, Dragan Damjanovic, and Nava Setter. "Temperature dependence of the direct piezoelectric effect in relaxor-ferroelectric single crystals: Intrinsic and extrinsic contributions". In: *Journal of Applied Physics* 100 (2006), p. 084103.

[Dev] URL: https://www.statista.com/statistics/471264/iot-number-of-connected-devices-worldwide/ (visited on 09/30/2023).

[Dev49] A.F. Devonshire. "XCVI. Theory of barium titanate". In: *The London, Edinburgh, and Dublin Philosophical Magazine and Journal of Science* 40 (1949), pp. 1040–1063.

[Dha+13] Lokesh Dhakar et al. "A new energy harvester design for high power output at low frequencies". In: *Sensors and Actuators A: Physical* 199 (2013), pp. 344–352.

[DUN97] Aydin Dogan, Kenji Uchino, and Robert E Newnham. "Composite piezoelectric transducer with truncated conical endcaps" cymbal"". In: *IEEE Transactions on Ultrasonics, Ferroelectrics, and Frequency Control* 44 (1997), pp. 597–605.

[Elf+09] R Elfrink et al. "Vibration energy harvesting with aluminum nitride-based piezoelectric devices". In: *Journal of Micromechanics and Microengineering* 19 (2009), p. 094005.

[Eri+05] M Ericka et al. "Energy harvesting from vibration using a piezoelectric membrane". In: *Journal de Physique IV (Proceedings)*. Vol. 128. 2005, pp. 187–193.

[Est+17] Giovanni Esteves et al. "Electric-field-induced structural changes in multilayer piezoelectric actuators during electrical and mechanical loading". In: *Acta materialia* 132 (2017), pp. 96–105.

[Fan+06] Hua-Bin Fang et al. "Fabrication and performance of MEMS-based piezoelectric power generator for vibration energy harvesting". In: *Microelectronics Journal* 37 (2006), pp. 1280–1284.

[FC00] Huaxiang Fu and Ronald E Cohen. "Polarization rotation mechanism for ultrahigh electromechanical response in single-crystal piezoelectrics". In: *Nature* 403 (2000), pp. 281–283.

Thèse accessible à l'adresse : https://theses.insa-lyon.fr/publication/2024ISAL0017/these.pdf © [G. Taxil], [2024], INSA Lyon, tous droits réservés

[FGS08] Joel Feenstra, Jon Granstrom, and Henry Sodano. "Energy harvesting through a backpack employing a mechanically amplified piezoelectric stack". In: *Mechanical Systems and Signal Processing* 3 (2008), pp. 721–734.

[Fri+12] Michael I Friswell et al. "Non-linear piezoelectric vibration energy harvesting from a vertical cantilever beam with tip mass". In: *Journal of Intelligent Material Systems and Structures* 23 (2012), pp. 1505–1521.

[GG02] Gustav Gautschi and Gustav Gautschi. "Piezoelectric sensors". In: *Piezoelectric Sensorics: Force Strain Pressure Acceleration and Acoustic Emission Sensors Materials and Amplifiers* (2002), pp. 73–91.

[GGL09] Vitaly L Ginzburg, Vitaly Lazarevich Ginzburg, and LD Landau. *On the theory of superconductivity*. Springer, 2009.

[Gig+22] Lorenzo Gigli et al. "Thermodynamics and dielectric response of BaTiO3 by data-driven modeling". In: *npj Computational Materials* 8 (2022), p. 209.

[GM59] Robert Gerson and Thomas C Marshall. "Development and Comparison of Two X-Ray Methods for Determining the Crystallinity of Cotton Cellulose". In: *Journal of Applied Physics* 30 (1959), pp. 1650–1653.

[GPS00] PM Gehring, S-E Park, and G Shirane. "Soft phonon anomalies in the relaxor ferroelectric Pb (Zn 1/3 Nb 2/3) 0.92 Ti 0.08 O 3". In: *Physical review letters* 84 (2000), p. 5216.

[GPS08a] Daniel Guyomar, Sebastien Pruvost, and Gael Sebald. "Energy harvesting based on FE-FE transition in ferroelectric single crystals". In: *IEEE Transactions on Ultrasonics, Ferroelectrics, and Frequency Control* 55 (2008), pp. 279–285.

[GPS08b] Daniel Guyomar, Sebastien Pruvost, and Gael Sebald. "Energy harvesting based on FE-FE transition in ferroelectric single crystals". In: *IEEE transactions on ultrasonics, ferroelectrics, and frequency control* 55 (2008), pp. 279–285.

[GPS08c] Daniel Guyomar, Sebastien Pruvost, and Gael Sebald. "Energy harvesting based on FE-FE transition in ferroelectric single crystals". In: *IEEE transactions on ultrasonics, ferroelectrics, and frequency control* 55 (2008), pp. 279–285.

[GSK11] D Guyomar, G Sebald, and Hiroki Kuwano. "Energy harvester of 1.5 cm3 giving output power of 2.6 mW with only 1 G acceleration". In: *Journal of intelligent material systems and structures* 22 (2011), pp. 415–420.

[Guo+21] X.W. Guo et al. In: *Acta Materialia* 206 (2021), p. 116639.

[Guy+05] D. Guyomar et al. "Toward energy harvesting using active materials and conversion improvement by nonlinear processing". In: *IEEE Transactions on Ultrasonics, Ferroelectrics, and Frequency Control* 52 (2005), pp. 584–595.

[GW08] Frank Goldschmidtboeing and Peter Woias. "Characterization of different beam shapes for piezoelectric energy harvesting". In: *Journal of micromechanics and microengineering* 18 (2008), p. 104013.

[Hae99] Gene H Haertling. "Ferroelectric ceramics: history and technology". In: *Journal of the American Ceramic Society* 82 (1999), pp. 797–818.

Thèse accessible à l'adresse : https://theses.insa-lyon.fr/publication/2024ISAL0017/these.pdf © [G. Taxil], [2024], INSA Lyon, tous droits réservés

[Ham13] Mahmoud Aly Hamad. In: *Phase Transitions* 86 (2013), p. 307.

[Han+07] Jiaguang Han et al. "Dielectric response of soft mode in ferroelectric SrTiO3". In: *Applied Physics Letters* 90.3 (2007).

[Han+19] Brendan Hanrahan et al. In: *Energy Technology* 7 (2019), p. 1900515.

[Har11] Adnan Harb. "Energy harvesting: State-of-the-art". In: *Renewable Energy* 36 (2011), pp. 2641–2654.

[HB20] T. E. Hooper and A. J. Bell. "Landau–Devonshire derived phase diagram of the $BiFeO_3$-$PbTiO_3$ solid solution". In: *Journal of Applied Physics* 127 (2020), p. 104102.

[He04] Yi He. In: *Thermochimica Acta* 419 (2004), p. 135.

[HLO05] Zhimin He, Han Tong Loh, and Eng Hong Ong. "A probabilistic approach to evaluate the reliability of piezoelectric micro-actuators". In: *IEEE Transactions on Reliability* 54 (2005), pp. 83–91.

[HM+10] AL Herrera-May et al. "Analytical modeling for the bending resonant frequency of sensors based on micro and nanoresonators with complex structural geometry". In: *IEEE Sensors Journal* 11 (2010), pp. 1361–1374.

[Hof+15] Michael Hoffmann et al. "Ferroelectric phase transitions in nanoscale HfO2 films enable giant pyroelectric energy conversion and highly efficient supercapacitors". In: *Nano Energy* 18 (2015), pp. 154–164.

[Hug18] Thomas Huguet. "Vers une meilleure exploitation des dispositifs de récupération d'énergie vibratoire bistables : Analyse et utilisation de comportements originaux pour améliorer la bande passante". PhD thesis. 2018.

[Iot] URL: https://www.mckinsey.com/capabilities/mckinsey-digital/our-insights/the-internet-of-things-the-value-of-digitizing-the-physical-world (visited on 09/30/2023).

[Jeo+05] YB Jeon et al. "MEMS power generator with transverse mode thin film PZT". In: *Sensors and Actuators A: Physical* 122 (2005), pp. 16–22.

[JH+15] Qiu Jian-Hua et al. In: *Communications in Theoretical Physics* 64 (2015).

[Joh+06] Thomas J Johnson et al. "Energy harvesting from mechanical vibrations using piezoelectric cantilever beams". In: *Smart structures and materials 2006: Damping and isolation*. Vol. 6169. 2006, pp. 81–92.

[Kan+23] Wenbin Kang et al. "Energy harvesting using ferroelectric/ferroelastic switching: the effect of pre-poling". In: *Smart Materials and Structures* (2023).

[KC98] VD Kugel and LE Cross. "Behavior of soft piezoelectric ceramics under high sinusoidal electric fields". In: *Journal of applied physics* 84 (1998), pp. 2815–2830.

[KCH22] Wenbin Kang, Lulu Chang, and John Huber. "Investigation of mechanical energy harvesting cycles using ferroelectric/ferroelastic switching". In: *Nano Energy* 93 (2022), p. 106862.

[Kho+09a] Akram Khodayari et al. In: *IEEE Transactions on Ultrasonics, Ferroelectrics, and Frequency Control* 56 (2009), p. 693.

[Kho+09b] Akram Khodayari et al. "Nonlinear pyroelectric energy harvesting from relaxor single crystals". In: *IEEE transactions on ultrasonics, ferroelectrics, and frequency control* 56 (2009), pp. 693–699.

Thèse accessible à l'adresse : https://theses.insa-lyon.fr/publication/2024ISAL0017/these.pdf © [G. Taxil], [2024], INSA Lyon, tous droits réservés

[Kia+02] Jean-Michel Kiat et al. "Monoclinic structure of unpoled morphotropic high piezoelectric PMN-PT and PZN-PT compounds". In: *Physical Review B* 65 (2002), p. 064106.

[Kim+18] Il-Hwan Kim et al. "A new higher-order Landau–Ginzburg–Devonshire theory for KNbO3 crystal". In: *Phase Transitions* 91 (2018), pp. 1189–1205.

[Kim+22] Il-Hwan Kim et al. "A phenomenological study on temperature-concentration-electric field phase diagram of relaxor ferroelectrics PMN-PT single crystals". In: *Physica B: Condensed Matter* 639 (2022), p. 413961.

[KKD20] Asif Islam Khan, Ali Keshavarzi, and Suman Datta. "The future of ferroelectric field-effect transistor technology". In: *Nature Electronics* 3 (2020), pp. 588–597.

[KKK11] Heung Soo Kim, Joo-Hyong Kim, and Jaehwan Kim. "A review of piezoelectric energy harvesting based on vibration". In: *International journal of precision engineering and manufacturing* 12 (2011), pp. 1129–1141.

[KKK18] Tae Yun Kim, Sung Kyun Kim, and Sang-Woo Kim. "Application of ferroelectric materials for improving output power of energy harvesters". In: *Nano convergence* 5 (2018), pp. 1–16.

[Kob+97] Tsuyoshi Kobayashi et al. "Improved growth of large lead zinc niobate titanate piezoelectric single crystals for medical ultrasonic transducers". In: *Japanese journal of applied physics* 36 (1997), p. 6035.

[Kou+08] Alain B Kounga et al. "High-temperature poling of ferroelectrics". In: *Journal of Applied Physics* 104 (2008).

[KSS16] Saurabh Kumar, Rajeev Srivastava, and RK Srivastava. "Design and analysis of smart piezo cantilever beam for energy harvesting". In: *Ferroelectrics* 505 (2016), pp. 159–183.

[Kum+15] P Kumari et al. "State-of-the-art of lead free ferroelectrics: A critical review". In: *Adv. Mater. Lett* 6 (2015), pp. 453–484.

[Lal08] Mickaël Null Lallart. "Amélioration de la conversion électroactive de matériaux piézoélectriques et pyroélectriques pour le contrôle vibratoire et la récupération d'énergie-Application au contrôle de santé structurale auto-alimenté". PhD thesis. INSA de Lyon, 2008.

[Lan37] L. D. Landau. "On the theory of phase transitions". In: *Zh. Eksp. Teor. Fiz.* 7 (1937), pp. 19–32.

[LB21] Junjie. Wu Hong-Hui. Zhou Ouwei. Chen Jun. Lookman Turab. Su Yanjing. Qiao Lijie Li Jianting. Li and Yang Bai. "Influence of Phase Transitions on Electrostrictive and Piezoelectric Characteristics in PMN–30PT Single Crystals". In: *ACS Applied Materials & Interfaces* 13 (2021), pp. 38467–38476.

[LCC05a] YL Li, LE Cross, and LQ Chen. "A phenomenological thermodynamic potential for BaTiO3 single crystals". In: *Journal of Applied Physics* 98 (2005).

[LCC05b] YL Li, LE Cross, and LQ Chen. "A phenomenological thermodynamic potential for BaTiO3 single crystals". In: *Journal of Applied Physics* 98 (2005).

Thèse accessible à l'adresse : https://theses.insa-lyon.fr/publication/2024ISAL0017/these.pdf © [G. Taxil], [2024], INSA Lyon, tous droits réservés

[Lee+09] BS Lee et al. "Piezoelectric MEMS generators fabricated with an aerosol deposition PZT thin film". In: *Journal of Micromechanics and Microengineering* 19 (2009), p. 065014.

[Lef+09] Elie Lefeuvre et al. "Materials, structures and power interfaces for efficient piezoelectric energy harvesting". In: *Journal of electroceramics* 22 (2009), pp. 171–179.

[Lef+14] E Lefeuvre et al. "Self-biased inductor-less interface circuit for electret-free electrostatic energy harvesters". In: *Journal of Physics: Conference Series*. Vol. 557. 2014, p. 012052.

[LG08] Mickaël Lallart and Daniel Guyomar. "An optimized self-powered switching circuit for non-linear energy harvesting with low voltage output". In: *Smart Materials and Structures* 17 (2008), p. 035030.

[LG+12] Florian Le Goupil et al. In: *Journal of Applied Physics* 111 (2012), p. 124109.

[Lhe+22] Pierre Lheritier et al. "Large harvested energy with non-linear pyroelectric modules". In: *Nature* 609 (2022), pp. 1–4.

[Li+02] Xiaoping Li et al. "Effect of a Transverse Tensile Stress on the Electric-Field-Induced Domain Reorientation in Soft PZT: In Situ XRD Study". In: *Journal of the American Ceramic Society* 85 (2002), pp. 844–850.

[Li+12] Jiang-Yu Li et al. "Unconventional phase field simulations of transforming materials with evolving microstructures". In: *Acta Mechanica Sinica* 28 (2012).

[Li+17a] Fei Li et al. "The Contributions of Polar Nanoregions to the Dielectric and Piezoelectric Responses in Domain-Engineered Relaxor-PbTiO3 Crystals". In: *Advanced Functional Materials* 27 (2017), p. 1700310.

[Li+17b] Fei Li et al. "The contributions of polar nanoregions to the dielectric and piezoelectric responses in domain-engineered relaxor-PbTiO3 crystals". In: *Advanced Functional Materials* 27 (2017), p. 1700310.

[Li+20a] Jianting Li et al. In: *Acta Materialia* 182 (2020), p. 250.

[Li+20b] Zhonghua Li et al. In: *Acta Materialia* 191 (2020), p. 13.

[Lin+22] Mingxiang Ling et al. "Enhancing dynamic bandwidth of amplified piezoelectric actuators by a hybrid lever and bridge-type compliant mechanism". In: vol. 11. 2022, p. 134.

[Liu+16] Zhiyong Liu et al. "Optical and tunable dielectric properties of K0. 5Na0. 5NbO3–SrTiO3 ceramics". In: *Journal of the American Ceramic Society* 99 (2016), pp. 146–151.

[Liu+23] Hui Liu et al. "Emergence of high piezoelectricity from competing local polar order-disorder in relaxor ferroelectrics". In: *Nature Communications* 14 (2023), p. 1007.

[Liv13] Lawrence Livermore. "U.S. Energy flow trends - 2012". In: (2013).

[LL03] Dan Liu and JiangYu Li. "The enhanced and optimal piezoelectric coefficients in single crystalline barium titanate with engineered domain configurations". In: *Applied Physics Letters* 83 (2003), pp. 1193–1195.

[Lom20] Giulia Lombardi. "Unified nonlinear electrical interfaces for hybrid piezoelectric-electromagnetic small-scale harvesting systems". PhD thesis. 2020.

Thèse accessible à l'adresse : https://theses.insa-lyon.fr/publication/2024ISAL0017/these.pdf © [G. Taxil], [2024], INSA Lyon, tous droits réservés

[LS14] Xiaofeng Li and Vladimir Strezov. "Modelling piezoelectric energy harvesting potential in an educational building". In: *Energy Conversion and Management* 85 (2014), pp. 435–442.

[Lu+21] Xiaoyan Lu et al. "Phase stability and Landau phenomenological model of relaxor ferroelectric single crystals 0.78Pb(Mg1/3Nb2/3)O3-0.22PbTiO3". In: *Ceramics International* 47 (2021), pp. 9842–9848.

[LWL16] Yingwei Li, Jie Wang, and Faxin Li. "Intrinsic polarization switching in $BaTiO_3$ crystal under uniaxial electromechanical loading". In: *Physical Review B* 94 (2016).

[Ma+17] Zhi Ma et al. "Ferroelectric phase transition of BaTiO3 single crystal based on a tenth order Landau-Devonshire potential". In: *Computational Materials Science* 135 (2017), pp. 109–118.

[Mar+17] Madhura Marathe et al. In: *Phys. Rev. B* 96 (2017), p. 014102.

[Mar+18] A. Marthinsen et al. "Goldstone-like phonon modes in a (111)-strained perovskite". In: *Phys. Rev. Mater.* 2 (2018), p. 014404.

[McK13] I. M McKinley. "Thermomechanical Energy Conversion Using Ferroelectric Materials". PhD thesis. UCLA, 2013.

[Mer54] Walter J Merz. "Domain formation and domain wall motions in ferroelectric bati o 3 single crystals". In: *Physical Review* 95 (1954), p. 690.

[Min+06] Erika Minazara et al. "Piezoelectric diaphragm for vibration energy harvesting". In: *Ultrasonics* 44 (2006), e699–e703.

[Mis+06] AS Mischenko et al. "Giant electrocaloric effect in thin-film PbZr0. 95Ti0. 05O3". In: *Science* 311 (2006), pp. 1270–1271.

[MJC09] Shahab Mehraeen, Sarangapani Jagannathan, and Keith A Corzine. "Energy harvesting from vibration with alternate scavenging circuitry and tapered cantilever beam". In: *IEEE Transactions on Industrial Electronics* 57 (2009), pp. 820–830.

[MK94] Hiroaki Makino Hiroaki Makino and Nobuo Kamiya Nobuo Kamiya. "Effects of dc electric field on mechanical properties of piezoelectric ceramics". In: *Japanese journal of applied physics* 33 (1994), p. 5323.

[MKP12] Ian M McKinley, Razmig Kandilian, and Laurent Pilon. "Waste heat energy harvesting using the Olsen cycle on $0.945Pb(Zn_{1/3}Nb_{2/3})O_3 - 0.055PbTiO_3$ single crystals". In: *Smart Materials and Structures* 21 (2012), p. 035015.

[MLL04] Elizabeth A McLaughlin, Tieqi Liu, and Christopher S Lynch. "Relaxor ferroelectric PMN-32PT crystals under stress and electric field loading: I-32 mode measurements". In: *Acta Materialia* 52 (2004), pp. 3849–3857.

[MLL05] Elizabeth A. McLaughlin, Tieqi Liu, and Christopher S. Lynch. "Relaxor ferroelectric PMN-32PT crystals under stress, electric field and temperature loading: II-33-mode measurements". In: *Acta Materialia* 53 (2005), pp. 4001–4008.

[MMG21] Abd El-razek Mahmoud, Samar Moeen, and MK Gerges. "Enhancing the tunability properties of pure (Ba, Sr) TiO3 lead-free ferroelectric by polar nanoregion contributions". In: *Journal of Materials Science: Materials in Electronics* 32 (2021), pp. 13248–13260.

Thèse accessible à l'adresse : https://theses.insa-lyon.fr/publication/2024ISAL0017/these.pdf © [G. Taxil], [2024], INSA Lyon, tous droits réservés

[Mor+10] Keiji Morimoto et al. "High-efficiency piezoelectric energy harvesters of c-axis-oriented epitaxial PZT films transferred onto stainless steel cantilevers". In: *Sensors and Actuators A: Physical* 163 (2010), pp. 428–432.

[MS22] Dennis Meier and Sverre M Selbach. "Ferroelectric domain walls for nanotechnology". In: *Nature Reviews Materials* 7 (2022), pp. 157–173.

[MTI05] M Matsushita, Yoshihito Tachi, and Yosuke Iwasaki. "Development of large diameter piezo-single crystal PMN-PT with high energy conversion efficiency". In: *JFE Tech. Rep* 6 (2005), pp. 46–53.

[Mun+16] Seongcheol Mun et al. "Enhanced electromechanical behavior of cellulose film by zinc oxide nanocoating and its vibration energy harvesting". In: *Acta Materialia* 114 (2016), pp. 1–6.

[Mur+09] P Muralt et al. "Vibration energy harvesting with PZT micro device". In: *Procedia Chemistry* 1 (2009), pp. 1191–1194.

[M03] J. Erhart M. Šulc and J. Nosek. "Interferometric Measurement of the Temperature Dependence of Piezoelectric Coefficients for PZN-8%PT Single Crystals". In: *Ferroelectrics* 293 (2003), pp. 283–290.

[Nat+20] GF Nataf et al. "Domain-wall engineering and topological defects in ferroelectric and ferroelastic materials". In: *Nature Reviews Physics* 2 (2020), pp. 634–648.

[NZ17] Seyedfakhreddin Nabavi and Lihong Zhang. "Design and optimization of piezoelectric MEMS vibration energy harvesters based on genetic algorithm". In: *IEEE Sensors Journal* 17 (2017), pp. 7372–7382.

[OBB85] Randall B. Olsen, David A. Bruno, and J. Merv Briscoe. "Pyroelectric conversion cycles". In: *Journal of Applied Physics* 58 (1985), pp. 4709–4716.

[Pan+00] Ming-Jen Pan et al. "Comparison of actuator properties for piezoelectric and electrostrictive materials". In: vol. 3992. 2000, pp. 80–90.

[Pan+18] Shishir Pandya et al. In: *Nature Materials,* 17 (2018).

[Pan+19] Shishir Pandya et al. In: *NPG Asia Materials* 11 (2019), p. 26.

[PCV14a] Satyanarayan Patel, Aditya Chauhan, and Rahul Vaish. "A technique for giant mechanical energy harvesting using ferroelectric/antiferroelectric materials". In: *Journal of Applied Physics* 115 (2014), p. 084908.

[PCV14b] Satyanarayan Patel, Aditya Chauhan, and Rahul Vaish. "Analysis of High-Field Energy Harvesting using Ferroelectric Materials". In: *Energy Technology* 2 (2014), pp. 480–485.

[PCV14c] Satyanarayan Patel, Aditya Chauhan, and Rahul Vaish. "Enhanced energy harvesting in commercial ferroelectric materials". In: *Materials Research Express* 1 (2014), p. 025504.

[Per+10] J. Peräntie et al. In: *Phys. Rev. B* 82 (2010), p. 134119.

[Per+13] J. Peräntie et al. "Electrocaloric properties in relaxor ferroelectric $(1-x)Pb(Mg_{1/3}Nb_{2/3})O_3-$ system". In: *Journal of Applied Physics* 114 (2013), p. 174105.

[Pir+11] Raša Pirc et al. "Electrocaloric effect in relaxor ferroelectrics". In: *Journal of Applied Physics* 110 (2011).

Thèse accessible à l'adresse : https://theses.insa-lyon.fr/publication/2024ISAL0017/these.pdf © [G. Taxil], [2024], INSA Lyon, tous droits réservés

[Pol75] Alexander M Polyakov. "Interaction of goldstone particles in two dimensions. Applications to ferromagnets and massive Yang-Mills fields". In: *Physics Letters B* 59 (1975), pp. 79–81.

[Pot+11] Stephen F Poterala et al. "Processing, texture quality, and piezoelectric properties of< 001> C textured (1-x) Pb (Mg1/3Nb2/3) TiO3-xPbTiO3 ceramics". In: *Journal of Applied Physics* 110 (2011).

[Pra+12] Abhijit Pramanick et al. "Domains, domain walls and defects in perovskite ferroelectric oxides: A review of present understanding and recent contributions". In: *Critical Reviews in Solid State and Materials Sciences* 37 (2012), pp. 243–275.

[Pro+20] Sergey Prosandeev et al. "Evidence for Goldstone-like and Higgs-like structural modes in the model $PbMg_{1/3}Nb_{2/3}O_3$ relaxor ferroelectric". In: *Phys. Rev. B* 102 (2020), p. 104110.

[PS97a] Seung-Eek Park and Thomas R Shrout. "Relaxor based ferroelectric single crystals for electro-mechanical actuators". In: *Materials Research Innovations* 1 (1997), pp. 20–25.

[PS97b] Seung-Eek Park and Thomas R Shrout. "Ultrahigh strain and piezoelectric behavior in relaxor based ferroelectric single crystals". In: *Journal of applied physics* 82 (1997), pp. 1804–1811.

[QD11] Antonio Carlos M de Queiroz and Marcelo Domingues. "The doubler of electricity used as battery charger". In: *IEEE Transactions on Circuits and Systems II: Express Briefs* 58 (2011), pp. 797–801.

[Qiu+15] J. H. Qiu et al. In: *Journal of Applied Physics* 117.7 (2015), p. 074101.

[QXZ19] Feng Qian, Tian-Bing Xu, and Lei Zuo. "Piezoelectric energy harvesting from human walking using a two-stage amplification mechanism". In: *Energy* 189 (2019), p. 116140.

[Rab+07] Karin M. Rabe et al. "Modern Physics of Ferroelectrics:Essential Background". In: *Physics of Ferroelectrics: A Modern Perspective*. Springer Berlin Heidelberg, 2007, pp. 1–30.

[Raj+07] K.K. Rajan et al. "Dielectric and piezoelectric properties of [001] and [011]-poled relaxor ferroelectric PZN–PT and PMN–PT single crystals". In: *Sensors and Actuators A: Physical* 133 (2007), pp. 110–116. DOI: https://doi.org/10.1016/j.sna.2006.03.036.

[Rav+11] SKT Ravindran et al. "A self-sustaining micro thermomechanic-pyroelectric generator". In: *Applied Physics Letters* 99 (2011).

[RC12] Maimon C Rose and Ronald E Cohen. "Giant electrocaloric effect around T c". In: *Physical review letters* 109 (2012), p. 187604.

[Ren+02] W Ren et al. "Nonlinear strain and DC bias induced piezoelectric behaviour of electrostrictive lead magnesium niobate-lead titanate ceramics under high electric fields". In: *Journal of Physics D: Applied Physics* 35 (2002), p. 1550.

[Ren+14] Pengrong Ren et al. "Phase transition, high figure of merit and polar nano-regions in dielectric tunable lanthanum substituted barium titanate". In: *Journal of Alloys and Compounds* 617 (2014), pp. 337–344.

[Rol+22] Krystian Roleder et al. "Monoclinic domain populations and enhancement of piezoelectric properties in a PZT single crystal at the morphotropic phase boundary". In: *Phys. Rev. B* 105 (2022), p. 144104.

Thèse accessible à l'adresse : https://theses.insa-lyon.fr/publication/2024ISAL0017/these.pdf © [G. Taxil], [2024], INSA Lyon, tous droits réservés

[Ros+16] Hossein Roshani et al. "Energy harvesting from asphalt pavement roadways vehicle-induced stresses: A feasibility study". In: *Applied Energy* 182 (2016), pp. 210–218.

[RWR03] Shad Roundy, Paul K Wright, and Jan Rabaey. "A study of low level vibrations as a power source for wireless sensor nodes". In: *Computer communications* 26 (2003), pp. 1131–1144.

[RYK19] Hanjun Ryu, Hong-Joon Yoon, and Sang-Woo Kim. "Hybrid energy harvesters: toward sustainable energy harvesting". In: *Advanced Materials* 31 (2019), p. 1802898.

[Sal+07] E. K. H. Salje et al. In: *Applied Physics Letters* 90 (2007), p. 221903.

[SC10] Aneta Slodczyk and Philippe Colomban. "Probing the Nanodomain Origin and Phase Transition Mechanisms in (Un)Poled PMN-PT Single Crystals and Textured Ceramics". In: *Materials* 3 (2010), pp. 5007–5028.

[SC14] Enwei Sun and Wenwu Cao. "Relaxor-based ferroelectric single crystals: Growth, domain engineering, characterization and applications". In: *Progress in materials science* 65 (2014), pp. 124–210.

[Sch+17] Jutta Schwarzkopf et al. "Strain engineering of ferroelectric domains in KxNa1- xNbO3 epitaxial layers". In: *Frontiers in Materials* 4 (2017), p. 26.

[SCZ07] K Kirk Shung, JM Cannata, and QF Zhou. "Piezoelectric materials for high frequency medical imaging applications: A review". In: *Journal of Electroceramics* 19 (2007), pp. 141–147.

[Seb+23] Gael Sebald et al. "Piezoelectric small scale generator: towards near-Joule output energy generation". In: *Smart Materials and Structures* 32 (2023), p. 085009.

[ŠEN03] M Šulc, J Erhart, and J Nosek. "Interferometric measurement of the temperature dependence of piezoelectric coefficients for PZN-8% PT single crystals". In: *Ferroelectrics* 293 (2003), pp. 283–290.

[SH20] A. N. Smith and B. M. Hanrahan. In: *Journal of Applied Physics* 128.2 (2020), p. 024103.

[Sha+07] M. Shanthi et al. "Dielectric and piezoelectric properties of [0 0 1] and [0 1 1]-poled relaxor ferroelectric PZN–PT and PMN–PT single crystals". In: *Sensors and Actuators A-physical - SENSOR ACTUATOR A-PHYS* 133 (2007), pp. 110–116.

[Sha+21] Amrit Sharma et al. In: *Scientific Reports* 11 (2021), p. 111.

[She+08] Dongna Shen et al. "The design, fabrication and evaluation of a MEMS PZT cantilever with an integrated Si proof mass for vibration energy harvesting". In: *Journal of Micromechanics and Microengineering* 18 (2008), p. 055017.

[She+09] Dongna Shen et al. "Micromachined PZT cantilever based on SOI structure for low frequency vibration energy harvesting". In: *Sensors and actuators A: physical* 154 (2009), pp. 103–108.

[She+10] Guang Sheng et al. "A modified Landau–Devonshire thermodynamic potential for strontium titanate". In: *Applied Physics Letters* 96 (2010).

Thèse accessible à l'adresse : https://theses.insa-lyon.fr/publication/2024ISAL0017/these.pdf © [G. Taxil], [2024], INSA Lyon, tous droits réservés

[Shi+70] G Shirane et al. "Soft ferroelectric modes in lead titanate". In: *Physical Review B* 2 (1970), p. 155.

[SK21] Nurettin Sezer and Muammer Koç. "A comprehensive review on the state-of-the-art of piezoelectric energy harvesting". In: *Nano Energy* 80 (2021), p. 105567.

[SL12] Vladimir V Shvartsman and Doru C Lupascu. "Lead-free relaxor ferroelectrics". In: *Journal of the American Ceramic Society* 95 (2012), pp. 1–26.

[SLG08] Gael Sebald, Elie Lefeuvre, and Daniel Guyomar. "Pyroelectric energy conversion: optimization principles". In: *IEEE transactions on ultrasonics, ferroelectrics, and frequency control* 55 (2008), pp. 538–551.

[Smi+08] Millicent B Smith et al. "Crystal structure and the paraelectric-to-ferroelectric phase transition of nanoscale BaTiO3". In: *Journal of the American Chemical Society* 130 (2008), pp. 6955–6963.

[Sod+07] Henry A. Sodano et al. In: *Journal of Intelligent Material Systems and Structures* 18 (2007), pp. 3–10.

[Son+16] Yewon Song et al. "Road energy harvester designed as a macro-power source using the piezoelectric effect". In: *International Journal of Hydrogen Energy* 41 (2016), pp. 12563–12568.

[SPG07] Gael Sebald, Sebastien Pruvost, and Daniel Guyomar. In: *Smart Materials and Structures* 17 (2007), p. 015012.

[Ste06] Neil G Stephen. "On energy harvesting from ambient vibration". In: *Journal of sound and vibration* 293 (2006), pp. 409–425.

[Sul+18] Ayesha Sultana et al. In: *Applied Energy* 221 (2018), pp. 299–307.

[Sun+22] Shengdong Sun et al. "Large piezoelectricity and potentially activated polarization reorientation around relaxor MPB in complex perovskite". In: *Journal of the European Ceramic Society* 42 (2022), pp. 112–118.

[SVP16] Nathan Sharpes, Dušan Vučković, and Shashank Priya. "Floor Tile Energy Harvester for Self-Powered Wireless Occupancy Sensing". In: *Energy Harvesting and Systems* 3 (2016), pp. 43–60.

[Tan+16] Peng Tan et al. "Temperature field driven polar nanoregions in KTa1-xNbxO3". In: *Applied Physics Letters* 109 (2016).

[Tan69] Kensuke Tani. "Dynamics of displacive-type ferroelectrics–soft modes–". In: *Journal of the Physical Society of Japan* 26 (1969), pp. 93–107.

[Tax+22] G. Taxil et al. "Modeling of Olsen cycle for pyroelectric energy harvesting and assessment of abnormal electrocaloric effect in ferroelectric single crystals". In: *Journal of Applied Physics* 132 (2022), p. 144101.

[Tax+23] Gaspard Taxil et al. "Stress and electric field induced phase transitions for ultra high energy conversion in ferroelectrics". In: *Acta Materialia* 261 (2023), p. 119367.

[TFT02] D. Munz T. Fett and G. Thun. "Young's Modulus of Soft PZT from Partial Unloading Tests". In: *Ferroelectrics* 274 (2002), pp. 67–81.

[TOY93] Toshio Tanimoto, Kiyoshi Okazaki Kiyoshi Okazaki, and Kohji Yamamoto Kohji Yamamoto. "Tensile Stress-Strain Behavior of Piezoelectric Ceramics". In: *Japanese Journal of Applied Physics* 32 (1993), p. 4233.

Thèse accessible à l'adresse : https://theses.insa-lyon.fr/publication/2024ISAL0017/these.pdf © [G. Taxil], [2024], INSA Lyon, tous droits réservés

[Tun+22] Nguyen Thanh Tung et al. "Ultimate electromechanical energy conversion performance and energy storage capacity of ferroelectric materials under high excitation levels". In: *Applied Energy* 326 (2022), p. 119984.

[Unr+19] Muangjai Unruan et al. "Estimation of energy density of PMN-PT ceramics utilizing mechanical stress". In: *Integrated Ferroelectrics* 195 (2019), pp. 39–45.

[Val20] Marco Vallone. "Higgs and Goldstone modes in crystalline solids". In: *physica status solidi (b)* 257 (2020), p. 1900443.

[Vas04] Aleksandr Nikolaevich Vasil'ev. *The field theoretic renormalization group in critical behavior theory and stochastic dynamics*. CRC press, 2004.

[VC01] David Vanderbilt and Morrel H. Cohen. "Monoclinic and triclinic phases in higher-order Devonshire theory". In: *Phys. Rev. B* 63 (2001), p. 094108.

[Vil+13] LG Villanueva et al. "Nonlinearity in nanomechanical cantilevers". In: *Physical Review B* 87 (2013), p. 024304.

[VK15] Elena Vanz and Justyna Karakiewicz. "Pedestrian as Generator: Implementing a Stand-Alone Piezo Power Generating Device in the Urban Context". In: *Computer-Aided Architectural Design Futures. The Next City - New Technologies and the Future of the Built Environment*. 2015, pp. 154–171.

[Wad+05] Satoshi Wada et al. "Enhanced piezoelectric properties of barium titanate single crystals with different engineered-domain sizes". In: *Journal of Applied Physics* 98 (2005), p. 014109.

[Wad+99] Satoshi Wada et al. "Enhanced Piezoelectric Property of Barium Titanate Single Crystals with Engineered Domain Configurations". In: *Japanese Journal of Applied Physics* 38 (1999).

[Wan+10a] J. J. Wang et al. In: *Journal of Applied Physics* 108 (2010), p. 114105.

[Wan+10b] J. J. Wang et al. "Temperature-pressure phase diagram and ferroelectric properties of $BaTiO_3$ single crystal based on a modified Landau potential". In: *Journal of Applied Physics* 108 (2010), p. 114105.

[Wan+12] Wei Wang et al. "Vibration energy harvesting using a piezoelectric circular diaphragm array". In: *IEEE transactions on ultrasonics, ferroelectrics, and frequency control* 59 (2012), pp. 2022–2026.

[Wan+22a] Jianjun Wang et al. "A piezoelectric smart backing ring for high-performance power generation subject to train induced steel-spring fulcrum forces". In: *Energy Conversion and Management* 257 (2022), p. 115442.

[Wan+22b] Keng Wang et al. "Pressure-induced room temperature electrocaloric effect in BiFeO3-PbTiO3 solid solution based on Landau-Devonshire theory". In: *Materials Today Communications* 31 (2022), p. 103396.

[Wan+23] Jiajia Wang et al. "High piezoelectricity and low strain hysteresis in PMN–PT-based piezoelectric ceramics". In: *Journal of Advanced Ceramics* 12 (2023), pp. 792–802.

[WC17] H. H. Wu and R. E. Cohen. "Electric-field-induced phase transition and electrocaloric effect in PMN-PT". In: *Phys. Rev. B* 96 (2017), p. 054116.

[Wei+22] Xian-Kui Wei et al. "Progress on emerging ferroelectric materials for energy harvesting, storage and conversion". In: *Advanced Energy Materials* 12 (2022), p. 2201199.

Thèse accessible à l'adresse : https://theses.insa-lyon.fr/publication/2024ISAL0017/these.pdf © [G. Taxil], [2024], INSA Lyon, tous droits réservés

[Wha91] RW Whatmore. "Pyroelectric ceramics and devices for thermal infrared detection and imaging". In: *Ferroelectrics* 118 (1991), pp. 241–259.

[Won+08] N Wongdamnern et al. "Comparative studies of dynamic hysteresis responses in hard and soft PZT ceramics". In: *Ceramics international* 34 (2008), pp. 731–734.

[Wu+09] Liying Wu et al. "Relaxor behavior of (1- x) BaTiO 3–x (Bi 3/4 Na 1/4)(Mg 1/4 Ti 3/4) O 3 (0.2 x 0.9) ferroelectric ceramic". In: *Journal of materials science* 44 (2009), pp. 5420–5427.

[WZL08] Kyle G. Webber, Ruzhong Zuo, and Christopher S. Lynch. "Ceramic and single-crystal (1-x)PMN-xPT constitutive behavior under combined stress and electric field loading". In: *Acta Materialia* 56 (2008), pp. 1219–1227.

[Xio14] Haocheng Xiong. "Piezoelectric energy harvesting for public roadways". PhD thesis. 2014.

[Xu+13] Qing Xu et al. "Evolution of dielectric properties in BaZrxTi1xO3 ceramics: Effect of polar nano-regions". In: *Acta Materialia* 61 (2013), pp. 4481–4489.

[Xu+18a] Xiaochen Xu et al. "Application of piezoelectric transducer in energy harvesting in pavement". In: *International Journal of Pavement Research and Technology* 11 (2018), pp. 388–395.

[Xu+18b] Xiaochen Xu et al. "Application of piezoelectric transducer in energy harvesting in pavement". In: *International Journal of Pavement Research and Technology* 11 (2018), pp. 388–395.

[Xue+15] A'Xi Xue et al. "Uniaxial stress-induced ferroelectric depolarization in <001>-oriented $0.72Pb(Mg_{1/3}Nb_{2/3})O_3 - 0.28PbTiO_3$ single crystal". In: *Journal of Alloys and Compounds* 647 (2015), pp. 14–17.

[Yan+04] Hong Yang et al. "Dielectric breakdown properties of Zr-rich lead zirconate titanate ceramics". In: *Japanese journal of applied physics* 43 (2004), p. 7579.

[Yan+22a] Xiaodong Yan et al. "Ultrahigh energy harvesting performance in lead-free piezocomposites with intragranular structure". In: *Acta Materialia* 222 (2022), p. 117450.

[Yan+22b] Liya Yang et al. "Simultaneously achieving giant piezoelectricity and record coercive field enhancement in relaxor-based ferroelectric crystals". In: *Nature Communications* 13 (2022).

[Yao+22] Kui Yao et al. "Enabling distributed intelligence with ferroelectric multifunctionalities". In: *Advanced Science* 9 (2022), p. 2103842.

[Ye+14] Hui-Jian Ye et al. "Giant electrocaloric effect in BaZr0. 2Ti0. 8O3 thick film". In: *Applied Physics Letters* 105 (2014).

[Ye98] ZG Ye. "Relaxor ferroelectric complex perovskites: structure, properties and phase transitions". In: *Key Engineering Materials* 155 (1998), pp. 81–122.

[Yin+99] Zhi-Wen Yin et al. "Growth, characterization and properties of relaxor ferroelectric PMN-PT single crystals". In: *Ferroelectrics* 229 (1999), pp. 207–216.

Thèse accessible à l'adresse : https://theses.insa-lyon.fr/publication/2024ISAL0017/these.pdf © [G. Taxil], [2024], INSA Lyon, tous droits réservés

[Yos05] TACHI Yoshihito. "Development of Large Diameter Piezo-single Crystal PMN-PT of High Energy Transfer Efficiency". In: *JFE Technical Report* (2005).

[Zgo+94] M. Zgonik et al. "Dielectric, elastic, piezoelectric, electro-optic, and elastooptic tensors of $BaTiO_3$ crystals". In: *Phys. Rev. B* 50 (1994), pp. 5941–5949.

[Zha+05] X. Zhao et al. "Relaxor ferroelectric characteristics and temperature-dependent domain structure in a (110)-cut $(PbMg_{1/3}Nb_{2/3}O_3) - 0.75(PbTiO_3)_{0.25}$ single crystal". In: *Phys. Rev. B* 72 (2005), p. 064114.

[Zha+17] Hangbo Zhang et al. "Phase coexistence and Landau expansion parameters for a 0.70Pb(Mg1/3Nb2/3)O30.30PbTiO3 single crystal". In: *Physical Review B* 96 (2017).

[Zha+18] Yulong Zhang et al. "Micro electrostatic energy harvester with both broad bandwidth and high normalized power density". In: *Applied Energy* 212 (2018), pp. 362–371.

[Zha+20] Y Zhao et al. "Effect of phase transition on electrocaloric effect in Indium substituted BaTiO3 ceramics". In: *Journal of Alloys and Compounds* 822 (2020), p. 153632.

[Zha+22] H. Zhang et al. In: *Acta Materialia* 228 (2022), p. 117761.

[Zhu+17] Fangping Zhuo et al. In: *Journal of Applied Physics* 121 (2017), p. 064104.

Thèse accessible à l'adresse : https://theses.insa-lyon.fr/publication/2024ISAL0017/these.pdf © [G. Taxil], [2024], INSA Lyon, tous droits réservés

FOLIO ADMINISTRATIF

THESE DE L'INSA LYON, MEMBRE DE L'UNIVERSITE DE LYON

NOM : TAXIL DATE de SOUTENANCE : 01/02/2024

Prénoms : Gaspard

TITRE : Modeling, characterization and implementation of ferroelectric materials and their phase transitions for energy harvesting under extreme conditions.

NATURE : Doctorat Numéro d'ordre : 2024ISAL0017

Ecole doctorale : Électronique, Électrotechnique et Automatique (EEA)

Spécialité : Génie électrique

RESUME : Ce travail de recherche se concentre sur l'utilisation des transitions de phases des matériaux ferroélectriques pour la récupération d'énergie mécanique. La récupération d'énergie mécanique est une approche alternative pour alimenter des dispositifs et des capteurs. Cela est d'un grand intérêt, surtout compte tenu de l'essor des dispositifs interconnectés et du besoin de produire de l'électricité décarbonée. Cette thèse a la particularité de s'intéresser aux systèmes non résonnants, ce qui reste encore peu exploité en récupération d'énergie. L'un des principaux défis avec cette approche est la nécessité de maximiser la récupération d'énergie par cycle pour la rendre viable. Ainsi, l'utilisation de cycles thermodynamiques permet d'optimiser l'énergie récoltée. Le cycle d'Ericsson, communément appelé cycle d'Olsen dans le domaine de la récupération d'énergie pyroélectrique, a attiré l'attention en raison de ses remarquables capacités de conversion d'énergie. Ce cycle comprend deux processus isostatiques et deux processus isoélectriques et il offre une bonne solution pour la récupération d'énergie mécanique non résonante. Dans ce contexte, les matériaux ferroélectriques (une classe particulière des matériaux piézoélectriques) montrent un potentiel significatif pour être utilisés dans la récupération d'énergie mécanique en tant que transducteur en raison de leurs propriétés exceptionnelles. Une caractéristique notable de ces matériaux est leur capacité à afficher des transitions de phase induites par des variations de température, de champ électrique et de contrainte. L'exploitation de ces transitions de phases peut s'avérer prometteur pour améliorer la récupération d'énergie, étant donné que les matériaux présentent des propriétés non linéaires à proximité de ces transitions. Ainsi, ce travail propose grâce à la modélisation, la caractérisation et l'implémentation de ces matériaux ferroélectriques dans des dispositifs de récupération d'énergie, d'utiliser ces non-linéarités induites par la contrainte et par le champ électrique pour améliorer la conversion d'énergie mécanique.

MOTS-CLÉS : Récupération d'énergie – Transitions de phases – Ferroélectricité – Modélisation – Systèmes mécanique
Energy harvesting – Phase transitions – Ferroelectricity – Modeling – Mechanical Systems

Laboratoire (s) de recherche : Laboratoire de Génie Électrique et Ferroélectricité (LGEF) - INSA Lyon, Graduate School of Engineering – Tohoku University

Directeur de thèse : Mickaël LALLART

Président de jury : GAUTIER Brice

Composition du jury :

DEFAY Emmanuel	Professeur/University of Luxembourg	Rapporteur
KANNO Isaku	Professeur/Kobe University	Rapporteur
LAFFEZ Isabelle	Professeur/Université de Tours	Examinatrice
GAUTIER Brice	Professeur/INSA Lyon	Examinateur
LALLART Mickaël	Professeur/INSA Lyon	Directeur de thèse
ONO Takahito	Professeur/Tohoku University	Directeur de thèse
SEBALD Gaël	Professeur/INSA Lyon	Invité
DUCHARNE Benjamin	Maître de conférences/INSA Lyon	Invité

Thèse accessible à l'adresse : https://theses.insa-lyon.fr/publication/2024ISAL0017/these.pdf © [G. Taxil], [2024], INSA Lyon, tous droits réservés